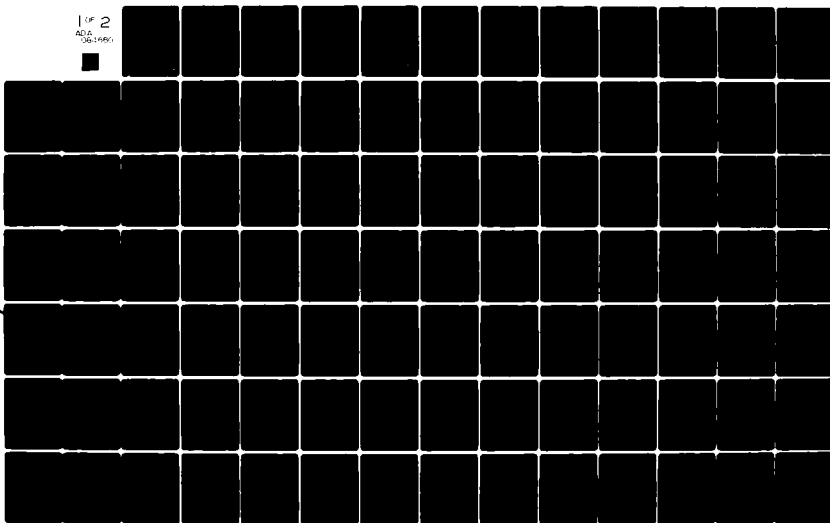


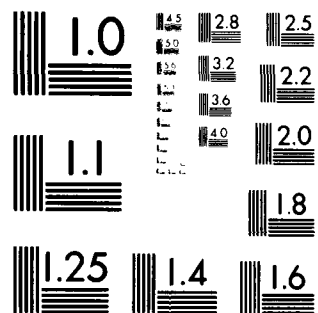
AD-A084 660

SYSTEMS SCIENCE AND SOFTWARE LA JOLLA CA F/G 8/11
BLOCK MOTION ESTIMATES FROM SEISMOLOGICAL OBSERVATIONS OF MIGHT--ETC(U)
JUL 79 T C BACHE, W E FARRELL, D G LAMBERT DNA001-77-C-0260
SSS-R-79-4080 DNA-5007F NL

UNCLASSIFIED

1 OF 2
ADA
06-1165





MICROCOPY RESOLUTION TEST CHART
NATIONAL BUREAU OF STANDARDS-1963-A

AD-E300755

LEVEL

12

✓DNA 5007F

ADA084660

BLOCK MOTION ESTIMATES FROM SEISMOLOGICAL OBSERVATIONS OF MIGHTY EPIC AND DIABLO HAWK

T. C. Bache
W. E. Farrell
D. G. Lambert
Systems, Science and Software
P.O. Box 1620
La Jolla, California 92038

1 July 1979

Final Report for Period 30 October 1978—30 June 1979

CONTRACT No. DNA 001-77-C-0260

APPROVED FOR PUBLIC RELEASE;
DISTRIBUTION UNLIMITED.

THIS WORK SPONSORED BY THE DEFENSE NUCLEAR AGENCY
UNDER RDT&E RMSS CODES B344077464 Y99QAXS804909 H2590D
AND B344078464 Y99QAXSC37014 H2590D.

FILE COPY

Prepared for
Director
DEFENSE NUCLEAR AGENCY
Washington, D. C. 20305

DTIC
ELECTE
MAY 27 1980
S D

80 4 4 017

Destroy this report when it is no longer needed. Do not return to sender.

PLEASE NOTIFY THE DEFENSE NUCLEAR AGENCY,
ATTN: STTI, WASHINGTON, D.C. 20305, IF
YOUR ADDRESS IS INCORRECT, IF YOU WISH TO
BE DELETED FROM THE DISTRIBUTION LIST, OR
IF THE ADDRESSEE IS NO LONGER EMPLOYED BY
YOUR ORGANIZATION.



UNCLASSIFIED

SECURITY CLASSIFICATION OF THIS PAGE (When Data Entered)

REPORT DOCUMENTATION PAGE		READ INSTRUCTIONS BEFORE COMPLETING FORM
1. REPORT NUMBER DNA 5007F	2. GOVT ACCESSION NO. AD-A034660	3. RECIPIENT'S CATALOG NUMBER
4. TITLE (and Subtitle) BLOCK MOTION ESTIMATES FROM SEISMOLOGICAL OBSERVATIONS OF MIGHTY EPIC AND DIABLO HAWK		5. TYPE OF REPORT & PERIOD COVERED Final Report for Period 30 Oct 78—30 Jun 79
		6. PERFORMING ORG. REPORT NUMBER SSS-R-79-4080
7. AUTHOR(s) T. C. Bache W. E. Farrell D. G. Lambert		8. CONTRACT OR GRANT NUMBER(s) DNA 001-77-C-0260
9. PERFORMING ORGANIZATION NAME AND ADDRESS Systems, Science and Software P.O. Box 1620 La Jolla, California 92038		10. PROGRAM ELEMENT, PROJECT, TASK AREA & WORK UNIT NUMBERS Subtasks Y99QAXSB049-09 and Y99QAXSC370-14
11. CONTROLLING OFFICE NAME AND ADDRESS Director Defense Nuclear Agency Washington, D.C. 20305		12. REPORT DATE 1 July 1979
		13. NUMBER OF PAGES 186
14. MONITORING AGENCY NAME & ADDRESS (if different from Controlling Office)		15. SECURITY CLASS (of this report) UNCLASSIFIED
		15a. DECLASSIFICATION DOWNGRADING SCHEDULE
16. DISTRIBUTION STATEMENT (of this Report) Approved for public release; distribution unlimited.		
17. DISTRIBUTION STATEMENT (of the abstract entered in Block 20, if different from Report)		
18. SUPPLEMENTARY NOTES This work sponsored by the Defense Nuclear Agency under RDT&E RMSS Codes B344078464 Y99QAXSC37014 H2590D and B344077464 Y99QAXSB04909 H2590D.		
19. KEY WORDS (Continue on reverse side if necessary and identify by block number) Nuclear Explosion Seismology Regional Seismograms Tectonic Stress Release		
20. ABSTRACT (Continue on reverse side if necessary and identify by block number) Seismological observations of the underground explosions MIGHTY EPIC and DIABLO HAWK were used to infer the extent of the block motions associated with these events. The data were three-component velocity recordings from the nine station seismic network operated by Lawrence Livermore Laboratory (LLL) and Sandia Laboratories at ranges from 131 to 368 km. Five additional stations were fielded by Systems, Science and Software (S ³) for DIABLO HAWK. The two events were first compared by cross-spectral analysis of common recordings.		

DD FORM 1473

EDITION OF 1 NOV 65 IS OBSOLETE

UNCLASSIFIED

SECURITY CLASSIFICATION OF THIS PAGE (When Data Entered)

385

UNCLASSIFIED

SECURITY CLASSIFICATION OF THIS PAGE(When Data Entered)

20. ABSTRACT (Continued)

A key conclusion of this analysis is that the long period waves generated by MIGHTY EPIC were about 75 percent larger than for DIABLO HAWK while the short period source levels differed by about 15 percent. This difference was observed on almost all common recordings.

The events were individually analyzed using a narrow-band filter program to identify the long period fundamental mode Love and Rayleigh waves. The source was then assumed to consist of a spherically symmetric explosion and the block motion generated double-couple. For DIABLO HAWK the amplitudes of the six second Love, Rayleigh and Love/Rayleigh ratio were fit by a solution with faulting oriented N16°E and a seismic moment of 1.3×10^{21} dyne-cm. The sparser data for MIGHTY EPIC were fit with less confidence and a moment of 2.6×10^{21} dyne-cm. For both events, rather small average displacements on a total fault plane area of 0.1-0.5 km² are sufficient to account for the observed seismic waves. Large displacements (> 50 cm) can only occur on smaller areas which are characterized by large stress concentrations. The block motions were somewhat larger for MIGHTY EPIC than for DIABLO HAWK.

UNCLASSIFIED

SECURITY CLASSIFICATION OF THIS PAGE(When Data Entered)

PREFACE

Most of the data used in this analysis was kindly provided by seismologists at Lawrence Livermore Laboratory (LLL) and Sandia Laboratories. The assistance of the staff at these institutions, especially Robert Rohrer and Marvin Denny at LLL and Leo Brady, Doris Tendall and Douglas Gabin at Sandia is gratefully acknowledged. The authors derived great benefit from the advice and assistance of many of our colleagues at Systems, Science and Software (S³), especially Russell Duff, the Principal Investigator on the project. We also wish to acknowledge the contributions of William Rodi, John Savino and Steven Day.

Accession For	
NTIS GRA&I	<input checked="checked" type="checkbox"/>
DDC TAB	<input type="checkbox"/>
Unannounced	<input type="checkbox"/>
Justification	
By	
Distribution/	
Availability Codes	
Dist.	Avail and/or special
A	

DTIC
ELECTE
S MAY 27 1980 D

TABLE OF CONTENTS

	Page
I. INTRODUCTION AND SUMMARY	11
1.1 INTRODUCTION	11
1.2 BLOCK MOTION IMPLICATIONS OF SEISMOLOGICAL DATA	13
1.3 DESCRIPTION OF THE DATA	14
1.4 OUTLINE OF THE REPORT	14
1.5 CONCLUSIONS ABOUT THE RELATIVE MOTIONS . .	15
1.6 CONCLUSIONS ABOUT THE DOUBLE-COUPLE . . .	17
1.7 BOUNDS OF THE BLOCK MOTION	19
1.8 SUMMARY REMARKS	21
II. SOURCES OF DATA	24
2.1 LAWRENCE LIVERMORE DATA	27
2.2 SANDIA DATA	29
2.3 SYSTEMS, SCIENCE AND SOFTWARE DATA	30
2.4 OTHER DATA	43
III. ANALYSIS METHODS	44
3.1 SPECTRAL RATIOS	44
3.2 PASSBAND FILTERING	46
3.3 MULTIPLE ARRIVAL RECOGNITION SYSTEM (MARS) ANALYSIS	47
IV. RELATIVE GROUND MOTIONS	56
4.1 GENERAL DEPENDENCE OF ADMITTANCE ON FREQUENCY	58
4.2 RESULTS FOR MINA	62
4.3 RESULTS FOR LANDERS	69

	Page
4.3.1 Transfer Functions for Three Different Time Windows	69
4.3.2 Transfer Functions with Five Frequency Resolutions	74
4.3.3 Transfer Function Between the Three Components of Motion	75
4.4 RESULTS FOR LEEDS	78
4.5 CONCLUDING REMARKS	81
V. DOUBLE-COUPLE AMPLITUDES	83
5.1 INTRODUCTION	83
5.2 THEORETICAL MODEL	84
5.3 TRAVEL PATH MODELS AND STATION CLASSIFI- CATION	88
5.4 LOVE AND RAYLEIGH WAVE AMPLITUDES	103
5.5 ESTIMATION OF THE DOUBLE-COUPLE	123
5.5.1 DIABLO HAWK Double-Couple	123
5.5.2 MIGHTY EPIC Double-Couple	135
5.6 SUMMARY	145
VI. BOUNDS FOR THE BLOCK MOTIONS	149
REFERENCES	156
APPENDIX A	159

LIST OF ILLUSTRATIONS

Number		Page
2.1	Polar plot centered on the MIGHTY EPIC/ DIABLO HAWK source location showing the distance and azimuth to the LLL, Sandia and S ³ seismic stations.	28
2.2	Amplitude response of the Sprengnether seismograph model, plotted on a logarithmic frequency scale between 0.1 Hz and 10 Hz . . .	34
2.3	Phase response of the Sprengnether seismo- graph model, plotted on a logarithmic fre- quency scale between 0.1 Hz and 10 Hz.	35
2.4	The vertical component seismograms from NTS event LOWBALL recorded at Landers by the S ³ Sprengnether digital seismograph and the LLL broad-band seismometers.	37
2.5	The power spectrums of the two LOWBALL seis- mograms displayed in Figure 2.4.	38
2.6	The coherency between the S ³ LOWBALL record- ing and the LLL LOWBALL recording.	39
2.7	The admittance of the S ³ Sprengnether seismom- eter system estimated by the cross spectrum analysis	41
2.8	Comparison between the Sprengnether transfer function estimated by modeling the seismograph system response (H_m) and the transfer function (H_0) calculated from a cross spectrum analysis of event LOWBALL recorded at LLL station Landers by the LLL and S ³ seismographs	42
3.1	The amplitude response of the zero phase shift filter used to isolate the 4 to 8 second period range on all the seismograms.	48
3.2	The MIGHTY EPIC seismograms recorded at Mina, and the long period surface waves obtained by band pass filtering the recorded signal using the filter displayed in Figure 3.1	49
3.3	Flowchart of the MARS operation.	50
3.4	The equations applied during analysis of seismograms by MARS.	51

LIST OF ILLUSTRATIONS (Continued)

Number		Page
3.5	The result of processing the DIABLO HAWK vertical component seismogram recorded by S ³ at Shellbourne with the staggered narrow band filters used in the MARS analysis.	53
3.6	The result of processing the DIABLO HAWK transverse component seismogram recorded by S ³ at Shellbourne with the staggered narrow band filters used in the MARS analysis.	54
4.1	The power spectrums calculated for the vertical component of ground velocity at Mina from MIGHTY EPIC and DIABLO HAWK	63
4.2	The coherency squared calculated between the MIGHTY EPIC and DIABLO HAWK vertical component seismograms recorded at Mina.	64
4.3	The admittance or modulus of the transfer function, relating to the DIABLO HAWK and MIGHTY EPIC vertical component seismograms at Mina	65
4.4	The phase angle of the transfer function relating the MIGHTY EPIC and DIABLO HAWK vertical component seismograms at Mina	67
4.5	The impulse response of the smoothed filter relating the MIGHTY EPIC and DIABLO HAWK vertical component seismograms recorded at Mina.	68
4.6	Demonstration of the degree to which the filter plotted in Figure 4.5 turns the MIGHTY EPIC vertical component seismogram (A) into the DIABLO HAWK seismogram for station Mina . .	70
4.7	Transfer functions for three different time windows applied to the Landers recordings . . .	72
4.8	The coherency and admittance relating the three components of motion for MIGHTY EPIC recorded at Landers	76
4.9	Power spectra for the three components of motion for MIGHTY EPIC recorded at Landers. . .	77

LIST OF ILLUSTRATIONS (Continued)

Figure		Page
4.10	The coherency and admittance relating the three components of motion for MIGHTY EPIC recorded at Leeds.	79
4.11	Power spectra for the three components of motion for MIGHTY EPIC recorded at Leeds . . .	80
5.1	Shear velocity is plotted versus depth for two crustal models	89
5.2	Group velocity dispersion for the theoretical models of Figure 5.1	92
5.3a	Vertical velocities for MIGHTY EPIC.	95
5.3b	Vertical velocities for DIABLO HAWK.	96
5.4a	Tangential velocities for MIGHTY EPIC.	97
5.4b	Tangential velocities for DIABLO HAWK.	98
5.5a	Vertical velocities for MIGHTY EPIC after filtering with a 4-8 second bandpass filter. .	99
5.5b	Vertical velocities for DIABLO HAWK after filtering with a 4-8 second bandpass filter. .	100
5.6a	Tangential velocities for MIGHTY EPIC after filtering with a 4-8 second bandpass filter. .	101
5.6b	Tangential velocities for DIABLO HAWK after filtering with a 4-8 second bandpass filter. .	102
5.7	Observed group velocity dispersion at the eleven stations recording MIGHTY EPIC and/or DIABLO HAWK	104
5.8	Spectral amplitudes from MARS processing of the DIABLO HAWK and MIGHTY EPIC seismograms. .	109
5.9	MIGHTY EPIC amplitudes versus range.	120
5.10	DIABLO HAWK amplitudes versus range.	121
5.11	Error contours for LQ/LR, F versus θ_s , for DIABLO HAWK assuming, $\delta = 90$, $\lambda = 0$	125

LIST OF ILLUSTRATIONS (Continued)

Figure		Page
5.12	Error contours for DIABLO HAWK LQ/LR for several parameter combinations.	127
5.13	Comparison of theoretical LQ/LR radiation patterns to the observed data with and without path corrections.	129
5.14	Theoretical Rayleigh wave radiation patterns are compared to the DIABLO HAWK observations normalized to a range of 250 km	134
5.15	Theoretical Love wave radiation patterns are compared to DIABLO HAWK observations normalized to 250 km.	136
5.16	Error contours for LQ/LR, F versus θ_s for MIGHTY EPIC assuming $\delta = 90$, $\lambda = 0$	137
5.17	MIGHTY EPIC LQ/LR data compared to several theoretical radiation patterns.	138
5.18	MIGHTY EPIC LR data compared to theoretical radiation patterns.	141
5.19	MIGHTY EPIC LR data compared to theoretical radiation patterns for the DIABLO HAWK double-couple orientation	142
5.20	MIGHTY EPIC LQ data compared to theoretical patterns for $\theta_s = 152$, $\delta = 90$, $\lambda = 0$, $F = 0.65$ and two values of the moment in dyne-cm.	143
5.21	MIGHTY EPIC LR and LQ data compared to theoretical radiation patterns.	144
A.1	Radial velocities for MIGHTY EPIC	160
A.2	Radial velocities for DIABLO HAWK	161
A.3	Radial velocities for MIGHTY EPIC after filtering with a 4-8 second bandpass filter.	162
A.4	Radial velocities for DIABLO HAWK after filtering with a 4-8 second bandpass filter.	163
A.5	Sprengnether seismograms for DIABLO HAWK recorded at Big Pine, California.	164

LIST OF ILLUSTRATIONS (Concluded)

Figure		Page
A.6	Sprengnether seismograms for DIABLO HAWK re- corded at Minersville, Utah.	165
A.7	Sprengnether seismograms for DIABLO HAWK re- corded at Shellbourne, Nevada.	166
A.8	Seismograms for MIGHTY EPIC recorded at Sandia station, Nelson, Nevada	167
A.9	Seismograms for DIABLO HAWK recorded at LLL station, Kanab, Utah	168
A.10	The first ten seconds of the seismograms from MIGHTY EPIC recorded at Tonopah.	169
A.11	The first ten seconds of the seismograms from DIABLO HAWK recorded at Tonopah.	170
A.12	The first ten seconds of the seismograms from MIGHTY EPIC recorded at Darwin	171
A.13	The first ten seconds of the seismograms from DIABLO HAWK recorded at Darwin	172
A.14	The first ten seconds of the seismograms from MIGHTY EPIC recorded at Mina	173
A.15	The first ten seconds of the seismograms from DIABLO HAWK recorded at Mina	174
A.16	The first ten seconds of the seismograms from MIGHTY EPIC recorded at Leeds.	175
A.17	The first ten seconds of the seismograms from DIABLO HAWK recorded at Leeds.	176
A.18	The first ten seconds of the seismograms from DIABLO HAWK recorded at Kanab.	177

LIST OF TABLES

Number		Page
2.1	STATION LOCATIONS RELATIVE TO MIGHTY EPIC AND DIABLO HAWK	25
2.2	MIGHTY EPIC AND DIABLO HAWK SEISMOGRAM INFORMATION	26
4.1	RECORD LENGTHS OF THE SEISMOGRAMS USED TO STUDY RELATIVE GROUND MOTION	57
4.2	SUMMARY OF SPECTRAL RATIO CALCULATIONS . . .	59
4.3	Pg AND Lg AMPLITUDES.	61
5.1	CRUSTAL MODELS	91
5.2	PATH PARAMETERS	94
5.3	STATION CLASSIFICATION	108
5.4	SIX SECOND AMPLITUDES FROM MARS ANALYSIS . .	118
5.5	RELATIVE AMPLITUDES, MIGHTY EPIC/DIABLO HAWK	119
5.6	DISTANCE ATTENUATION, r^{-n} AT T = 5.7 SECONDS.	122
5.7	LQ/LR DATA	124
5.8	LR DATA	131
5.9	LQ DATA	132

I. INTRODUCTION AND SUMMARY

1.1 INTRODUCTION

Since the beginning of the underground test program, it has been known that the seismological waves from these explosions include a substantial component of earthquake-like ground motion. Rather large horizontally polarized shear waves (SH) and Love surface waves, which are generated by SH waves, are always observed for NTS explosions. If we insist on viewing the explosion as a spherically symmetric source in a plane-layered isotropic medium, this motion cannot be explained. However, we know the situation is far more complicated, though difficult to model.

It is not only the seismological observations that suggest the presence of an earthquake-like component with the explosion source, but there are direct observations of fault movements and aftershocks that are in most respects like those seen in the vicinity of earthquakes. Thus, there is no question that there are substantial amounts of block motions along faults in the vicinity of explosions. However, the connection between the direct near-field observations and the seismological data has not been satisfactorily made. The current understanding of the seismological data and its relationship to near-field block motion observations was reviewed in some detail in a report by Bache and Lambert (1976).

The MIGHTY EPIC and DIABLO HAWK experiments provided a good opportunity to study the seismological data for experiments which included especially careful underground observations of motions along known faults. Our objective in this research program was therefore to infer the extent of the block motions from seismological observations. These estimates can then be compared to the direct observations.

To accomplish our objective we analyzed ground motion recordings from seven (MIGHTY EPIC) and ten (DIABLO HAWK) stations at ranges from 131 to 368 km. From these recordings we determined the amplitude of the fundamental mode Love and Rayleigh waves at a period of six seconds. From these data we estimate the size of the explosion and earthquake-like components of the source using techniques previously applied for this purpose by Toksöz and Kehrler (1972).

We concluded that there is indeed a substantial earthquake-like (double-couple) component in the source for both events. Further, this portion of the source is larger for MIGHTY EPIC than for DIABLO HAWK. Our analysis indicates that the double-couple is associated with block motions on faults tending north-south. Our best solution is for a fault with strike N16°E which is in good agreement with the strike of Fault 5 and the general trend of faults in this area.

We estimate the size of the explosion and double-couple components of the source. Our estimate for the explosion source function is in excellent agreement with independent estimates which enhances confidence in our ability to account for the effect of the path on the recorded amplitudes. From the size of the double-couple we can bound the extent of the block motions. In Section 1.7 we give a table with various combinations of fault area and average dislocation that are consistent with the observed double-couple amplitude. Rather small average displacements on a total fault plane area of 0.1 to 0.5 km² are sufficient to account for the observed double-couple. Large differential displacements (> 50 cm) occur only on small segments and are associated with large stress concentrations.

We believe we have analyzed the data with exceptional care and the fit of the theory to the observations is probably near the best that can be done. However, there are some

features of the data that are very difficult to fit with currently available theory. We discuss these aspects, which are also of considerable interest to those concerned with monitoring a nuclear test ban treaty, in Section 1.8.

1.2 BLOCK MOTION IMPLICATIONS OF SEISMOLOGICAL DATA

As we have said, earthquake-like ground motions are observed from all underground nuclear explosions. There are a number of mechanisms which have been proposed as explanations. It is convenient to consider five broad classes of mechanisms:

1. Wave conversion along the path.
2. Departure of the source from spherical symmetry.
3. Driven block motions along joints and planes of weakness in the local medium.
4. Tectonic strain release due to the creation of the cavity and surrounding region of reduced shear strength in the prestressed source region.
5. Tectonic strain release on nearby faults triggered by the explosion (small triggered earthquakes).

Comparative observations of explosions and associated cavity collapse (e.g., Brune and Pomeroy, 1963) suggest that the first mechanism is relatively unimportant. The other mechanisms are certainly operating to some extent. We point out that the differential motion or strain release would have to be oriented vertically to generate the large Love waves that are observed. Slippage along horizontal planes of weakness would generate shear waves, but not the horizontally polarized shear waves (SH) that generate Love waves.

We assume that the seismic source for the two events is a composite source including a spherically symmetric explosion and a double-couple component. The latter is the elementary source representation for an earthquake. The last four mechanisms on the list can all be represented by a

double-couple. For the second and third mechanisms, the explosion energy is repartitioned into an explosion plus a double-couple. Tectonic strain release adds energy to the source.

Our analysis of the seismological data requires two steps. First, we estimate the size and orientation of the double-couple. Next, we use the double-couple estimate to bound the near source block motions consistent with this estimate.

1.3 DESCRIPTION OF THE DATA

To estimate the double-couple we require three-component digital data from many stations. Lawrence Livermore Laboratory (LLL) and Sandia Laboratory maintain nine excellent stations at ranges from 131 to 368 km from Rainier Mesa. For MIGHTY EPIC we were able to recover the data from seven of these stations. This is a rather sparse data set which made it difficult to get a good solution.

For DIABLO HAWK the LLL and Sandia data were augmented by three portable stations operated by Systems, Science and Software (S^3). For this event we ended up with a total of ten stations. Observations of both events were made on all three components at five stations and on the vertical component at a sixth station. This is a total of 16 common recordings.

1.4 OUTLINE OF THE REPORT

In Section II we describe the data used in this analysis in some detail. This includes a description of the instrument response for the various recorders and a description of a separate experiment carried out to check the consistency of the instruments. The S^3 seismometers were deployed at the LLL Landers site for the LOWBALL event. All the recorded seismograms are displayed in Appendix A.

In Section III we describe the methods used to analyze the seismograms. Basically, there are two distinct methods. In one we apply an S³ developed signal analysis program called MARS (Multiple Arrival Recognition System) to estimate the amplitude of the fundamental mode Love and Rayleigh waves at discrete periods. This is a measure of the amplitude of a particular portion of the seismogram. These data are used to infer the size and orientation of the double-couple component of the source.

In the second method we compare the entire seismogram recordings of DIABLO HAWK and MIGHTY EPIC from common stations. This is done with the techniques of random time series analysis. Significant differences in the character of the signals for two sources in such close proximity should be due to differences in the sources themselves.

In Section IV we discuss the relative ground motions from common recordings of the two events. Then in Section V we estimate the size of the explosion source and the accompanying double-couple. There are trade-offs between the parameters characterizing the double-couple and these are also discussed. Finally, in Section VI we bound the block motions consistent with our estimate of the double-couple.

1.5 CONCLUSIONS ABOUT THE RELATIVE MOTIONS

The first thing to be noticed about common observations of the two events is that the seismograms appear, on casual inspection, to be nearly identical. If we lay the recordings of one event on top of those from the other, we see that the zero crossings and relative amplitudes of the peaks are nearly the same. From this superficial point of view, one experiment appears to be nearly a repeat of the other. What do we find by a more quantitative examination?

We treat the entire wavetrains recorded at common stations as if they were random time series and study their common properties. The coherency between pairs of seismograms is quite high showing that the two are very much alike, though not identical. This confirms our conclusion based on casual comparison of the records. As a side-light to the study of the coherency between common DIABLO HAWK and MIGHTY EPIC recordings, we compute the coherency between different components at the same station. These coherencies are comparatively quite low, indicating that we have three independent observations of the wavefield. This is particularly important for the two horizontal components since Rayleigh waves arriving from other than the true station-source azimuth will show up on the transverse component where they would be interpreted as Love waves.

Our most important conclusion from comparing the common recordings of the two events is that the DIABLO HAWK/MIGHTY EPIC seismic amplitude ratio is strongly dependent on frequency. At high frequencies (1.5 to 2.5 Hz) the DIABLO HAWK amplitude is about 90 percent of that for MIGHTY EPIC. Phases like P_n that are often used to indicate seismic yield have most of their energy in this band. We would conclude from this that the ratio of seismic yields is also about 0.90.

On the other hand, at long periods (0.1-0.3 Hz) the DIABLO HAWK/MIGHTY EPIC amplitude ratio is 0.56, on the average. This important conclusion about the relative size of the two events at high and low frequencies is remarkably consistent for all common observations but one (the tangential component at Leeds) where DIABLO HAWK is larger.

Our inference of the double-couple is based on the spectral amplitudes of the fundamental mode Love and Rayleigh wave at long period (6 seconds). These amplitudes are not whole wavetrain spectral amplitudes like those discussed

above, but are associated with a distinct portion of the wave-train. The results, however, turn out to be quite consistent. That is, at almost every common station the long period amplitude from MIGHTY EPIC is substantially larger than that from DIABLO HAWK.

1.6 CONCLUSIONS ABOUT THE DOUBLE-COUPLE

The source is assumed to consist of a spherically symmetric explosion plus a double-couple to represent the earthquake-like component. For such a source there is a well-developed theory for predicting the Love (LQ) and Rayleigh (LR) waves. We use the theory together with good estimates for the crustal structure in the region to correct the observed LR and LQ amplitudes for differences in path structure. We then find the source that best fits the LQ/LR ratios and, secondarily, the LR and LQ data taken separately.

In the data inversion we estimate three parameters. These are the strike of the dominant faulting, the long period amplitude of the explosion source (displacement potential, ψ_∞) (Ψ_∞) and the moment (M_0) of the double-couple. In carrying out the inversion we assume a horizontal shear prestress field; that is, vertical strike-slip faulting. This gives a lower limit estimate for M_0 . Assumed fault orientations other than vertical strike-slip result in larger estimates for the moment. This trade-off between M_0 and the fault orientation is described in some detail in Section 5.5.

DIABLO HAWK

The solution for DIABLO HAWK is fairly well constrained. We find that the tectonic strain release is associated with faulting that strikes N16°E. This is in agreement with the trend of existing faults in the vicinity. The fit to the LR pattern indicates an explosion source with $\psi_\infty = 2,200 \text{ m}^3$. This, in turn, leads to a moment estimate of $M_0 = 1.3 \times 10^{21}$ dyne-cm.

There is a range of uncertainty in these parameters. However, we feel comfortable about the inferred strike. The Ψ_{∞} and M_0 estimates require accurate knowledge of many other factors, especially characteristics of the travel path. A factor of two error in our Ψ_{∞} and M_0 estimate would not be surprising. However, values that are much more different would conflict with a wealth of independent evidence about the size of the explosion source for Area 12 events, the crustal models in the Basin and Range Tectonic Province, etc. The range of uncertainty in M_0 is somewhat greater than in Ψ_{∞} , but it should not be greater than a factor of 2-4.

MIGHTY EPIC

We found it much more difficult to fit the MIGHTY EPIC data. First, we have the evidence from the high frequency observations that the explosions have the same seismic yield to within 10 percent. But at most stations MIGHTY EPIC excited larger long period waves on all three components. There are two possible explanations. First, it could be that the reduced displacement potentials for the two explosions have a different frequency dependence. Our knowledge of the material properties for the two events indicate no reason why this should be so (N. Rimer, private communication). The second explanation is that the MIGHTY EPIC double-couple (or combination of double-couples at different strike angles) is such as to enhance the long period radiation at the rather sparse sampling of common stations.

Our best fitting solution for the MIGHTY EPIC LQ/LR data strikes N28°W. However, considering all three data sets, LQ/LR, LR and LQ, we believe the weight of the evidence indicates that the strike for MIGHTY EPIC is about the same as for DIABLO HAWK; that is, N16°E. Our best fit to the data, which is admittedly not very good, has $\Psi_{\infty} = 3,200 \text{ m}^3$ and $M_0 = 2.6 \times 10^{21} \text{ dyne-cm}$.

Comparing the DIABLO HAWK and MIGHTY EPIC solutions, note that the ψ_{∞} for the latter is 1.45 times larger than for DIABLO HAWK and the moment is a factor of two larger. If we insist that the ψ_{∞} for the two events be the same within 10 percent, as suggested by the seismic yield determined from high frequency phases, the fit to the data definitely deteriorates. We believe the range of uncertainty for MIGHTY EPIC is much larger than for DIABLO HAWK. However, the differences in the inferred parameters for the two events are considered to be significant.

1.7 BOUNDS ON THE BLOCK MOTION

Our estimates for the moment allow us to bound the block motions associated with earthquake-like faulting, i.e., the relative displacement across a fault. This motion can be due to the release of tectonic strain energy or it can be passive faulting or driven block motion which releases no seismic energy (though it does convert some of the compressional wave energy to shear waves).

In Section VI we give a table with several combinations of parameters that give the correct moment. These are the stress drop ($\Delta\sigma$), fault area (S) and average displacement (D) on the fault. This table is replicated below.

<u>M_0 (dyne-cm)</u>	<u>$\Delta\sigma$ (bars)</u>	<u>a (m)</u>	<u>S (km²)</u>	<u>D (cm)</u>
1.3×10^{21} (DIABLO HAWK)	20	305	0.29	11
	40	242	0.18	18
	80	192	0.12	28
	120	168	0.089	37
2.6×10^{21} (MIGHTY EPIC)	20	385	0.46	14
	40	305	0.29	22
	80	242	0.18	35
	120	212	0.14	46

For this model the fault plane is circular and $S = \pi a^2$. Other models give similar results for S and D.

The moment is proportional to S times D , which is the quantity held constant for each event in the table. The stress drop values were introduced via a side condition relating D , S and $\Delta\sigma$. For block motions due to tectonic strain release, this is clearly the correct thing to do. Even when we are dealing with driven block motions, it is not reasonable to suppose that D and S are entirely independent. Large displacements on small fault areas would lead to large stress concentrations. Thus, even for this case the stress values in the table are qualitatively correct.

From the table we see that rather small average displacements on a total fault plane area of $0.1-0.5 \text{ km}^2$ are enough to account for the observed double-couple moment. Large average displacements ($> 50 \text{ cm}$) occur only on segments with quite large stress drops ($> 120 \text{ bars}$) or lead to large stress concentrations.

We also note that the factor of two difference in the inferred moment for the two events means only that the product of fault area and average dislocation differ by a factor of two. The bounds on the block motions are therefore not very different.

Finally, we point out that the bounds we have derived for the block motions are based on elastic theory. Thus, for example, large stress concentrations occur for large driven block motions on small fault planes because the fault is assumed to occur within an elastic continuum. Any fault motions that are decoupled from the larger elastic continuum are not bounded by this analysis and, in fact, cannot be estimated from observations of seismic waves. The same can be said for block motions that occur within the region where the material behavior is highly nonlinear. The elastic radius for these events is about 160 meters (N. Rimer, personal communication).

1.8 SUMMARY REMARKS

We close this summary section with some general remarks about this project and its relevance to problems of current interest. The stated purpose of the project was to use seismological data to impose some bounds on the near-source block motions. We began with a theoretical idea of how to do this and we applied this theory with, we think, great care. However, the data contained some surprises, some features that are difficult to explain with our models. But these aspects, while making it more difficult to bound the block motions, are of considerable interest from a purely seismological point of view, especially for those concerned with monitoring a test ban treaty.

The major data characteristics that are difficult to explain with currently available models for nuclear explosions and seismic wave propagation are these:

- A. The observed Love wave amplitudes cannot be fit very well with a double-couple radiation pattern. In fact, we can fit the data as well by supposing that the Love waves are radiated equally at all azimuths (see Figures 5.15 and 5.20).
- B. The long period radiation from MIGHTY EPIC is larger than that from DIABLO HAWK almost everywhere while the short period radiation is nearly the same amplitude.

Both of these surprising aspects of the data can be explained away with some effort, but we are not satisfied that we clearly understand what is happening. Considering A, we could explain the poor fit to the Love waves in a number of ways, including,

- 1. Some of the Rayleigh wave motion is being seen on the tangential (Love wave) component. The

Love wave amplitudes we have measured have the right group arrival time and are generally the largest amplitudes at that period on the tangential component (see Section 5.4). We are quite certain that they are indeed Love waves. However, the amplitudes could be contaminated by Rayleigh wave motion arriving at the same time.

2. The double-couple portion of the source, which is the only source for true Love waves, is not dominated by slip along one azimuth but includes contributions from many double-couples at many azimuths. If this were the case, the Love wave source would not be strongly dependent on azimuth. If this is what is happening, our source model is much too simple. Still, our moment estimate might not be too different from the total moment for the several sources.
3. Our seismic network provides only a sparse sampling of the radiation pattern. There may be station and path peculiarities such as multipathing and focusing that bias the data. If we had a denser data set to average, we might obtain an excellent double-couple radiation pattern.

Now consider B. The MIGHTY EPIC/DIABLO HAWK spectral ratios can be explained by supposing that the explosion sources have different long period levels. This is our conclusion in Section V. The trouble with this supposition is that it is difficult to explain from our knowledge of the material properties in the vicinity of these events (N. Rimer, personal communication). The alternative is to suppose that the apparently larger MIGHTY EPIC block motion is the cause. For this to happen on all three ground motion components at nearly all stations, we would again have to suppose that the

source includes many double-couples at different azimuths. Further, these double-couples must have a source spectrum that is much larger at long periods than at frequencies of 1 Hz and higher (see Sections 4.1 and 4.2). Since the double-couple source dimensions are quite small, this would imply that the block motions occur with extraordinarily slow (compared to earthquakes) rupture velocities, on the order of 0.1 km/sec.

These are interesting aspects of the data. They have some importance for detecting and discriminating underground explosions, especially at regional distances.

The bounds we have derived for the block motions are approximate. Our fit to the data is not perfect and there are aspects that we have not completely explained. Even if the data were fit perfectly, the theory includes some ambiguity, some trade-offs among the controlling parameters. Taking all these factors into consideration, we view our estimates as bounds for the order of magnitude of the block motions. We are certain that the data will not support large block motions on large fault areas and have an estimate for what "large" means. The block motions for MIGHTY EPIC were almost certainly greater than those for DIABLO HAWK, but not by a great amount.

II. SOURCES OF DATA

Data from three different organizations were used in this study. For both MIGHTY EPIC and DIABLO HAWK digital seismograms were obtained from Lawrence Livermore Laboratories (LLL) (four stations) and Sandia Laboratory (five stations). In addition, Systems, Science and Software (S³) recorded the DIABLO HAWK test at five temporary locations (of which three provided useful data) using Sprengnether S6000 three-component seismometers and DR-100 digital recorders.

The need for both the digital seismograms and the additional DIABLO HAWK recordings was pointed out by Bache and Lambert (1978), who studied the analog records of MIGHTY EPIC to infer possible block motions associated with that test. The reasons for these suggestions were the desirability of digitally filtering the data, and the need to improve the azimuthal coverage for DIABLO HAWK.

The collection of stations spanned a range of distances between 131 km (Tonopah) and 402 km (Elko) from the shot locations. The azimuthal coverage was reasonably complete in three of the four quadrants surrounding the source, particularly for DIABLO HAWK where the S³ stations are available. Instrument malfunction at the S³ Lake Mead site and the Sandia Nelson site caused a total lack of data in the southeast quadrant (Kanab and Landers are 90 degrees apart) for DIABLO HAWK, although Nelson did function properly for the earlier MIGHTY EPIC event. This gap is not particularly severe, however, since the northwest quadrant is well covered, and since, as our radiation pattern calculations have shown, there is a Love wave nodal plane oriented approximately S30E.

General information pertaining to seismograph stations is given in Table 2.1, and Table 2.2 presents some details

TABLE 2.1

STATION LOCATIONS RELATIVE TO MIGHTY EPIC AND DIABLO HAWK

Co.	Station Name	Code	Distance (km)	Azimuth		Geographic Coordinates		Digital Data		
				EPI-STA	STA-EPI	Lat. (N)	Long. (W)	MIGHTY	DIABLO	HAWK
S	Tonopah Nevada	TNP	130.7	317.0°	136.4°	38°03'57.0"	117°13'40.8"	✓		✓
S	Darwin California	DAC	161.0	230.5°	49.6°	36°16'37.2"	117°35'37.2"	✓		✓
S'	Big Pine California	BGP	178.1	269.4°	88.2°	37°10'30.0"	118°13'00.0"			✓
S'	Lake Mead Nevada	LMN	184.3	106.8°	288.0°	36°42'45.0"	114°14'15.0"			
S	Nelson Nevada	NEL	206.5	143.1°	324.0°	42°44'44.0"	114°50'37.0"	✓		
LLL	Mina Nevada	MNV	218.4	309.0°	127.8°	38°25'56.0"	116°24'41.4"	✓		✓
S	Leeds Utah	LEE	251.8	88.3°	270.0°	37°14'34.8"	113°22'36.0"	✓		✓
LLL	Kanab Utah	KNB	302.0	93.0°	275.1°	37°00'59.8"	112°49'20.7"	*		✓
S'	Minersville Utah	MVL	302.9	68.3°	250.3°	38°10'30.0"	113°00'00.0"			✓
LLL	Landers California	LAC	313.3	183.4°	3.2°	34°23'23.2"	116°24'41.4"	✓		✓
S'	Shellbourne Nevada	SHL	317.2	24.4°	205.4°	39°48'00.0"	114°40'48.0"			✓
S'	Palmdale California	PIM	322.9	207.1°	26.2°	34°36'30.0"	117°49'00.0"			
S	Battle Mountain Nevada	BMN	368.4	346.5°	165.9°	40°25'53.3"	117°13'18.4"	✓		✓
LLL	Elko Nevada	ELK	401.6	11.8°	192.4°	40°44'41.4"	115°14'19.6"	*		

✓ = Three-component data usable at these stations
 * = Vertical-component data usable at these stations

Companies:
 LLL = Lawrence Livermore Laboratories
 S = Sandia Laboratories
 S' = Systems, Science and Software

TABLE 2.2

MIGHTY EPIC AND DIABLO HAWK SEISMOGRAM INFORMATION*

Station Code	Event	Start (s)	P _n (s)	End (s)	Length (s)	Comments
TNP	M	17.6	23.0	117.0	99.4	Good data
	D	19.8	23.0	80.0	60.2	Ends in surface wave coda
DAC	M	22.1	27.3	145.3	123.2	
	D	24.8	27.3	96.2	71.4	Horizontal components noisy, short
BGP	D	23.0	26.1	147.2	124.2	
NEL	M					
	D					
MNV	M	0.0	34.6	248.5	248.5	
	D	0.0				
LEE	M	30.8	38.6	226.8	196.0	
	D	34.8	38.6	145.4	110.6	Horizontal components noisy
KNB	M					
	D	0.0		198.6	198.6	
MVL	D	44.0			131.4	
LAC	M					
	D	1.4	46.0	240.0	238.6	
SHL	D	28.2			147.0	
BMN	M	43.0	54.3	246.4	203.4	
	D	49.8	54.3	173.0	123.2	

* List, by station code, of seismogram parameters, giving start and end times, relative to shot time, length of seismogram, time of P_n arrival and general comments.

about the available seismograms. In Figure 2.1 we show the location of the stations on a polar diagram centered on the source location.

2.1 LAWRENCE LIVERMORE DATA

Through the courtesy of Mr. M. Denny and Mr. R. Rohrer, of LLL, the archive analog tapes for MIGHTY EPIC and DIABLO HAWK were digitized and made available to us. The MIGHTY EPIC seismograms were digitized at the rate of 20 samples/second and the DIABLO HAWK at 50 samples/second. Scale factors and start times were provided with each seismogram. We verified these (where possible) by direct comparison between the digital records and the analog records. Several small (one to two second) discrepancies in the start times were discovered and rectified. For MIGHTY EPIC, both Elko and Kanab recorded just the vertical component of ground motion, and no data at all was provided by Elko for DIABLO HAWK. Elko is being used as the prototype system for a new digital telemetry link soon to be installed at all four LLL stations, so we did not use this station in our analyses.

The LLL network uses three-component Sprengnether long period seismometers with velocity transducers to record ground motion. The data is sent over telephone lines using analog frequency modulation methods. Although this method has less dynamic range than the planned digital telemetry system, we found no difficulty in recovering the low amplitude surface waves in the presence of the much larger short period signal.

The transfer functions for the LLL stations have been described by Denny (1977). For frequencies less than 1 Hz, the instrument responses are well modeled as a quadratic system with period of order 20s for the vertical component

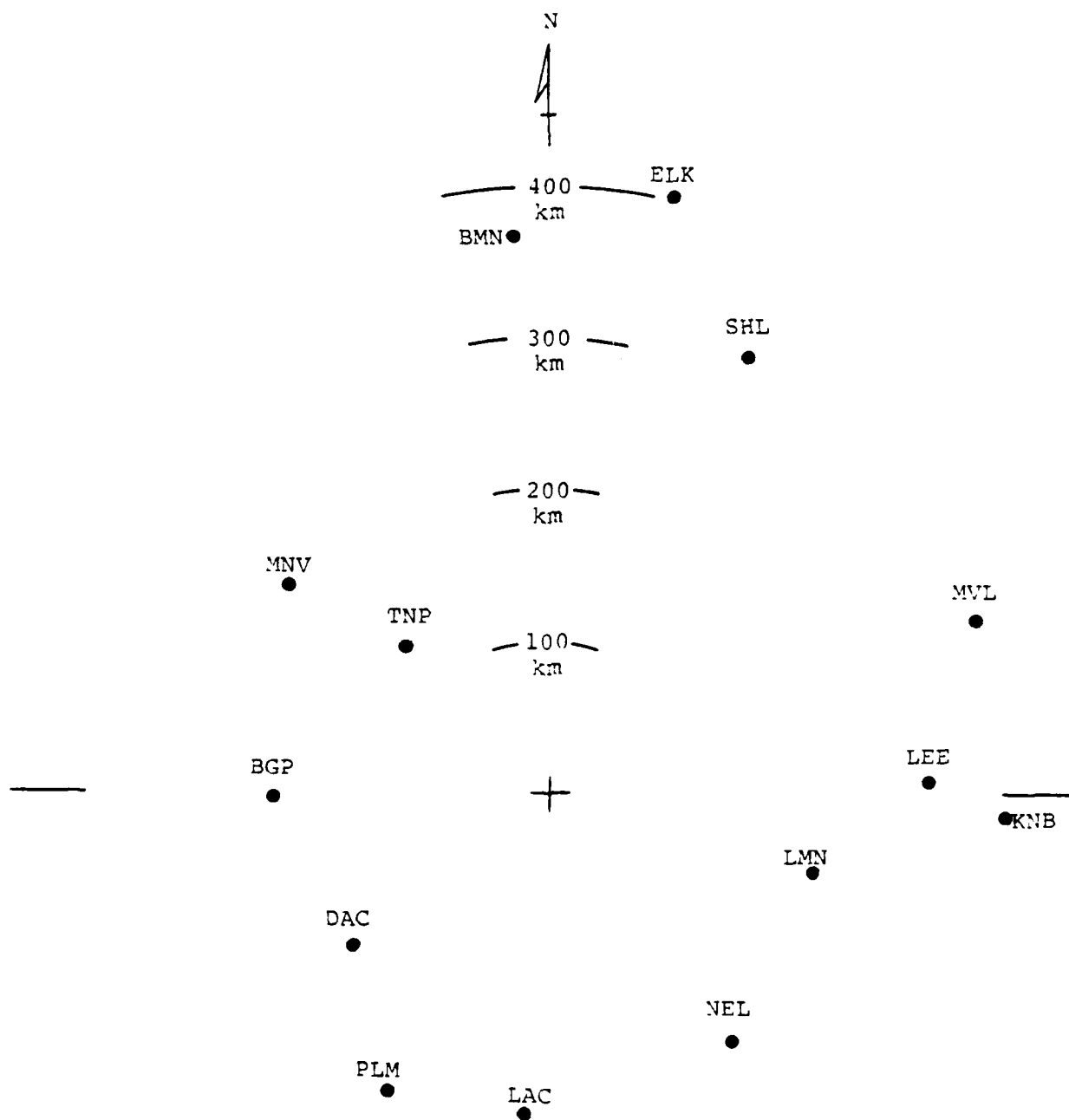


Figure 2.1. Polar plot centered on the MIGHTY EPIC/DIABLO HAWK source location showing the distance and azimuth to the LLL, Sandia and S³ seismic stations.

and 40s for the two horizontals and a damping of about 0.6 times critical. The velocity response is flat between the lower corner and 10 Hz and becomes like f^2 below the lower corner.

There are small differences (of order 2 percent) between the nominal instrument constants and any individual seismometer, but we have ignored them. Since the frequency range encompassed by the study spans 0.1 Hz to 2 Hz, we have not found it necessary to account for the frequency dependence in the instrument responses.

To prepare the raw data for further processing, the digital seismograms were all filtered through a lowpass, zero phase convolution filter and decimated to a uniform 0.1s sample interval, yielding data with a 5 Hz bandwidth. The P_n arrival on the filtered data was again checked to verify the seismogram start times. The amplitudes were all scaled to yield a digital sensitivity of 1 $\mu\text{m/s}$ per count.

2.2 SANDIA DATA

Through the courtesy of Mr. D. G. Gabin of Sandia, the archive analog tapes for MIGHTY EPIC and DIABLO HAWK were digitized and made available to us. Both sets of seismograms were digitized at the rate of 30 samples/second. Scale factors and start times were provided with each seismogram, and we verified these (where possible) by direct comparison between the digital and analog records. For DIABLO HAWK, the horizontal signals at both Darwin and Leeds were anomalously noisy, and furthermore, no data was obtained from the station Nelson.

The Sandia network used three-component seismometers, originally fabricated by National Geophysical Company, now

part of Teledyne Geotech. The transducer itself has a period of about 1 Hz, but electronic feedback is used to shape the response so that it is flat with respect to ground velocity over the band 0.1 to 20 Hz rising like f^3 towards the lower corner frequency and falling like f^{-3} above the upper corner.

All seismometer systems were calibrated in 1974 on the Teledyne Geotech shake table (Brady, 1974). The calibration results presented by Brady show small differences from system to system, but again they occur at the level of a few percent, so are not of major significance.

As with the LLL data, the raw Sandia seismograms were filtered through a lowpass, zero phase convolution filter and decimated to a uniform 0.1 second sample interval, yielding data with a 5 Hz bandwidth. The amplitudes were scaled to give a digital sensitivity of 1 $\mu\text{m/s}$ per count.

2.3 SYSTEMS, SCIENCE AND SOFTWARE DATA

Systems, Science and Software deployed five digital seismographs to record DIABLO HAWK in the range of distances between 178 km and 322 km from the source location, at azimuths which otherwise are poorly covered by the permanent LLL and Sandia networks. Table 2.1 and Figure 2.1 show, respectively, a list of station coordinates and a display of their positions on a polar diagram.

The transducer for the Sprengnether seismic system is the S6000 three-component seismograph with a 2 Hz natural frequency and a damping of about 0.6 times critical. The seismometer voltage, which is proportional to ground velocity (130 volts-seconds/meter), is amplified by the three channel PTS-9 amplifier with variable gain and variable filtering.

The amplified signals then are recorded on cassette tape by a Sprengnether DR-100 digital recorder. The DR-100

contains also an event detection circuit which monitors the vertical component signal. The event detector uses the familiar STA/LTA method, in which the ratio of the short period energy to the long period energy is continually compared against a predetermined threshold. If the STA/LTA ratio crosses the threshold, data are digitized and written on magnetic tape. Several seconds of data before the event trigger instant are also saved by using an internal memory.

The DIABLO HAWK data were digitized to a 12 bit (1 part in 4096) accuracy, yielding a least count level of 4.88 mv, with a sample interval of 0.02s. At this rate, a cassette lasts about 20 minutes. Because of the limited recording time and the possibility of an unannounced delay in the NTS schedule, our field procedure consisted first of recording 13 minutes of data following the announced shot time. A new tape was then placed in the recorder, the automatic event detector was switched on, and the station operator then left the site to place a call to S³ to obtain the current schedule. In fact, DIABLO HAWK was shot 15 minutes late, but all recorders triggered satisfactorily. Except for Palmdale, they all remained triggered well into the surface wave coda. The Palmdale signal amplitudes were surprisingly small, so at this site the recorded data did not last long enough to be useful.

The control settings on the DR-100 recorder used for the event trigger (see Sprengnether DR-100 manual) were as follows:

Long term average	200s
Short term average	2s
Ratio	18db
Duration	50s

To achieve the greatest possible dynamic range in the recorded waveforms, it was important that the seismometer amplifiers be set so that the maximum signal amplitude was in the range 10 to 15 volts (2000 to 3000 digital counts) peak-to-peak. This was necessary so that the lower amplitude long period signals could be accurately recorded. In order to choose the proper amplifier settings, the LLL and Sandia seismograms for MIGHTY EPIC were scanned to pick the largest signal amplitudes. On this basis, the Sprengnether amplifier gains were set at 60 db (10^3) for all stations. With the S6000 transducer sensitivity of 130 vs/m, this yielded an overall system sensitivity of 0.13 vs/ μ m, so that one count in the digital record corresponded to a ground velocity, at the maximum response frequency, of 0.0375 μ m/s. The DIABLO HAWK signals had a peak-to-peak amplitude of 30 μ m/s typically, giving amplified signals of 4V peak-to-peak, or recorded signals of about 1000 counts.

Another consideration in the recording system was the necessity to attenuate all signal energy with frequencies higher than 10 Hz, so that the digital records would not be aliased. The amplitude of the long period, \sim 0.1 Hz, signal was only a few millivolts due to the 2 Hz resonant frequency of the seismometers, so the lowpass filters in the signal amplifiers were all set at 10 Hz.

Two methods have been used to derive the Sprengnether instrument response function. The first method, which we call the modeling method, consisted of an analysis of the entire seismograph system, from seismometer transducers, through the frequency dependent amplifier, to the digital recorder. From this analysis, the following equations for

the transfer function were derived, relating the Fourier transform of the digital signal, $D(f)$, to the ground velocity $V(f)$

$$D(f) = H_S(f) H_A(f) V(f) \quad , \quad (2.1)$$

where H_S is the frequency dependent seismometer response function (with dimension volts seconds/meter) and H_A is the amplifier/digitizer response function (with dimensions counts/volt). Using the manufacture's specification for the seismometer characteristics and the circuit components used in the amplifier and recorder section, we find that

$$H_S(f) = \frac{130 \text{ s}^2}{157.9 + 15.08s + s^2} \quad , \quad (2.2)$$

and

$$H_A(f) = \frac{204.8 \times 10^3 (1 + 26.05s)^2}{(1 + 0.7914s)^2 (1 + 0.0165s)^2} \quad , \quad (2.3)$$

where Laplace transform variable s is given by $s = i2\pi f$.

The seismograph model amplitude response, measured in decibels, is plotted over a two decade frequency range in Figure 2.2. Reading the right-hand ordinate axis, it can be seen that at about 3 Hz, a 1 $\mu\text{m/s}$ harmonic ground motion causes an output of about 29 db (or about 28.971 counts amplitude). Equivalently, the same ground motion exites a voltage of -17 db (or about 0.141 volts). The phase response of the seismometer model is shown in Figure 2.3. The derivative of the phase response is equal to the seismometer group delay. For this phase function we

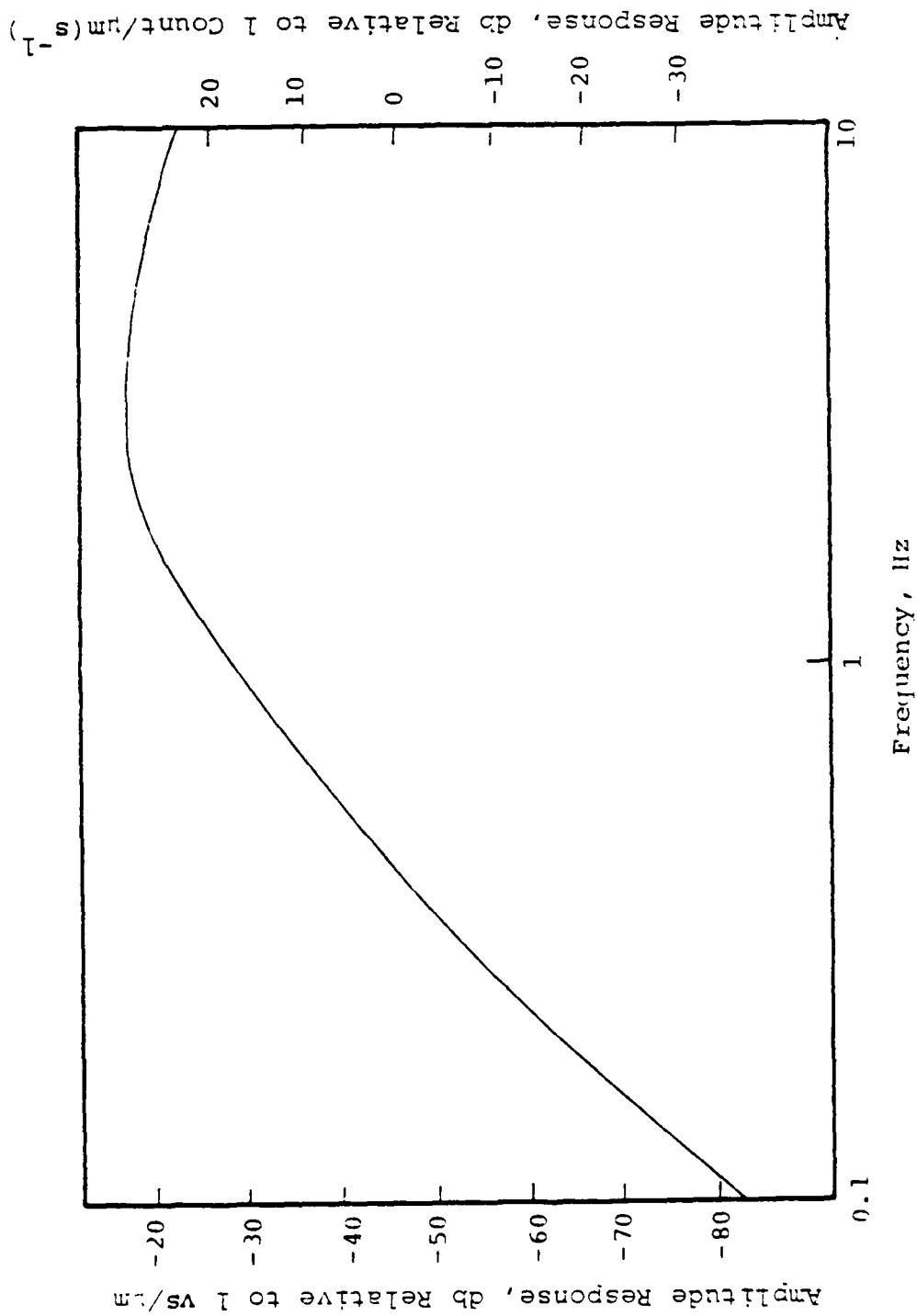


Figure 2.2. Amplitude response of the Sprengnether seismograph model, plotted on a logarithmic frequency scale between 0.1 Hz and 10 Hz. At the response maximum (~ 3 Hz), a $1 \mu\text{m/s}$ sine wave generates about 0.14 volt at the amplifier outputs (left-hand amplitude scale), and is digitized as a 29 count digital signal (right-hand amplitude scale).

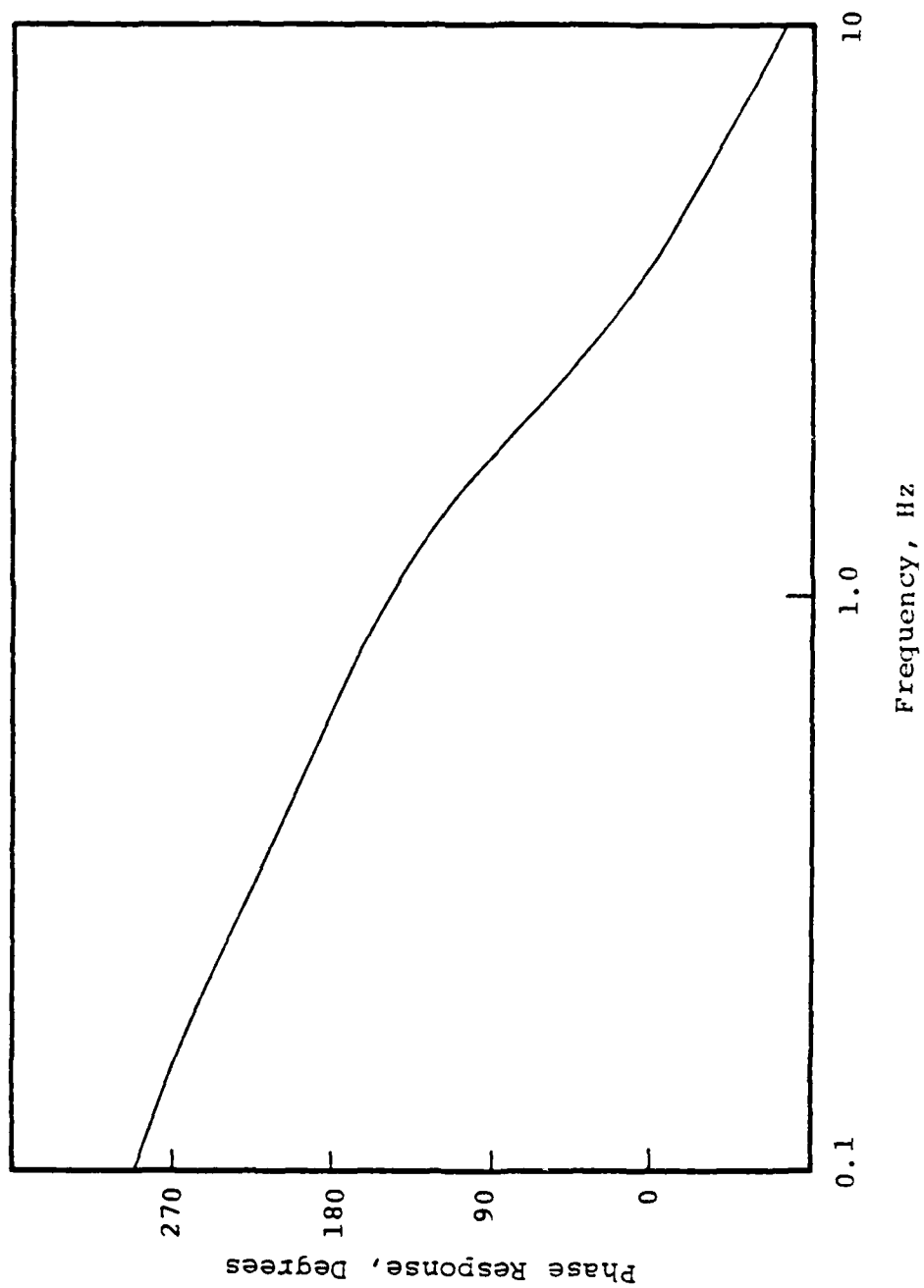


Figure 2.3. Phase response of the Sprengnether seismograph model, plotted on a logarithmic frequency scale between 0.1 Hz and 10 Hz.

find that, at 4s period, $t_g = 0.6955s$, and at 8s period, $t_g = 1.46s$.

The seismograph model response has been verified experimentally by a simultaneous recording of NTS shot LOWBALL at the LLL station Landers. For the analysis, the S^3 Sprengnether seismometer was placed on the LLL instrument pad, and the two transverse components were aligned along the LLL fiducial directions. The two vertical component signals obtained for LOWBALL are displayed in Figure 2.4. To relate the S^3 instrument response to earth motion, we assume that over the frequency band of interest (0.125 Hz to 4 Hz) the LLL response is flat, and find the transfer function between the LLL recording of LOWBALL and the S^3 recording.

To find the relationship, a cross-spectrum analysis was performed. The details of the method are described in Section 3.2, and here we merely show the results of the calculation. Figure 2.5 shows the first part of the calculation, the estimates of the power spectrum of each record. This figure indicates that at about 1.5 Hz, the LLL and S^3 instrument responses are identical, and that at a higher frequency the S^3 record is about twice as sensitive (+6 db) as the digitized LLL record, whereas at low frequencies, the S^3 response falls rapidly. Both power spectra fall rapidly above 4 Hz, the corner frequency of the digital antialias filter used in the preprocessing stage of the analysis. That there is a faithful recording of the low frequency motion contained in the S^3 signal is indicated by Figure 2.6, a plot of the frequency-dependent coherency between the two signals shown in Figure 2.4. At frequencies where the coherency is high, we presume that the two instruments are measuring actual earth motion. The coherency is high between 0.3 Hz and 4.0 Hz. Note that there is a slight decrease in coherency above 1 Hz - this is possibly due to

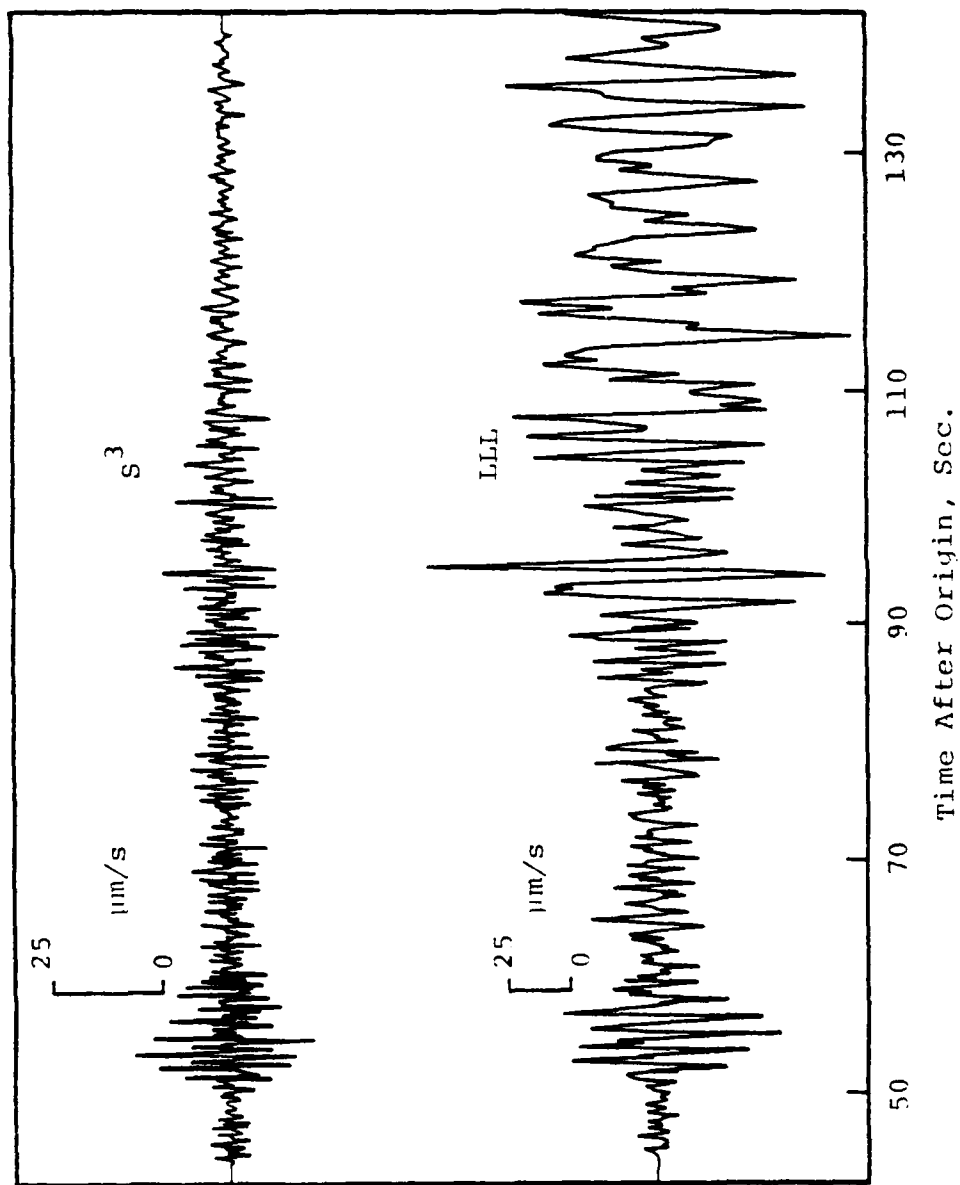


Figure 2.4. The vertical component seismograms for NTS event LOWBALL recorded at Landers by the S^3 Sprengnether digital seismograph (upper trace) and the LLL broad-band seismometers (lower trace). The greater long period sensitivity of the LLL system is apparent in this plot.

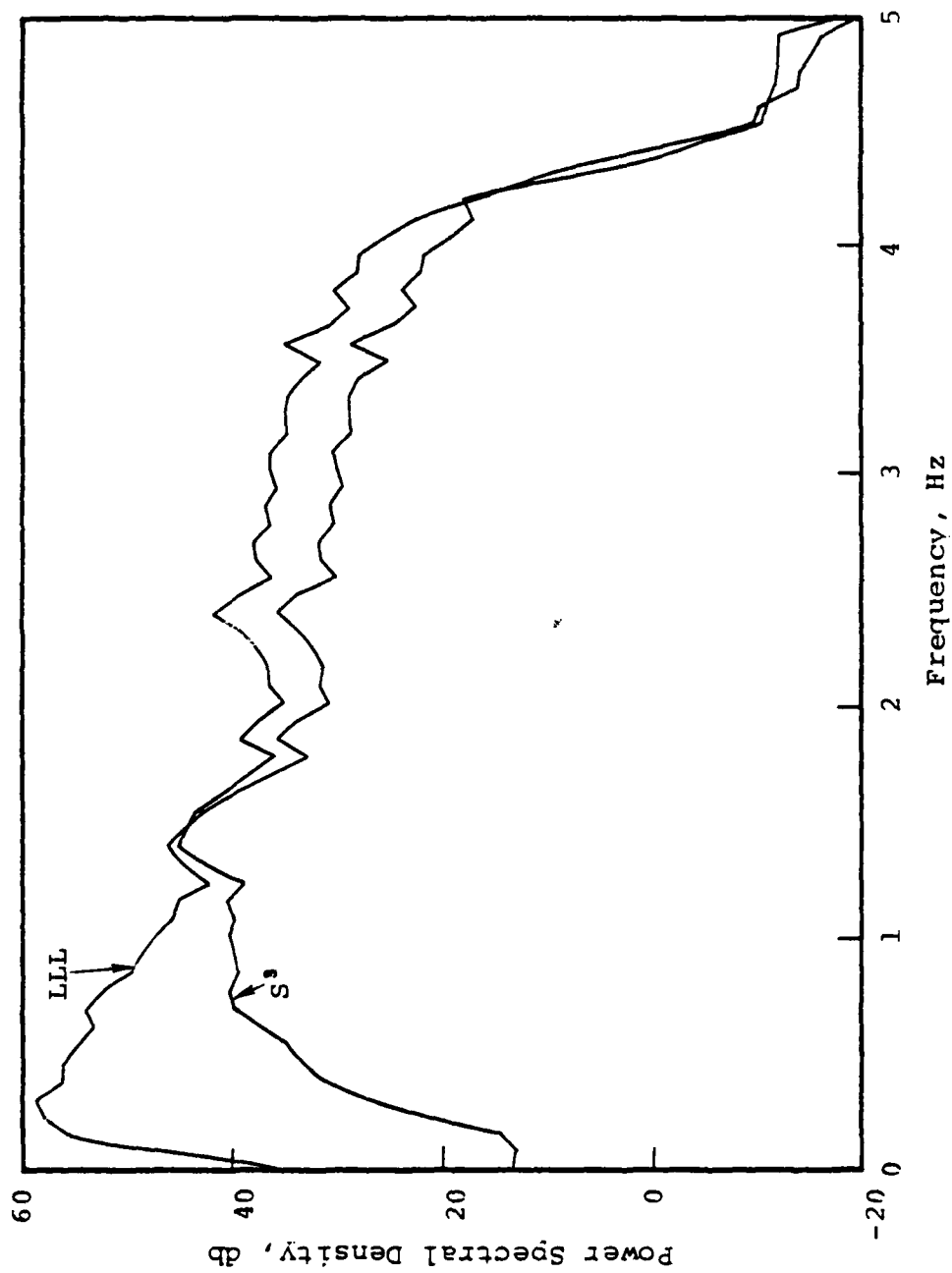


Figure 2.5. The power spectrums of the two LOWBALL seismograms displayed in Figure 2.4.

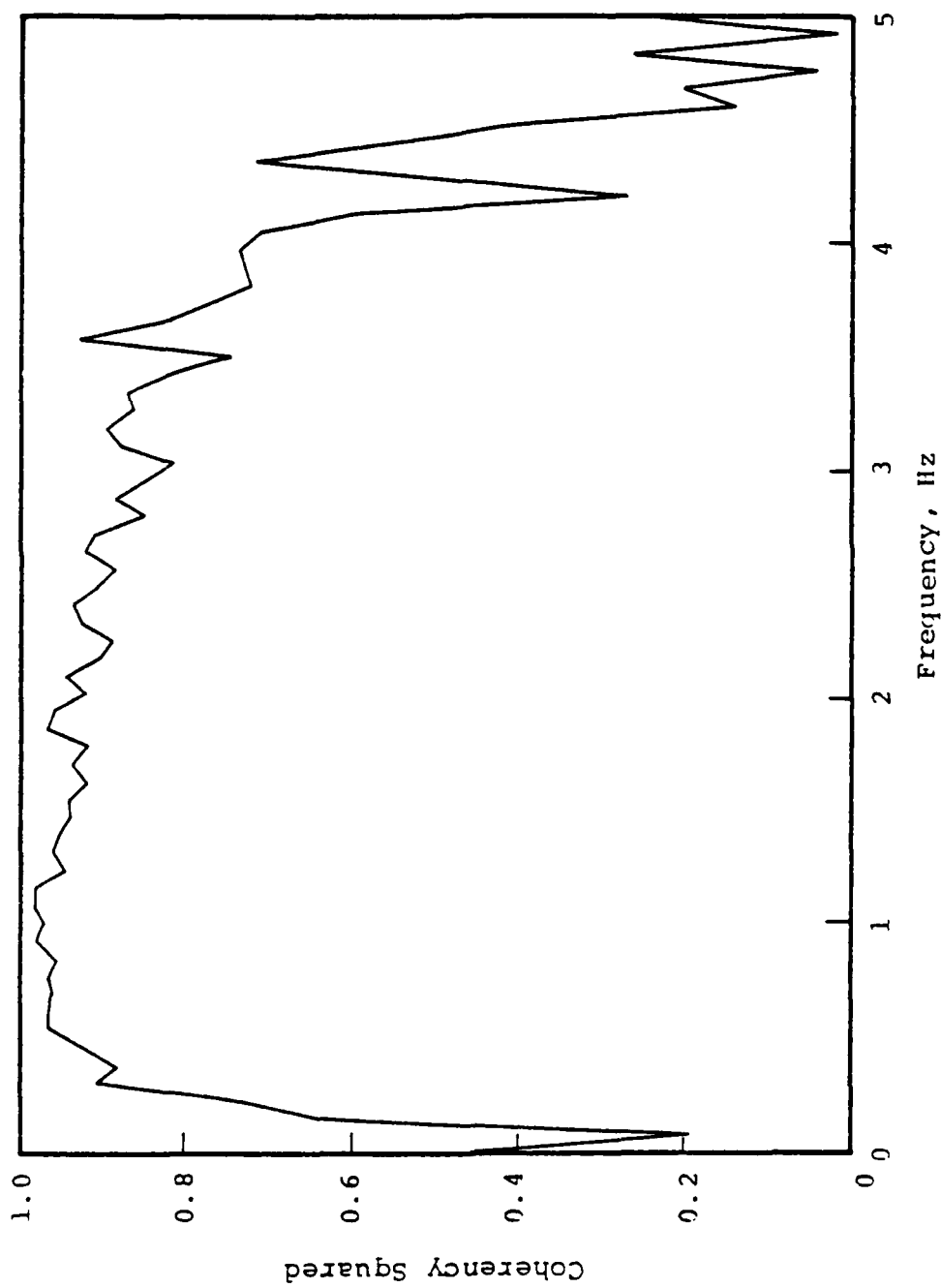


Figure 2.6. The coherency between the S³ LOWBALL recording and the LLL LOWBALL recording.

electronics noise in the LLL analog telemetry system. At the low frequency end, the coherency falls because of the decrease in the Sprengnether sensitivity. Yet, signals with periods of 8 seconds at least are accurately recoverable from the Sprengnether recordings, as is shown by the seismograms displayed in the Appendix, Figures A.5, A.6 and A.9. Above 4 Hz the coherency falls because of the attenuation of the digital antialias filters.

The primary use of the joint LOWBALL recordings was to derive the empirical Sprengnether response function from the cross-spectrum calculation. The result of this calculation is shown in Figures 2.7 and 2.8. Figure 2.7 shows, over the frequency range 0 to 5 Hz, the modulus of the transfer function (also called the admittance) which relates the LLL seismogram to the S^3 seismogram. As stated before, since the LLL instrument response is constant between 0.125 Hz and 5 Hz, this is also the filter relating earth velocity to Sprengnether output. Also shown on this plot are four points, at frequencies of 1, 2, 3 and 4 Hz, giving the model Sprengnether response obtained from the parametric equation (Equations (2.1) through (2.3)). A more detailed examination of the agreement between the model response and the empirical response is shown in Figure 2.8, giving the ratio of the two response estimates. It can be seen that over most of the frequency band there is at most a 10 percent variation in the model response about the empirical response. The hump around 2.5 Hz is probably a consequence of the actual seismometer being slightly less damped than it was assumed to be in the model calculation. The large discrepancy at very low frequencies we think is a pessimistic indication of the accuracy of the model, and arises from the smoothing effect of the cross-spectrum calculation. Above 4 Hz, again, the results are not significant because of the digital antialias filter.

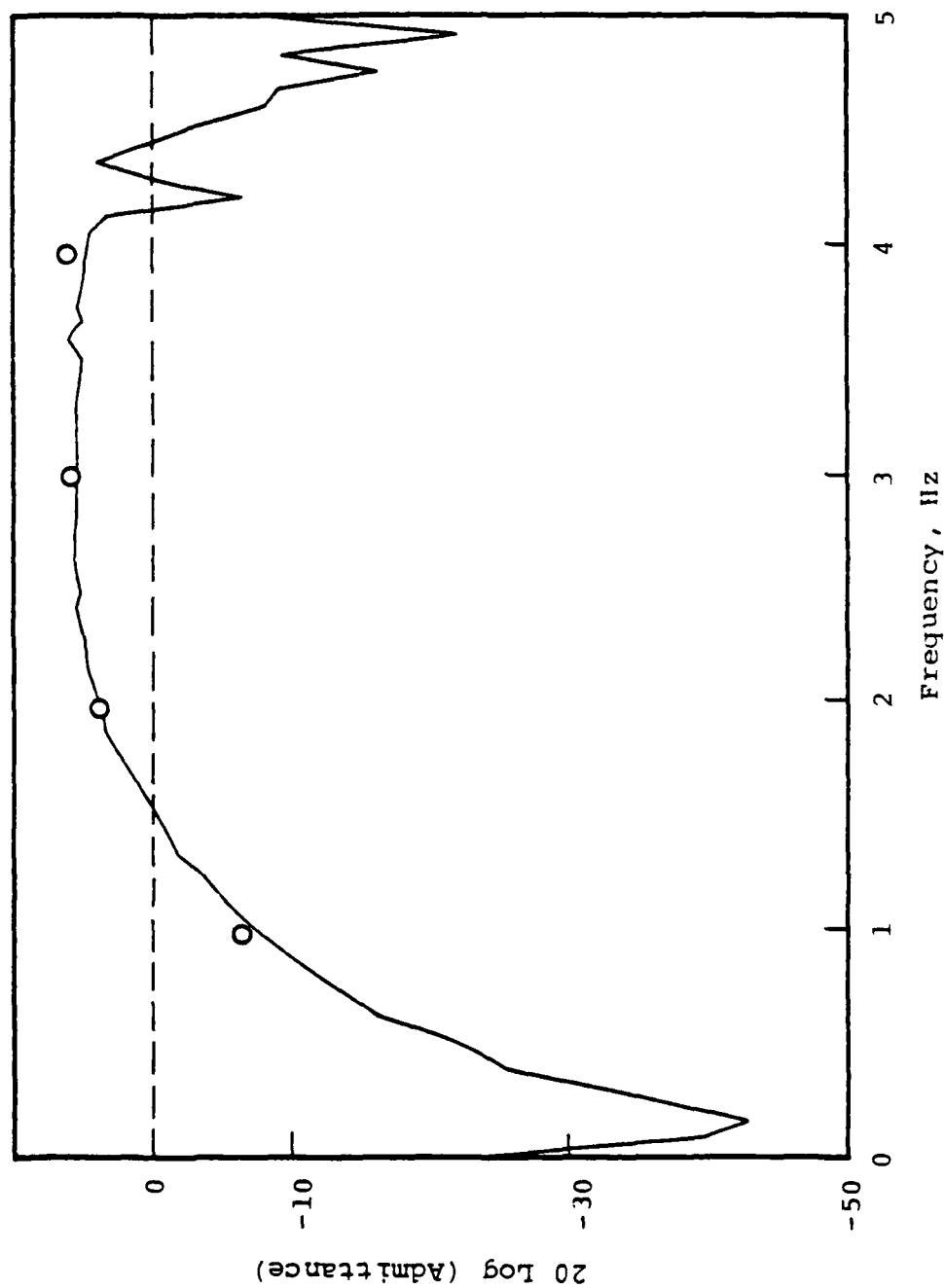


Figure 2.7. The admittance (in decibels) of the S³ Sprengnether seismometer system estimated by the cross spectrum analysis. The circles show the estimate of the admittance (or transfer function) at selected frequencies obtained from the model results plotted in Figure 2.2.

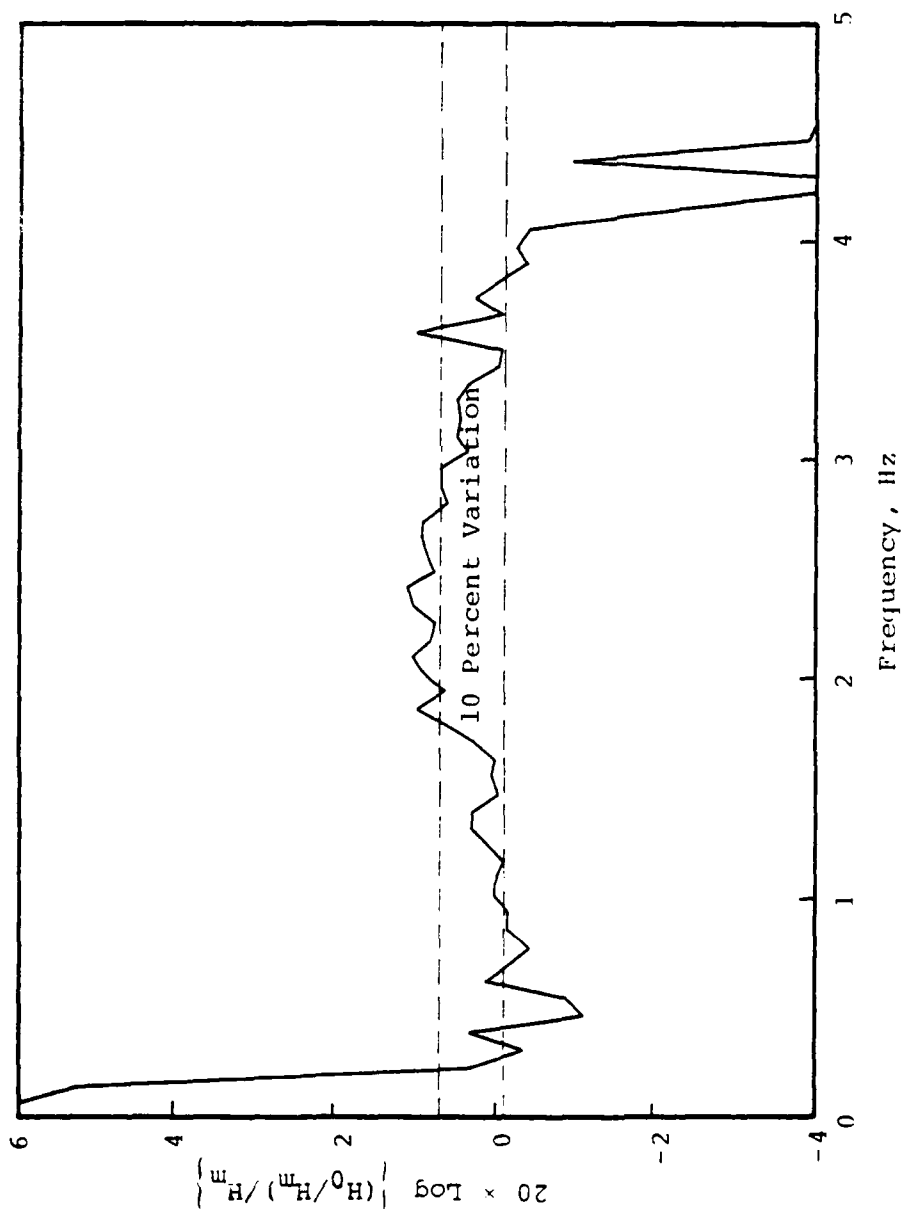


Figure 2.8. Comparison between the Sprengnether transfer function estimated by modeling the seismograph system response (H_M) and the transfer function (H_0) calculated from a cross spectrum analysis of event LOWBALL recorded at LLL station landers by the LLL and S^3 seismographs. The 10 percent variation is due to slight deviation in the model parameters (seismometer period and damping, or filter capacity values), and is not significant for this study. The larger errors for frequencies below 0.2 Hz are probably caused by side bands in the cross spectrum distorting the cross spectrum calculation. They could be reduced by first prefiltering the LLL seismogram with the Sprengnether model impulse response.

To prepare the DIABLO HAWK digital data for analysis, the field cassettes were read on the Sprengnether DP-100 playback system, and the data were copied into the Univac computer using the S³ designed DI-100 digital interface. Then the true start time was determined, the time code marks were stripped from the seismograms and the data were lowpass filtered and decimated to yield signals with a sample interval of 0.1 second (5 Hz Nyquist frequency).

2.4 OTHER DATA

Several requests were made to universities in the Western United States for digital records of MIGHTY EPIC and DIABLO HAWK, but these were not aggressively pursued, mainly because of the effort needed to analyze the data already in hand. Nevertheless, because of the great seismological interest in further study of these two underground tests, we believe that it would be useful to study other data, particularly from the California Institute of Technology, University of California, Berkeley, University of Nevada, Reno and University of Utah.

III. ANALYSIS METHODS

Three methods have been used to study the seismic signals excited by MIGHTY EPIC and DIABLO HAWK. In this section we briefly describe these methods and show typical results of the calculations. The bulk of the results obtained, however, and the interpretation of them, is described later, in Sections IV and V.

3.1 SPECTRAL RATIOS

A very basic question to be asked is what are the similarities and differences between the seismograms obtained from the two events? Since we have recordings of each made by identical instruments, and since the two shot points were just 150 m apart, whereas the recorder locations were further than 100 km, one might expect the two events to yield "identical" seismograms. They did not.

To quantify the relationship between the seismic signals excited by MIGHTY EPIC and DIABLO HAWK, we hypothesized the following linear model:

If $m(t)$ and $d(t)$ is the pair of seismograms obtained from one instrument (vertical, radial or transverse velocity sensors), and if d is linearly related to m , then there exists a convolution operator, $h(t)$ such that

$$d(t) = \int_{-\infty}^{\infty} h(\zeta)m(t-\zeta)d\zeta \quad . \quad (3.1)$$

With our supposition that the transmission path and the instruments were unchanged between the two events, the kernel function $h(t)$ says something about the difference between the two source functions.

It is easiest, however, to consider $H(f)$, the Fourier transform of $h(t)$. Taking the transform of (3.3), we have

$$D(f) = H(f) M(f) . \quad (3.2)$$

To determine $H(f)$ it is not correct simply to divide the transform of d by the transform of m , because in the presence of noise this leads to a biased and uncertain estimate of H . The proper procedure is to perform a cross spectrum analysis (Bendat and Piersol, 1971). We have done this using the method of segment averaging. Each seismogram pair was divided into equal length overlapping sections, starting with the earliest arrival and ending well past the maximum in the envelope of the short period surface wave train. The ending times corresponded to group velocities between 1.6 and 2.3 km/s. For each section pair we computed the powers and cross powers, after applying a cosine taper to the time series,

$$\begin{aligned} P_d^i(\omega) &= DD^* , \\ P_m^i(\omega) &= MM^* , \\ C_{dm}^i(\omega) &= DM^* . \end{aligned} \quad (3.3)$$

The powers and cross power for all N section were then averaged,

$$P_d(f) = \frac{1}{N} \sum_i P_d^i(f) , \quad (3.4)$$

(and likewise for P_m and C_{dm}).

From the averaged powers and cross powers, the coherency was estimated by the relationship

$$\gamma_{dm}^2(f) = \frac{|C_{dm}(f)|^2}{P_d P_m}, \quad (3.5)$$

and the transfer function (or spectral ratio) by the relationship

$$H(f) = \frac{C_{dm}}{P_m}. \quad (3.6)$$

The transfer function was further resolved into an amplitude function, or admittance

$$\text{Admittance} = |H(f)|, \quad (3.7a)$$

and a phase function

$$\text{Phase} = \text{Arg } H(f), \quad (3.7b)$$

where

$$H(f) = |H(f)| e^{i \text{Arg } H(f)}. \quad (3.7c)$$

3.2 PASSBAND FILTERING

The MARS analysis method (Section 3.3) uses rather narrow Gaussian filters to provide, in essence, a time dependent spectrum analysis. We have found it useful also to filter the seismograms with a somewhat broader filter to capture more of the dispersed surface waves in a single figure. To do this, an equiripple filter (Kaiser and Reed, 1978) was designed which isolated the period range $8s < T < 4s$ and attenuated longer and shorter periods by about 40 db. We focused on this period range because the previous MARS calculation indicated that the energy outside this band was confused by

either noise or higher mode surface waves. Furthermore, in some of the MARS analyses, the signals within the band sometimes had erratic amplitudes, an effect we anticipated would be smoothed out by application of a broader filter. It is also known (Denny and Chin, 1976) that, at least for the Livermore stations, the predominant Rayleigh wave consistently observed from NTS explosion has a period of about 8 seconds.

As an example of the passband filter analysis, we show in Figure 3.1 the amplitude response of the bandpass filter (the time domain kernel is symmetric so the phase response is zero at all frequencies). Figure 3.2 gives the three Mina seismograms for MIGHTY EPIC and the result of bandpass filtering the three seismograms with the filter shown in Figure 3.1.

3.3 MULTIPLE ARRIVAL RECOGNITION SYSTEM (MARS) ANALYSIS

To isolate the dispersed surface waves buried within the broad band seismograms, a more refined analysis method than the simple passband filtering described in Section 3.2 is needed. Such an analysis is possible with the S³ MARS program which, among many other functions, processes a seismogram through a comb of filters each having a Gaussian frequency response. Gaussian filters have been often used to analyze dispersed signals in seismology (Dziewonski, et al., 1969; Denny and Chin, 1976), but the power of the MARS analysis lies in the ancillary calculations that can be made on the filtered signals. Figure 3.3 (using words), and Figure 3.4 (using equations), outline the steps of a MARS analysis.

The MARS analysis had two objectives. The first objective was simply the identification of the surface wave arrival. This was not always unambiguous because of background noise signals, multipathing, the existence of Love wave and Rayleigh wave overtone (higher) modes. The latter two problems are particularly acute in the shorter

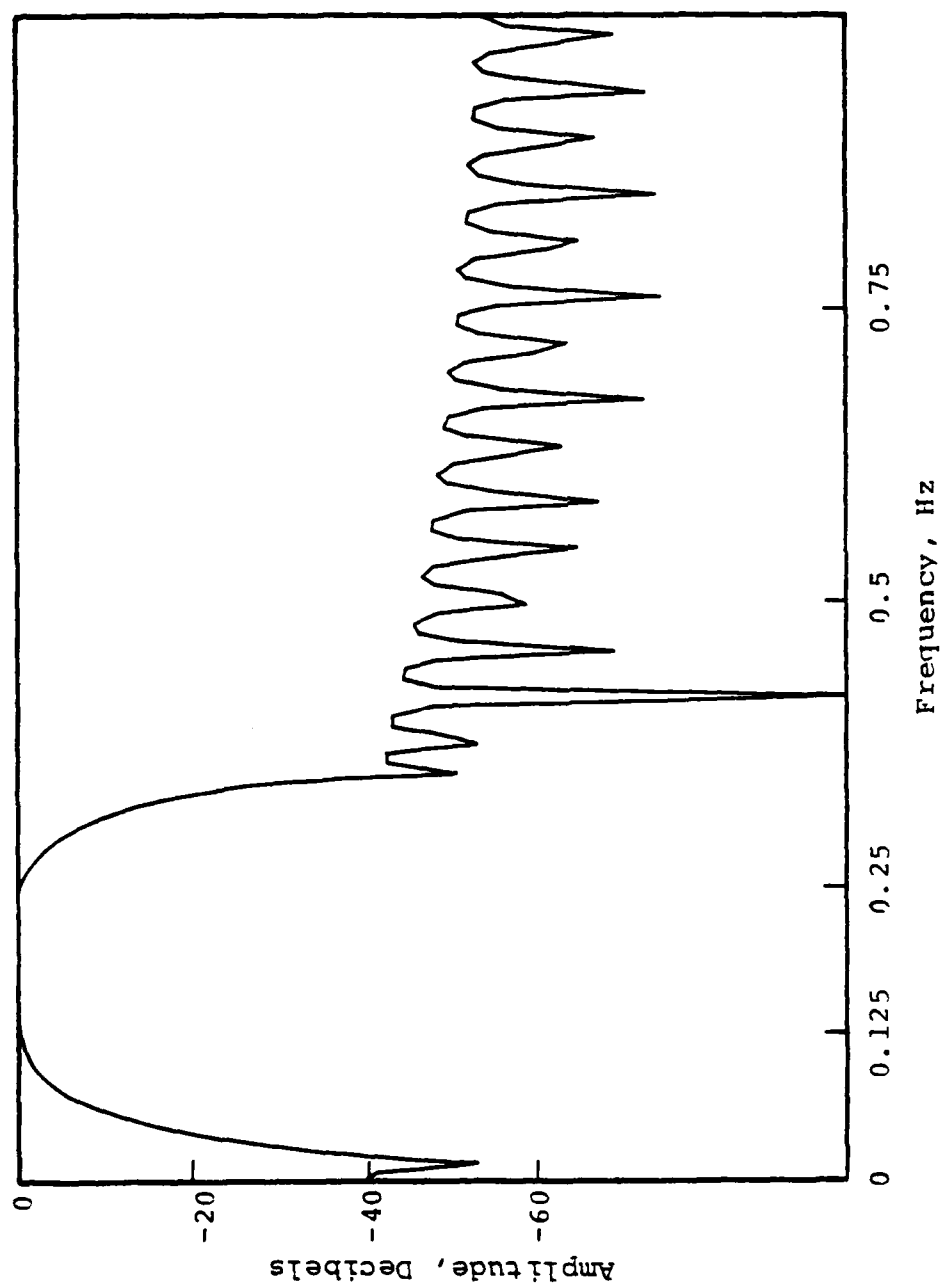


Figure 3.1. The amplitude response of the zero phase shift filter used to isolate the 4 to 8 second period range on all the seismograms. The side bands are more than 40 db below the pass band amplitude, and the attenuation is 6 db at 0.075 Hz (13.3s) and 0.3 Hz (3.3s).

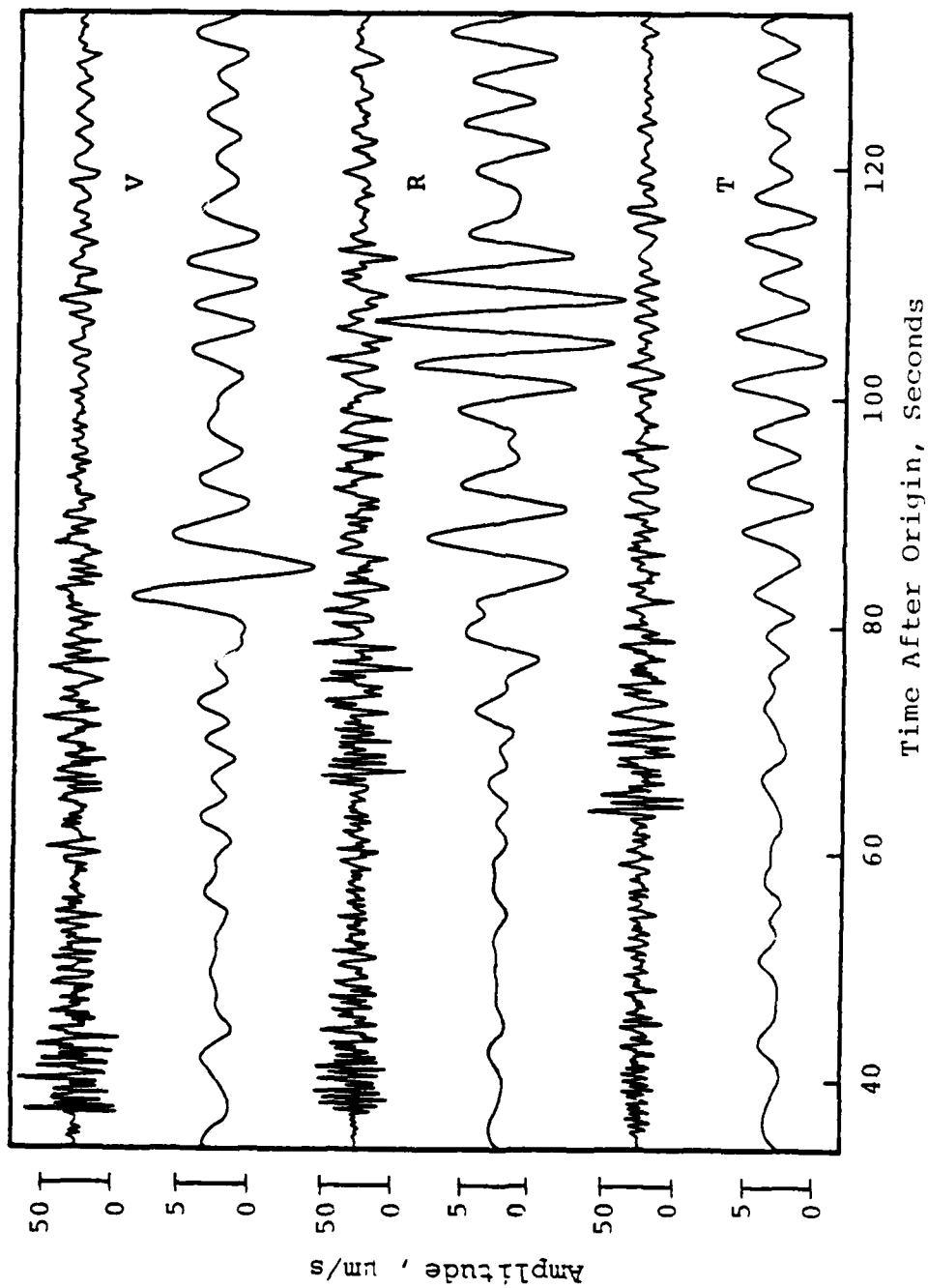


Figure 3.2. The MIGHTY EPIC seismograms recorded at Mina, and the long period (4 to 8 second period) surface waves obtained by band pass filtering the recorded signal using the filter displayed in Figure 3.1.

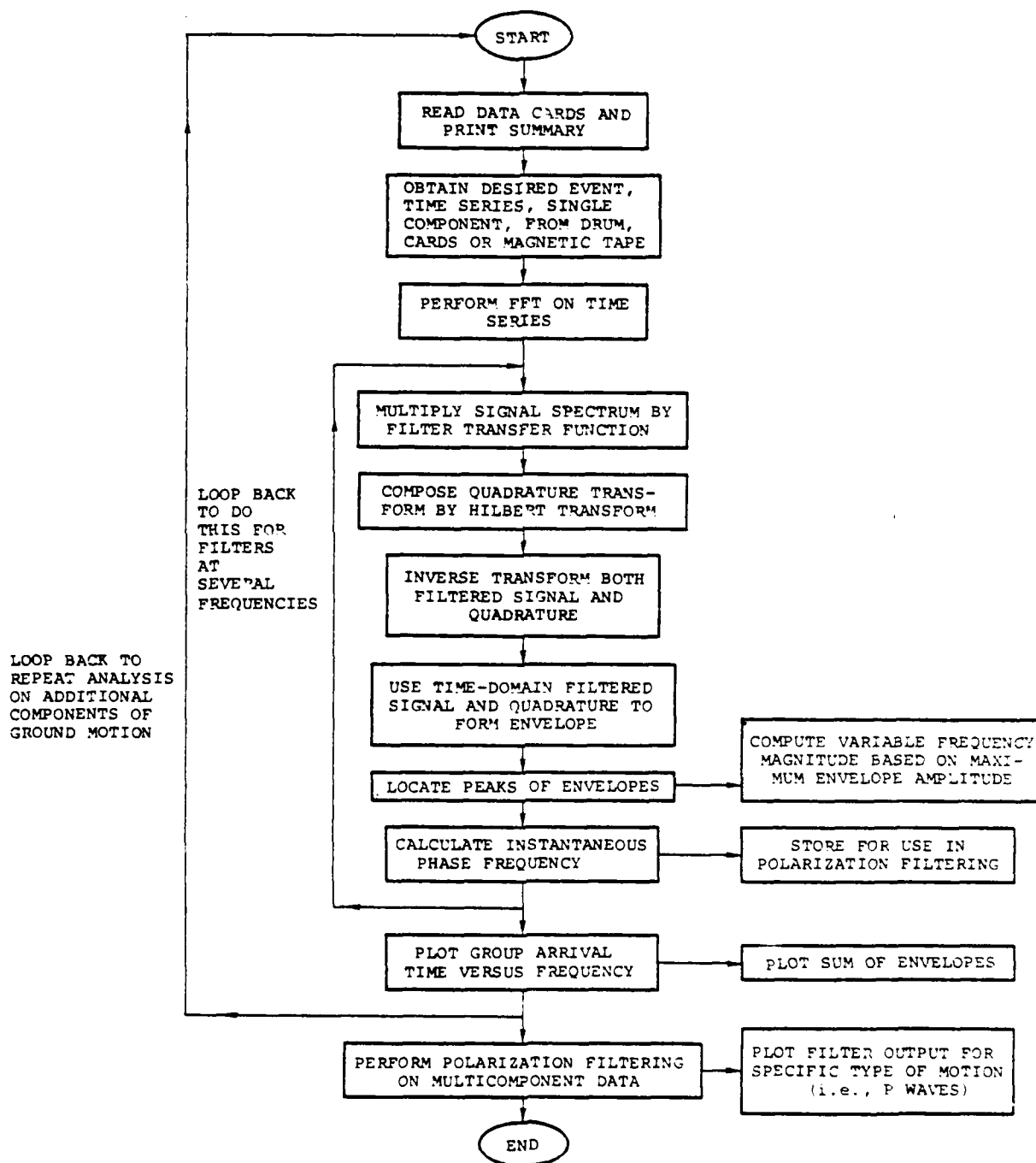


Figure 3.3. Flowchart of the MARS operations.

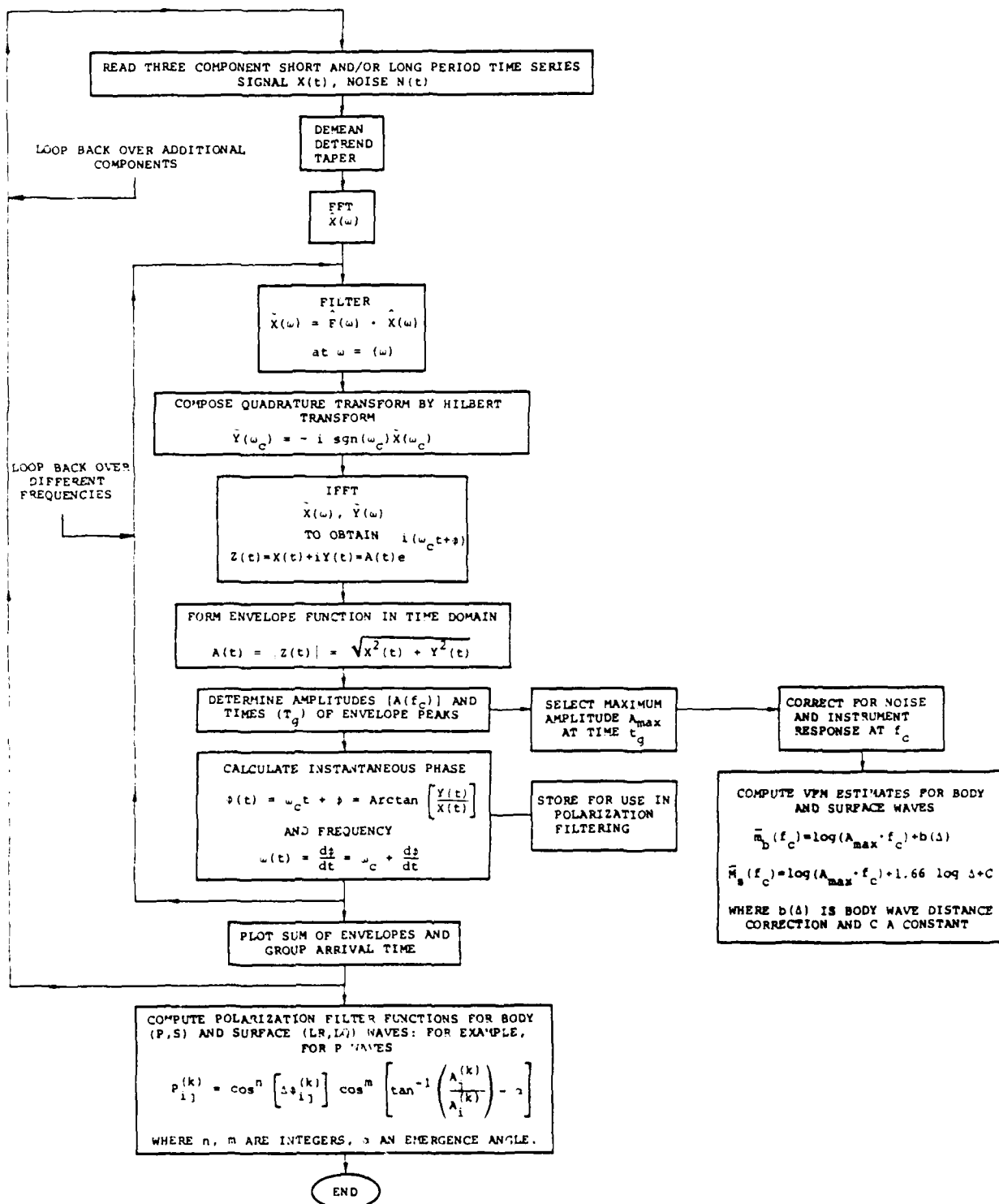


Figure 3.4. The equations applied during analysis of seismograms by MARS.

period bands of the MIGHTY EPIC and DIABLO HAWK events, and it was decided early on to limit the surface wave analysis to periods greater than four seconds.

The primary criterion used to identify the surface wave arrivals was the frequency dependent group velocity. Priestly and Brune (1978) in a study of surface wave propagation across the Great Basin, derived Love wave and Rayleigh wave dispersion curves, using both the single station and two-station methods, for events outside the basin itself. At the shortest period for which they give results, five seconds, the inferred group velocities are about 2.5 km/s for Rayleigh waves and 2.1 km/s for Love waves. This is roughly in accord with our observation of the bandpass filter processing (Figures 5.5a, 5.5b, 5.6a and 5.6b for MIGHTY EPIC and DIABLO HAWK, respectively). The signals plotted in those figures show that 2.5 km/s is a good average for the Rayleigh wave (vertical component) group velocities. The Love waves (transverse component) are not so clear, but especially at TNP and LAC the slower Love wave propagation speed is apparent.

Examples of the MARS processing are given in Figures 3.5 and 3.6, showing the time domain filtered seismograms for the vertical and transverse component of the DIABLO HAWK seismogram recorded at the S³ station Shellbourne. On each figure 10 traces are displayed, giving, for times between 80 and 160 seconds after origin times, the signals passed by each filter, where the filter center frequencies are listed on the left abscissa. Also shown on each figure is a locus of asterisks. Each asterisk appears at the time at which the envelope function of a given signal achieved a local maximum. For the lower frequency traces towards the top of each figure, it is clear that the local envelope maximum is a global maximum over the entire displayed signal. For the higher frequency signals, however, we have placed the asterisks at the local maximum which best defines a smooth curve running across

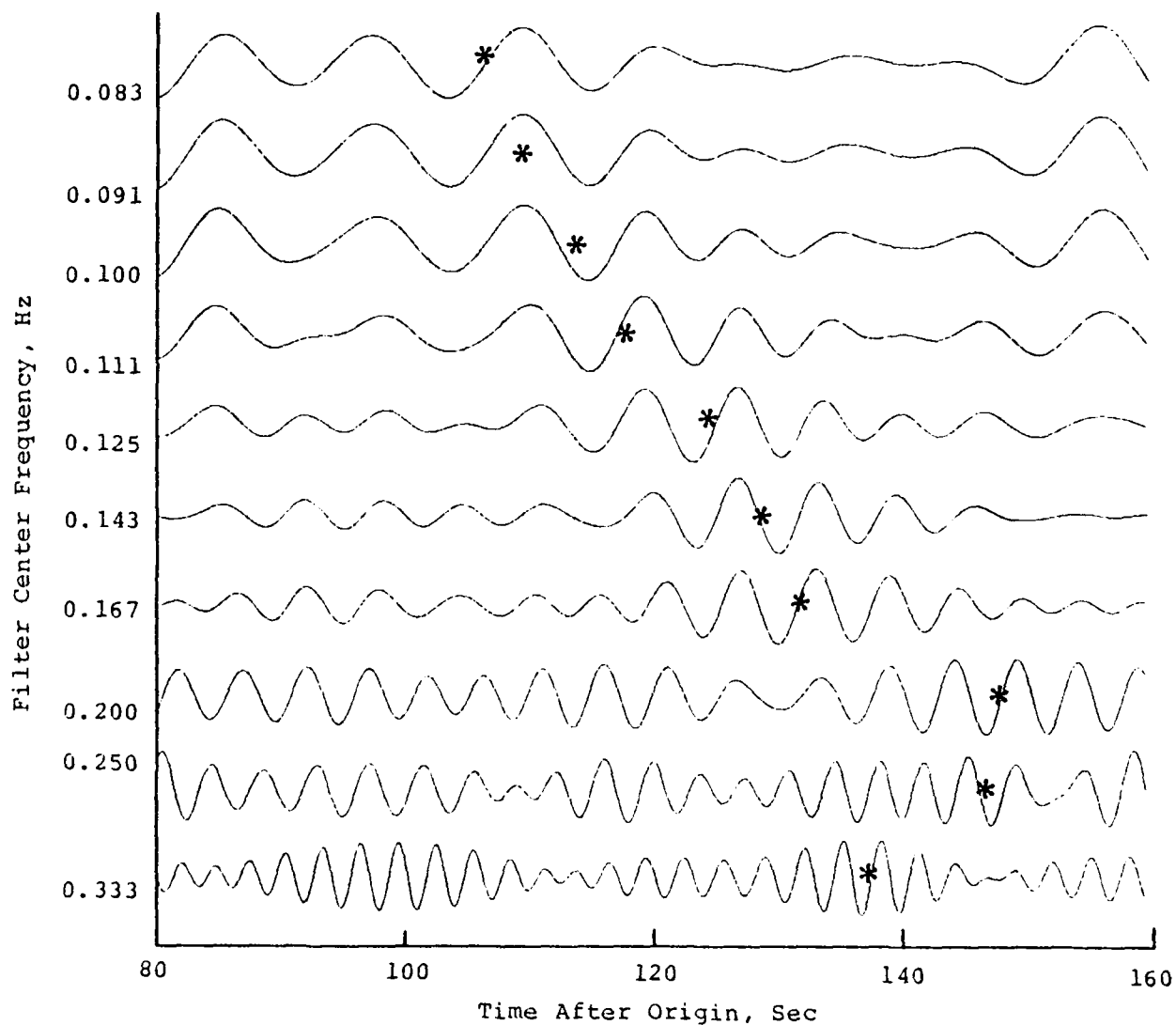


Figure 3.5. The result of processing the DIABLO HAWK vertical component seismogram recorded by S^3 at Shellbourne (317 km) with the staggered narrow band filters used in the MARS (Multiple Arrival Recognition System) analysis. The center frequency of each filter is given on the left axis. The stars indicate the envelope maximum in each filter output. The time axis spans the range of group velocities between 4.0 km/s (left side) and 2.0 km/s (right side).

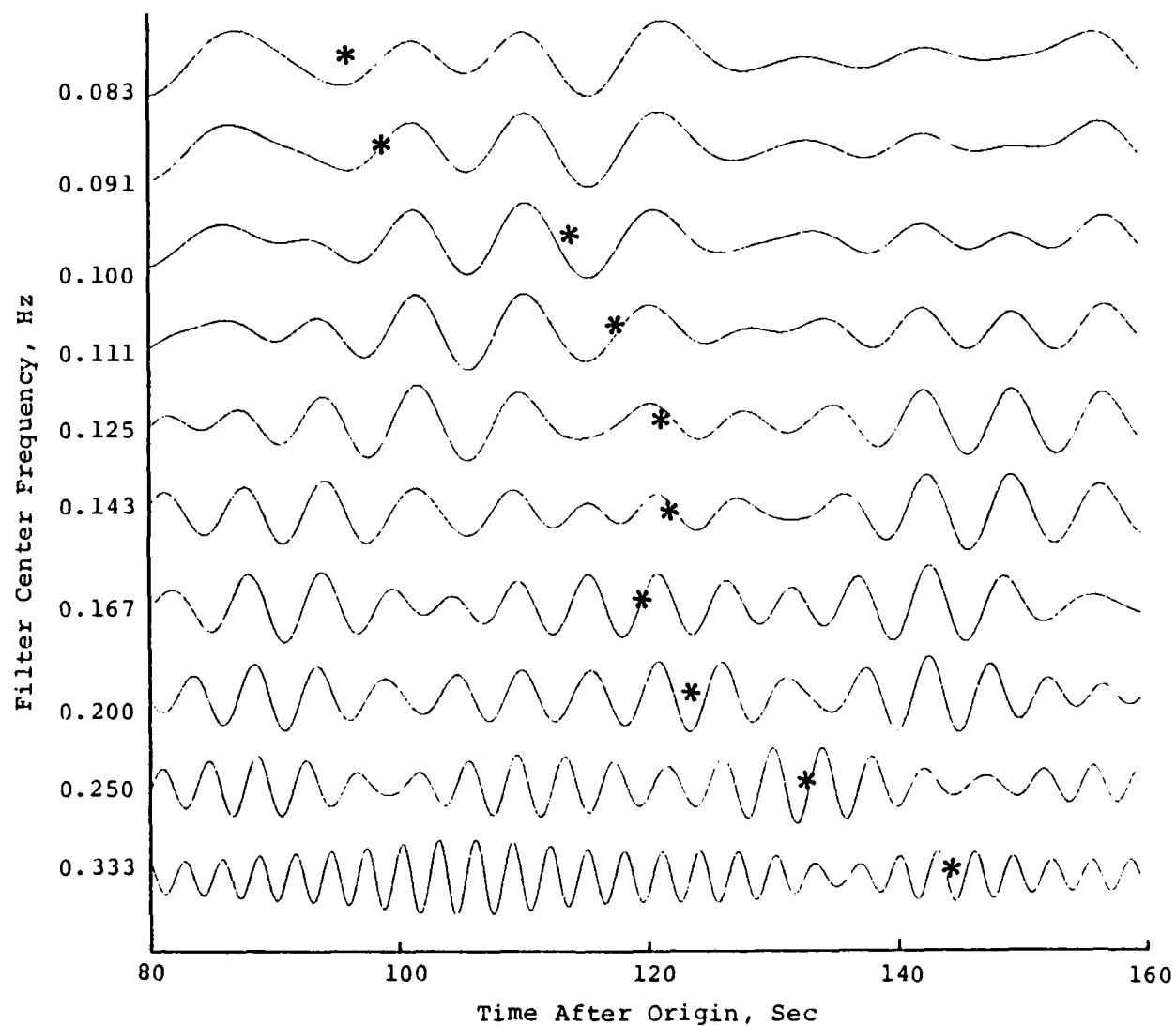


Figure 3.6. The result of processing the DIABLO HAWK transverse component seismogram recorded by S³ at Shellbourne (317 km) with the staggered narrow band filters used in the MARS (Multiple Arrival Recognition System) analysis. This figure and the previous one indicate that the higher frequency bands (the two bottom traces in each figure) give ambiguous results as a consequence of many modes arriving within the 2 km/s to 4 km/s group velocity window.

all traces. The locus of asterisks thus defines the dispersion curve for this station. On the vertical component diagram, Figure 3.5, the inferred group velocities range between 3 km/sec (0.083 Hz) and 2.44 km/sec (0.167 Hz).

The advantage of the MARS analysis can be seen by comparing Figures 3.5 and 3.6 with the bandpass signal shown in Figure A.7. The signal amplitudes are so low that the surface waves arriving between 100 and 140 seconds after the origin time are barely visible.

IV. RELATIVE GROUND MOTIONS

Numerous joint recordings of MIGHTY EPIC and DIABLO HAWK are available in the LLL and Sandia data sets. We have used these in a comparative study of the ground motion excited by the two events. There are significant differences between the MIGHTY EPIC and DIABLO HAWK ground motions which must be caused by differences in the character of the source.

Five stations (Tonopah, Mina, Leeds, Landers and Battle Mountain) supplied three-component seismograms for both events. For Darwin, only the vertical component was available. This is a total of 16 common recordings.

To study the relative ground motions at these six stations, we did not measure the amplitude of any particular seismic phase. Instead of analyzing individual seismic phases, many tens of seconds of the seismogram were processed to calculate the spectral ratios according to the method described in Section 3.1. In most instances, each seismogram was segmented into 12.8 second blocks, giving between four and twelve independent sections for the spectral averaging. Table 4.1 shows the parameters for each station.

It may seem bizarre to treat a deterministic, dispersed (hence non-stationary) signal with the techniques of random time-series analysis. Our reasoning is that although in any one section of the seismogram the destructive and constructive interference of waves might seriously distort the spectrum, these effects would tend to average out. Furthermore, by taking the whole signal into consideration, we are including essentially all of the signal energy in the calculation.

TABLE 4.1

RECORD LENGTHS OF THE SEISMOGRAMS USED TO STUDY RELATIVE
GROUND MOTION*

<u>Station</u>	<u>Record Length (sec)</u>	<u>Slowest Group Velocity in the Window (km/sec)</u>	<u>Number of Segments</u>
Tonopah	51.2	1.8	4
Darwin	76.8	1.6	6
Mina	102.4	1.6	8
Leeds	102.4	1.8	8
Landers	153.6	1.6	12
Battle Mountain	102.4	2.3	8

* Each record started with the first motion (P_n or P_g) and included all phases arriving with group velocities faster than those shown in the second column.

4.1 GENERAL DEPENDENCE OF ADMITTANCE ON FREQUENCY

Our basic conclusion from the spectral ratio (or admittance) calculations is that at long periods ($T > 4$), DIABLO HAWK excited smaller amplitude seismic waves than did MIGHTY EPIC. On the other hand, at high frequencies ($f \approx 2$ Hz), the seismic waves were of comparable amplitude for each event. The contrast between the low frequency and high frequency spectral ratio results holds for nearly all stations and azimuths and also for all three components at each station.

The finding that the spectral ratio is about unity at 2 Hz is in accord with the observation that the P_n waves for each event were, within experimental error, the same, because P_n is typically a wavelet whose spectrum peaks near 2 Hz. The P_n phase is the first arriving P wave, which is often used as an indicator of seismic yield (e.g., Springer and Hannon, 1973). Thus, we conclude that the seismic yields of the two events are the same.

Recall (Equation (3.2)) that the cross-spectrum is a technique for finding the filter, $H(f)$, which in some sense "best" relates the MIGHTY EPIC and DIABLO HAWK seismograms:

$$D(f) = H(f) M(f). \quad (4.1)$$

For 16 seismogram pairs, and at 65 discrete frequencies spaced uniformly in the interval 0 to 5 Hz, we have calculated $H(f_i)$. From each function H , we have estimated a long period average \hat{H}_1 , and a short period average \hat{H}_2 . An example will be shown in Section 4.2. Here we summarize the results which are given in Table 4.2.

The average \hat{H}_1 is the mean value of the amplitude over the band $0.07 < f < 0.31$ Hz, and \hat{H}_2 is a similar average for $1.5 < f < 2.5$ Hz. There are certain limitations in this simple presentation of the calculation results. For example, since different bandwidths were used in the two averages, the

TABLE 4.2
SUMMARY OF SPECTRAL RATIO CALCULATIONS*

<u>Station</u>	<u>Component</u>	<u>\hat{H}_1</u>	<u>\hat{H}_2</u>	<u>\hat{H}_2/\hat{H}_1</u>
Tonopah	V	0.60	0.90	1.50
	R	0.58	0.86	1.48
	T	0.63	0.92	1.46
Darwin	V	0.75	0.90	1.20
Mina	V	0.55	1.02	1.85
	R	0.62	0.92	1.48
	T	0.60	1.00	1.67
Leeds	V	0.55	0.82	1.49
	R	0.50	0.83	1.66
	T	1.00	0.62	0.62
Landers	V	0.50	0.91	1.82
	R	0.45	0.86	1.91
	T	0.50	0.80	1.60
Battle Mtn.	V	0.70	0.76	1.08
	R	0.50	0.70	1.40
	T	0.47	0.77	1.64
Logarithmic Mean**		0.56	0.86	1.53
Standard Deviation		16%	11%	17%

* \hat{H}_1 is an average over the frequency band 0.07 Hz to 0.3 Hz of the DIABLO HAWK/MIGHTY EPIC admittance (Equation (3.7)). \hat{H}_2 is a similar average taken over the frequency band 1.5 to 2.5 Hz.

** Excluding T at Leeds.

statistical uncertainties are different. We took no account of the uncertainties attached to each admittance function. The average \hat{H}_1 is dangerously close to zero frequency, where spectrum analysis often encounters difficulties because only a few cycles of motion are present in the data. In many instances there are sharp peaks and troughs in $H(f)$ and it is not clear that a straight average is the best method of smoothing H . Nevertheless, the results listed in Table 4.2 illustrate dramatically the contrast between the short period and long period spectral ratios of the seismograms recorded for each pair of events. With the single exception of the transverse component at Leeds, the high frequency estimate is close to 1.5 times larger than the low frequency estimate, \hat{H}_1 . Discounting this component, the logarithmic mean of the \hat{H}_2/\hat{H}_1 ratios is

$$\text{mean } \frac{\hat{H}_2}{\hat{H}_1} = 1.53 \quad (4.2)$$

and the standard deviation is only 17 percent of the mean.

It is interesting to compare these spectral results to time domain measurements of the most prominent high frequency phases on the records. These are the P_n and P_g on the vertical and the L_g on the tangential. The P_n is the first arrival at these ranges and is considered to be a reliable indicator of seismic yield (e.g., Springer and Hannon, 1973). The P_g is defined to be the largest amplitude arrival which occurs near the beginning of the record (apparent velocity near 6 km/sec) while the L_g is a large high frequency arrival with apparent velocity near 3.5 km/sec. The P_n , P_g and L_g amplitudes are listed in Table 4.3. For P_n we list the amplitude of the first (a), second (b) and third (c) peaks. The DIABLO HAWK/MIGHTY EPIC ratios for these phases are compared to the appropriate (vertical or tangential) spectral ratio \hat{H}_2 from

TABLE 4.3

Pg AND Lg AMPLITUDES*

<u>Station</u>	<u>Phase</u>	<u>MIGHTY EPIC</u>	<u>DIABLO HAWK</u>	<u>Ratio</u>	<u>\hat{H}_2</u>
Tonopah	P _n a	21.8	21.9	1.00	0.90
	b	53.4	54.7	1.02	0.90
	c	66.6	64.2	0.96	0.90
	Pg	59.4	51.8	0.87	0.90
	Lg	25.3	29.2	1.15	0.92
Darwin	P _n a	13.3	20.7	1.56	0.90
	b	47.5	53.3	1.12	0.90
	c	62.0	66.9	1.08	0.90
	Pg	57.6	58.1	1.01	0.90
	Lg	77.0	52.8	0.69	0.90
Mina	P _n a	3.7	4.3	1.16	1.02
	b	9.7	10.5	1.08	1.02
	c	8.7	10.9	1.25	1.02
	Pg	33.4	39.7	1.19	1.02
	Lg	36.6	34.7	0.95	1.00
Leeds	P _n a	7.1	5.7	0.80	0.82
	b	13.9	13.4	0.96	0.82
	c	14.0	14.9	1.06	0.82
	Pg	48.6	36.0	0.74	0.82
	Lg	63.0	60.0	0.95	0.62
Kanab	P _n a	3.8	3.1	0.82	--
	b	9.9	8.3	0.84	--
	c	8.6	8.0	0.93	--
Landers	Pg	6.5	6.4	0.98	0.91
	Lg	20.3	15.5	0.76	0.80
Battle Mountain	Pg	27.0	28.2	1.04	0.76
	Lg	32.4	27.0	0.83	0.77

* Amplitudes are given in microns/seconds.

Table 4.2. In nearly all cases, the two estimates for the relative amount of high frequency energy in the seismograms are reasonably close to the same.

4.2 RESULTS FOR MINA

The vertical component seismograms from Mina exemplify the differences between the short period and long period spectral ratios. In Figure 4.1 are plotted the power spectrums of MIGHTY EPIC (dashed line) and DIABLO HAWK (solid line), calculated by using Equation (3.4), where 102.4 seconds of data were divided into eight 12.8 second sections. Even without allowing for coherency between the two seismograms, it can be seen that above 2 Hz, the dashed line follows closely the solid line, indicating equal signal energy in the two seismograms. Below 1 Hz, however, the MIGHTY EPIC power is roughly 4 db greater than the DIABLO HAWK power, implying that the long period MIGHTY EPIC amplitude is $10^{+0.2}$ (1.58) times as large as the DIABLO HAWK amplitudes. This is consistent with the ratio given in Equation (4.2).

The close similarity between the two seismograms is indicated by the high coherencies evident in Figure 4.2. The modulus of the transfer function relating the MIGHTY EPIC seismogram to the DIABLO HAWK seismogram is plotted in Figure 4.3. Also shown there, bracketed in dashed lines, are the frequency bands used to estimate the average long period admittance, \hat{H}_1 , and short period admittance, \hat{H}_2 , with a dot in the center of each band placed at the value listed in Table 4.2. A sharp dip in the admittance can be seen at a frequency near 2.6 Hz. With reference to the coherency function plotted in Figure 4.2, this is also a frequency where the signals are not all alike, so that the admittance here has a very large error bar attached to it.

Superimposed on the general tendency of the admittance to rise with frequency, there are narrow peaks and troughs.

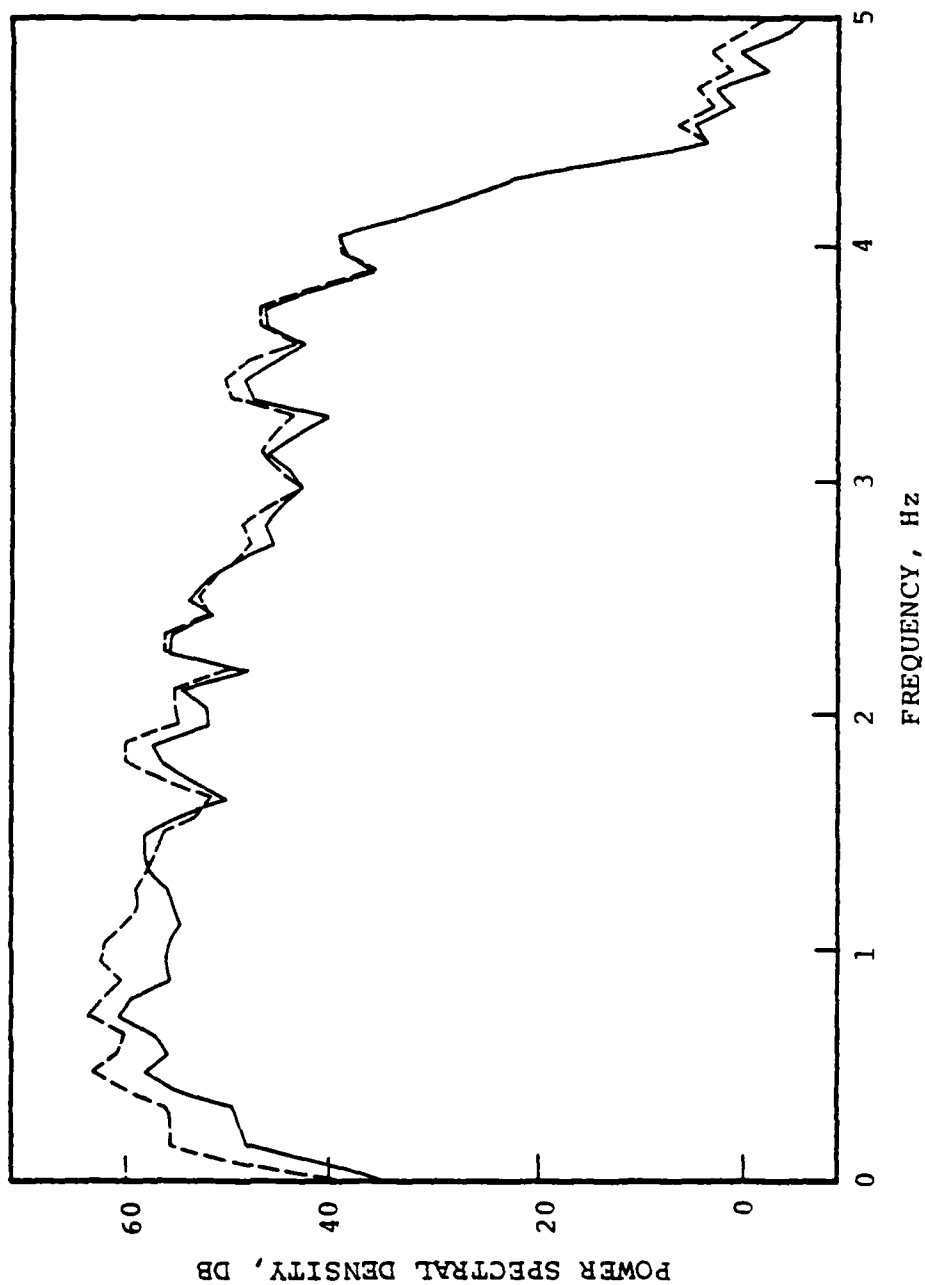


Figure 4.1. The power spectrums (Equation (3.4)) calculated for the vertical component of ground velocity at Mina from MIGHTY EPIC (broken line) and DIABLO HAWK (continuous line). For this, and the succeeding calculation, 102.4 seconds of data following the P_n arrival were analyzed in eight groups, each 12.8 seconds long. This figure shows that over most of the 5 Hz frequency band the MIGHTY EPIC signals were stronger than the DIABLO HAWK signals.

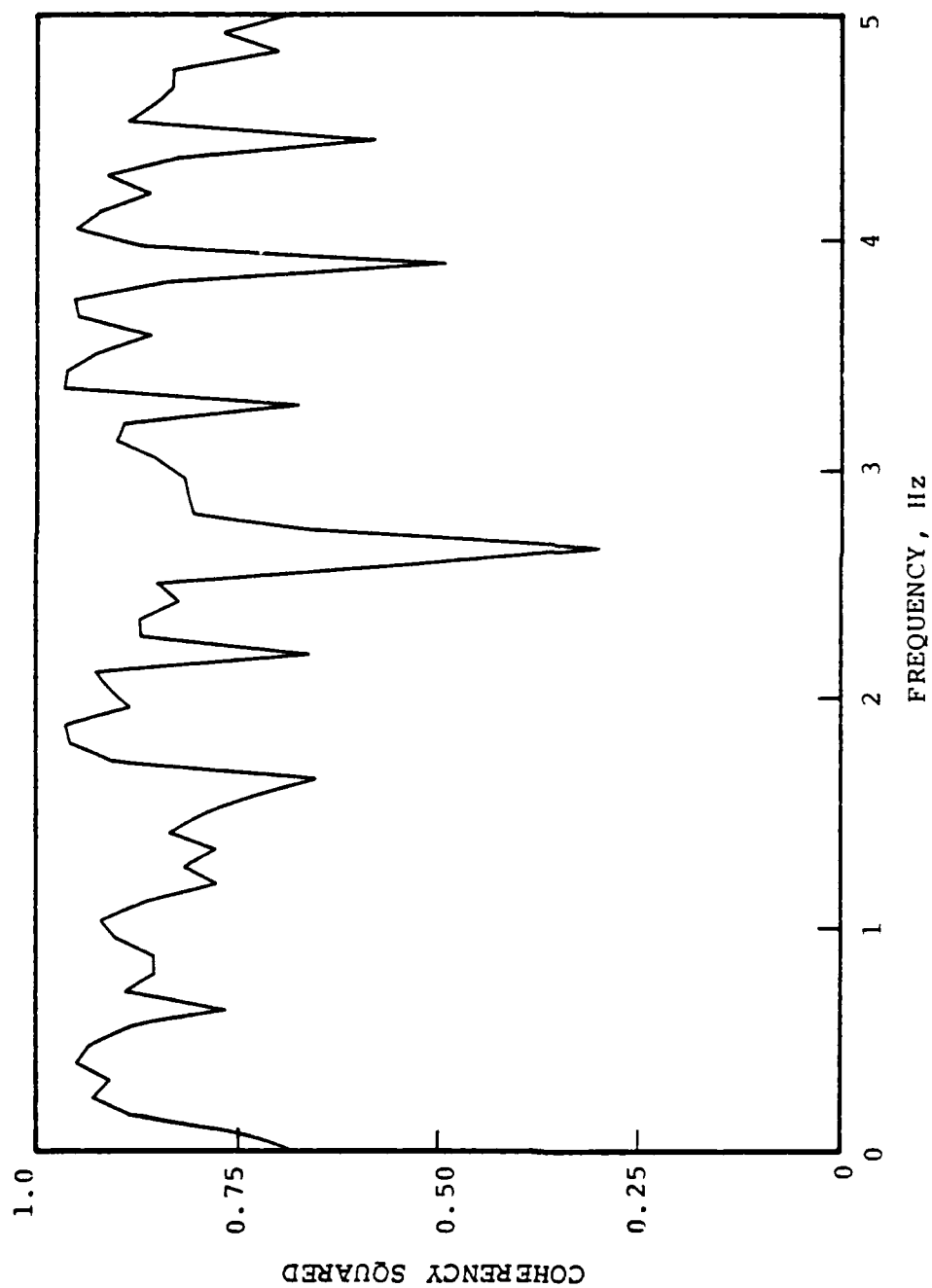


Figure 4.2. The coherency squared (Equation (3.5)) calculated between the MIGHTY EPIC and DIABLO HAWK vertical component seismograms recorded at Mina. This figure shows that the two signals are very similar, but not identical.

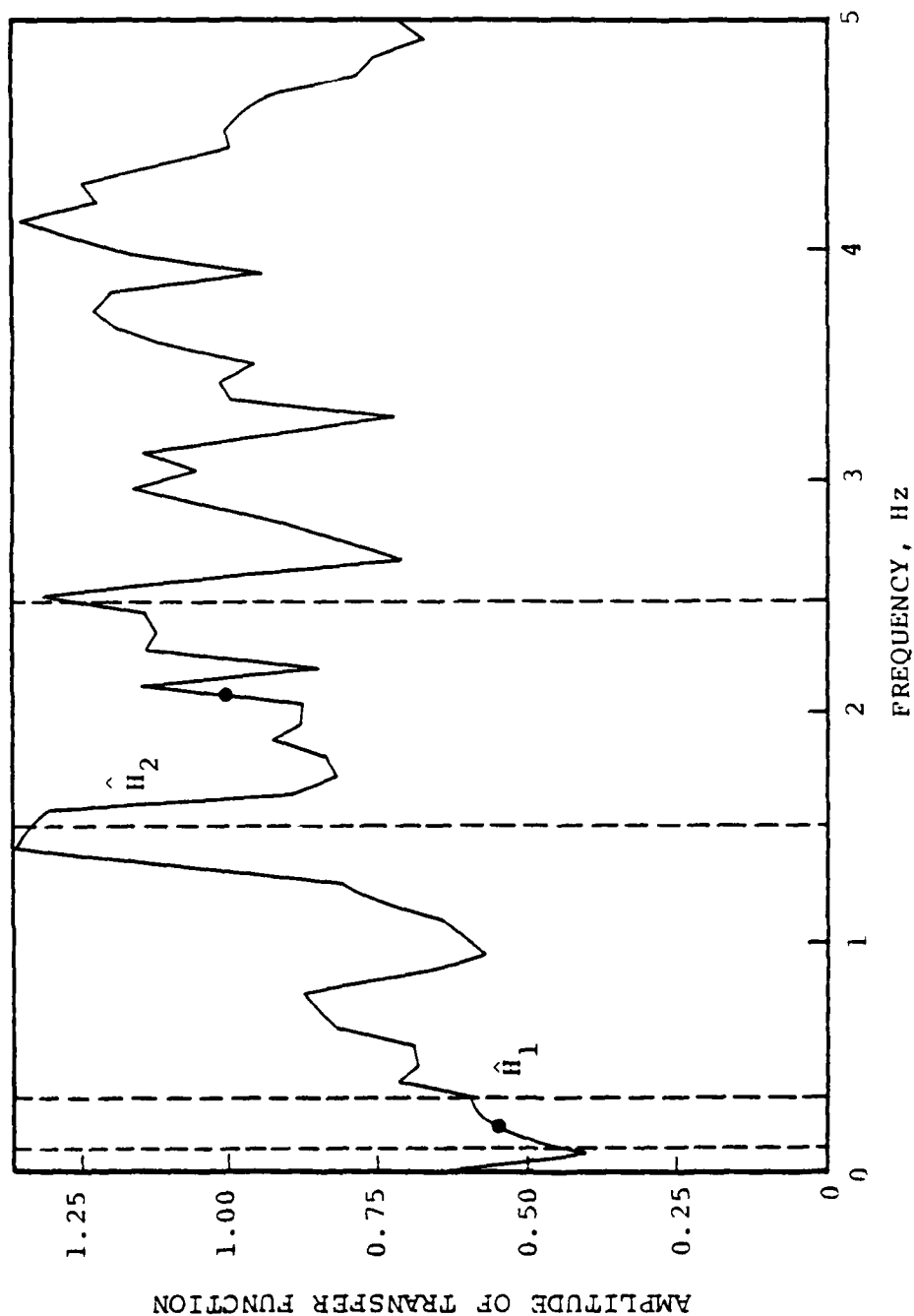


Figure 4.3. The admittance (Equation (3.7a)) or modulus of the transfer function, relating to the DIABLO HAWK and MIGHTY EPIC vertical component seismograms at Mina. This figure shows that at low frequencies the DIABLO HAWK signal was smaller in amplitude than the MIGHTY EPIC signal (admittance less than 1). This figure is not calculated simply by taking the ratio of the two power spectrums (see Figure 3.1), because the power spectrums do not distinguish between the 'signal' and the 'noise'. The noise correction enters via the coherency function, which is implicitly allowed for in the cross spectrum analysis method (Equation (3.6)).

From these we can roughly estimate the temporal duration of the impulse response of the filter $h(t)$ which relates the MIGHTY EPIC seismogram to the DIABLO HAWK seismogram. For example, the peak near 1.5 Hz has a width of 0.2 Hz. From the uncertainty principle relating the time and frequency domain, this implies $h(t)$ has important structure out to times of order five seconds. This is, of course, a time large compared to the time constant of the explosive shock, and must reflect differences in other contributions to the seismogram.

Figure 4.4 shows the phase of the transfer function relating the two Mina vertical component seismograms. In this case, the phase variation with frequency is weak. In other records we have analyzed, however, there sometimes appears a pronounced linear trend in the phase, a reflection of small discrepancies in the origin time of the two signals. We believe these are attributed to time discrepancies in digitizing the analog seismograms, and are not actually caused by delayed response in the earth.

A better physical understanding of the significance of the cross spectrum analysis is obtained by examining the results in the time domain. Recall, it has been hypothesized that there exists a convolution operator, $h(t)$, which maps m , a MIGHTY EPIC seismogram, into d , a DIABLO HAWK seismogram. We used the cross spectrum analysis to estimate $H(f)$, the Fourier transform of $h(t)$. Then the inverse transform of $H(f)$ yields $h(t)$. We have calculated the operator $h(t)$ which relates the two vertical component Mina seismograms by transforming the transfer function displayed in Figures 4.3 and 4.4. The resulting impulse response function is plotted in Figure 4.5.

The impulse response is mostly a spike located at zero time. If the two seismograms had been absolutely identical, then $h(t)$ would have been just a unit spike at the origin. If they had differed by a constant, the spike would have had

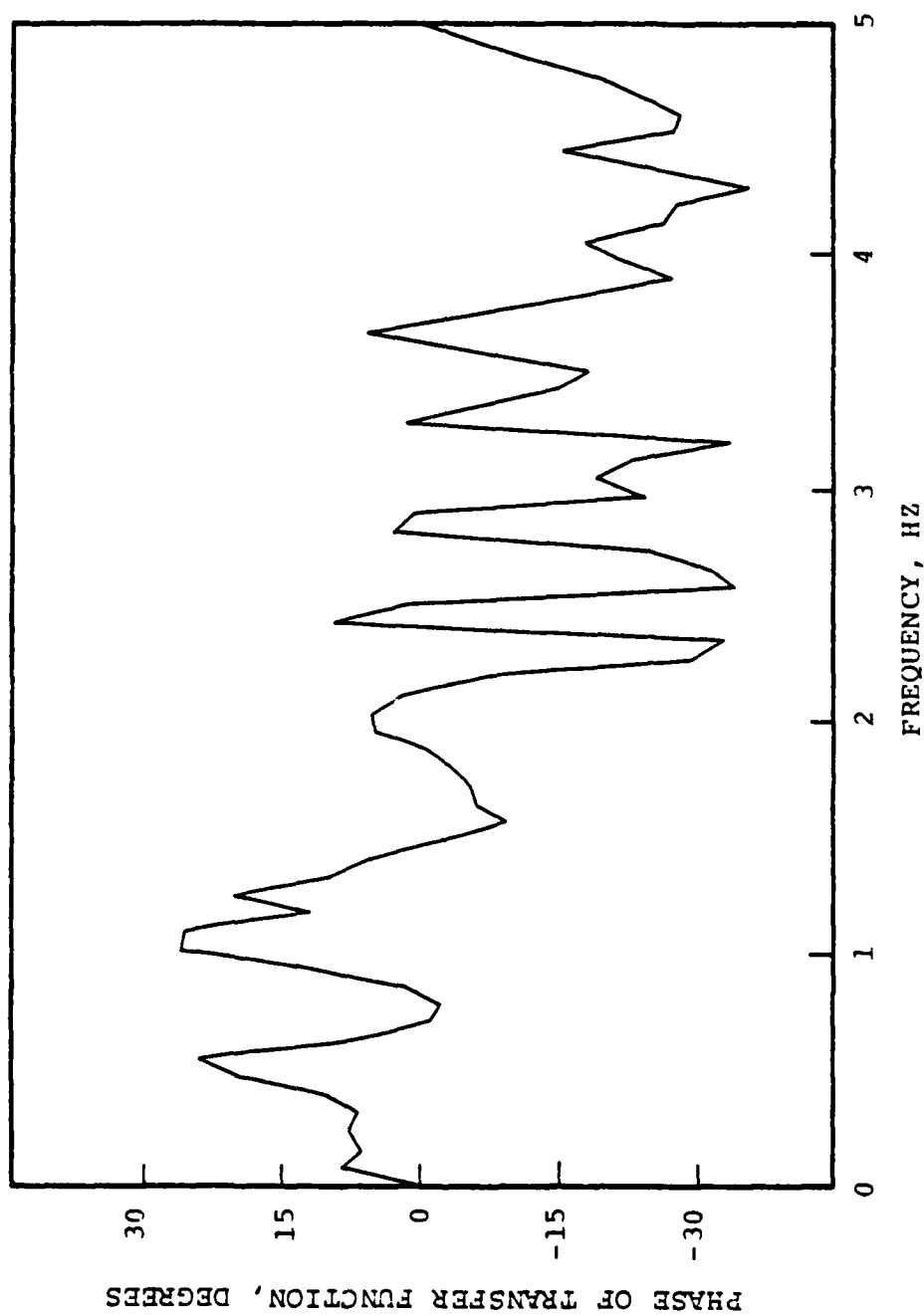


Figure 4.4. The phase angle of the transfer function relating the MIGHTY EPIC and DIABLO HAWK vertical component seismograms at Mina. The phase is small or positive at low frequencies, but negative above 2 Hz.

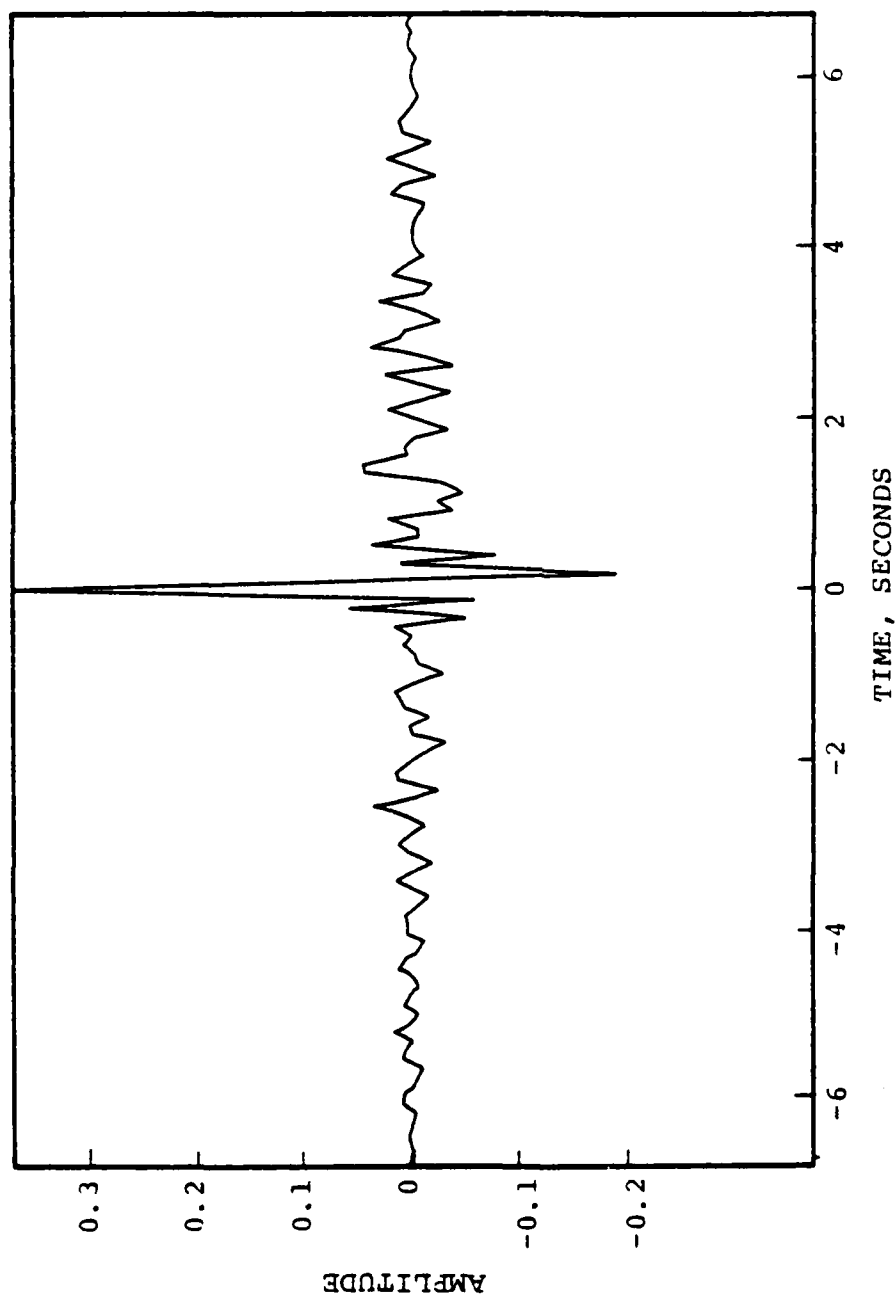


Figure 4.5. The impulse response of the smoothed filter relating the MIGHTY EPIC and DIABLO HAWK vertical component seismograms recorded at Mina. The impulse response is predominantly a spike at $t = 0$, showing that the two series are very much alike and are aligned in time. The impulse response is 'mostly causal', but there is a significant non-causal part shown for negative times.

an amplitude given by the ratio of the two gains. The additional structure displayed by $h(t)$ is another way of visualizing more complex differences between the two signals.

Having calculated the impulse response, $h(t)$, it is possible actually to pass the MIGHTY EPIC seismogram (call it m) through the filter to produce a "predicted" DIABLO HAWK seismogram, d^* , and compare d^* with the actual obtained DIABLO HAWK seismogram, d . The results of this calculation are displayed in Figure 4.6. Trace D, the error time series, $d - d^*$, is roughly a third of either d or d^* . This represents the error introduced by the smoothing and averaging (Equations (3.4) - (3.7)) employed in the cross spectrum method to compute the convolution operator $h(t)$.

4.3 RESULTS FOR LANDERS

Analysis of the vertical component signals recorded at Landers has shown that the transfer function between the MIGHTY EPIC and DIABLO HAWK seismograms does not depend on the time segment upon which the calculation is based. We take this observation as strong evidence of the reality of the conclusion that the two sources had different high frequency/low frequency energy ratios. Although other stations in our data set have not been studied in such detail, we believe that were this to be done, the results would be similar to the Landers results discussed here.

4.3.1 Transfer Functions for Three Different Time Windows

The two Landers vertical component seismograms were processed in the standard manner (see Section 4.2) to yield the power spectrum of the signal from each source, the coherency between the two signals, and transfer function relating one to the other. The transfer function was then Fourier transformed to yield the corresponding impulse response, through which the MIGHTY EPIC seismogram was passed. This yielded a "predicted"

Vertical Component

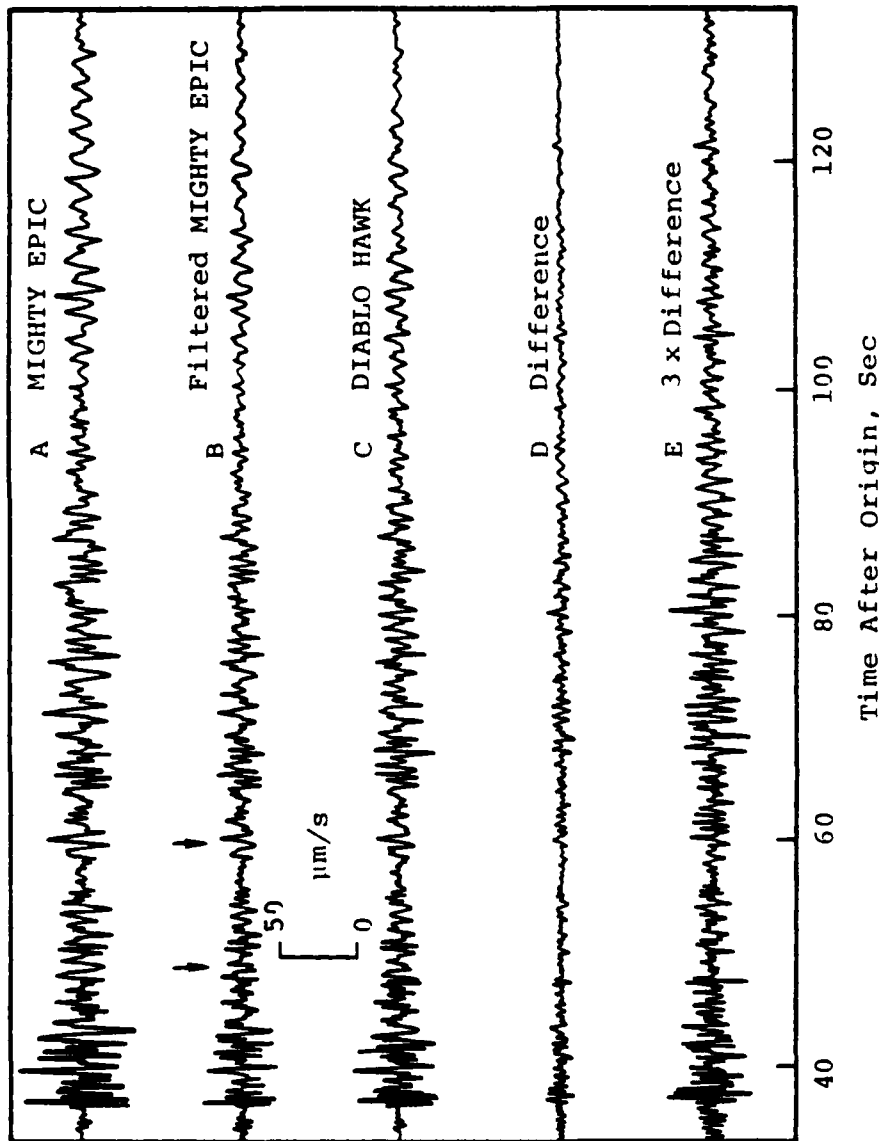


Figure 4.6. Demonstration of the degree to which the filter plotted in Figure 4.5 turns the MIGHTY EPIC vertical component seismogram (A) into the DIABLO HAWK seismogram (C), for station Mina. Arrows above the filtered MIGHTY EPIC seismogram (trace B) show recognizable phases where the filter operation improves the coherence between B and C. Trace D is the difference signal obtained by subtracting B from C, and trace E is the same difference signal plotted at a three times larger magnification. This example shows that about 66 percent of the filtered MIGHTY EPIC signal is identical to the DIABLO HAWK signal, but about 33 percent is different.

DIABLO HAWK seismogram, d^* , and an "error" seismogram, $d - d^*$. In the first instance, 153.6 seconds of data was included in the time window used for the transfer function estimation. Then, the record was split in half, and a transfer function was calculated for only the first 76.8 seconds. A third transfer function was found using just the last 76.8 seconds of data. The first half of the record included all events from the first arrival out to a group velocity of 2.5 km/sec. The second half of the record straddled the group velocity window from 2.5 km/sec to 1.6 km/sec. A summary of the calculation results is presented in Figure 4.7. The three panes in the left column of Figure 4.1 show the MIGHTY EPIC (dashed line) and DIABLO HAWK (solid line) power spectrums for the whole time window (A), the first half window (C), and the last half window (E). The drastic decrease (20 db) in the power above 1 Hz in moving from the first half to the second half of the record is clear, whereas the power below 1 Hz is, if anything, slightly greater in the second half window.

The three panes adjacent to the power spectrum curves show, respectively, the coherency (upper half) and transfer function admittance (lower half) for the three time windows.

It is seen that B (whole record) and D (first half only) are nearly identical, both for the coherency function and the admittance. Furthermore, the admittance curves both exhibit the diminished low frequency response, already discussed in Sections 4.1 and 4.2. Turning to the coherency and admittance for the last half of the record, Figure 4.7F, we see, as in the other curves, a hump about at 1.5 Hz, a droop for frequencies less than 1 Hz, and very erratic behavior above 2.5 Hz. The admittance does not quite get to unity before it turns back down. This is a consequence of the low coherency between the two signals, as is shown in the curve plotted in the top half of this pane. This, in turn, reflects the low signal amplitudes, and the consequent lowering of the signal to noise ratio.

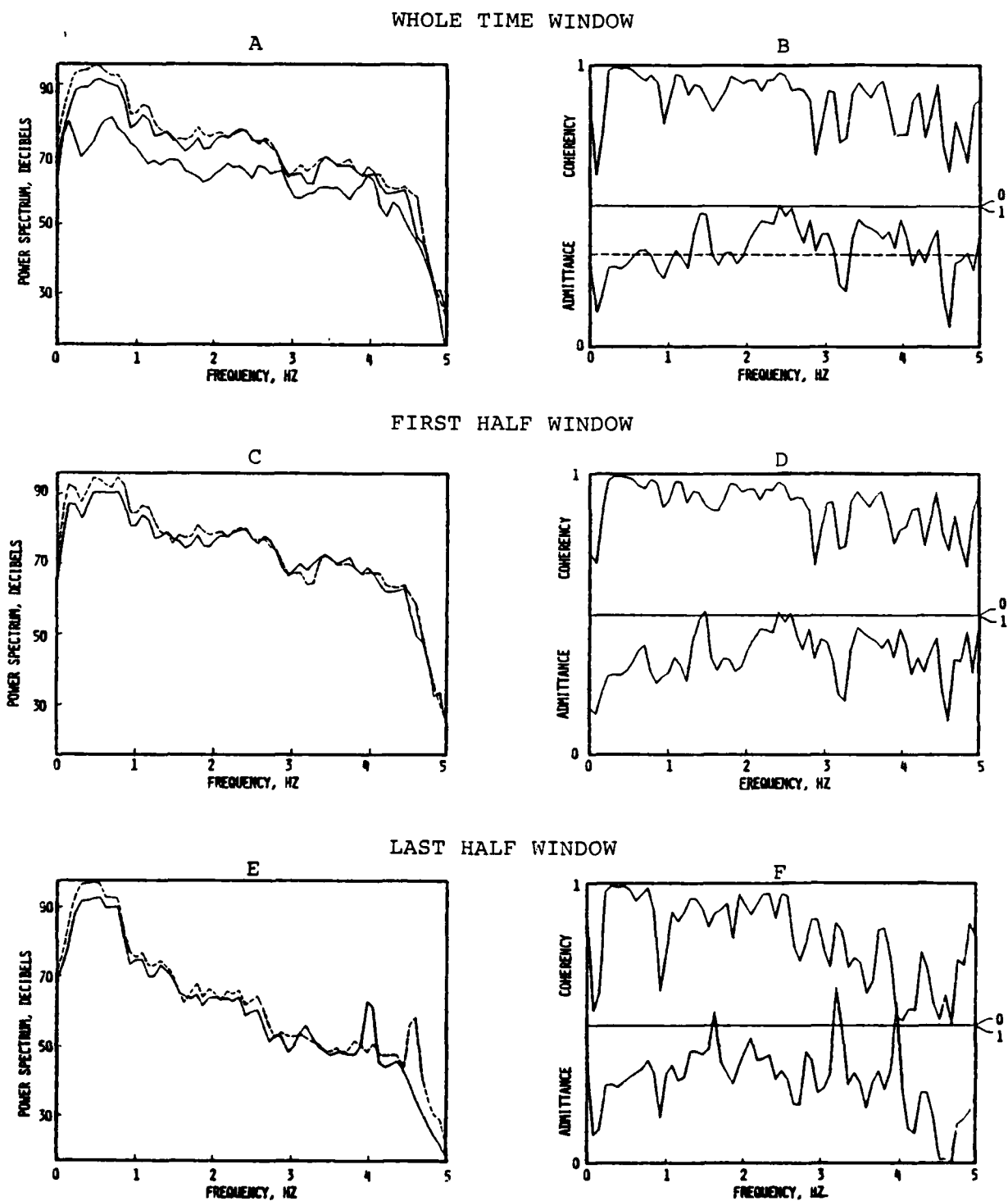


Figure 4.7. Transfer functions for three different time windows applied to the Landers recordings. The dashed line is for MIGHTY EPIC and the solid line for DIABLO HAWK. In A the lower solid line is the power spectrum of the error signal (see text).

Since the three transfer functions just discussed appear so similar in the frequency domain, it is not surprising that the impulse responses, obtained after Fourier transformation, also are quite similar. All three look very much like the impulse response previously described in the discussion (Section 4.2) of the Mina results. There is a large spike at zero time, a smaller negative dip at 0.1 to 0.2 seconds, and then a more oscillatory character prevails for the rest of the positive time values.

The three filters have been used to process the MIGHTY EPIC seismogram, yielding three "predicted" DIABLO HAWK seismograms and three "error" seismograms. The time domain results, qualitatively, appear much like the Mina result displayed in Figure 4.6. Closer inspection reveals that the filter $h_1(t)$ based upon the first half DIABLO HAWK seismogram, makes a slightly better prediction of the first half DIABLO HAWK seismogram than does either of the others. Likewise, the second half filter gives a slightly smaller error signal over the second half of the data. Much more noticeable is the inability of the second half filter to predict the high frequency ($f > 2$ Hz) part of the seismogram. This is a consequence of the imperfect calculation of the high frequency transfer function when just the second half of the data is analyzed. The visual impression that all three filter operators do an adequate job of making MIGHTY EPIC look like DIABLO HAWK, is confirmed by power spectrum analysis. The power spectrum of three error signals (each error signal is the observed DIABLO HAWK seismogram minus the filtered MIGHTY EPIC seismogram) was calculated. Figure 4.7A gives the result for the error signal resulting when the whole record impulse response is applied to MIGHTY EPIC. In general, the power spectrum of the error signal is 10 db less than the DIABLO HAWK power spectrum, confirming the time domain observation that the unpredicted signal amplitudes, using these operators, is about 30 percent of the DIABLO HAWK signal amplitude.

Although we have not displayed the power spectra of the other two error signals, they differ little from the bottom curve of Figure 4.7A. There is, however, a slightly poorer cancellation of high frequency energy by filter h_2 for the reasons noted previously, but the error signal spectrum for this case is only a few db above the other two.

4.3.2 Transfer Function with Five Different Frequency Resolutions

There was no particular reason for settling on a spectrum calculation with frequency resolution $\Delta f = 0.078$ Hz, which yields an impulse response, $h(t)$ of length $1/\Delta f = 12.8$ seconds. We have made further calculations, based on the entire 153.6 second seismograms recorded on the vertical component instruments, to explore the effect of operators longer and shorter than the 12.8 second length of 12.8 seconds work at turning the MIGHTY EPIC signal into the DIABLO HAWK signal. As the time duration of $h(t)$ increases, the error signal decreases, because allowing more free parameters always reduces the residual variance in a statistical calculation of this sort.

Operators as short as 1.7 seconds and as long as 25.7 seconds gave very similar results. Power spectra were calculated for each error signal, and were found to lie within a few db of the bottom power spectrum displayed in Figure 4.7A. Thus, we conclude that a filter only 1.7 seconds long (frequency resolution of 0.6 Hz) is nearly as effective at turning the MIGHTY EPIC signal into the DIABLO HAWK signal as is the 25.7 second operator with sixteen times the frequency resolution ($\Delta f = 0.04$ Hz).

It at first seems peculiar that a convolution operator as short as 1.7 seconds properly corrects MIGHTY EPIC signal energy with periods as great as 10 seconds. The reason the short operator is efficacious at long periods is that the

important characteristic of the transfer function governing operator length is not the absolute frequency, but the frequency interval over which the admittance changes appreciably. With reference to Figure 4.7B, it can be seen that smoothing the spectrum with a 0.6 Hz averaging distance still preserves much of the character of the admittance.

4.3.3 Transfer Function Between The Three Components of Motion

The MIGHTY EPIC seismograms recorded at Landers have been used to study the correlation between the three components of motion. We find that the coherency between the three pairs of seismograms (vertical-radial, vertical-transverse and transverse-radial) for no frequency band rises as high as the coherency previously obtained when comparing the signals on the same component, but for two different sources.

The dependence on frequency of the coherency between each pair of components and the corresponding admittance function is shown in Figure 4.8. The upper pane indicates that there is a modest, but not exceptionally large, correlation between the vertical and radial motion in a low frequency band around 0.25 Hz, and a mid-frequency band around 1.5 Hz, and for both bands the radial amplitude is about $3/4$ as large as the vertical amplitude. Panel B in this figure shows that the vertical motion is statistically independent of the transverse motion except in a frequency band around 3.5 Hz, over which zone the transverse motion is 1.25 times larger than the vertical motion. The transverse and radial components are almost uncorrelated, as is shown by the coherency function for this pair of components plotted in Panel C at the bottom of Figure 4.8.

Another way of comparing the three components of ground motion at Landers is to examine the power spectra of the seismograms. These are shown in Figure 4.9. There is a 30 db

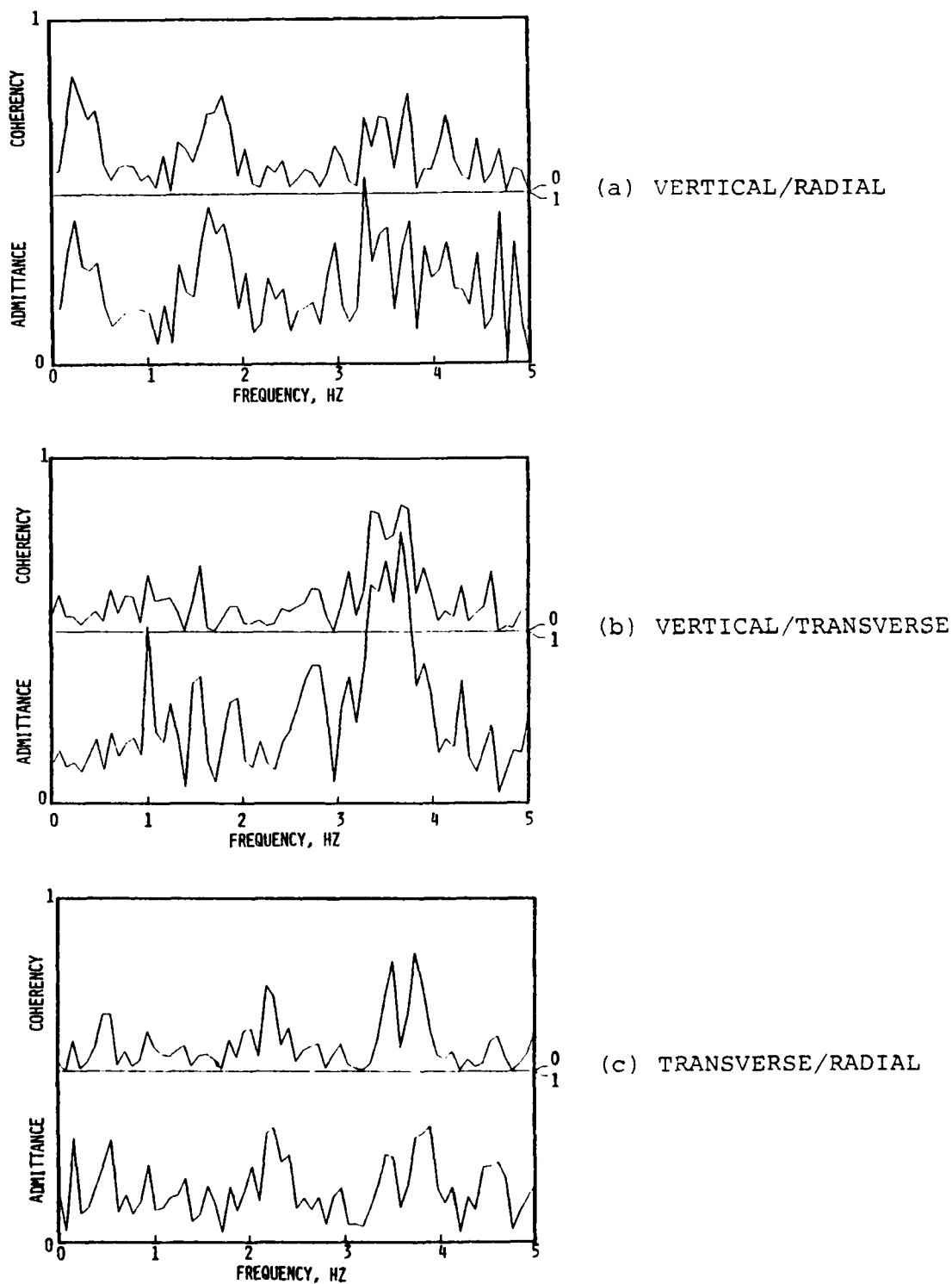


Figure 4.8. The coherency and admittance relating the three components of motion for MIGHTY EPIC recorded at Landers.

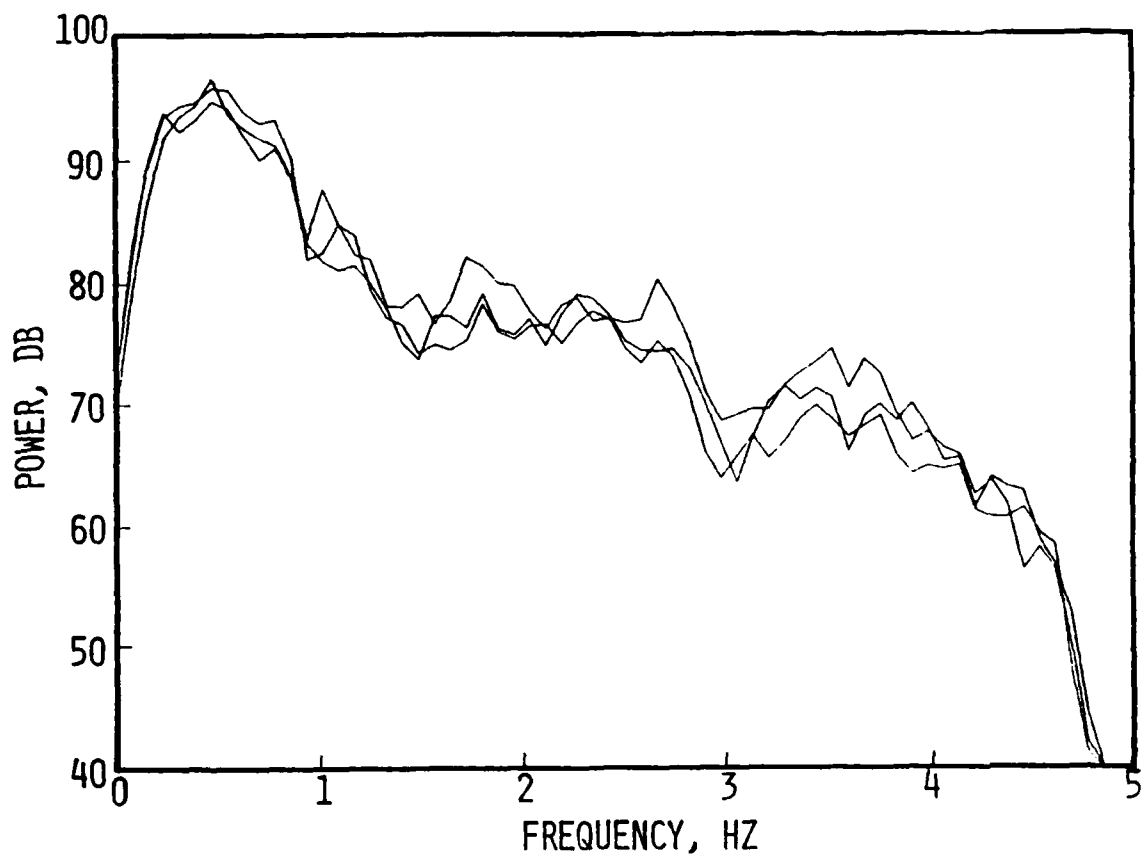


Figure 4.9. Power spectra for the three components of motion for MIGHTY EPIC recorded at Landers.

fall in the power spectral density from 0.5 Hz to 4 Hz, but the trend and even the details of the three power spectra are so similar that there is no obvious distinction between the three components of motion.

4.4 RESULTS FOR LEEDS

The recordings at Leeds of MIGHTY EPIC and DIABLO HAWK showed an admittance function similar to those already discussed (see Table 4.2). We have also studied the relationship between the three components of the MIGHTY EPIC seismogram, and obtained results analogous to the results obtained from analysis of the Landers data (Section 4.3.3). Figure 4.10, for example, shows coherencies and admittances between the three pairs of channels, and should be compared with Figure 4.8, the coherencies and admittances for the Landers recording of MIGHTY EPIC. As before, the coherencies are generally small. We find that the vertical and radial components are modestly coherent for frequencies around 0.25 Hz. There is a weak rise in the coherency near 1.5 Hz, but it is much less pronounced in the Leeds data than it was in the Landers. The vertical and transverse coherencies at Leeds do not exhibit the high values for a frequency of 3.5 Hz that appeared in the Landers analysis.

The power spectra of the three components of the Leeds MIGHTY EPIC seismogram in Figure 4.11 show the same droop towards high frequencies as the Landers seismograms. As with Landers, there is no feature in the power spectrum which, even ex post facto, would allow one to associated a particular power spectrum with one specific component of motion, although at Leeds the vertical component power spectrum is several db less than the other two near 1.5 Hz.

If we compare the power spectra for Leeds (Figure 4.11) to those from Landers (Figure 4.9) we see that the latter are

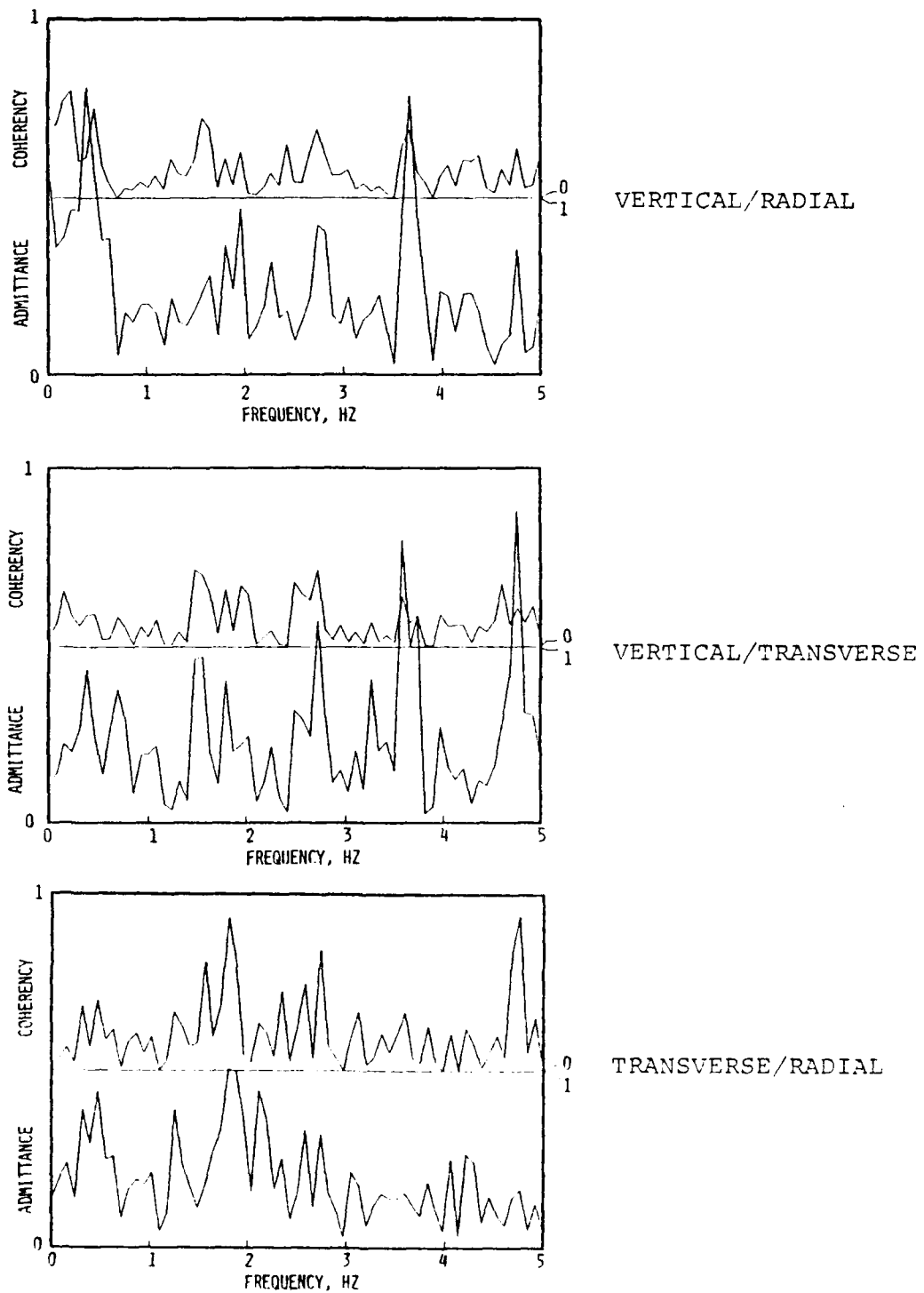


Figure 4.10. The coherence and admittance relating the three components of motion for MIGHTY EPIC recorded at Leeds.

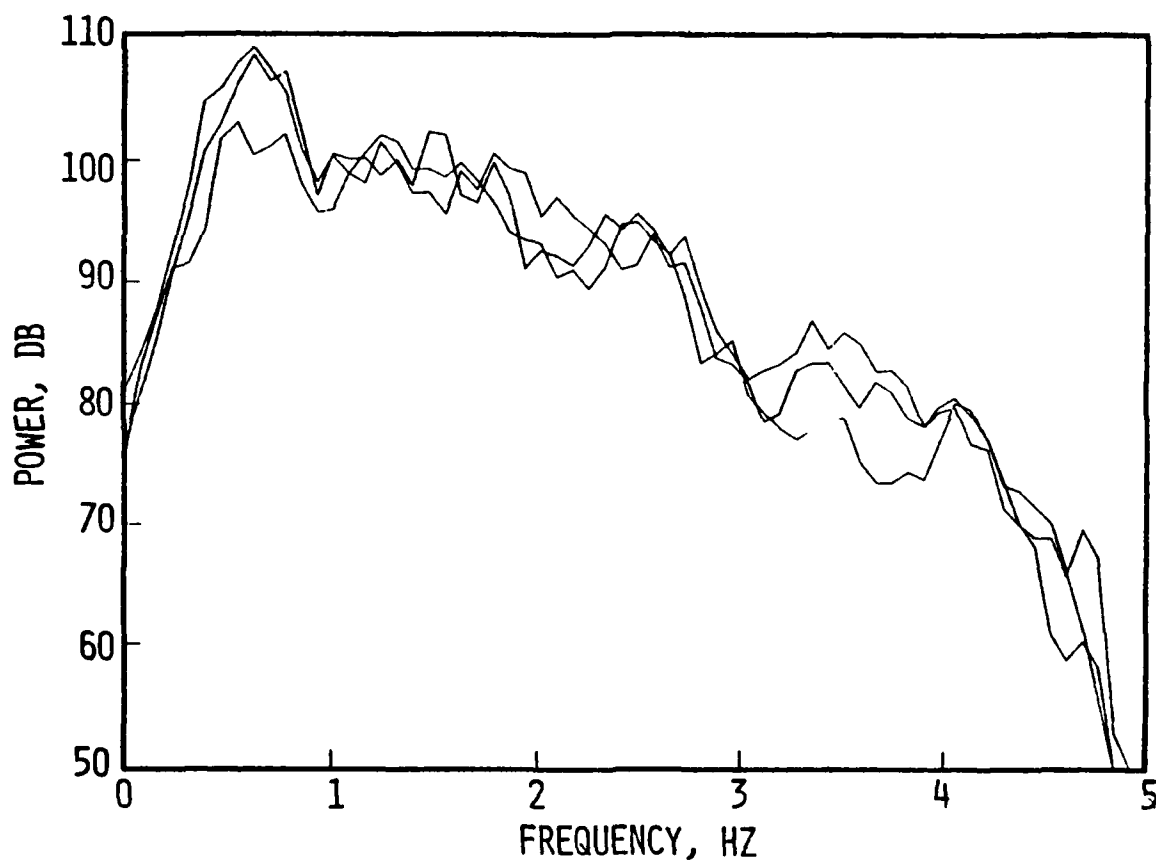


Figure 4.11. Power spectra for the three components of motion for MIGHTY EPIC recorded at Leeds.

smaller by a factor of 3 to 10. The two stations are at about the same distance from the source. It might be thought that this effect is due to the propagation characteristics of the Mojave Desert. However, the character of the Leeds power spectrum is very similar to the character of the Landers power spectrum. Comparing Figures 4.9 and 4.11, it is seen that for all three components, both sets of spectra show the following features:

- A hump between 0 and 1 Hz.
- A plateau between 1 and 2.5 Hz.
- A cliff at 2.8 Hz down to a second level plateau extending from 3 Hz to 4.5 Hz.

If one supposes that scattering or anelastic absorption of seismic energy is the cause of the low amplitude Landers signals, the effect ought to be more pronounced at high frequencies than at low. If anything, we find that Landers has lost more midband energy ($1.5 \leq f \leq 2.5$ Hz) than either high frequency or low frequency energy. Thus source radiation pattern effects may be responsible for most of the amplitude differences.

4.5 CONCLUDING REMARKS

In this section we have analyzed the seismogram recordings of the two events with no preconceptions about the nature of the source. Our most important conclusions may be listed as follows:

- At high frequencies ($f > 1.5$ Hz) the amplitude of the seismic waves from DIABLO HAWK and MIGHTY EPIC are nearly the same.
- The low frequencies ($f < 0.3$ Hz) waves from MIGHTY EPIC are substantially larger than those from DIABLO HAWK on almost every common recording.

- The common recordings of the two events show high coherency at most frequencies. Thus, the two events produce very similar, though not identical, seismograms.
- The coherency between the three seismogram pairs (vertical-radial, vertical-transverse, radial-transverse) at a given station is nowhere as high as the coherency between the same components for the two events. Over most of the frequency band the three components appear to be independent, though there are small regions where the coherency reaches 0.75 or so.

In the next section we will look at the data in an entirely different way in an attempt to deduce the nature of the source.

V. DOUBLE-COUPLE AMPLITUDES

5.1 INTRODUCTION

Our ultimate objective in this project has been to estimate the block motion associated with the MIGHTY EPIC and DIABLO HAWK events. We proposed to infer this from measurements of the seismic radiation from these events. This, of course, implies that we have some model for the process by which the seismic radiation is generated and that we interpret the observations within the context of this model.

Stated in simple terms, the model we use to interpret the observations is that the seismic source is composed of two parts, a center of dilatation to represent the explosion and a double-couple to represent the earthquake-like component. From the latter the extent of block motion can be estimated. In Section 5.2 we briefly outline the theoretical formulation used to analyze the data.

The most important result of the spectral analysis presented in Section IV is that the long period radiation from MIGHTY EPIC is larger than that from DIABLO HAWK on nearly all common recordings. Of the sixteen common recordings the only exception is the tangential motion at LEEDS (see Table 4.2). This is an unexpected result which is difficult to interpret in terms of our model. Still, it is based on spectral analysis of the entire seismogram.

For interpreting the data in terms of our model we need accurate estimates of the spectral amplitude of the fundamental mode Love and Rayleigh waves. This is a spectral amplitude from a particular portion of the wavetrain and could be quite different from the whole wavetrain amplitude discussed in Section IV. We estimate the Love and Rayleigh amplitudes by processing the data with the MARS narrow-band filter program described in Section 3.3. This processing also gives

an estimate of the group velocity dispersion of the Love and Rayleigh wave modes. This dispersion varies from station to station and indicates that the path amplification also varies. In Section 5.3 we classify the stations according to the similarity of the observed dispersion to that from two theoretical models for this tectonic province. The amplification factors computed for these models then can be used to correct the observed data for known path differences.

In Section 5.4 we summarize the observed Love and Rayleigh wave spectral amplitudes. These data are then used with the theory of Section 5.2 to estimate the size of the explosion and double-couple components of the source. Finally, in Section 5.6 we summarize our conclusions about the composite source for MIGHTY EPIC and DIABLO HAWK.

5.2 THEORETICAL MODEL

For inferring the double-couple we use the technique used by Toksöz and Kehler (1972) to determine the double-couple for a number of large Yucca Flat and Pahute Mesa explosions. In this section we will summarize this technique.

The analytical expressions for the Rayleigh and Love waves due to an explosion and a double-couple are given by Toksöz, et al. (1965, 1971). For a horizontal double-couple (vertical strike-slip faulting) the approximate expressions for the vertical Rayleigh wave displacement are

$$W_e(\omega) = - \frac{B_e K_0 A_R}{\sqrt{2\pi r \omega c_R}} e^{-\gamma_R r} e^{-i\omega r/c_R} D_e(\omega) \quad (5.1)$$

for the explosion and

$$W_{dc}(\omega) = - \frac{B_{dc} K_0 A_R}{\sqrt{2\pi r \omega c_R}} \sin 2\theta e^{-\gamma_R r} e^{-i\omega r/c_R} D_{dc}(\omega) \quad (5.2)$$

for the double-couple. Here ω is frequency, r is range, c_R is Rayleigh phase velocity, A_R is an amplification factor, K_0 is the depth-dependent excitation for a source near the surface (equal to the ellipticity), γ_R represents the attenuation and θ is the azimuth measured clockwise from θ_s , the strike of the fault plane. The $B_e D_e(\omega)$ and $B_{dc} D_{dc}(\omega)$ represent the source time functions for the two components of the source. For periods that are long compared to the source duration, $D_e(\omega) \approx D_{dc}(\omega) \approx 1$. In our analysis of the data we are concerned with periods of about 6 seconds. We assume the source duration is much less and ignore the difference in the time functions. The total Rayleigh wave is then

$$U_R = W_e (1 + F \sin 2\theta), \quad (5.3)$$

where

$$F = \frac{B_{dc}}{B_e}.$$

For Love waves the horizontal component of motion is

$$U_L(\omega) = \frac{B_{dc} A_L}{\sqrt{2\pi r \omega c_L}} \cos 2\theta e^{-\gamma_L r} e^{-i\omega r/c_L} D_{dc}(\omega) \quad (5.4)$$

Therefore, the ratio of the two is

$$\frac{|U_L|}{|U_R|} = \frac{\Gamma(\omega) F \cos 2\theta}{1 + F \sin 2\theta} \quad (5.5)$$

where

$$\Gamma(\omega) = \sqrt{\frac{c_R}{c_L}} \frac{A_L}{A_R K_0} e^{-r\gamma_L} e^{r\gamma_R}. \quad (5.6)$$

If the double-couple is due to a fault at an orientation other than vertical strike-slip, (5.5) becomes

$$\frac{|U_L|}{|U_R|} = \frac{\Gamma(\omega) F (\sin\lambda \sin 2\delta \sin 2\theta + \cos\lambda \sin\delta \cos 2\theta)}{\left[1 + F \left(\frac{1}{2} \sin\lambda \sin 2\delta \left(\frac{1+\nu}{1-\nu} - \cos 2\theta \right) + \cos\lambda \sin\delta \sin 2\theta \right) \right]} \quad (5.7)$$

where δ and λ are the dip and slip of the fault plane and ν is Poisson's ratio. There is very nearly a direct trade-off between F and δ and λ . For a vertical strike-slip fault $\delta = 90$, $\lambda = 0$ and F takes its minimum value. There are other δ , λ pairs giving the same values of the ratio for larger F .

Our objective is to infer the characteristics of the source of the double-couple. From these seismic data the most we can deduce is the orientation (θ_s , δ , λ) and strength (F) of the double-couple. The use of these quantities to bound the block motions is discussed in Section VI.

If we are to infer the F and fault orientation parameters, we must assume values for various path parameters in the expressions (5.1)-(5.6). Let us look more closely at these quantities.

Bache, Rodi and Harkrider (1978) write the expression for computing the Rayleigh waves from explosions. In the present notation, this is

$$W_e(\omega) = -4\pi\mu_s \Psi_\infty \frac{K_0 A_{R1}}{c_{R1}} \sqrt{\frac{2c_{R2}}{\pi\omega r}} T_R(\omega) e^{-\gamma_R r} e^{-i\omega r/c_{R2}} \quad (5.8)$$

where Ψ_∞ is the late time value of the reduced displacement potential and μ_s is the shear modulus at the source.

The subscripts 1 and 2 refer to crustal models for the local source region and for the remainder of the travel path. It is necessary to distinguish between the two because

the average path properties in the top few kilometers of the crust are not necessarily the same as in the local source region. Comparing (5.8) with (5.1), we see that these two equations are the same if

$$B_e = 8\pi\mu_s \Psi_\infty \quad (5.9)$$

and we make the substitution

$$\frac{c_{R2}}{c_{R1}} \frac{A_{R1}}{c_{R2}} T_R \rightarrow \frac{A_R}{\sqrt{c_R}}.$$

Now, it can easily be shown that

$$F = \frac{M_0}{8\pi\mu_s \Psi_\infty}. \quad (5.10)$$

Then $B_{dc} = M_0$, where M_0 is the double-couple moment.

Similar equations can be written for the Love wave giving

$$U_L = \frac{c_{L2}}{c_{L1}} \frac{M_0 A_{L1}}{\sqrt{2\pi r \omega c_{L2}}} T_L(\omega) \cos 2\theta e^{-\gamma_L r} e^{-i\omega r/c_{L2}} \quad (5.11)$$

to replace (5.4). The equation for the $|U_L|/|U_R|$ ratio is (5.5) or (5.7) with

$$\Gamma(\omega) = \frac{c_{R1}}{c_{L1}} \sqrt{\frac{c_{L2}}{c_{R2}}} \frac{A_{L1} T_L}{A_{R1} T_R K_0} e^{-\gamma_L r} e^{\gamma_R r}. \quad (5.12)$$

What are appropriate values for the path parameters? We will address this question in the next section where we discuss models for the travel path.

The Toksöz and Kehler (1972) method for finding the orientation and strength of the double-couple is to first process the observed seismograms to find the spectral Rayleigh and Love wave amplitudes $|U_L|$ and $|U_R|$. Using estimates for the path parameters, F , θ_s , δ , λ are then adjusted in Eq. (5.7) to find the best fit to the data. This is done by varying these quantities and plotting the "error" contours where the error, E , is defined by

$$E^2 = \frac{\frac{1}{N^2} \sum_{i=1}^N (A_{0i} - A_{Ti})^2}{\frac{1}{N^2} \sum_{i=1}^N A_{0i}^2} \quad (5.13)$$

where A_0 and A_T are the observed and theoretical values of $|U_L|/|U_R|$. The minimum error solutions are then selected from the contour plots.

We will mainly focus on the best fitting solution for the Love/Rayleigh ratios. However, the same approach will work for the individual components with theoretical values of $|U_L|$ and $|U_R|$ being computed with (5.3), (5.8) and (5.11).

5.3 TRAVEL PATH MODELS AND STATION CLASSIFICATION

We will discuss two crustal models for the travel paths of interest. One is TUC (Bache, Rodi and Harkrider, 1978) which was inferred from observations of NTS explosions at Tucson, Arizona. The other is PBGB (Priestly and Brune, 1978) which was deduced from observations of surface waves traveling across the Great Basin tectonic province. Their data included NTS explosions recorded at TNP, MNV and KNB.

The shear velocity-depth profile for the two models is plotted in Figure 5.1. We see that the two are not very

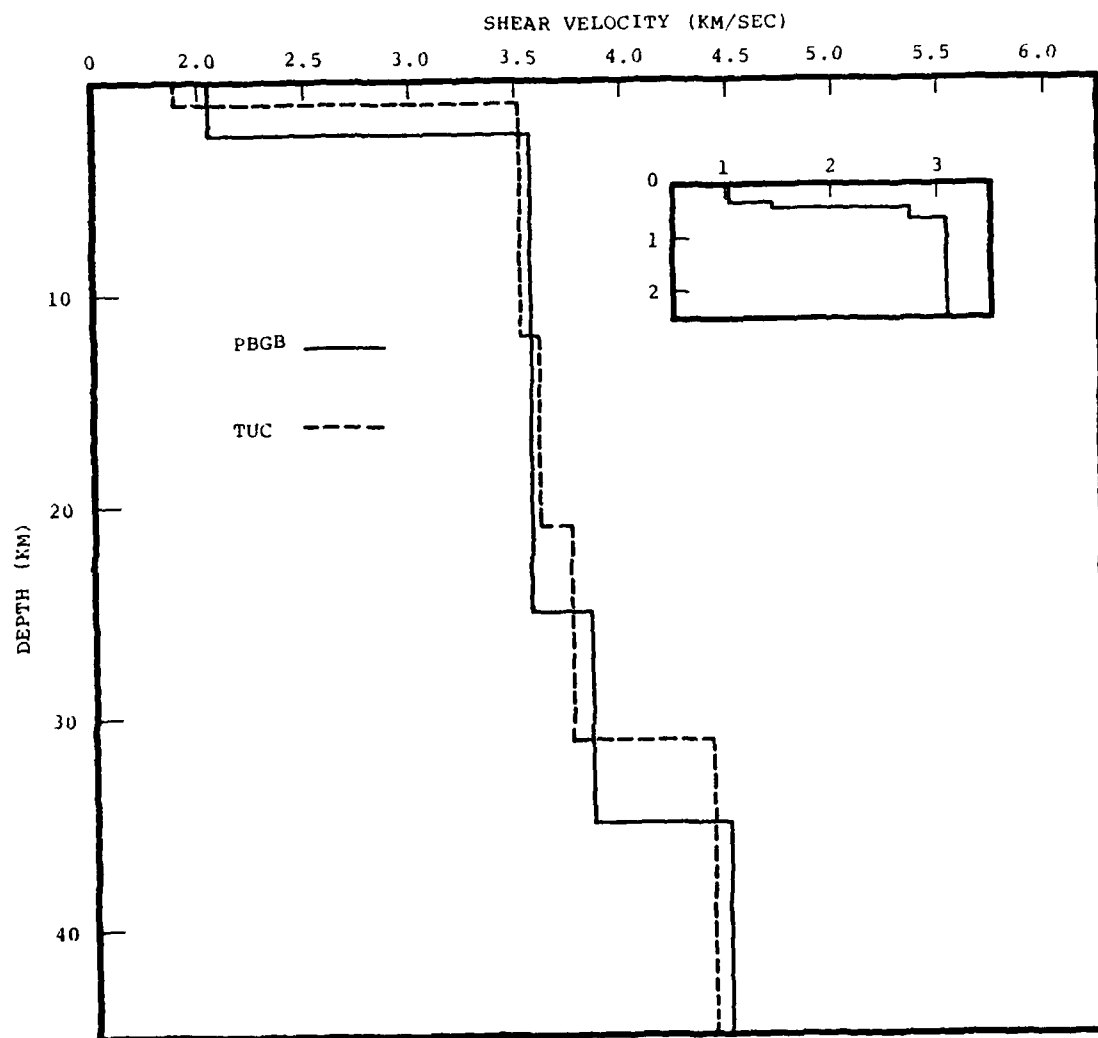


Figure 5.1. Shear velocity is plotted versus depth for two crustal models. The Rainier Mesa source region model is shown in the inset.

different in the middle crust. However, the crustal thicknesses are 31 km for TUC and 35 km for PBGB. One of the most important features of these models for our study is the thickness of the low velocity sedimentary layer which is 1.0 km for TUC and 2.5 km for PBGB. Unfortunately, this thickness is not very well constrained for either model.

Also plotted in Figure 5.1 is the shear velocity for the Rainier Mesa region. This model is substituted for the top 2.5 km of the two path models to compute the source excitation. The parameters of the models are listed in Table 5.1.

The group velocity dispersion for the two models is plotted in Figure 5.2 for the period range to be studied. In this range the two are quite different. The Love wave is sensitive to shallower structure at a given period than the Rayleigh wave. Thus, for PBGB the Love wave senses the thick sedimentary layer at fairly long periods and the group velocity decreases sharply. There is a period range where the Love wave actually arrives after the Rayleigh wave. The same thing happens with the thin sediment TUC model, but at much shorter periods.

Using the algorithm of Harkrider (1964) we compute the path parameters for the formulae of Section 5.2. The important combinations are:

$$G_R(\omega) = K_0 \frac{A_{R1}}{c_{R1}} \sqrt{c_{R2}} T_R,$$

$$G_L(\omega) = \frac{A_{L1}}{c_{L1}} \sqrt{c_{L2}} T_L,$$

$$J_R(\omega) = G_R e^{-\gamma_R r},$$

TABLE 5.1

CRUSTAL MODELS

<u>Depth</u>	<u>Thickness</u>	<u>α (km/sec)</u>	<u>β (km/sec)</u>	<u>ρ (gm/cm³)</u>	<u>Q</u>
Source Region					
0.35	0.35	2.03	1.03	1.70	
0.46	0.11	2.40	1.45	1.90	
0.69	0.23	4.4	2.75	2.20	
2.0 (TUC)	1.31 (TUC)	5.0	3.1	2.40	
2.5 (PBGB)	1.81 (PBGB)	5.0	3.1	2.40	
TUC					
1.0	1.0	3.21	1.89	2.33	75
12.0	11.0	5.96	3.52	2.78	350
21.0	9.0	6.11	3.61	2.80	375
31.0	10.0	6.37	3.76	2.84	400
Mantle		7.90	4.42	3.20	650
PBGB					
2.5	2.5	3.55	2.05	2.20	100
25.0	22.5	6.10	3.57	2.80	350
35.0	10.0	6.60	3.85	2.84	450
Mantle		7.80	4.50	3.30	700

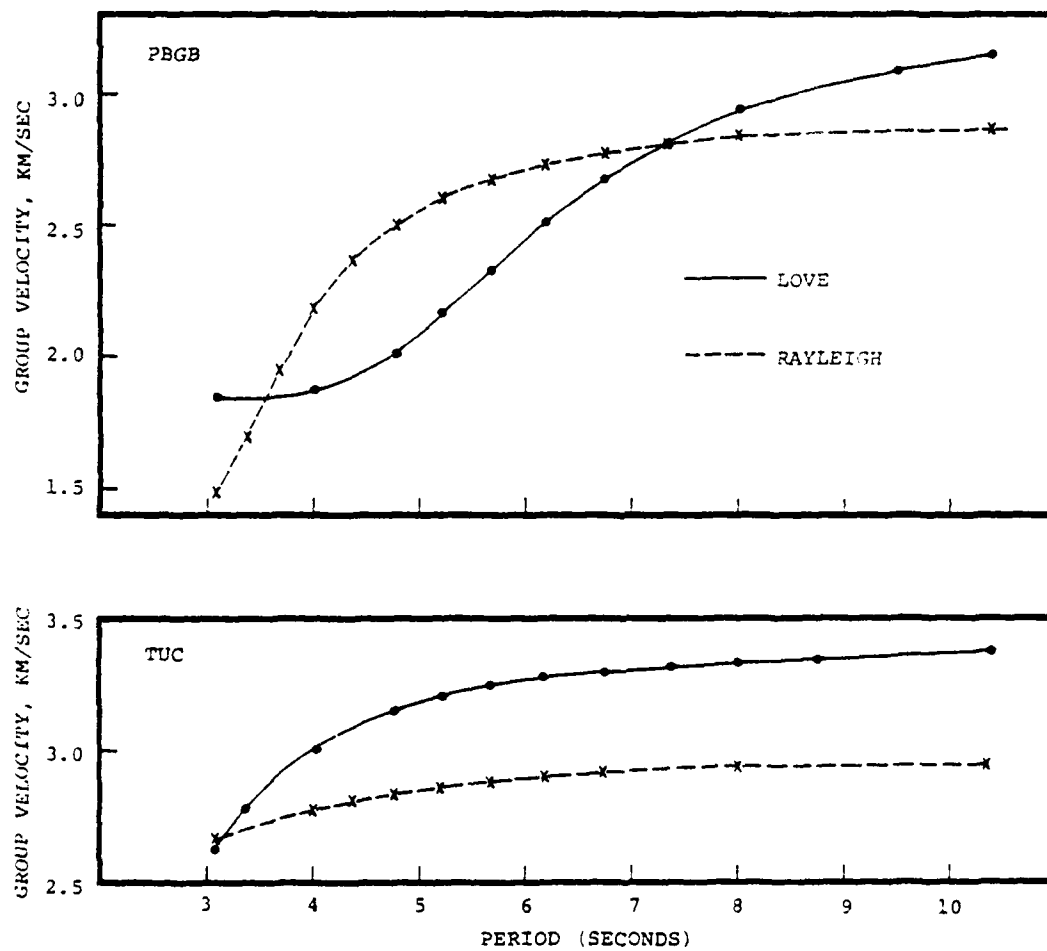


Figure 5.2. Group velocity dispersion for the theoretical models of Figure 5.1.

$$J_L(\omega) = G_L e^{-\gamma_L r},$$

$$\Gamma(\omega) = \frac{J_L(\omega)}{J_R(\omega)}, \quad (5.14)$$

The units of the G and J are 10^{-18} cm-sec^{1/2}/dyne-km^{1/2}. With this notation, the theoretical amplitudes for a vertical strike-slip double-couple are:

$$|U_R| = 4 \left(\frac{2\pi}{\omega r} \right)^{1/2} \mu_s \psi_\infty J_R(\omega) (1 + F \sin 2\theta),$$

$$|U_L| = \left(\frac{1}{2\pi\omega r} \right)^{1/2} M_0 J_L(\omega) \cos 2\theta \quad (5.15)$$

$$\frac{|U_L|}{|U_R|} = \Gamma(\omega) \frac{F \cos 2\theta}{1 + F \sin 2\theta}.$$

In Table 5.2 we give the values of the quantities defined in (5.14) for the PBGB and TUC structures. For computing the J and Γ in the table, we take $r = 250$ km. We see that there are rather large differences in the excitation of Rayleigh and Love waves in the two structures and that the largest difference is for the Love wave.

In Figures 5.3 and 5.4 we show most of the recorded vertical and transverse velocities for the two events displayed in a record section. The Rayleigh and Love waves are expected to arrive with group velocities from 2.0-3.5 km/sec and lines indicating arrivals in this time window are drawn on the figures. All the data are plotted in Appendix A.

The data were filtered by the 4-8 second bandpass filter described in Section 3.2. Record sections of the filtered data are shown in Figures 5.5 and 5.6. In these plots

AD-A084 660

SYSTEMS SCIENCE AND SOFTWARE LA JOLLA CA

F/G B/11

BLOCK MOTION ESTIMATES FROM SEISMOLOGICAL OBSERVATIONS OF NIGHT--ETC(U)

JUL 79 T C BACHE, W E FARRELL, D G LAMBERT

DNA001-77-C-0260

UNCLASSIFIED

SSS-R-79-4080

DNA-5007F

NL

2 OF 2

AD-A

35-5010



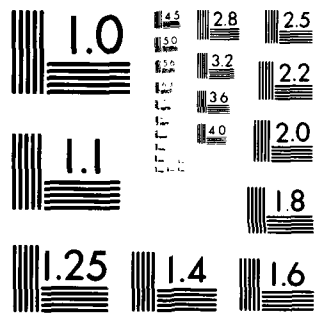
END

DATE

FILED

6-80

DTIC



MICROCOPY RESOLUTION TEST CHART

TABLE 5.2
PATH PARAMETERS

<u>Period</u> <u>(sec)</u>	<u>G</u> <u>R</u>	<u>G</u> <u>L</u>	<u>J</u> <u>R</u>	<u>J</u> <u>L</u>	<u>Γ</u>
PBGB					
8.00	0.89	1.20	0.81	1.05	1.30
7.34	1.02	1.45	0.91	1.23	1.35
6.33	1.17	1.77	1.04	1.44	1.39
6.17	1.37	2.10	1.19	1.67	1.41
5.66	1.62	2.71	1.38	1.91	1.38
5.19	1.96	3.36	1.64	2.14	1.30
4.76	2.42	4.12	1.96	2.30	1.17
4.36	3.06	4.99	2.38	2.43	1.02
4.00	4.02	5.98	2.91	2.52	0.89
3.67	5.43	7.13	3.48	2.62	0.75
3.36	6.14	8.50	3.16	2.73	0.86
TUC					
8.00	0.91	0.86	0.83	0.78	0.95
7.34	1.02	0.97	0.92	0.87	0.95
6.33	1.16	1.10	1.03	0.99	0.95
6.17	1.32	1.27	1.17	1.12	0.96
5.66	1.51	1.50	1.31	1.30	0.99
5.19	1.73	1.79	1.49	1.52	1.02
4.76	2.01	2.17	1.69	1.80	1.07
4.36	2.34	2.70	1.94	2.17	1.12
4.00	2.76	3.44	2.23	2.65	1.19
3.67	3.28	4.49	2.59	3.27	1.26
3.36	3.97	6.01	3.04	4.03	1.33

MIGHTY EPIC, V

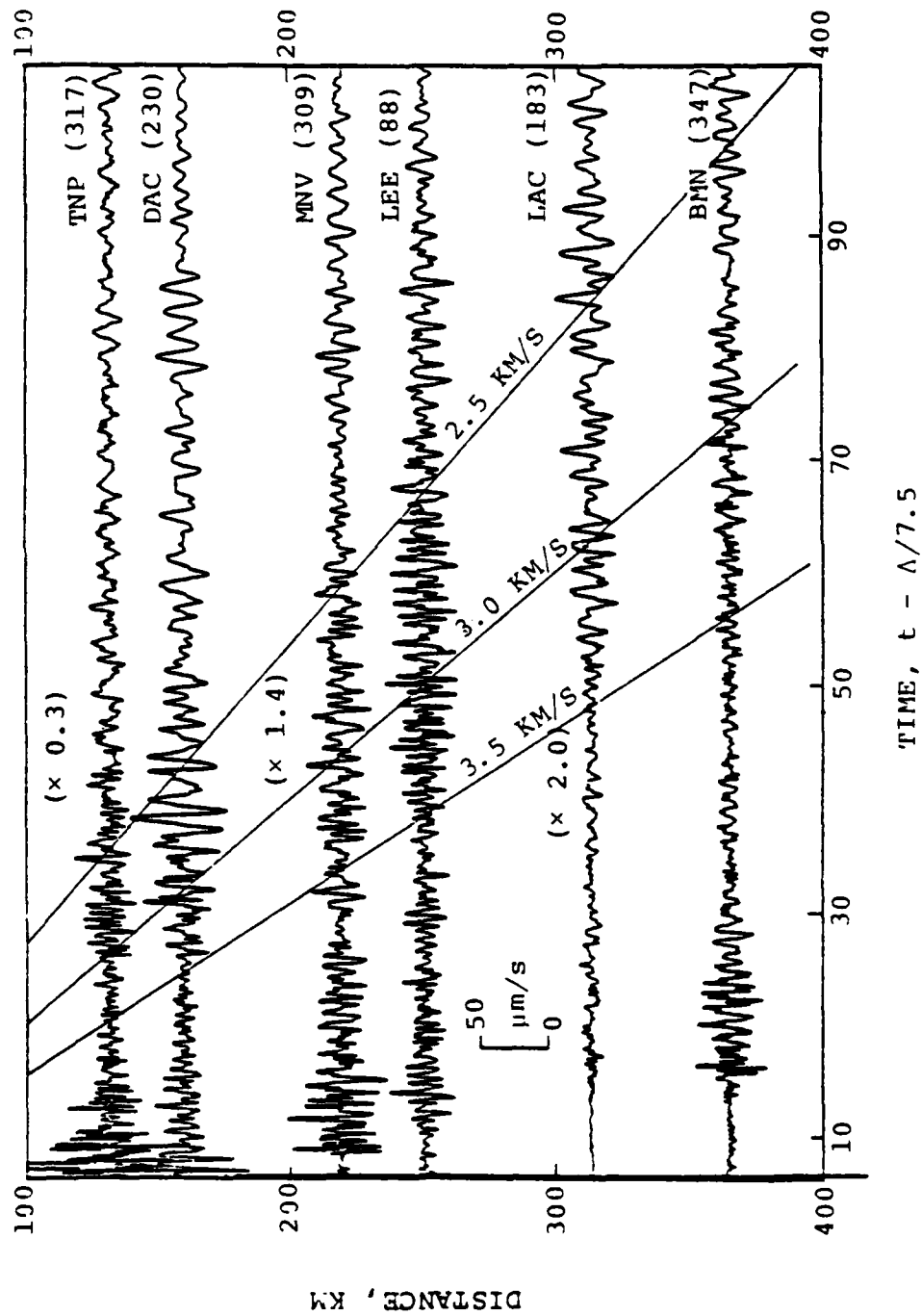


Figure 5.3a. Vertical velocities for MIGHTY EPIC.

DIABLO HAWK, V

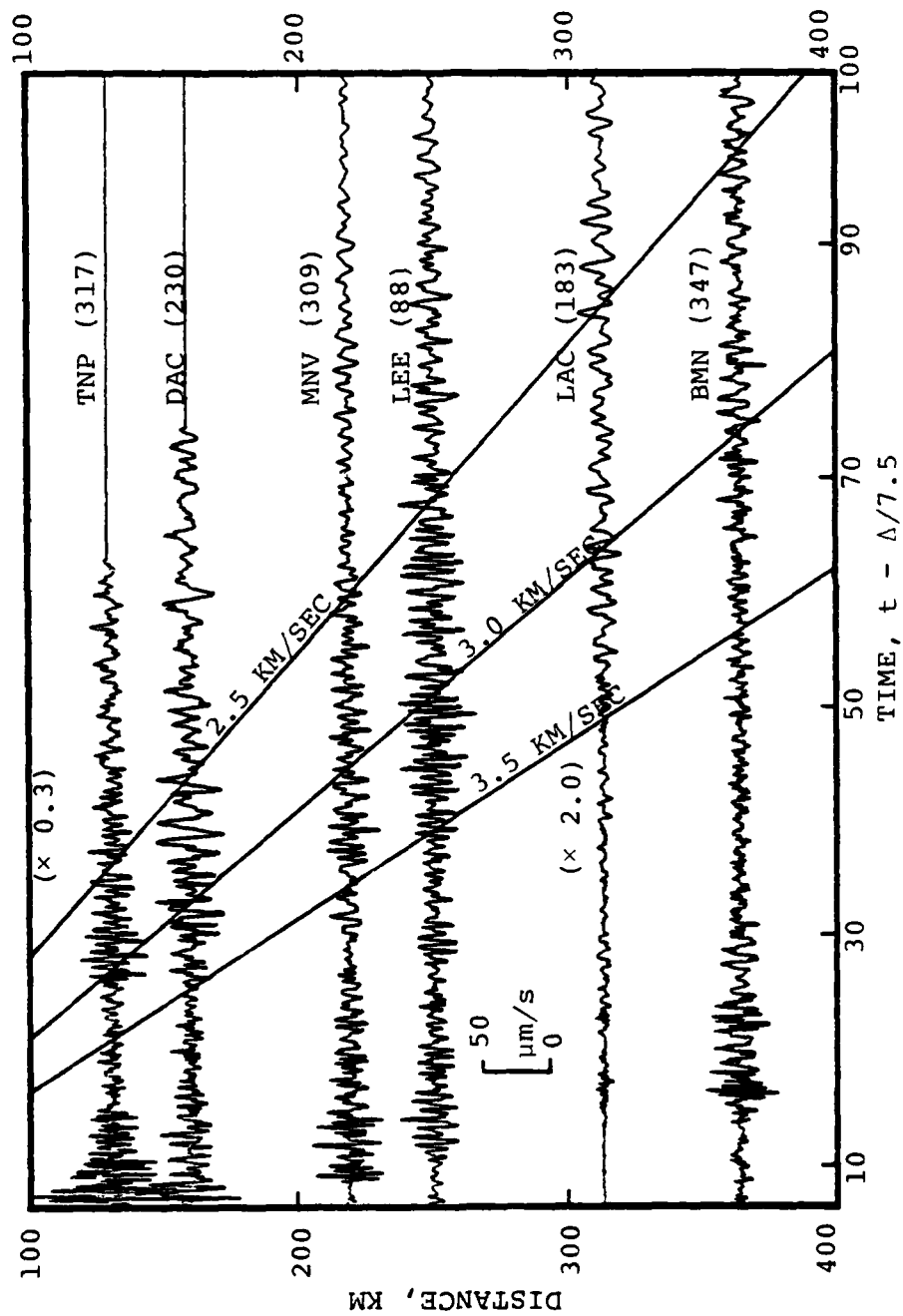


Figure 5.3b. Vertical velocities for DIABLO HAWK.

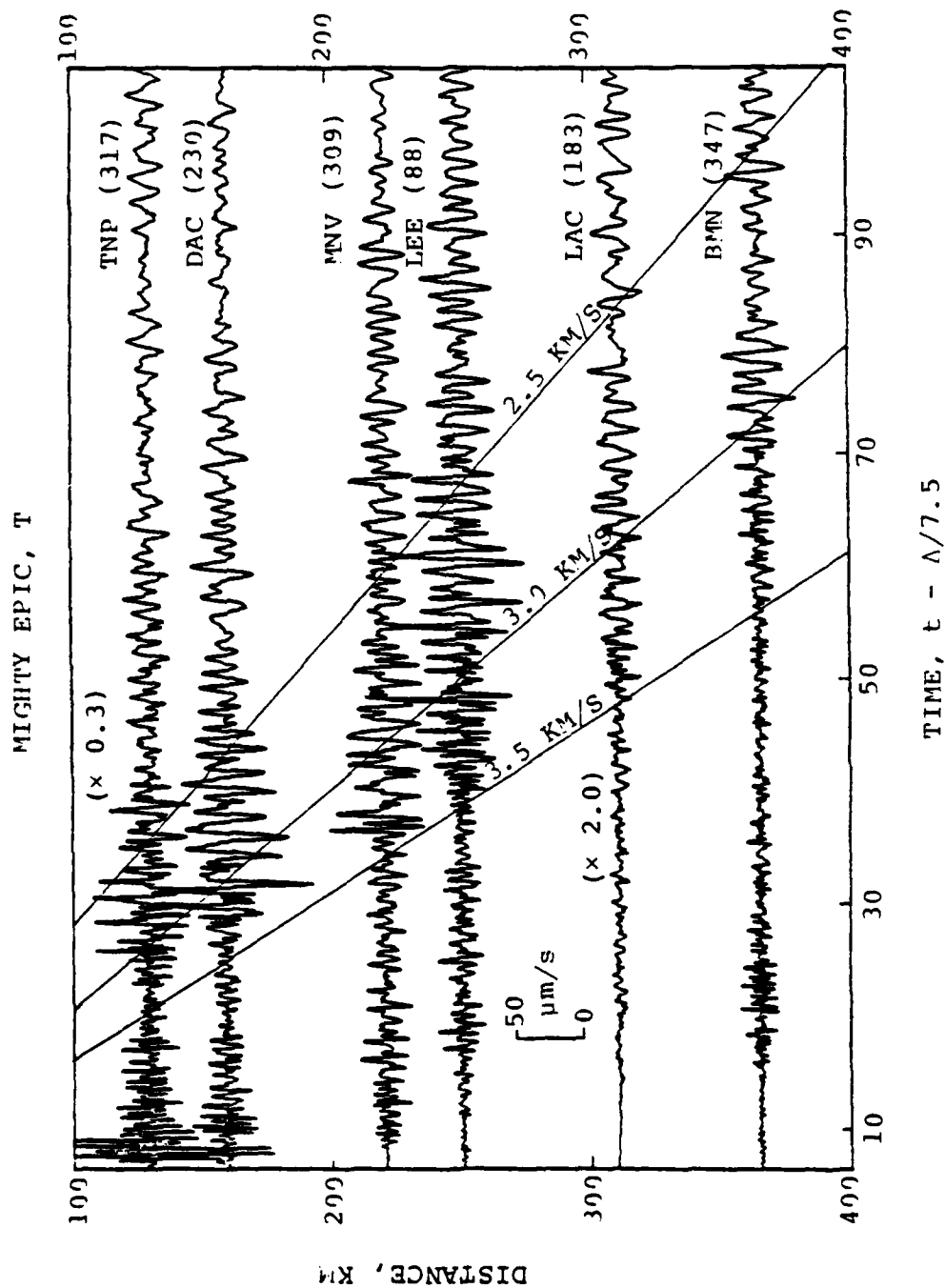


Figure 5.4a. Tangential velocities for MIGHTY EPIC.

DIABLO HAWK, T

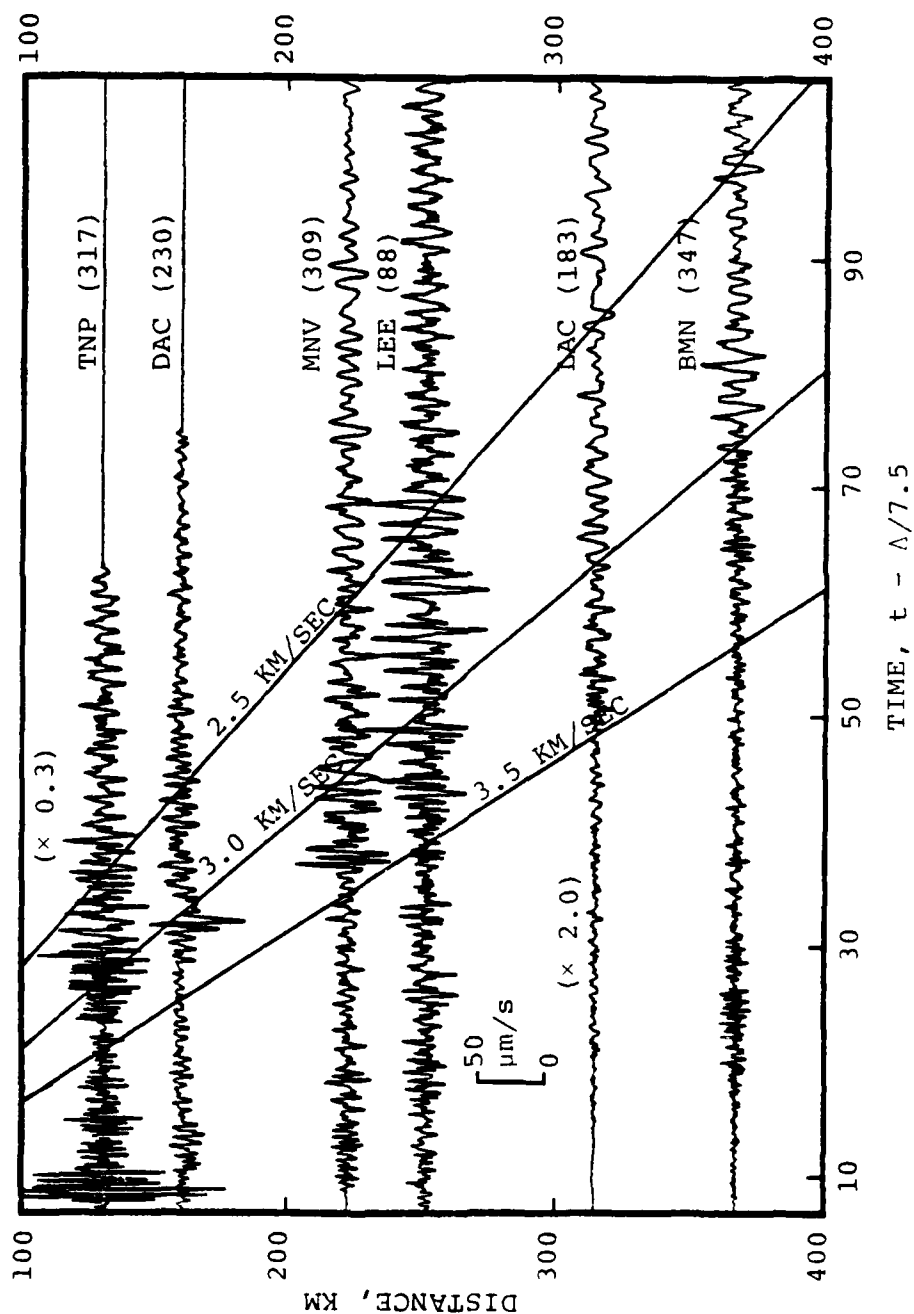


Figure 5.4b. Tangential velocities for DIABLO HAWK.

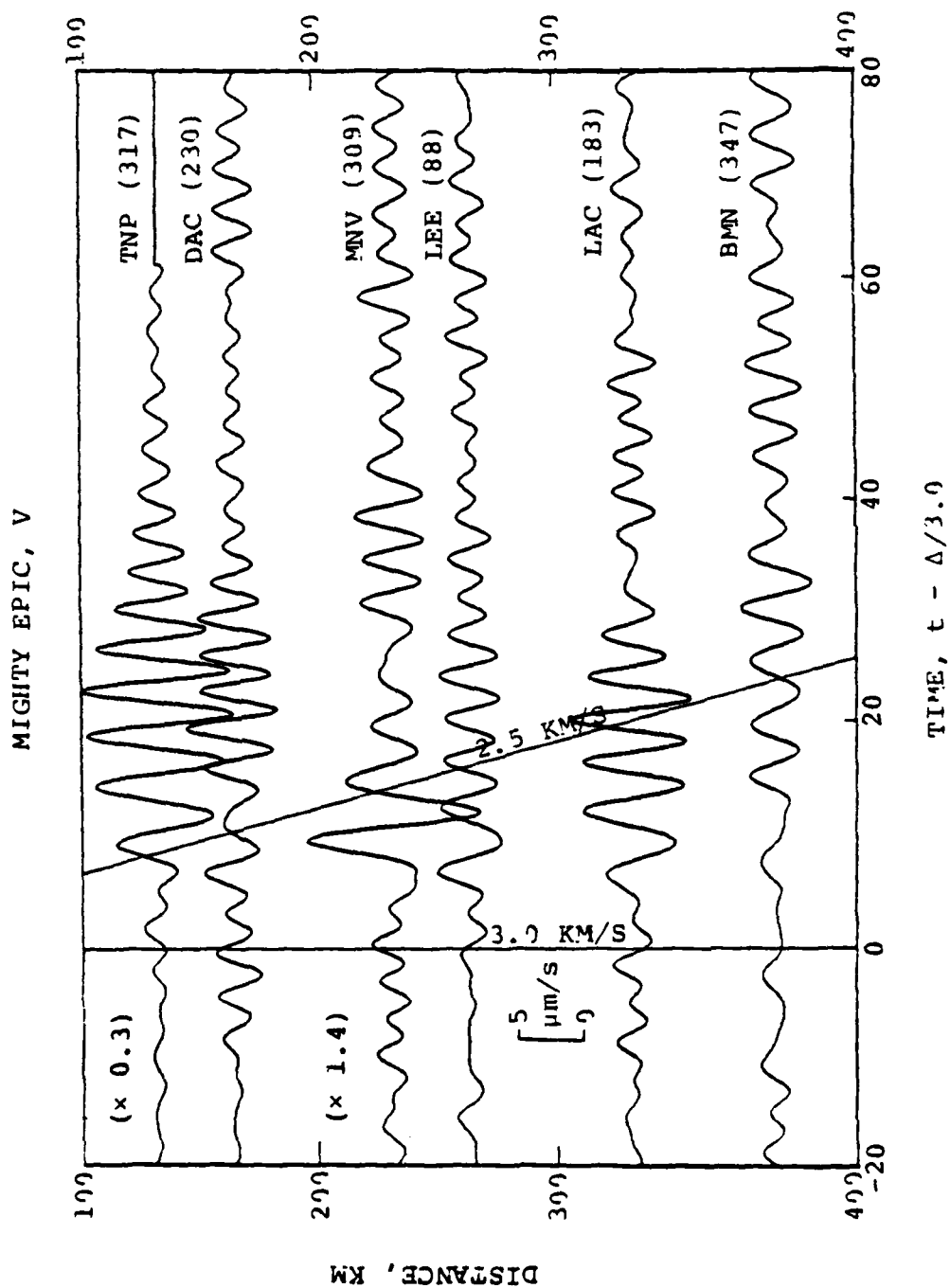


Figure 5.5a. Vertical velocities for MIGHTY EPIC after filtering with a 4-8 second bandpass filter.

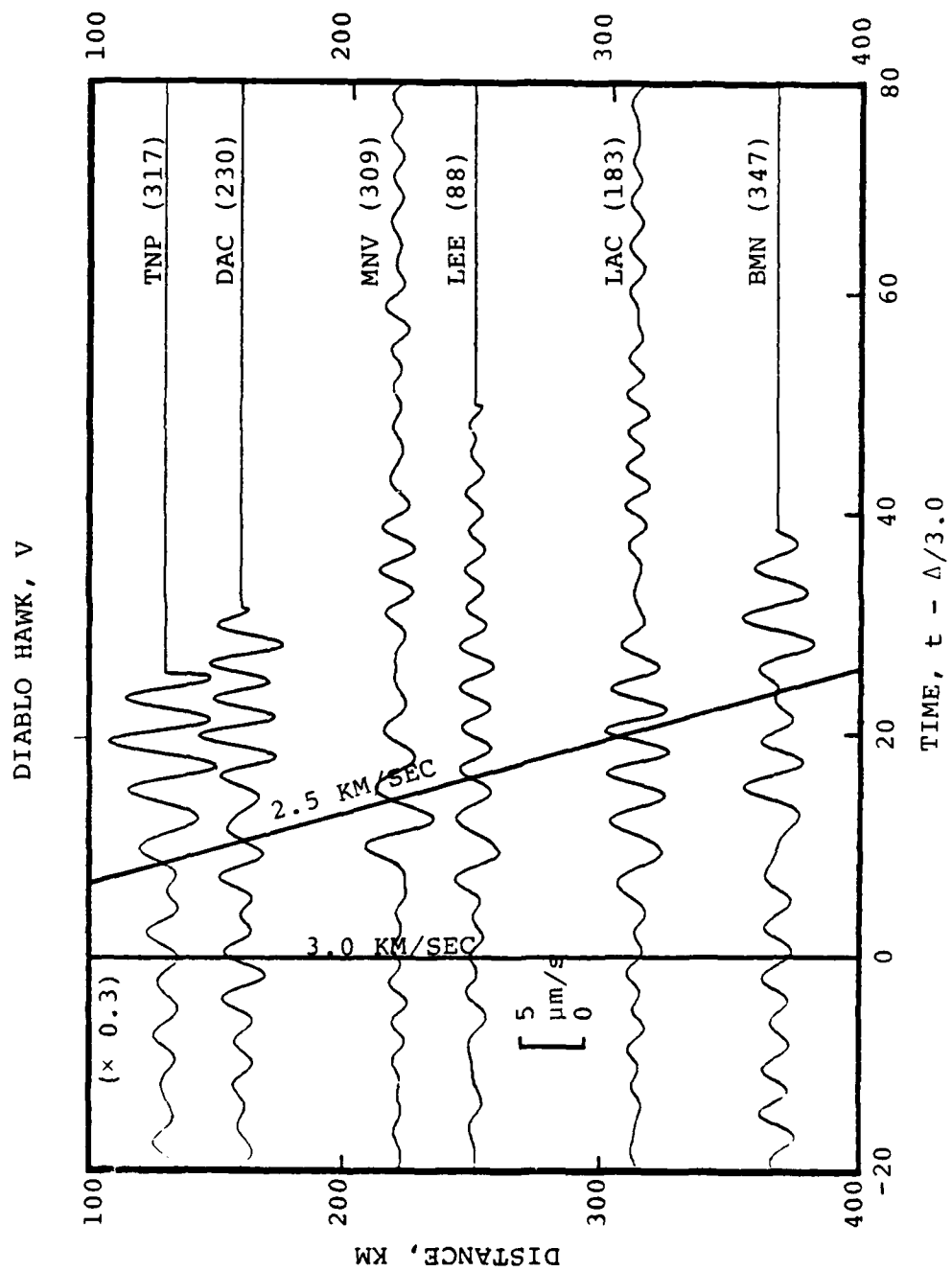


Figure 5.5b. Vertical velocities for DIABLO HAWK after filtering with a 4-8 second bandpass filter.

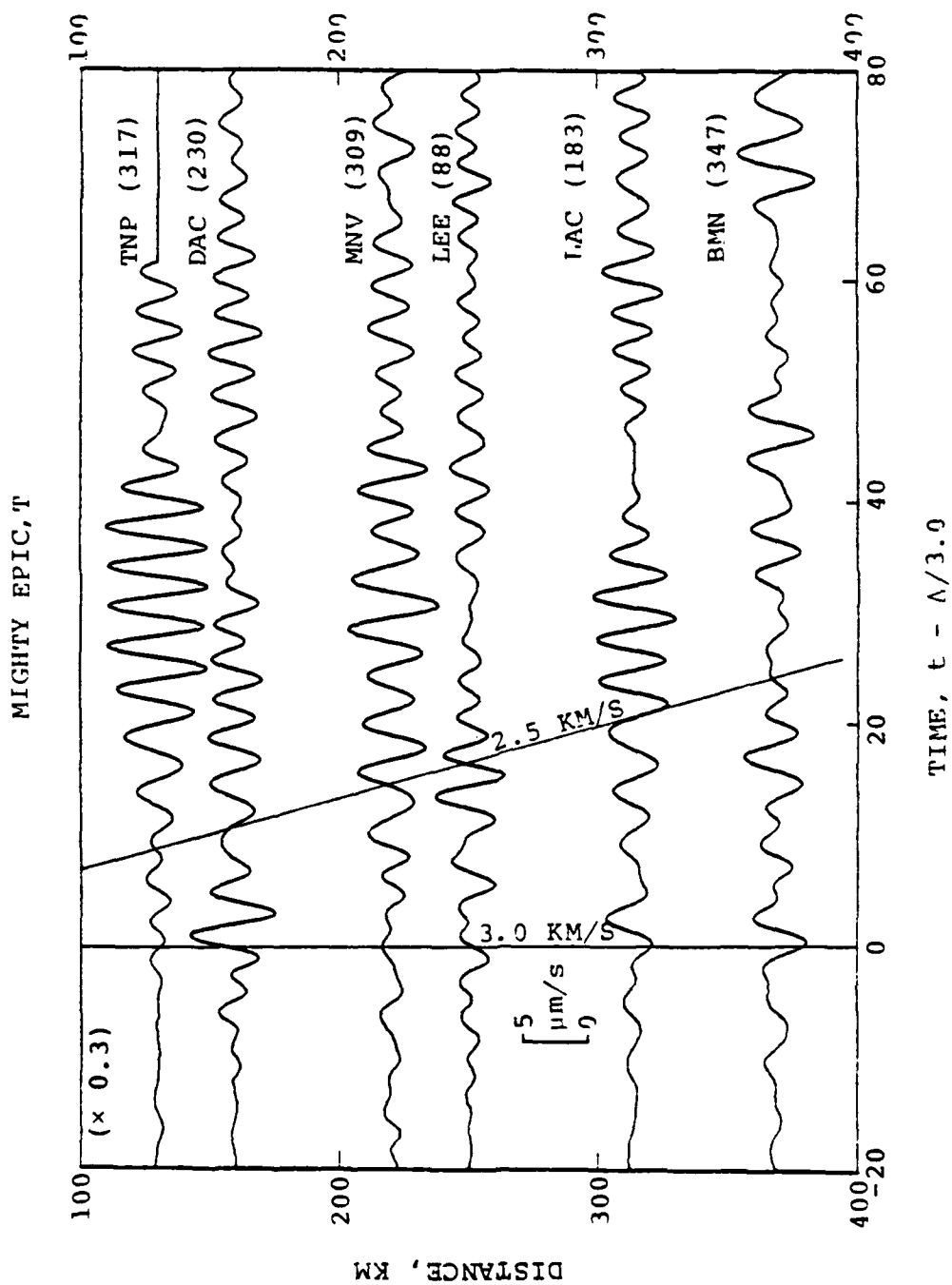


Figure 5.6a. Tangential velocities for MIGHTY EPIC after filtering with a 4-8 second bandpass filter.

DIABLO HAWK, T

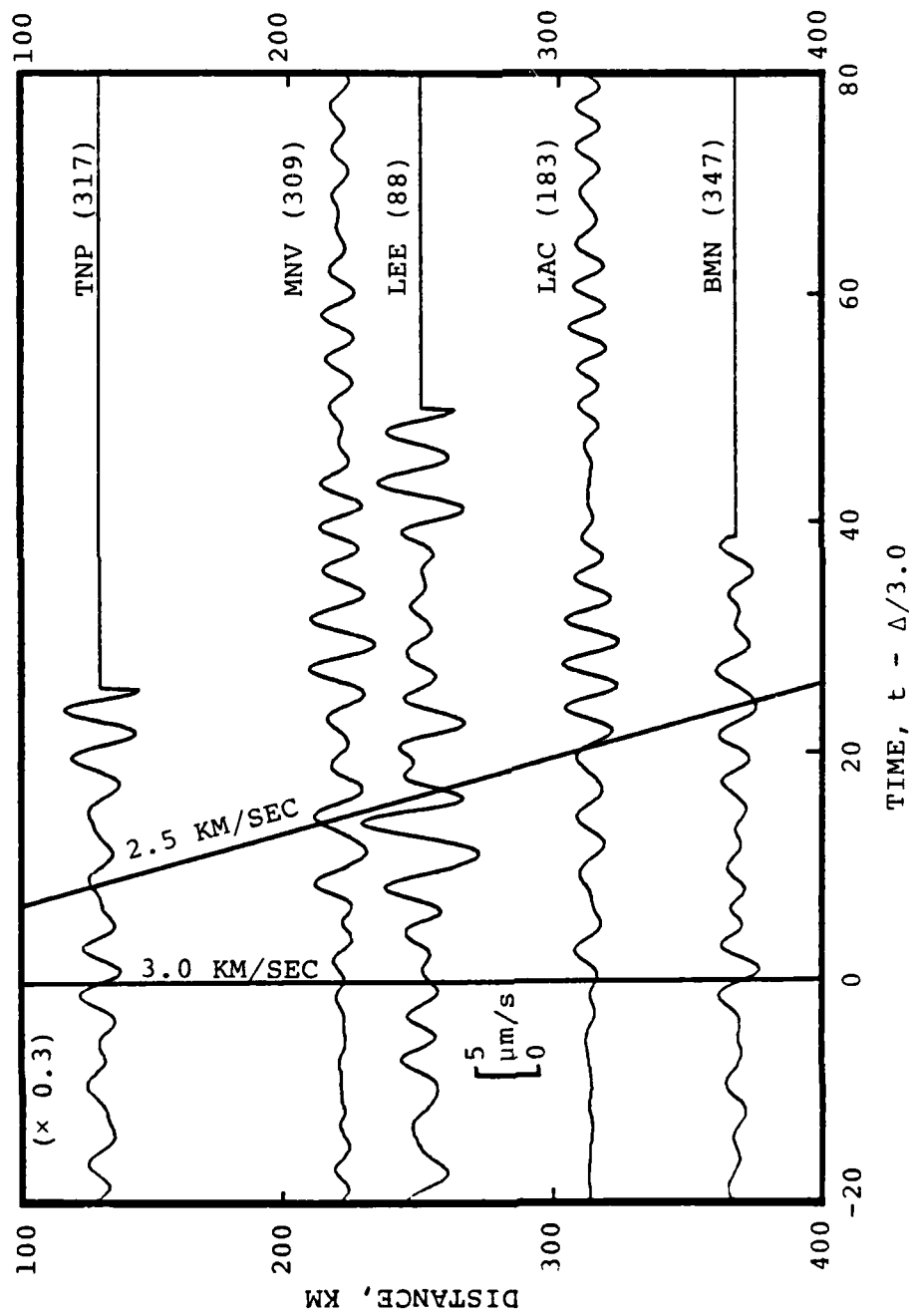


Figure 5.6b. Tangential velocities for DIABLO HAWK after filtering with a 4-8 second bandpass filter.

distinctly see the dispersed fundamental mode Love and Rayleigh wave at most stations.

To determine the group velocity dispersion for the observed Love and Rayleigh waves we applied the MARS narrow-band filter algorithm described in Section 3.3. The output is a table of amplitudes with a group arrival time associated with each amplitude. From this table we identified the fundamental mode Love and Rayleigh wave. At longer periods, these wave groups usually had the largest peaks. The resulting group velocity dispersion curves are plotted in Figure 5.7.

Comparing the observed dispersion, Figure 5.7, with the theoretical dispersion of Figure 5.2, we classify the NTS-station paths in four categories: strong and weak TUC, strong and weak PBGB. The classification is listed in Table 5.3. The stations to the east and northeast are classified as TUC-like stations. The others show group velocity dispersion more like PBGB. The only anomaly in the classification is the LEE-KNB pair which are at nearly the same azimuth. However, the dispersion at short periods is clearly different.

In later sections we will be attempting to fit the observed amplitudes. In Tab' 5.2 we gave amplification factors for each path. These factors can be used to "normalize" amplitudes from one path to those from another. The normalization factors are listed in Table 5.3 for a period of six seconds. We see that the correction is almost entirely due to the Love wave. That is, at six seconds the Rayleigh wave excitation is about the same for the two structures.

5.4 LOVE AND RAYLEIGH WAVE AMPLITUDES

In Figure 5.8 we plot the spectral amplitudes from the MARS processed data. In most cases these were the maximum amplitudes at the indicated period. If we had perfect data we would like to infer the double-couple at each period and

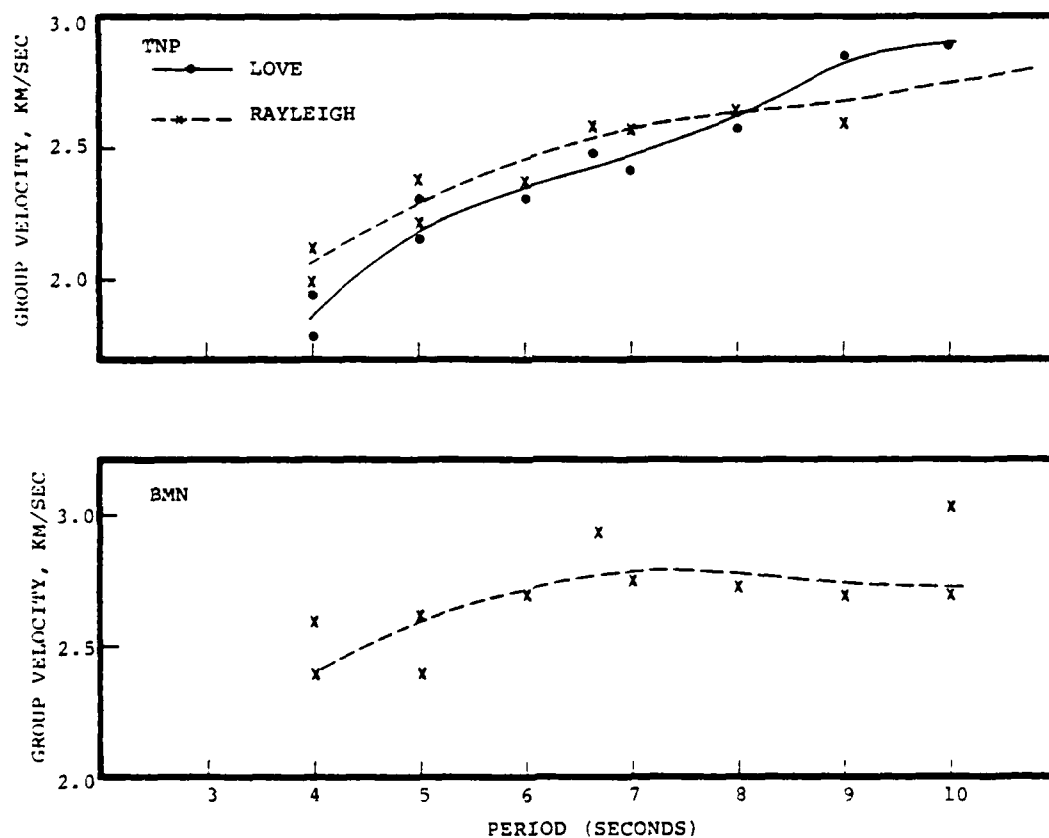


Figure 5.7. Observed group velocity dispersion at the eleven stations recording MIGHTY EPIC and/or DIABLO HAWK. Two data points at a particular period indicate that analysis of recordings of the two events gave different estimates for the group velocity.

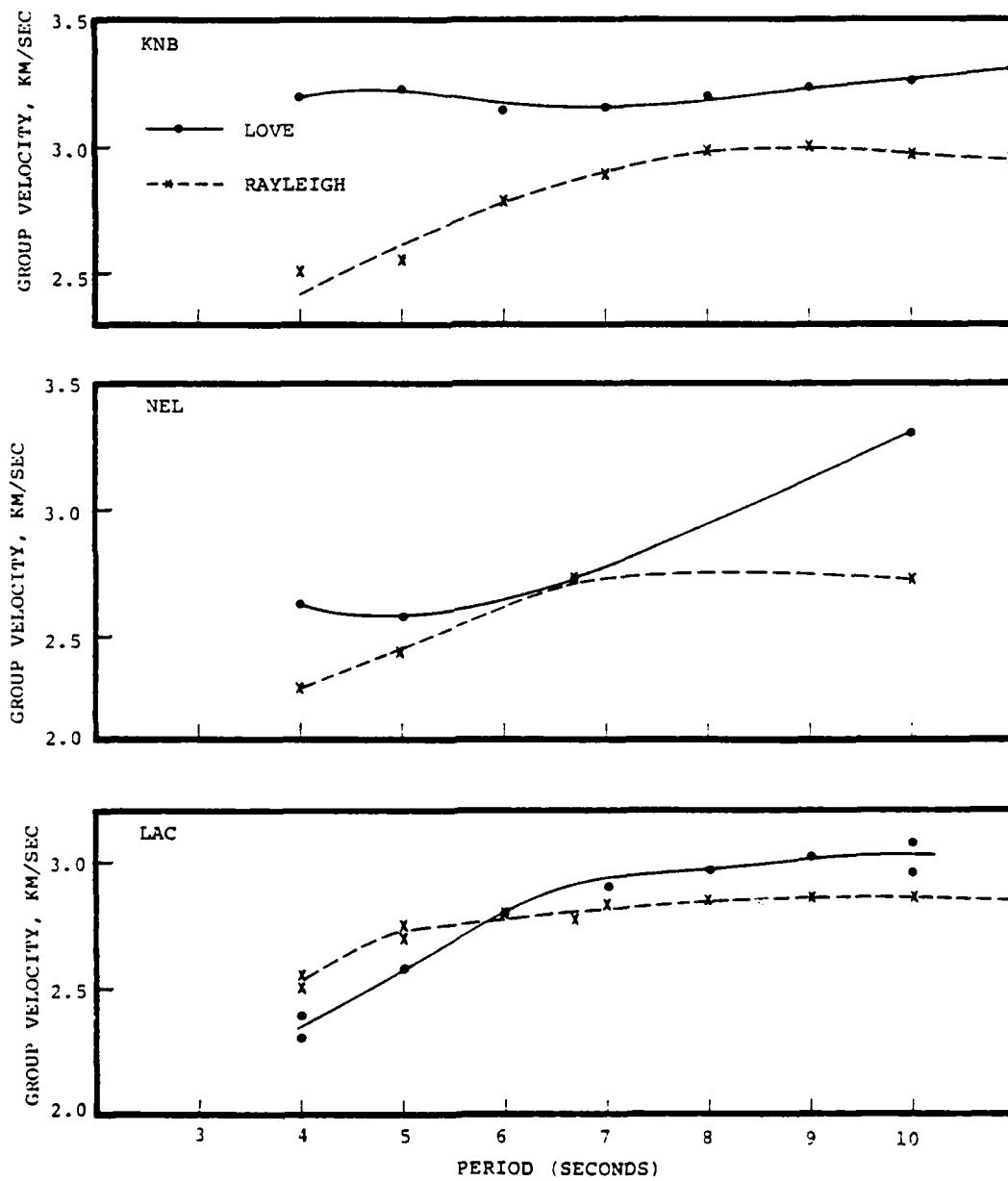


Figure 5.7. Continued

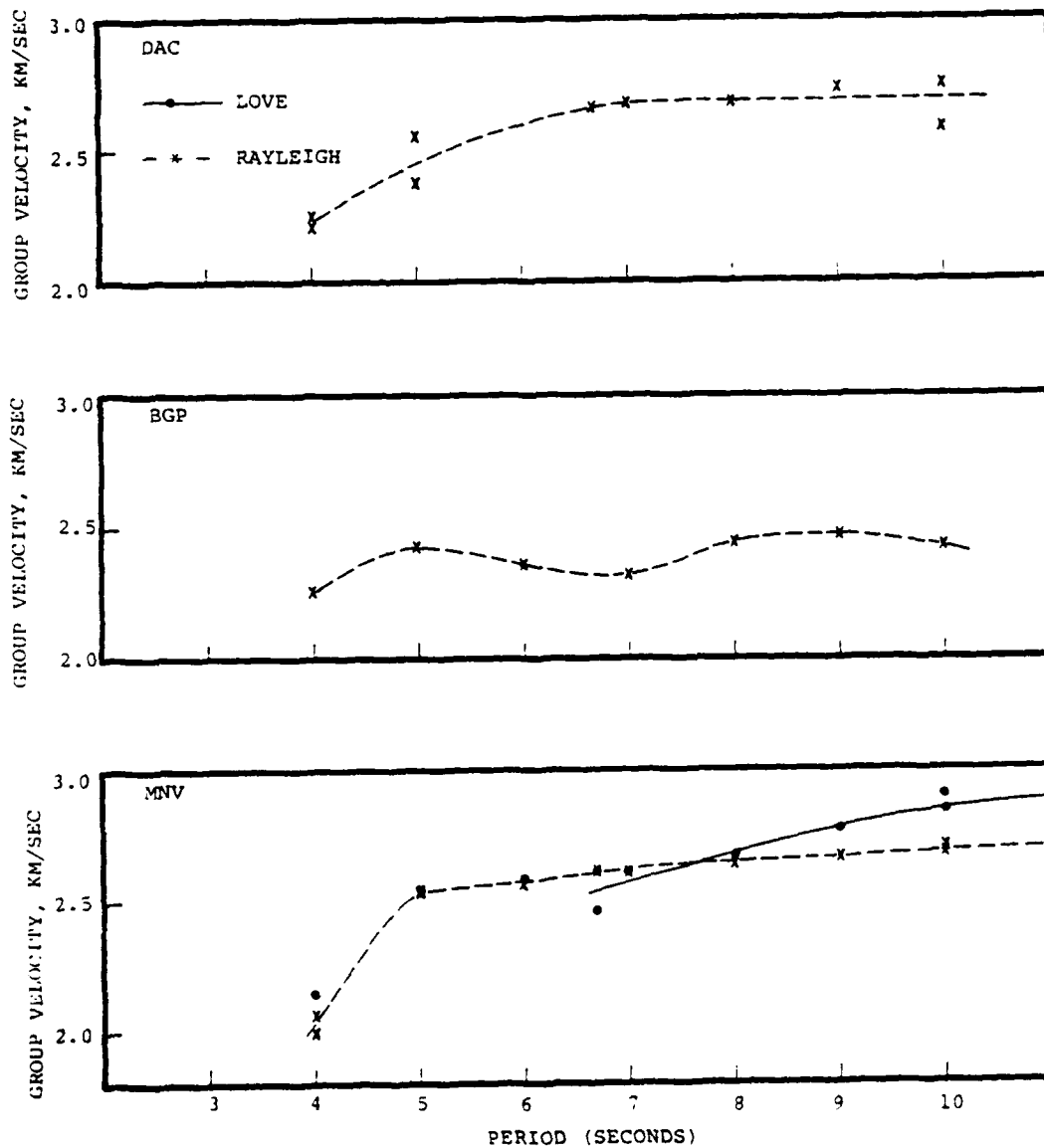


Figure 5.7. Continued

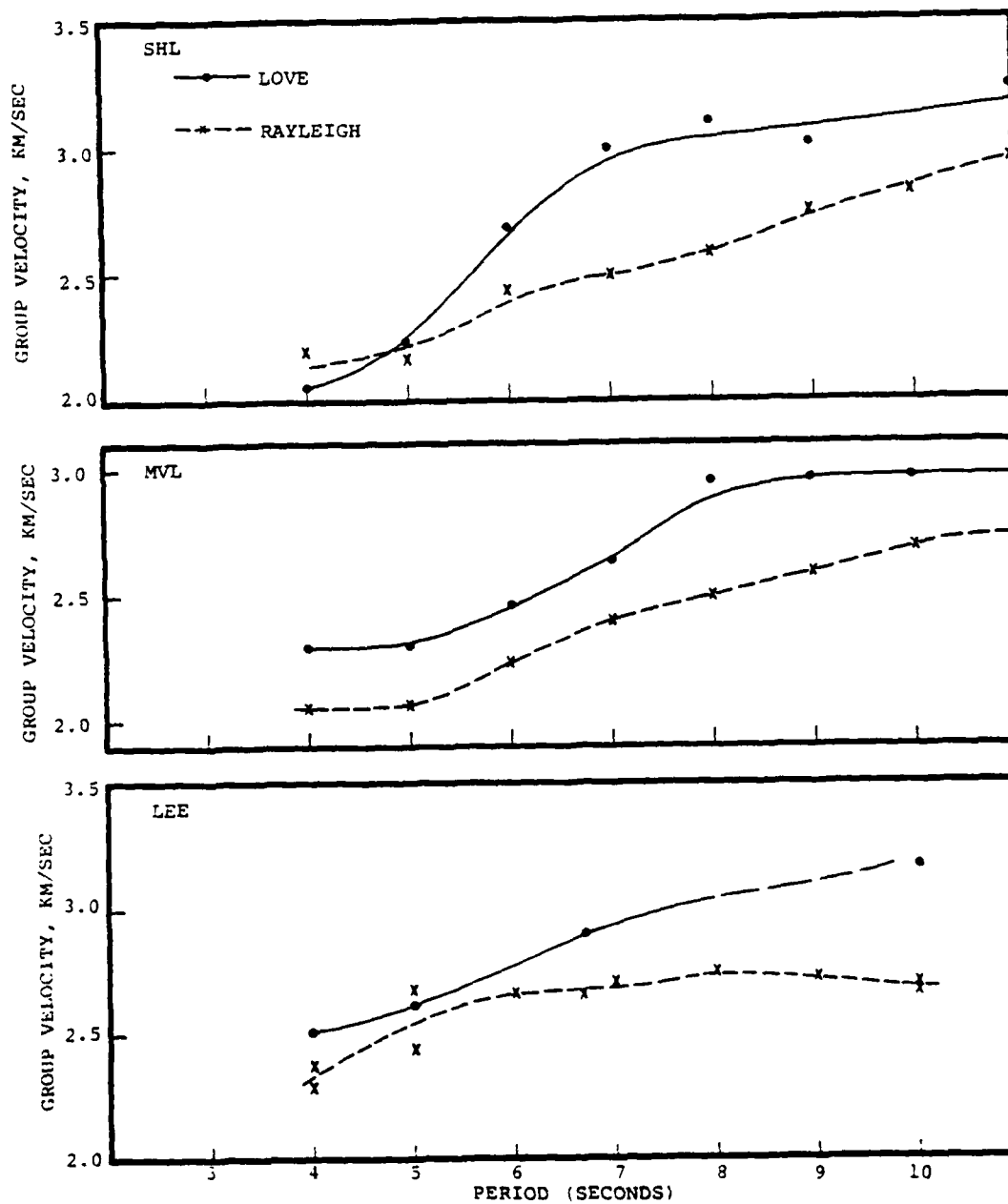


Figure 5.7. Concluded

TABLE 5.3
STATION CLASSIFICATION

<u>Station</u>	<u>Azimuth</u>	<u>Classification</u>	<u>Correction Factors*</u> <u>at Six Seconds</u>		
			<u>LR</u>	<u>LQ</u>	<u>LQ/LR</u>
SHL	25	Weak TUC	1.01	1.14	1.13
MVL	68	Strong TUC	1.00	1.00	1.00
LEE	88	Weak TUC	1.01	1.14	1.13
KNB	93	Strong TUC	1.00	1.00	1.00
NEL	143	Weak PBGB	1.02	1.30	1.27
LAC	183	Strong PBGB	1.03	1.44	1.40
DAC	231	Weak PBGB	1.02	1.30	1.27
BGP	269	Weak PBGB	1.02	1.30	1.27
MNV	309	Strong PBGB	1.03	1.44	1.40
TNP	317	Strong PBGB	1.03	1.44	1.40
BMN	317	Weak PBGB	1.02	1.30	1.27

*
LR denotes the Rayleigh wave
LQ denotes the Love wave

These correction factors are to be divided into each datum to correct it to the "strong TUC" path. For example, the "strong PBGB" factors are the J_R , J_L , Γ values for PBGB divided by the J_R , J_L , Γ values for TUC from Table 5.2. The "weak TUC" and "weak PBGB" values are a fraction of the maximum correction represented by the "strong PBGB" values. Since these correction values are based on the path amplification factors in Table 5.2, they are appropriate for a nominal range of 250 km. A separate correction is needed for ranges different from this.

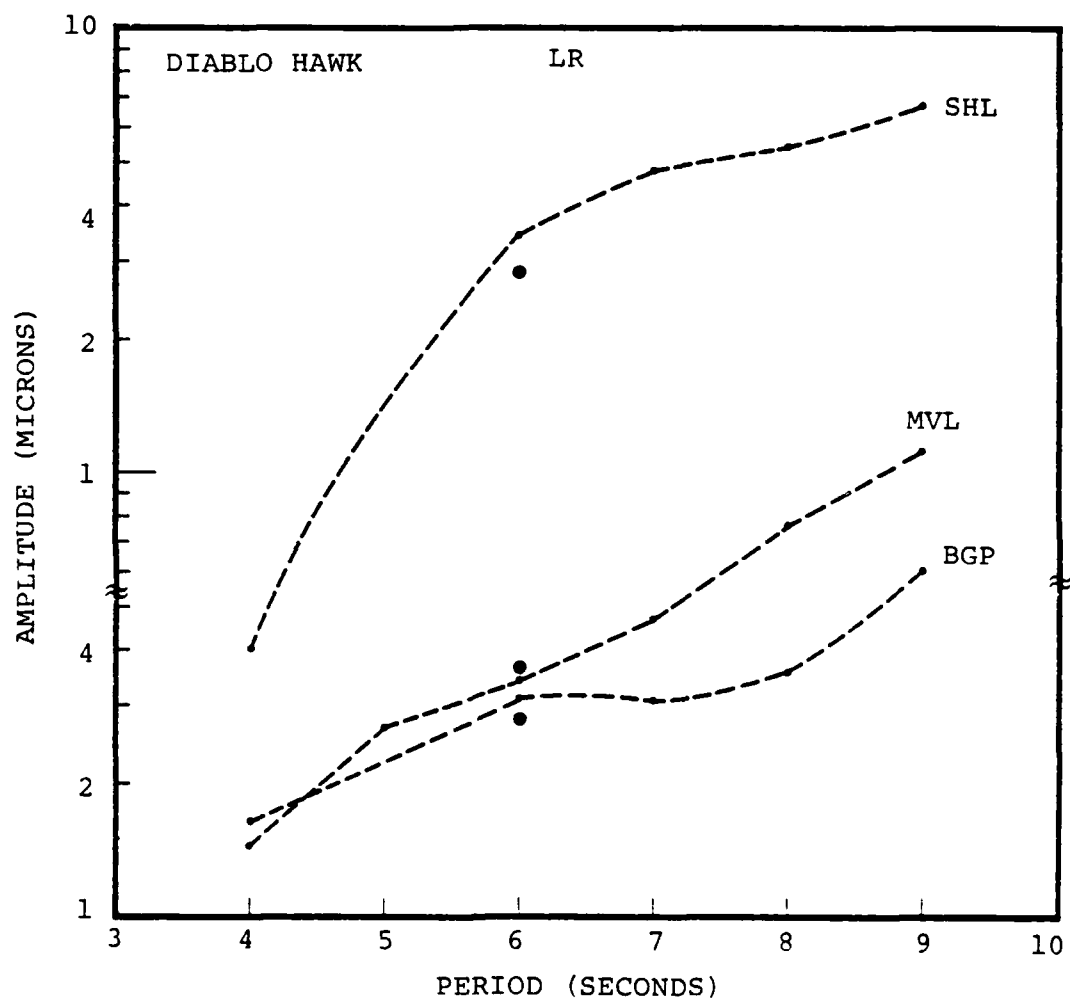


Figure 5.8. Spectral amplitudes from MARS processing of the DIABLO HAWK and MIGHTY EPIC seismograms. The large dot indicates the six second amplitude value used in the subsequent analysis.

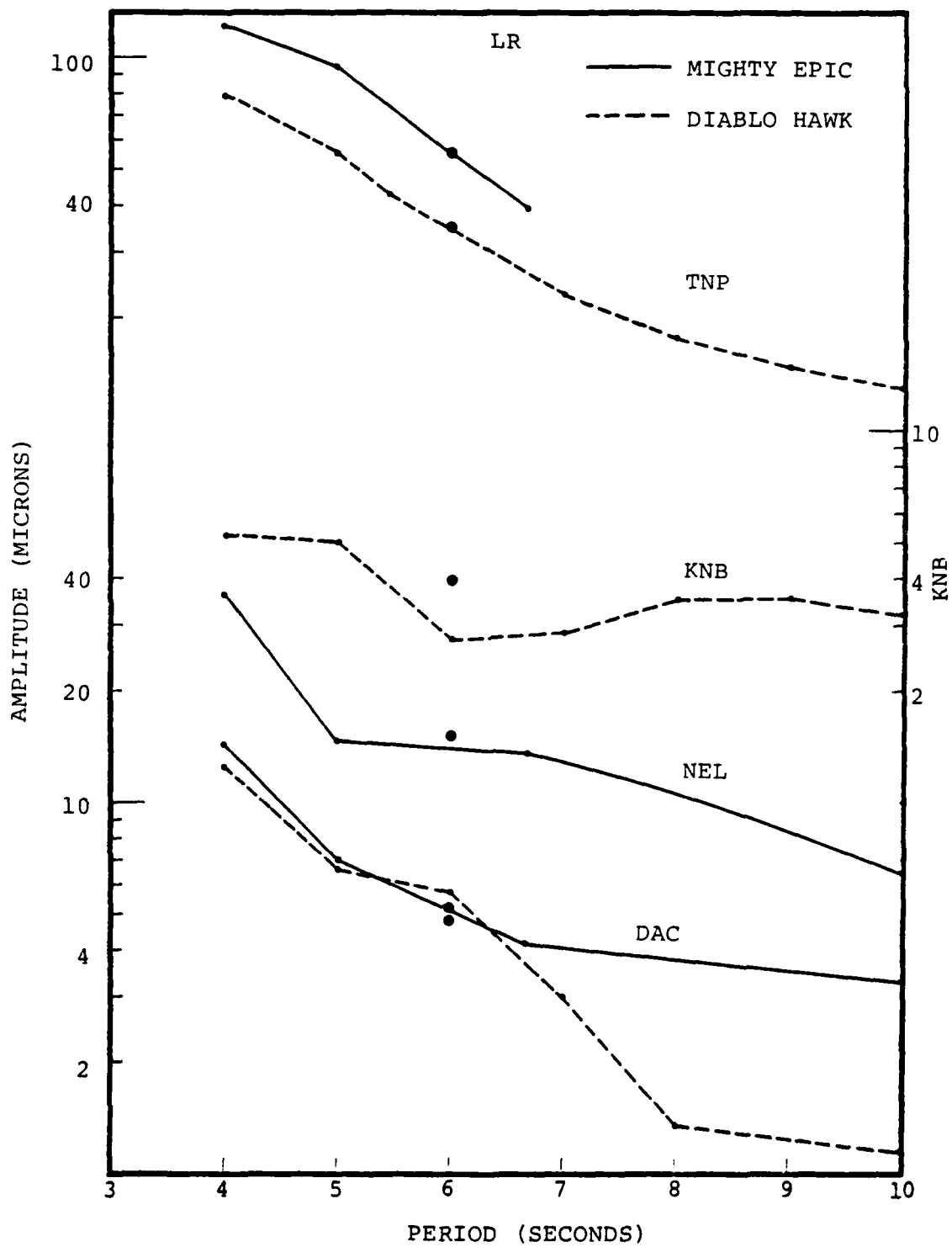


Figure 5.8. Continued

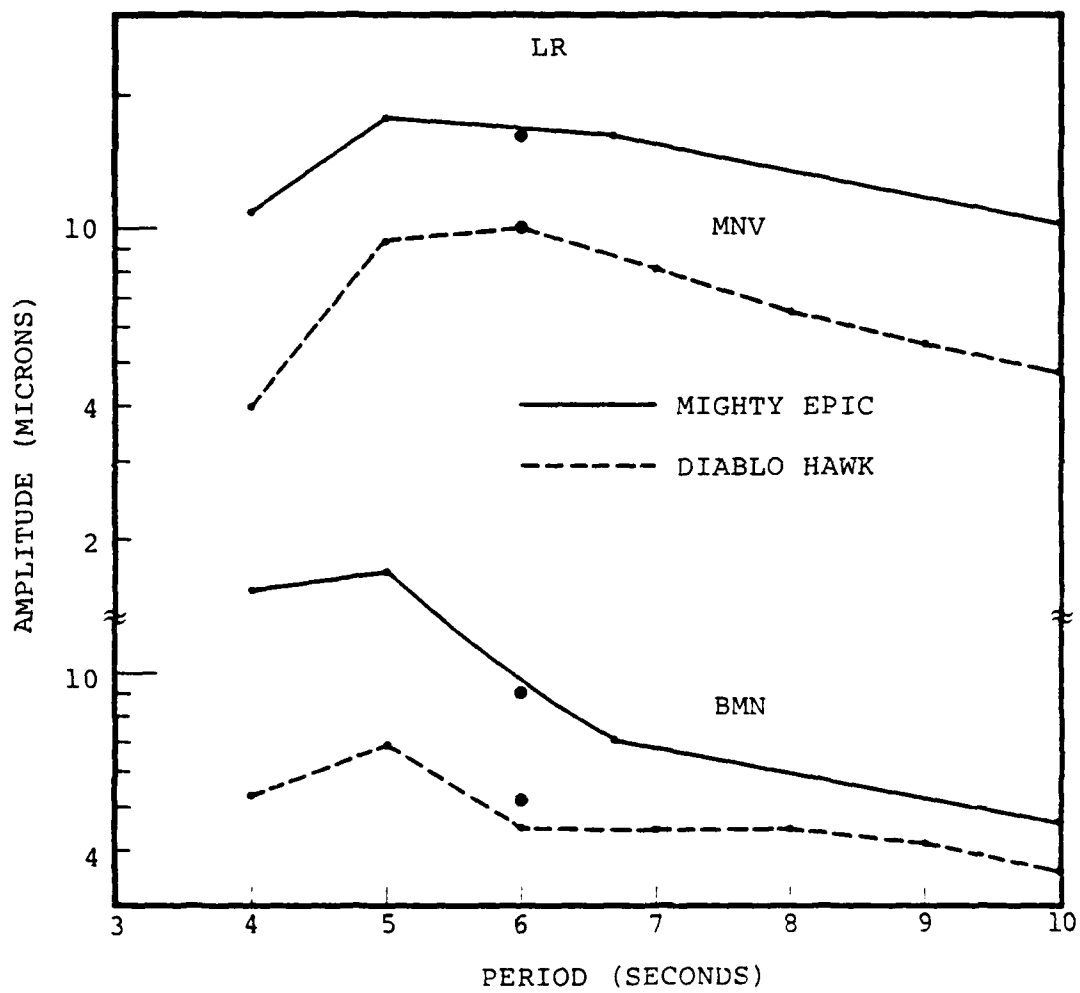


Figure 5.8. Continued

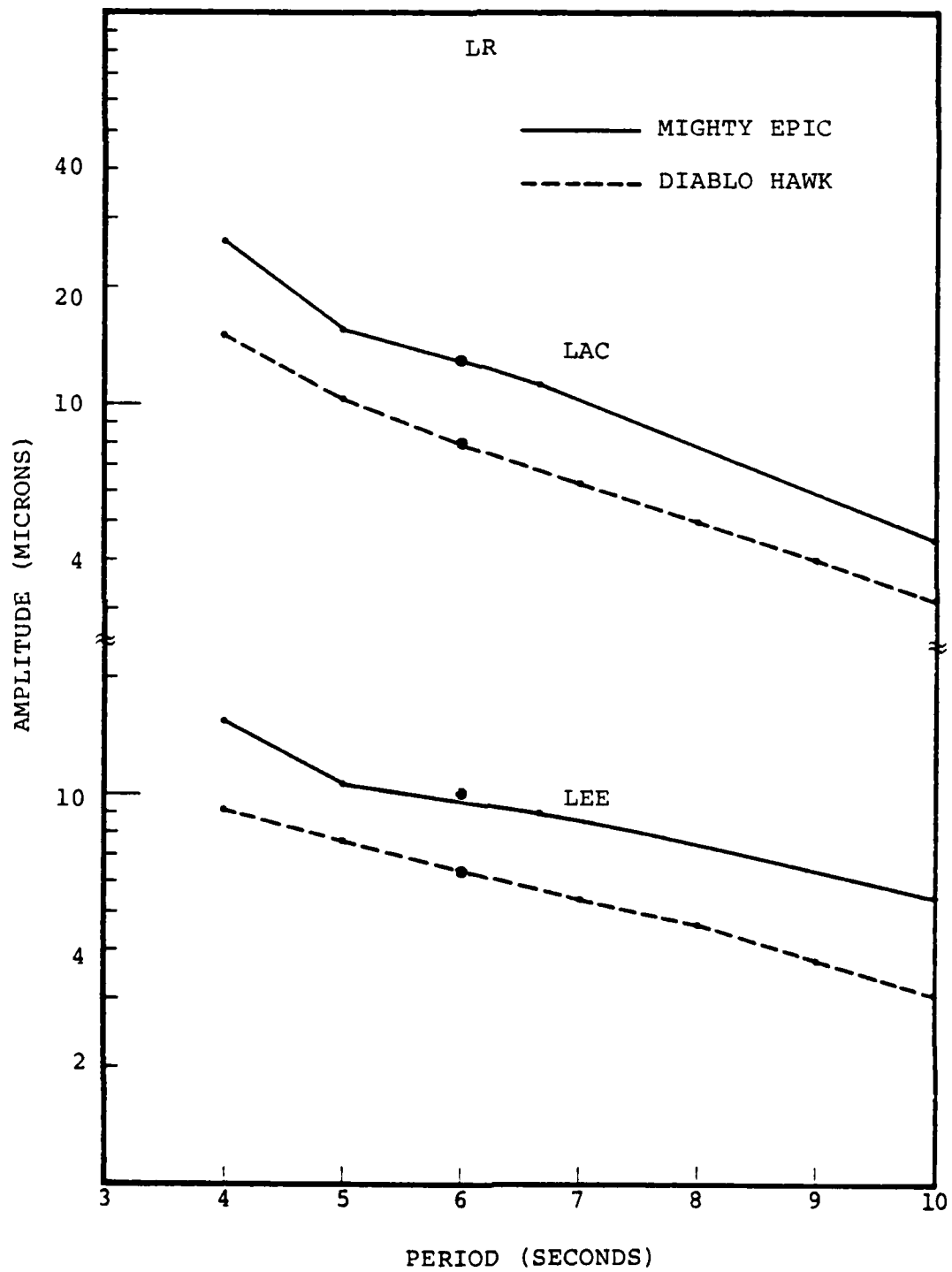


Figure 5.8. Continued

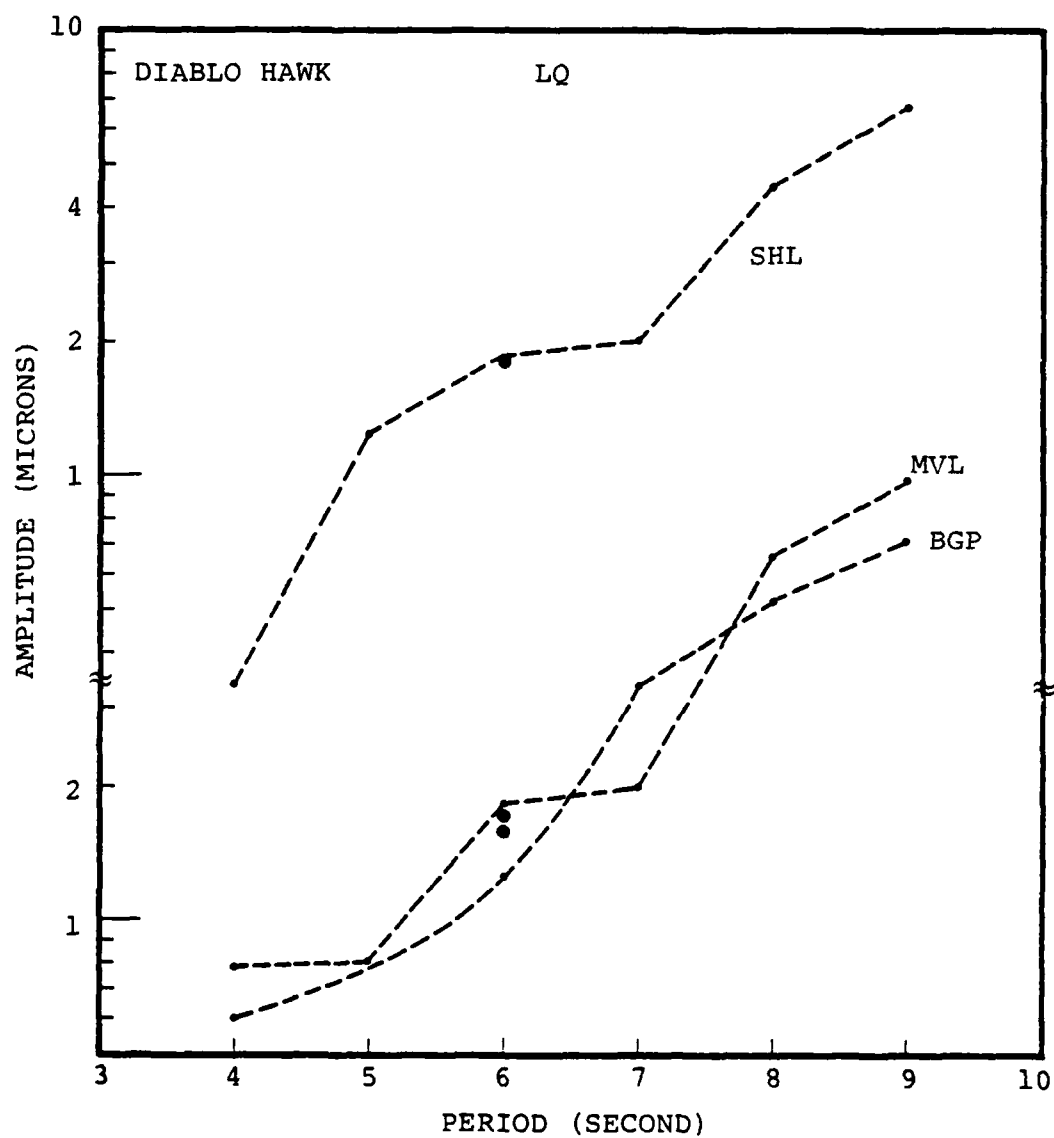


Figure 5.8. Continued

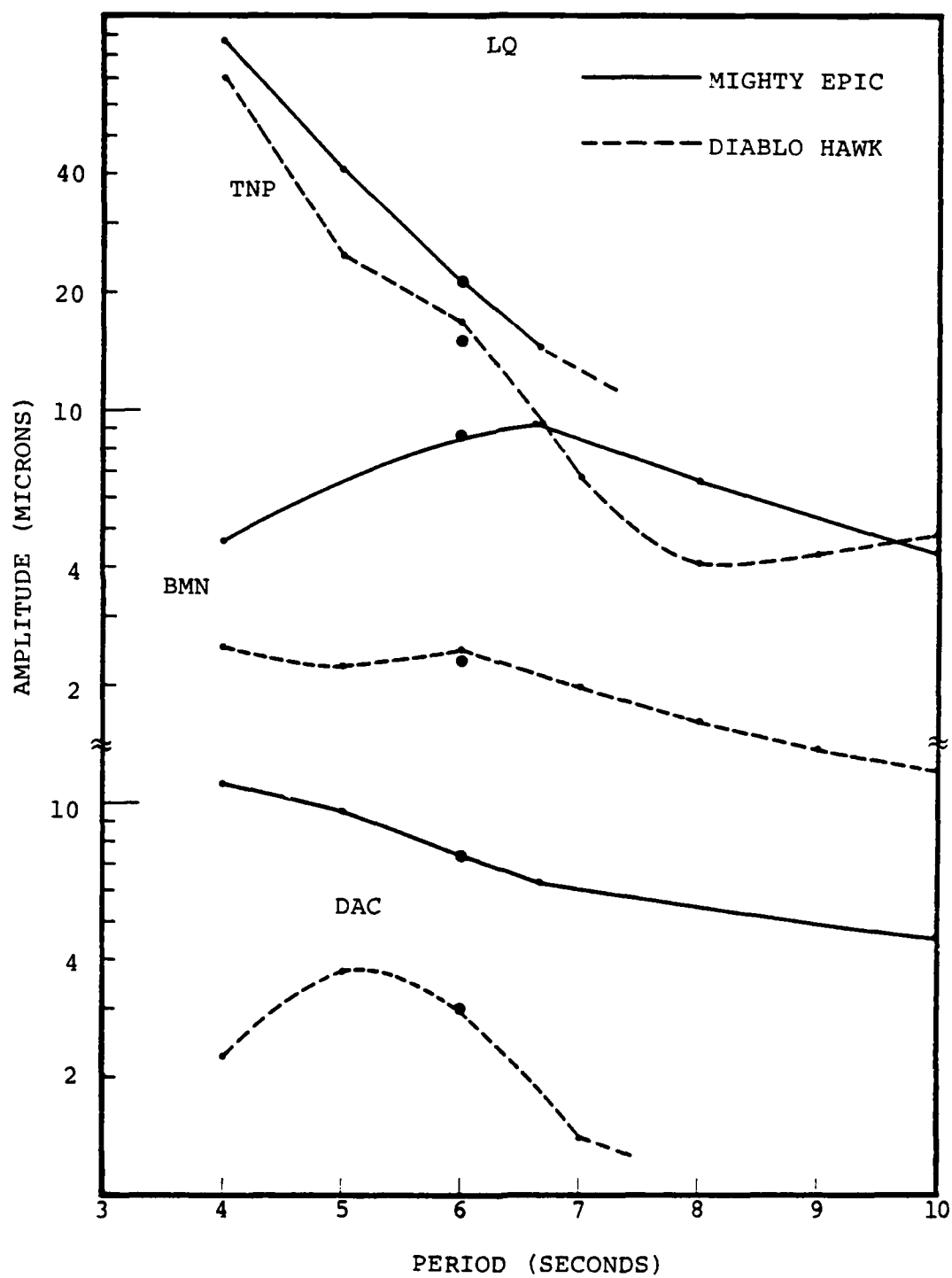


Figure 5.8. Continued

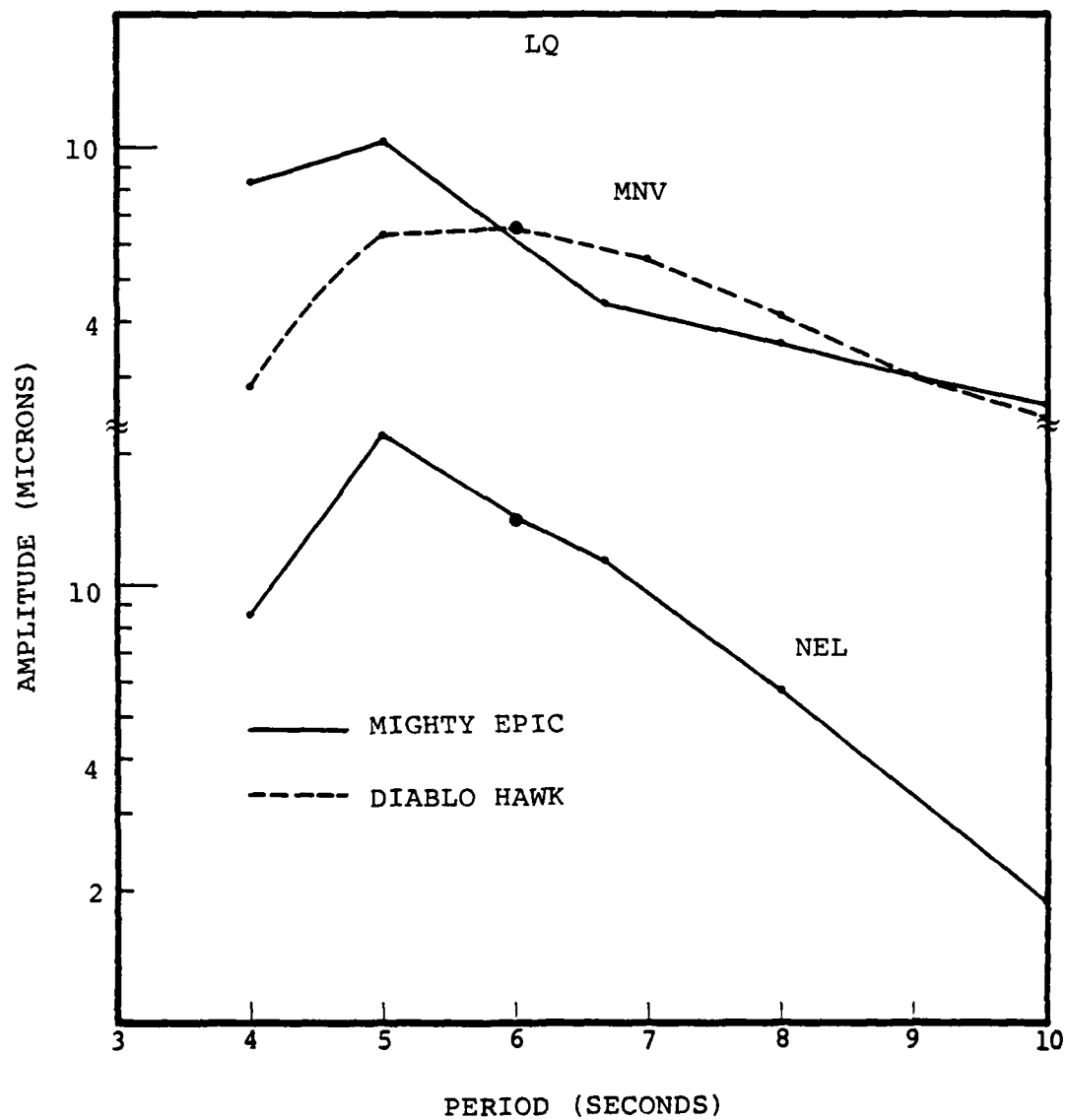


Figure 5.8. Continued

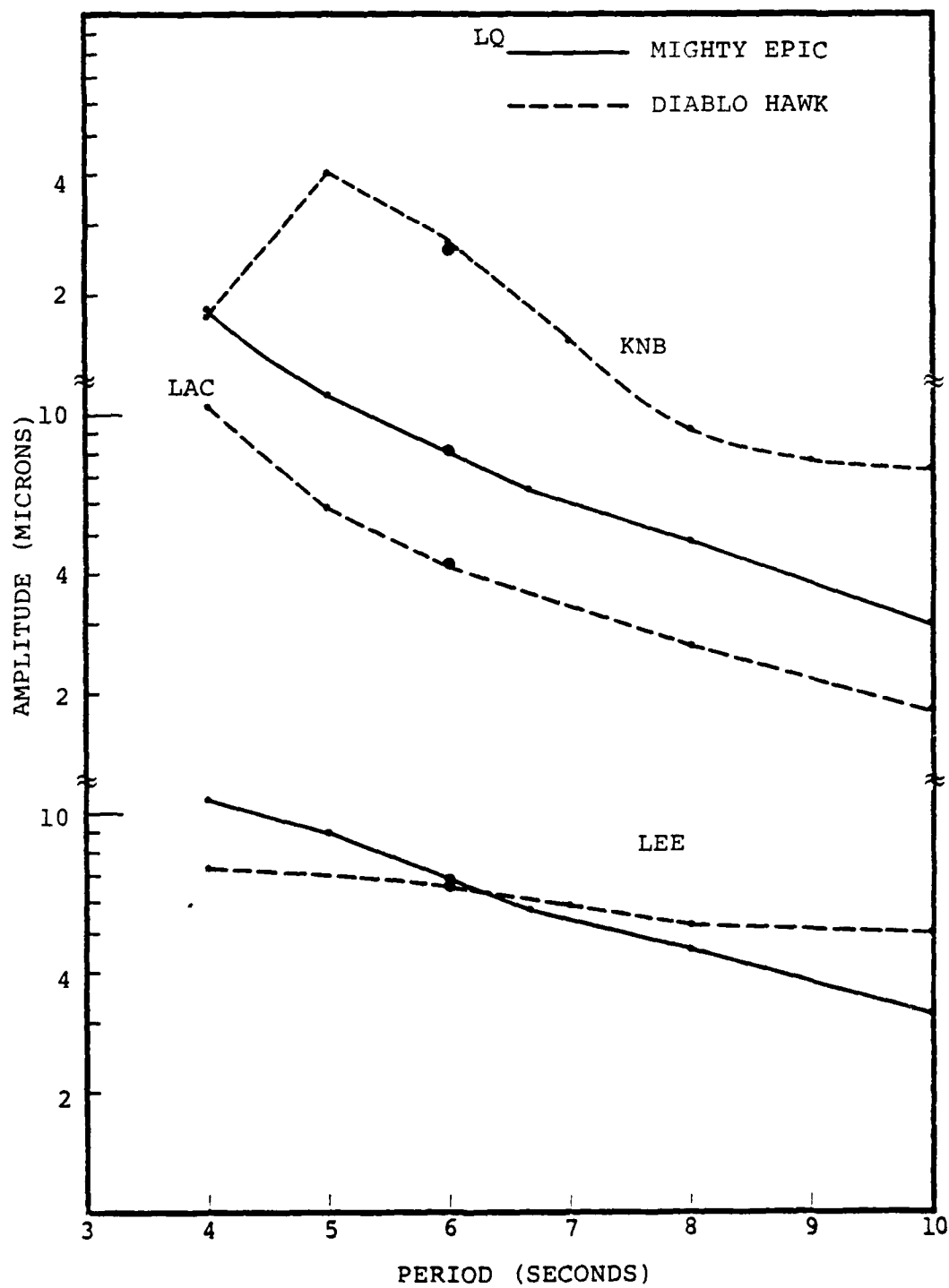


Figure 5.8. Concluded

determine the Fourier spectrum. However, there is only a narrow range of periods where we can determine the amplitude with much confidence. Therefore, we will use only one amplitude estimate for each record, that at six seconds. The six second amplitude was determined by "smoothing" (by eye) the plotted amplitudes and the value used is indicated on the plots. The amplitudes are summarized in Table 5.4.

Before using these data to solve for the double-couple, we directly compare the MIGHTY EPIC and DIABLO HAWK values. In Table 5.5 we give the amplitude ratios for twelve common observations. These are compared to relative amplitudes from analysis of total wavetrain spectra discussed in Section 4.2 and summarized in Table 4.2. The two ratios are very much the same. The only significant difference is for LQ at MNV. This is probably a result of the total wavetrain spectra being dominated by the fundamental mode surface waves at long periods.

In Figures 5.9 and 5.10 we plot the amplitudes from Table 5.4 versus range. The LQ/LR ratios are only weakly dependent on range (Eqs. (5.14) and (5.15)). However, if we are to fit the LR and LQ data separately, we must correct for the range.

Our theoretical formulae, Eqs. (5.14) and (5.15), predict a dependence on range that is approximately r^{-n} between two distances r_1 and r_2 , where

$$n = 0.5 + 0.434\gamma \frac{(r_2 - r_1)}{\log \frac{r_2}{r_1}} . \quad (5.16)$$

In Table 5.6 we list the values of γ for the theoretical models of the previous section and the rate of amplitude attenuation predicted across our distance range. Lines with slopes near the theoretical values in the table are shown with the data in

TABLE 5.4
SIX SECOND AMPLITUDES FROM MARS ANALYSIS*

<u>Station</u>	<u>Azimuth</u>	<u>Distance</u>	<u>LR</u>	<u>LQ</u>	<u>LQ/LR</u>
MIGHTY EPIC					
TNP	317	131	55.0	21.2	0.39
DAC	231	161	5.2	7.4	1.42
NEL	143	206	15.0	14.0	0.93
MNV	309	218	16.0	6.5	0.41
LEE	88	252	10.0	6.8	0.68
LAC	183	313	13.0	8.1	0.62
BMN	347	368	9.0	8.6	0.96
DIABLO HAWK					
TNP	317	131	35.0	15.0	0.43
DAC	231	161	4.8	3.0	0.63
BGP	269	178	--	--	0.57
MNV	309	218	10.0	6.5	0.65
LEE	88	252	6.3	6.6	1.05
KNB	93	302	4.0	2.6	0.65
MVL	68	303	--	--	0.47
LAC	183	313	8.0	4.1	0.51
SHL	25	317	--	--	0.64
BMN	347	368	5.2	2.3	0.44

*The LR and LQ spectral amplitudes are in microns.

TABLE 5.5
RELATIVE AMPLITUDES, MIGHTY EPIC/DIABLO HAWK

Station	LR		LQ	
	<u>Narrow-Band Spectral Amplitude</u>	<u>Total Spectra*</u>	<u>Narrow-Band Spectral Amplitude</u>	<u>Total Spectra*</u>
TNP	1.57	1.67	1.41	1.59
DAC	1.17	1.33	2.46	--
MNV	1.60	1.82	1.00	1.67
LEE	1.58	1.82	1.03	1.00
LAC	1.63	2.00	1.97	2.00
BMN	1.73	--	3.75	--

* $1/\hat{H}_1$ from Table 4.2.

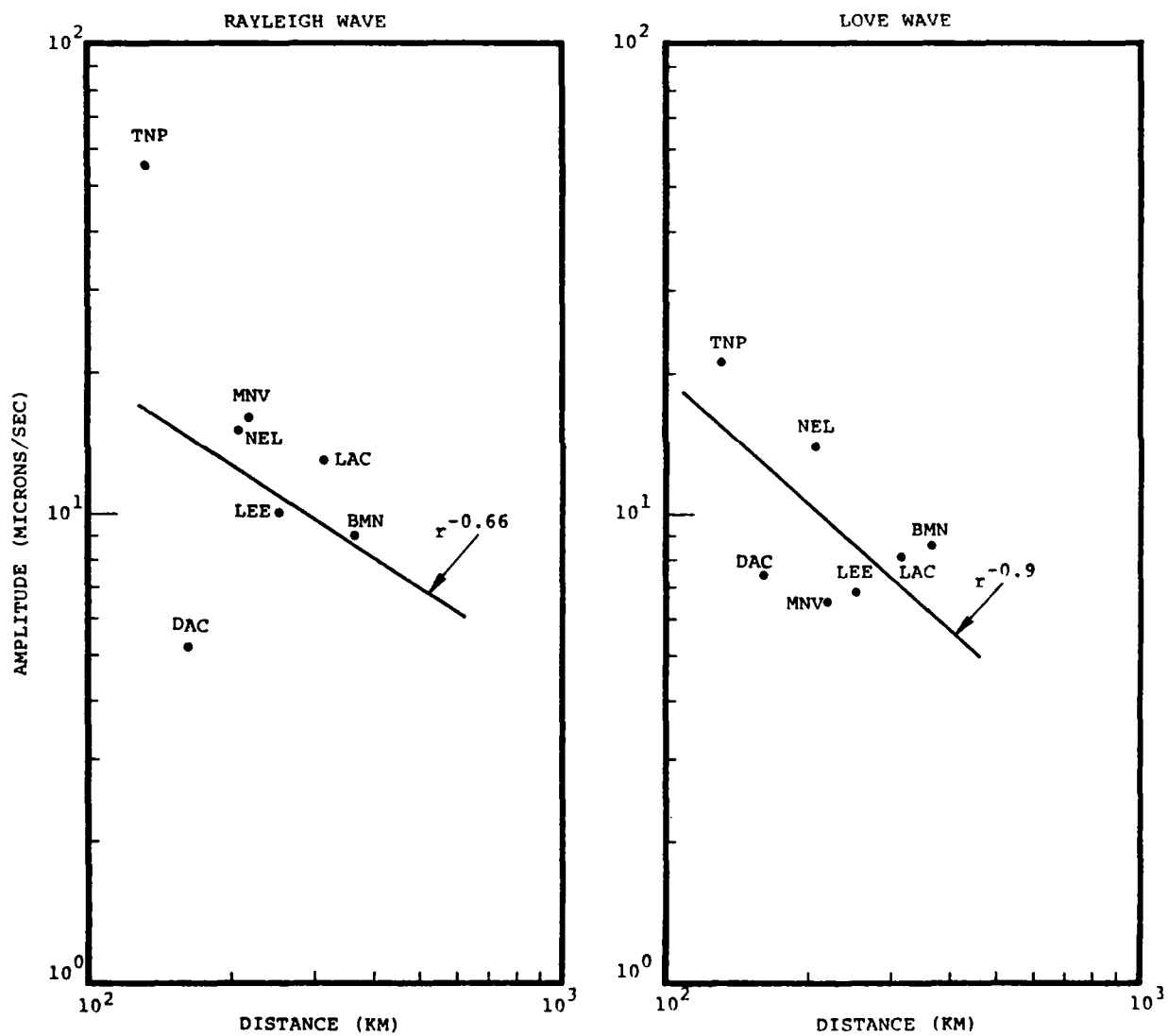


Figure 5.9. MIGHTY EPIC amplitudes versus range.

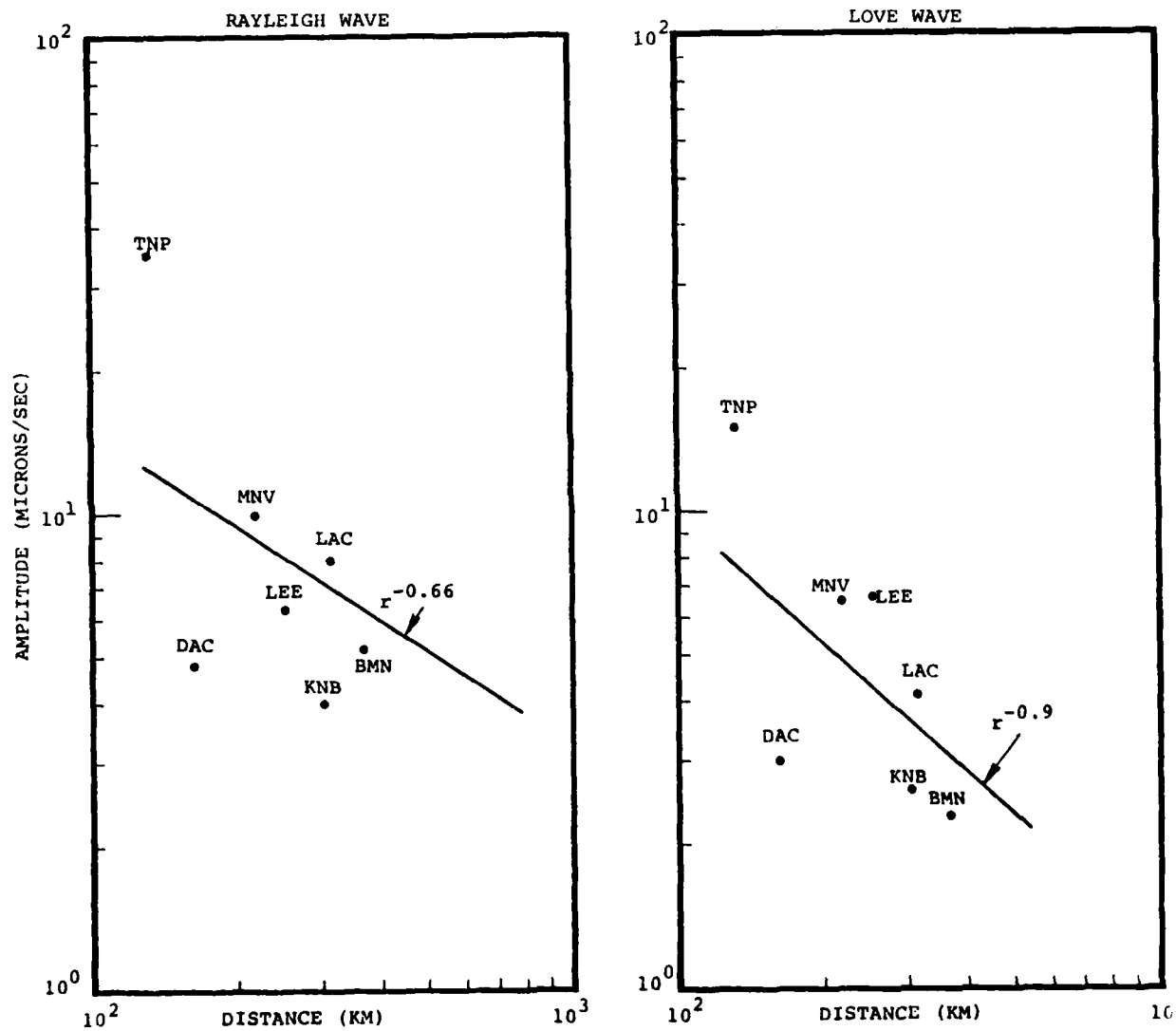


Figure 5.10. DIABLO HAWK amplitudes versus range.

TABLE 5.6

DISTANCE ATTENUATION, r^{-n} AT $T = 5.7$ SECONDS

Structure	γ_R, γ_L ($\times 10^{-4} \text{ km}^{-1}$)	130-250 km		250-370 km		130-370 km	
		n		n		n	
TUC, Rayleigh	5.5	0.60		0.67		0.63	
PGB, Rayleigh	6.3	0.62		0.69		0.64	
TUC, Love	5.7	0.60		0.67		0.63	
PGB, Love	13.9	0.76		0.93		0.82	

Figures 5.9 and 5.10. The data are not inconsistent with these curves, considering that radiation pattern effects have an influence on the amplitudes.

5.5 ESTIMATION OF THE DOUBLE-COUPLE

In this section we present our estimates for the size and orientation of the double-couple associated with the MIGHTY EPIC and DIABLO HAWK event. We begin with the LQ/LR data, which are supposed to be most reliable in that individual station peculiarities and propagation path effects tend to cancel. We will also use the LR and LQ data separately to help constrain the solution.

The LQ/LR data are summarized in Table 5.7. There are two sets of data. The original data are from Table 5.4. The path corrected data are these ratios after correcting by the factors given in Table 5.3. These ratios are used in Eqs. (5.15) and (5.13) to compute the contours of the error between the theoretical and observed values. In using (5.15) we assume vertical strike-slip faulting.

5.5.1 DIABLO HAWK Double-Couple

In Figure 5.11 we show the error contours for DIABLO HAWK for both the original and path corrected data from Table 5.7. For the original data we use $\Gamma = 1.4$ in (5.15) for all stations. This is the value of Γ for "strong PBGB" stations (Table 5.2). If we must choose one value for all stations, this is probably the best. Since the path correction is applied station-by-station for the "path corrected" data, the calculations are done with $\Gamma = 1$ for this case. The minimum error is quite clearly defined to occur at $\theta_s = 16^\circ$. That is, the best solution strikes N16°E. The F factor is dependent on our assumption about Γ . For the original data, changing Γ from 1.4 (assuming the excitation at all stations is like PBGB) to

TABLE 5.7
LQ/LR DATA

<u>Station</u>	<u>Azimuth</u>	<u>Original Data</u>	<u>Path* Corrected Data</u>
MIGHTY EPIC			
TNP	317	0.39	0.29
DAC	231	1.42	1.12
NEL	143	0.93	0.73
MNV	309	0.41	0.29
LEE	88	0.68	0.60
LAC	183	0.62	0.44
BMN	347	0.96	0.76
DIABLO HAWK			
TNP	317	0.43	0.31
DAC	231	0.63	0.45
BGP	269	0.57	0.50
MNV	309	0.65	0.46
LEE	88	1.05	0.93
KNB	93	0.65	0.65
MVL	68	0.47	0.47
LAC	183	0.51	0.36
SHL	25	0.64	0.57
BMN	347	0.44	0.35

*
The values from the adjacent column are corrected to the TUC path by the LQ/LR factors from Table 5.3.

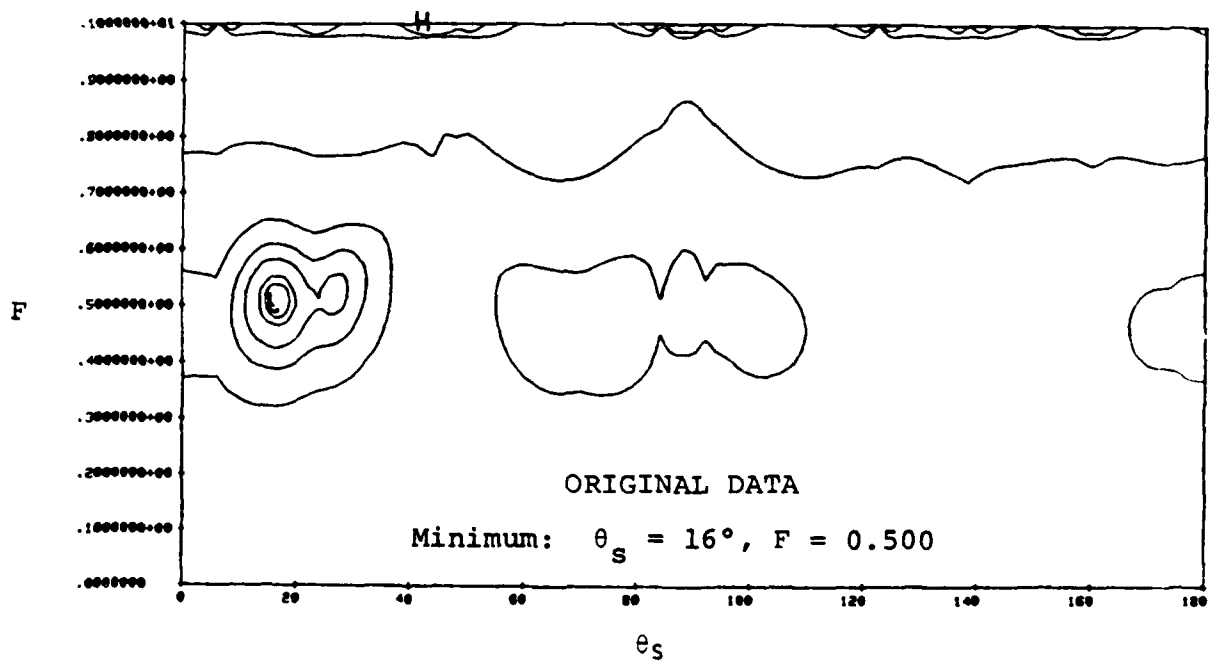
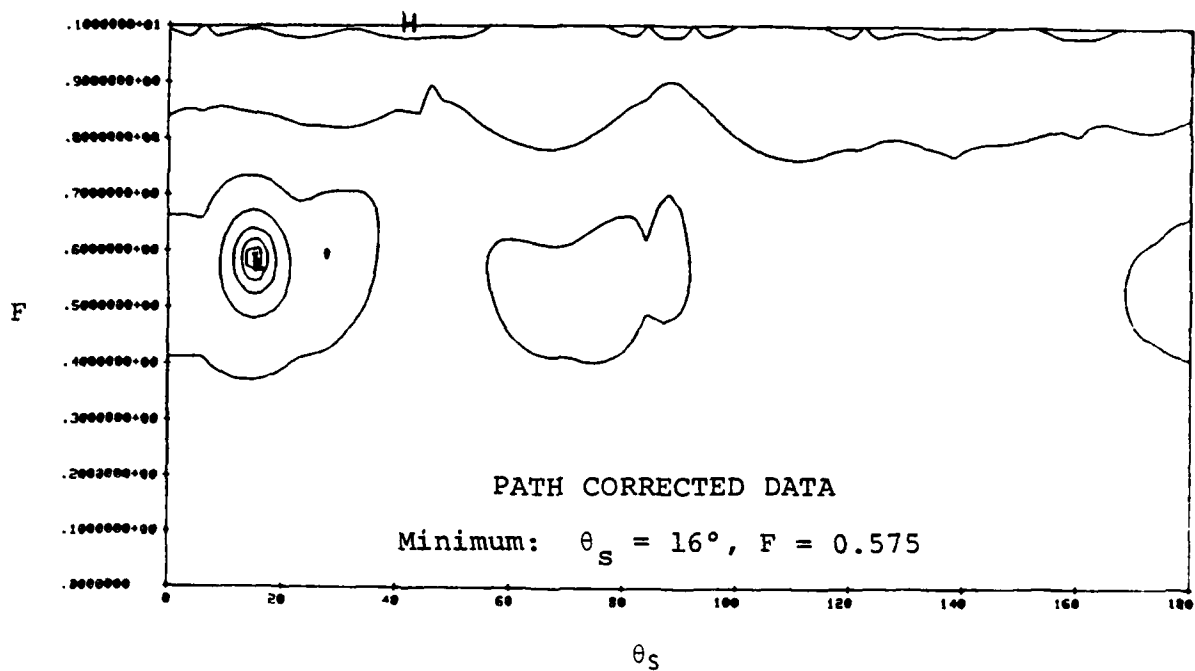


Figure 5.11. Error contours for LQ/LR, F versus θ_S , for DIABLO HAWK assuming, $\delta = 90$, $\lambda = 0$.

1.0 (assuming all paths are like TUC) changes the minimum error solution from $F = 0.500$ to $F = 0.65$. The F factor also depends on our assumption about the dip and slip (δ, λ) of the double-couple. Values other than $\delta = 90, \lambda = 0$ increase our estimate for F .

Let us look more closely at the dependence of the solution on δ and λ . In Figure 5.12 we show four error contours. These are:

- a. We assume $\delta = 45$ and $\lambda = 0$ (strike-slip faulting on a fault dipping 45°) and vary F and θ_s . Once again, the minimum error is for $\theta_s = 16^\circ$. In this case, $F = 0.825$. The θ_s value will henceforth be fixed.
- b. We fix $\theta_s = 16$ and $\lambda = 0$ and vary F (from 0 to 1) and δ . The minimum error solutions occur with $F = 0.575/\sin\delta$, $35 < \delta < 145$. For $F > 1$, this formula continues to be valid.
- c. We fix $\theta_s = 16$ and $\delta = 90$ and vary F (from 0 to 1) and λ . Again, there is an infinite number of minimum error solutions. In this case the solutions satisfy $F = 0.575/\cos\lambda$, $0 \leq \lambda < 55$.
- d. For each value of F there is a set of optimal δ, λ values. For example, we fix $\theta_s = 16$ and $F = 0.725$ and vary λ and δ . The minimum errors occur along the line $\delta = 54 + \lambda$, $0 \leq \lambda \leq 36$.

In summary, we have defined an entire family of solutions. For the minimum F of 0.575, the solution is $\theta_s = 16, \delta = 90, \lambda = 0$. If we are willing to accept larger values of F , solutions with the same minimum error can be found for a wide range of λ, δ pairs.

All the minimum error solutions of Figures 5.11 and 5.12 have the same LQ, LR and LQ/LR radiation patterns. In Figure 5.13 we plot this solution with the observed data.

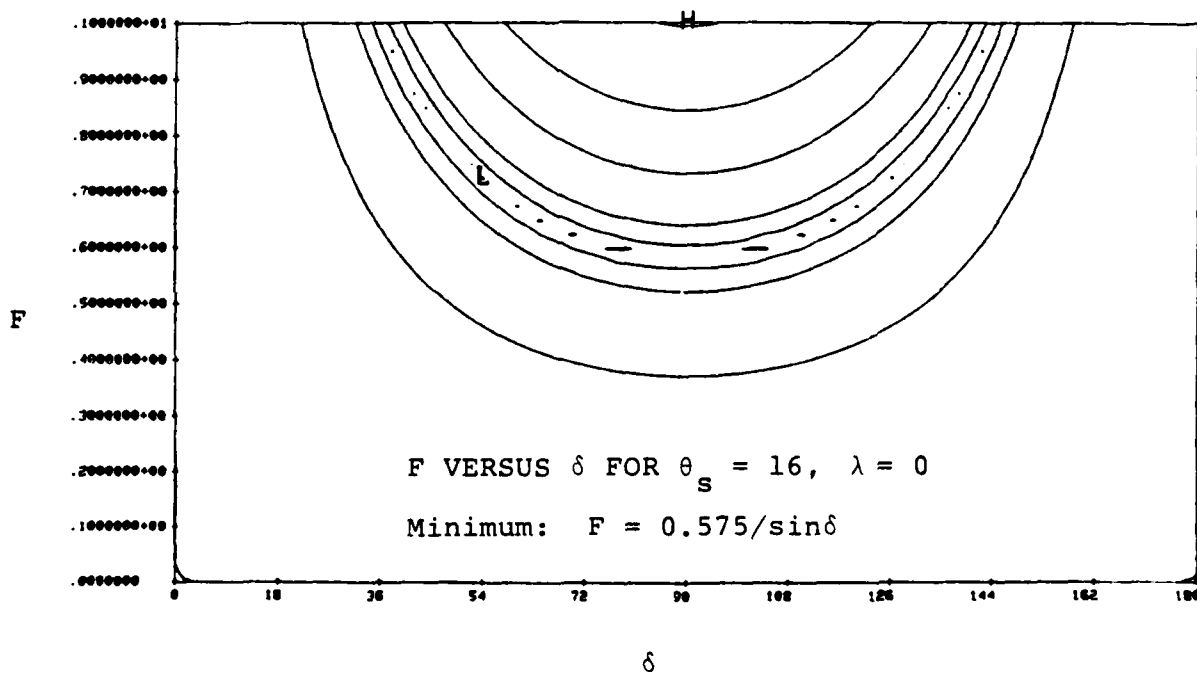
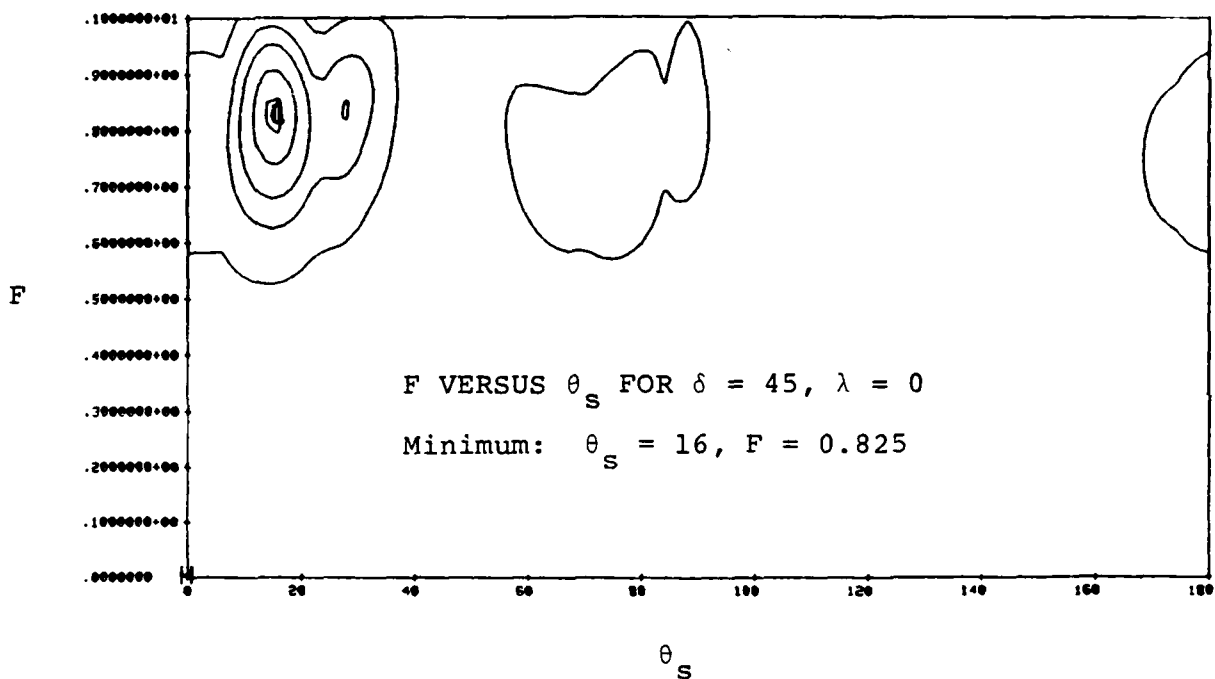


Figure 5.12. Error contours for DIABLO HAWK LQ/LR for several parameter combinations.

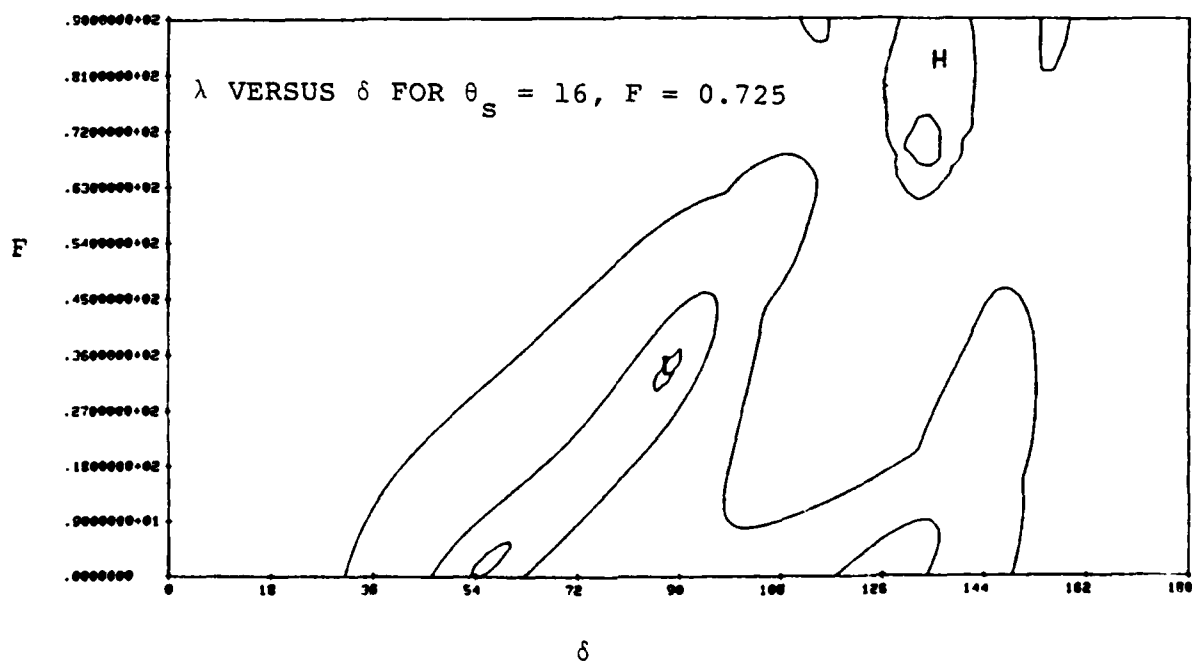
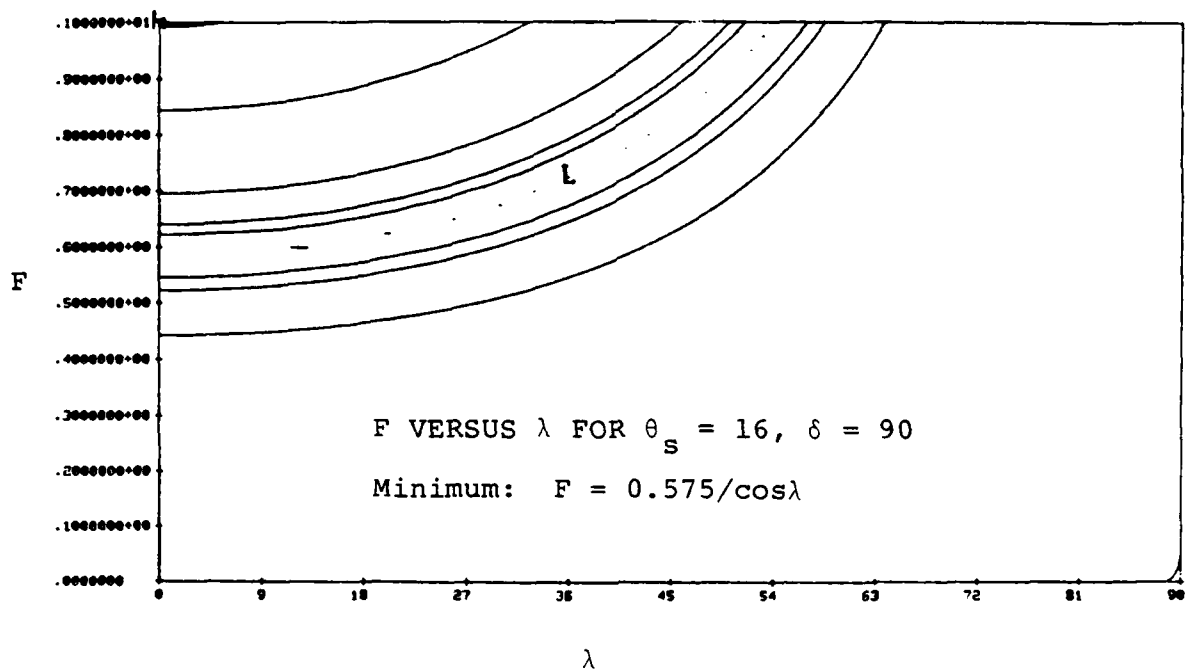


Figure 5.12. Concluded

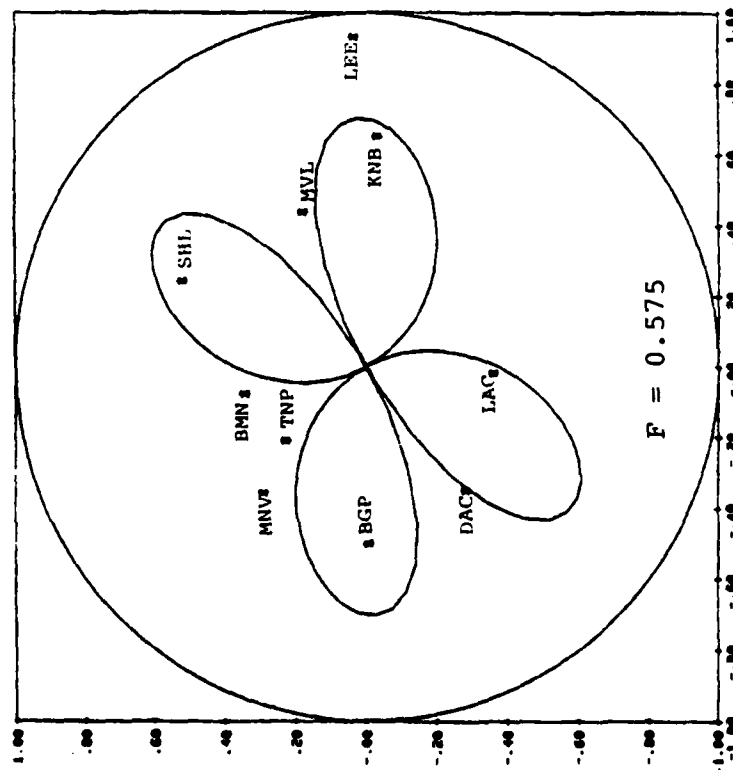
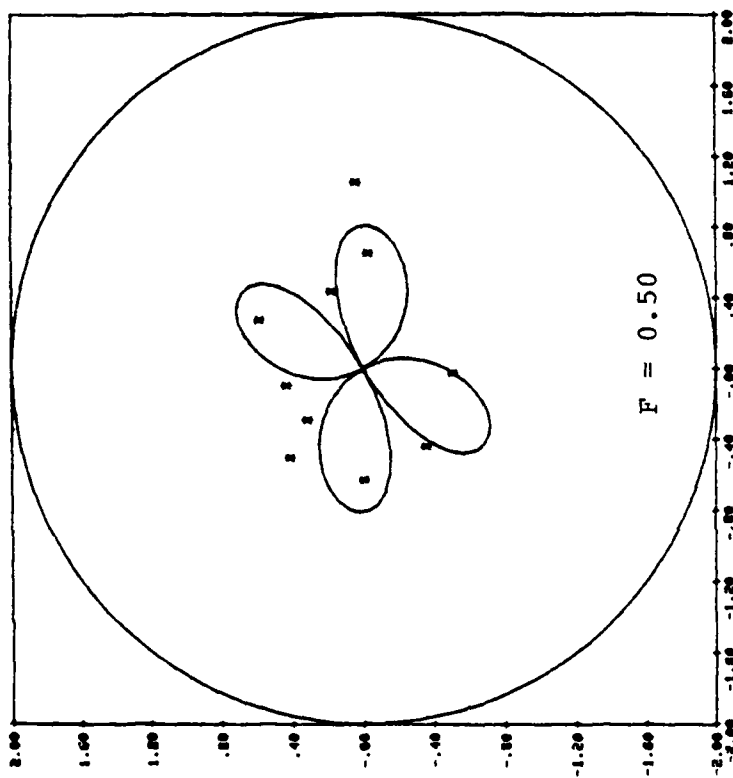


Figure 5.13. Comparison of theoretical LQ/LR radiation patterns ($\delta = 90$, $\lambda = 0$, strike = N16°E) to the observed data with and without path corrections.

Also shown in the figure is the radiation pattern for the minimum error fit to the original data (before applying path corrections). There is little to choose between the two in terms of the fit to the data.

The data fit the theoretical radiation pattern fairly well. The poorest fit is to LEE and MNV which are stations at nearly the same azimuth as two others (KNB and TNP). The LEE to KNB range is only 50 km while the TNP-MNV range is 87 km. Therefore, we cannot attribute this difference to inappropriate corrections for the range. The fault is probably that our path corrections are too simple and do not account for the influence of structure local to the recording station.

We look at the Rayleigh (LR) and Love (LQ) data separately. As our preferred solution, we take the vertical strike-slip, minimum F solution

$$\delta = 90, \lambda = 0, \theta_s = 16, F = 0.575, \quad (5.16)$$

recognizing that there are other parameter combinations that fit as well. Then the Rayleigh and Love wave solutions are given in (5.15). Our data is actually for velocity, so an ω is multiplied times both sides of the equations for $|U_R|$ and $|U_L|$.

In Tables 5.8 and 5.9 we list the LR and LQ amplitudes from Table 5.4 and after path corrections are applied. Recall from Tables 5.2 and 5.3 that the path corrections are for a nominal range of 250 km. We must also correct for the difference between the actual range and 250 km. In Tables 5.8 and 5.9 we first show the data after correcting only for distance with a station independent attenuation factor, $r^{-0.66}$ for LR and $r^{-0.8}$ for LQ. The values are based on the n listed in Table 5.6. They may not be the best exponents to use, but most of the data are rather insensitive to this parameter since the distance variation is not great.

TABLE 5.8

LR DATA

<u>Station</u>	<u>Azimuth</u>	<u>Distance</u>	<u>Original Data</u>	<u>Distance* Corrected $r^{-0.66}$</u>	<u>Path** Corrected</u>
MIGHTY EPIC					
TNP	317	131	55.0	35.9	34.9
DAC	231	161	5.2	3.9	3.8
NEL	143	206	15.0	13.2	12.9
MNV	309	218	16.0	14.6	14.2
LEE	88	252	10.0	10.1	10.0
LAC	183	313	13.0	15.1	14.7
BMN	347	368	9.0	11.6	11.4
DIABLO HAWK					
TNP	317	131	35.0	22.8	22.1
DAC	231	161	4.8	3.6	3.5
BGP	269	178	--	--	--
MNV	309	218	10.0	9.1	8.8
LEE	88	252	6.3	6.3	6.2
KNB	93	302	4.0	4.5	4.5
MVL	68	303	--	--	--
LAC	183	313	8.0	9.3	9.0
SHL	25	317	--	--	--
BMN	347	368	5.2	6.7	6.6

* Corrected to a range of 250 km.

** The distance corrected values from the adjacent column are corrected to the TUC path by the LR factors listed in Table 5.3.

TABLE 5.9

LQ DATA

DATA FROM MARS (6 SECONDS)

<u>Station</u>	<u>Azimuth</u>	<u>Distance</u>	<u>Original Data</u>	<u>Distance* Corrected r-0.8</u>	<u>Path** Dependent n</u>	<u>Path Corrected</u>
MIGHTY EPIC						
TNP	317	131	21.2	12.6	0.76	9.0
DAC	231	161	7.4	5.2	0.75	4.1
NEL	143	206	14.0	12.0	0.75	9.3
MNV	309	218	6.5	5.8	0.76	4.1
LEE	88	252	6.8	6.8	0.66	6.0
LAC	183	313	8.1	9.7	0.93	6.9
BMN	347	368	8.6	11.7	0.9	9.4
DIABLO HAWK						
TNP	317	131	15.0	8.9	0.76	6.4
DAC	231	161	3.0	2.1	0.75	1.7
BGP	269	178	--	--	--	--
MNV	309	218	6.5	5.8	0.76	4.1
LEE	88	252	6.6	6.6	0.66	5.8
KNB	93	302	2.6	3.0	0.66	2.9
MVL	68	303	--	--	--	--
LAC	183	313	4.1	4.9	0.93	3.5
SHL	25	317	--	--	--	--
BMN	347	368	2.3	3.1	0.9	2.5

* Corrected to 250 km.

** The original data are corrected to 250 km with the n listed in the adjacent column. They are then divided by the LQ factors listed in Table 5.3 to obtain values corrected to the TUC path.

For our final path corrected data we include our best knowledge about the propagation of these waves. For LR the distance attenuation is $r^{-0.66}$ and we apply the individual station correction factors listed in Table 5.3. These factors are intended to correct all data to be as if the path were in a TUC-type structure. For LQ the distance attenuation varies from station to station, and the exponents used are listed in the table. These exponents are based on the values listed in Table 5.6.

The equations (5.15) for the Rayleigh and Love wave velocities include the factors

$$4\omega \left(\frac{2\pi}{\omega r} \right)^{1/2} J_R(\omega) , \quad (5.17)$$

$$\omega \left(\frac{1}{2\pi\omega r} \right)^{1/2} J_L(\omega) .$$

We compute these factors for $r = 250$ km and a period of 6 seconds. Values of $J_R(\omega)$ and $J_L(\omega)$ are taken from Table 5.2 for TUC. Then equations (5.15) become

$$|\dot{U}_R| = 0.785 \mu_s \psi_\infty (1 + F \sin 2\theta) , \quad (5.18)$$

$$|\dot{U}_L| = 0.766 \mu_s \psi_\infty (F \cos 2\theta) ,$$

where the constant factor has units of 10^{-23} dyne and we have used (5.10) to relate F and M_0 . Then these are the theoretical amplitudes at 250 km for Rayleigh and Love waves in a TUC-type structure.

In Figure 5.14 we show the LR data (corrected to the TUC structure) plotted with the theoretical solution for three values of ψ_∞ . We have assumed $\mu_s = 40$ kbar. We think the best fit is for $\psi_\infty = 2,200 \text{ m}^3$. The value at TNP is clearly an anomaly. To improve the fit to TNP, larger values of ψ_∞ are required, but the other data are not fit as well.

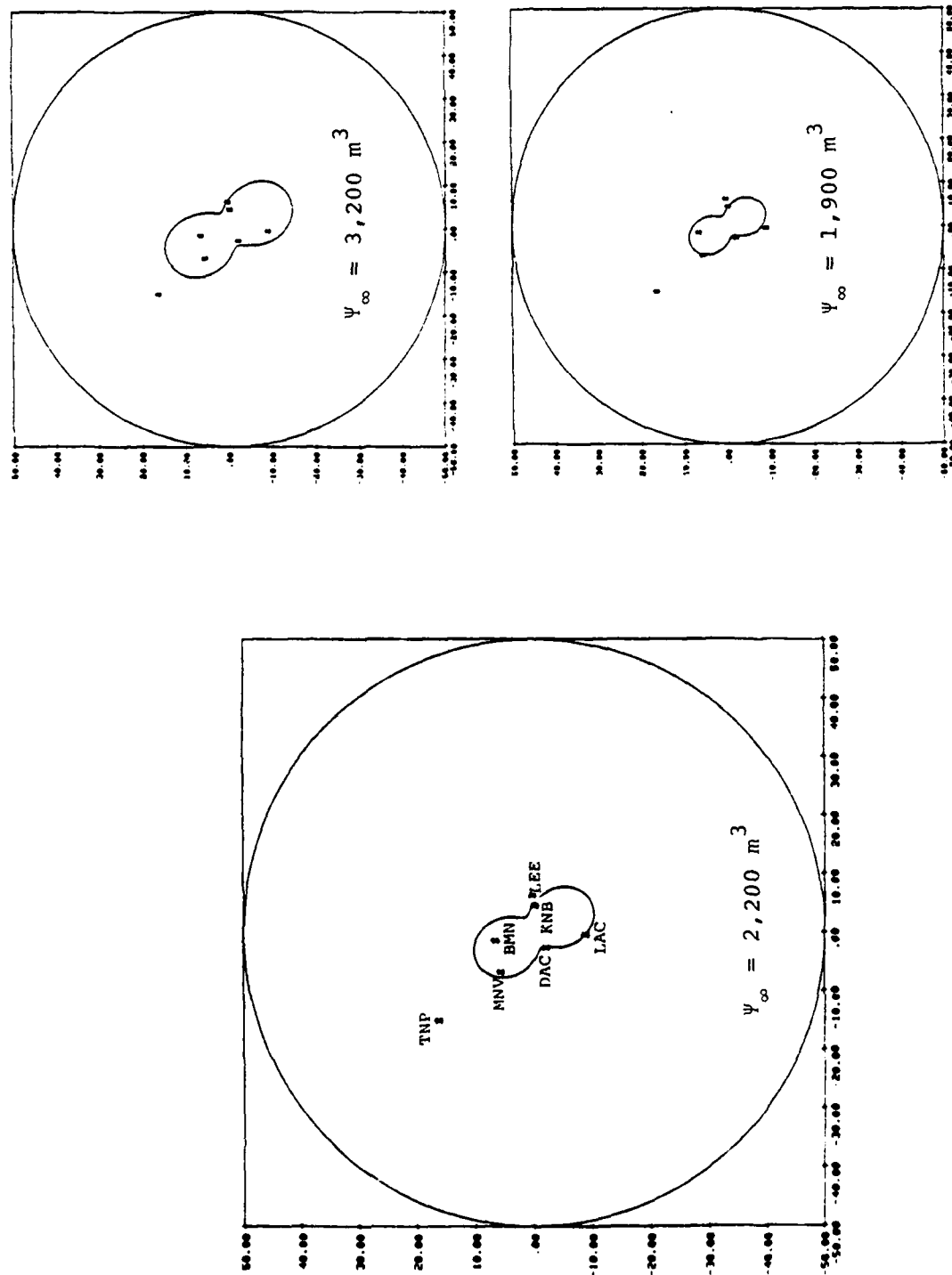


Figure 5.14. Theoretical Rayleigh wave radiation patterns are compared to the DIABLO HAWK observations normalized to a range of 250 km. The theoretical solution has $\delta = 90$, $\lambda = 0$, strike = N16°E, $F = 0.575$, $\mu_s = 40$ kbar and three values of ψ_∞ .

In Figure 5.15 we show the LQ data plotted with the theoretical solution for three values of the moment, M_0 . These moment values correspond to the Ψ_∞ values used for the Rayleigh wave in Figure 5.14. The relationship is

$$M_0 = 8\pi \mu_s \Psi_\infty F \quad (5.19)$$

where F is 0.575. Considering both the LR and LQ data, our preferred value, which goes with $\Psi_\infty = 2,200$, is $M_0 = 1.3 \times 10^{21}$ dyne-cm. The fit is reasonably good. As with LR, the TNP LQ amplitude is anomalously large. The other poorly fit data point is LEE. The large LQ amplitude at this station leads to the poor fit of LQ/LR for LEE in Figure 5.13.

5.5.2 MIGHTY EPIC Double-Couple

We now turn our attention to the MIGHTY EPIC data. In Figure 5.16 we show the error contours for MIGHTY EPIC for the LQ/LR path corrected data from Table 5.7. That is, these are the contours analogous to those on top of Figure 5.11 for DIABLO HAWK. We see that the minimum is quite clearly defined to be for a strike of N152°E (or N28°W) and an F of 0.65. All the trade-offs between F and the assumed values of δ , λ are, of course, the same as they were for DIABLO HAWK.

In Figure 5.17 we plot the theoretical radiation pattern for the best fitting solution ($\theta_s = 152^\circ$, $F = 0.65$) with the path-corrected data. We see that the fit is reasonably good, but is not very well constrained with only seven data points.

We now ask ourselves, how well are the data fit if we assume that the double-couple orientation is the same for both events? In Figure 5.17 we show the DIABLO HAWK LQ/LR solution ($\delta = 90$, $\lambda = 0$, $\theta_s = 16$) with three values of F and compare to the MIGHTY EPIC LQ/LR observations. We see that it is the NEL, LEE and BMN data points that cause the error to be much larger for $\theta_s = 16^\circ$ than for $\theta_s = 152^\circ$.

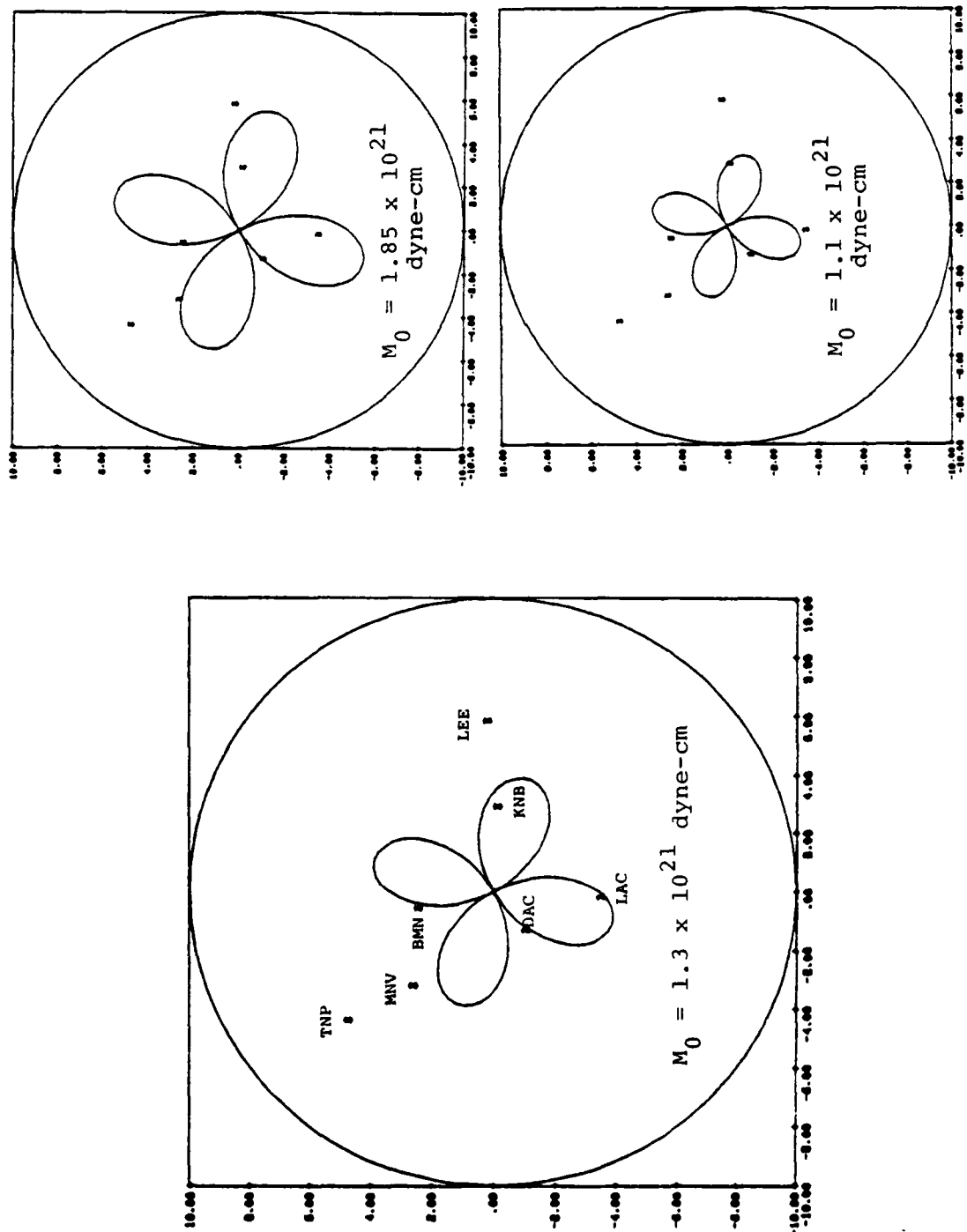


Figure 5.15. Theoretical Love wave radiation patterns are compared to DIABLO HAWK observations normalized to 250 km. The theoretical solutions have $\delta = 90^\circ$, $\lambda = 0$, strike = N16°E, $F = 0.575$, $\mu_s = 40$ kbar and three values of the moment, M_0 .

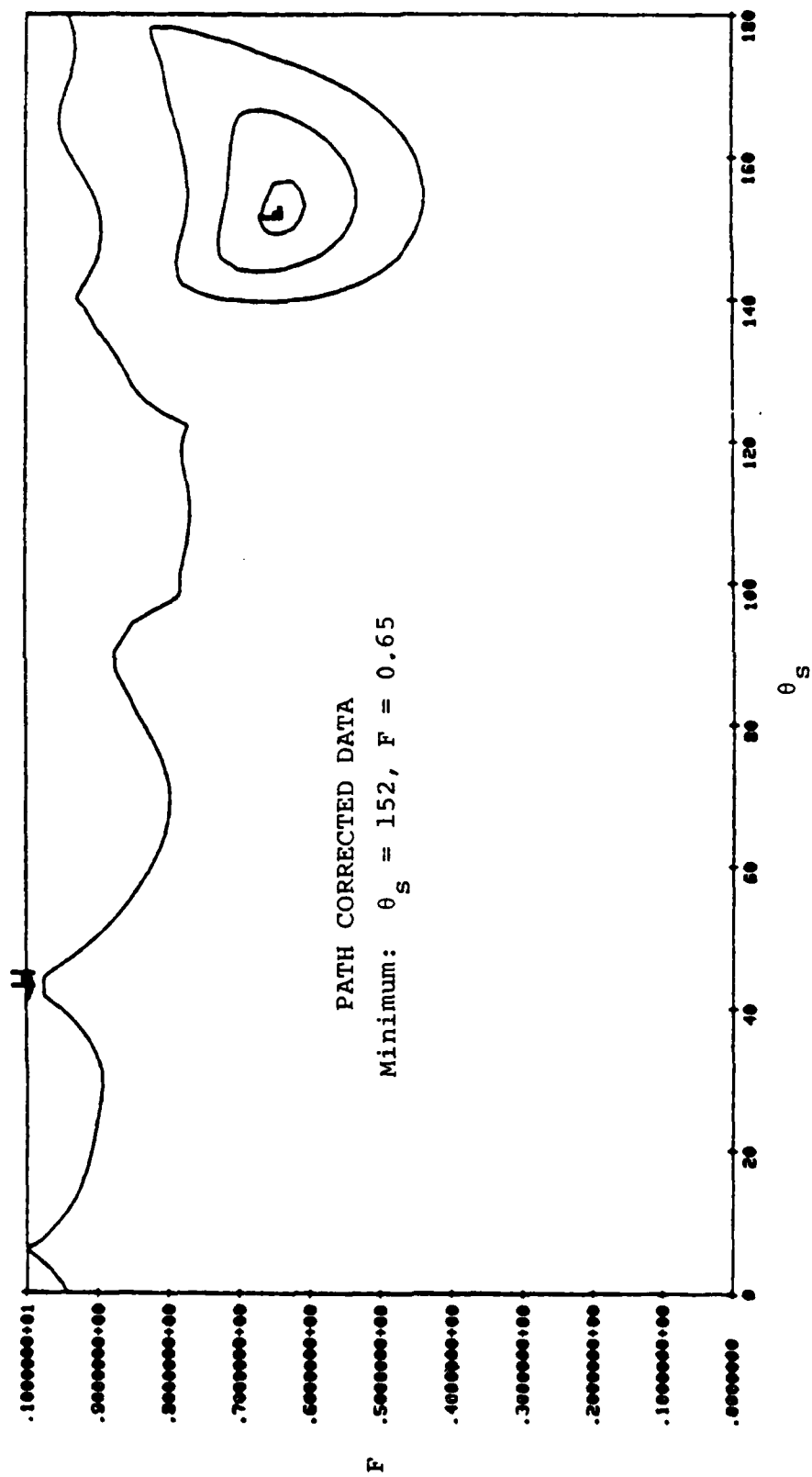


Figure 5.16. Error contours for LQ/LR, F versus θ_s for MIGHTY EPIC assuming $\delta = 90$
 $\lambda = 0$.

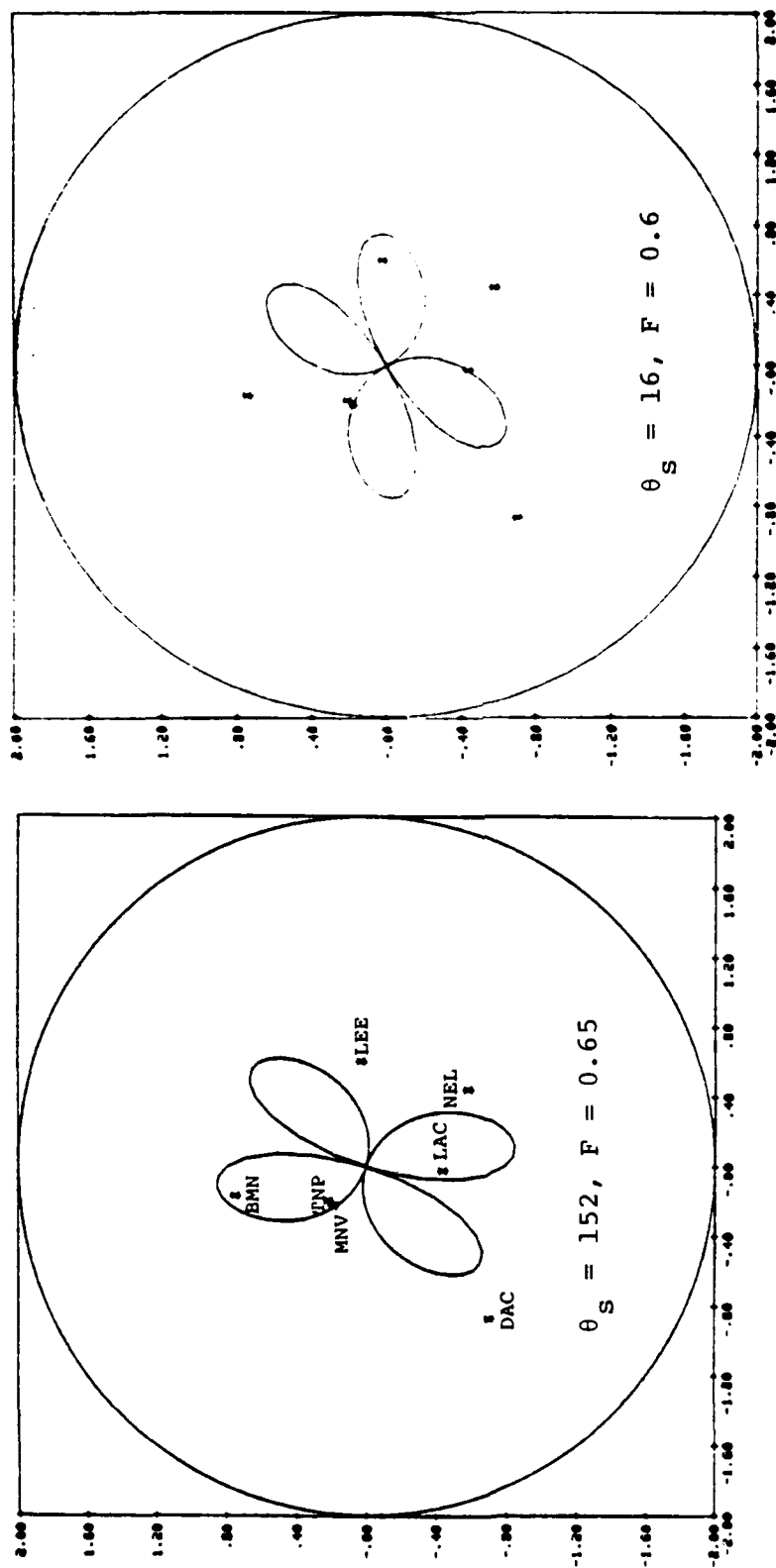


Figure 5.17. MIGHTY EPIC LQ/LR data compared to several theoretical radiation patterns. In each case we assume $\delta = 90$, $\lambda = 0$ and plot the path corrected observations from Table 5.7.

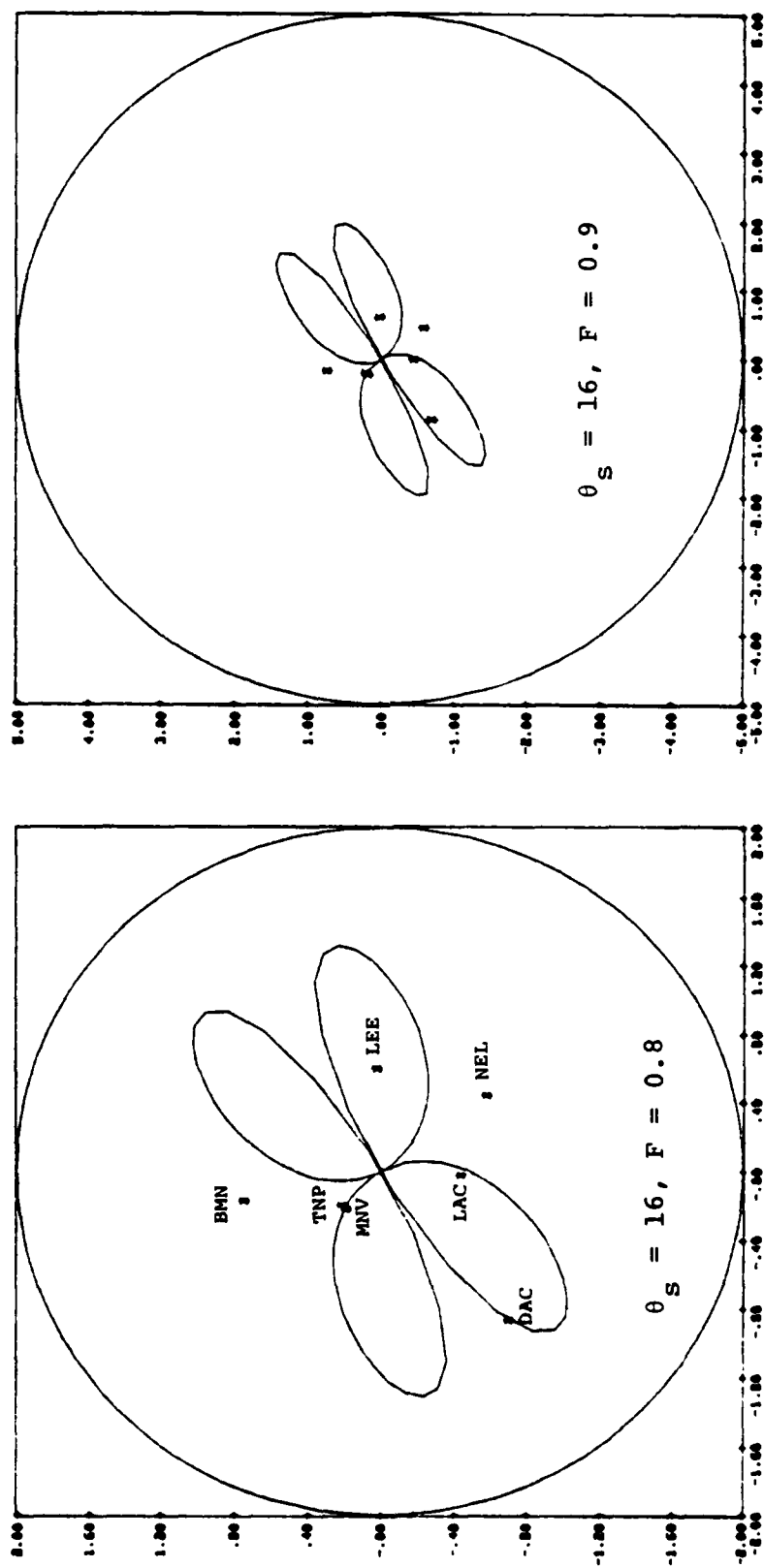


Figure 5.17. Concluded

In Figure 5.18 we plot the LR data with the theoretical solutions for $\theta_s = 152^\circ$, $F = 0.65$ and three values of Ψ_∞ . Compared to the analogous plots for DIABLO HAWK, Figure 5.14, we see that the MIGHTY EPIC LR data are not fit nearly as well. The solution with $\Psi_\infty = 3,200 \text{ m}^3$ is perhaps the best. This Ψ_∞ is 1.4 times larger than our best fitting Ψ_∞ for the DIABLO HAWK source which leads to some problems in interpretation as we have mentioned elsewhere in this report.

The LR data are clearly fit better with a solution near the DIABLO HAWK strike. In Figure 5.19 we show the $F = 0.65$ solution at a strike of $N16^\circ E$. These data, particularly with $\Psi_\infty = 3,200 \text{ m}^3$ are fit just about as well as the DIABLO HAWK data with $F = 0.575$, $\Psi_\infty = 2,200$ and the same strike.

Now, let us examine the LQ data. In Figure 5.20 we plot the data and theoretical radiation patterns for our minimum error solution, strike = $N152^\circ E$ and $F = 0.65$. The solutions are given for two values of M_0 which correspond (via Eq. (5.19)) to the $\Psi_\infty = 2,500$ and $3,200 \text{ m}^3$ cases for which the LR patterns were shown in Figure 5.18. These LQ data are fit poorly. If we had to choose, we would again prefer the larger value of Ψ_∞ .

What if the strike azimuth is $N16^\circ E$ as it was for DIABLO HAWK? The LQ/LR patterns shown in Figure 5.17 for this case suggested that the best F is about 0.8. In Figure 5.21 we show the LR and LQ data together with what we think are near the best fitting theoretical solutions to these data with strike = $N16^\circ E$. These solutions have $\Psi_\infty = 3,200 \text{ m}^3$ and $F = 0.8$. This gives a moment, $M_0 = 2.6 \times 10^{21} \text{ dyne-cm}$.

In summary, our conclusions about MIGHTY EPIC are as follows. Assuming $\delta = 90$, $\lambda = 0$, the least square error contours clearly indicate that the best fit to the LQ/LR data has the parameters

Strike = $N152^\circ E$, $F = 0.65$.

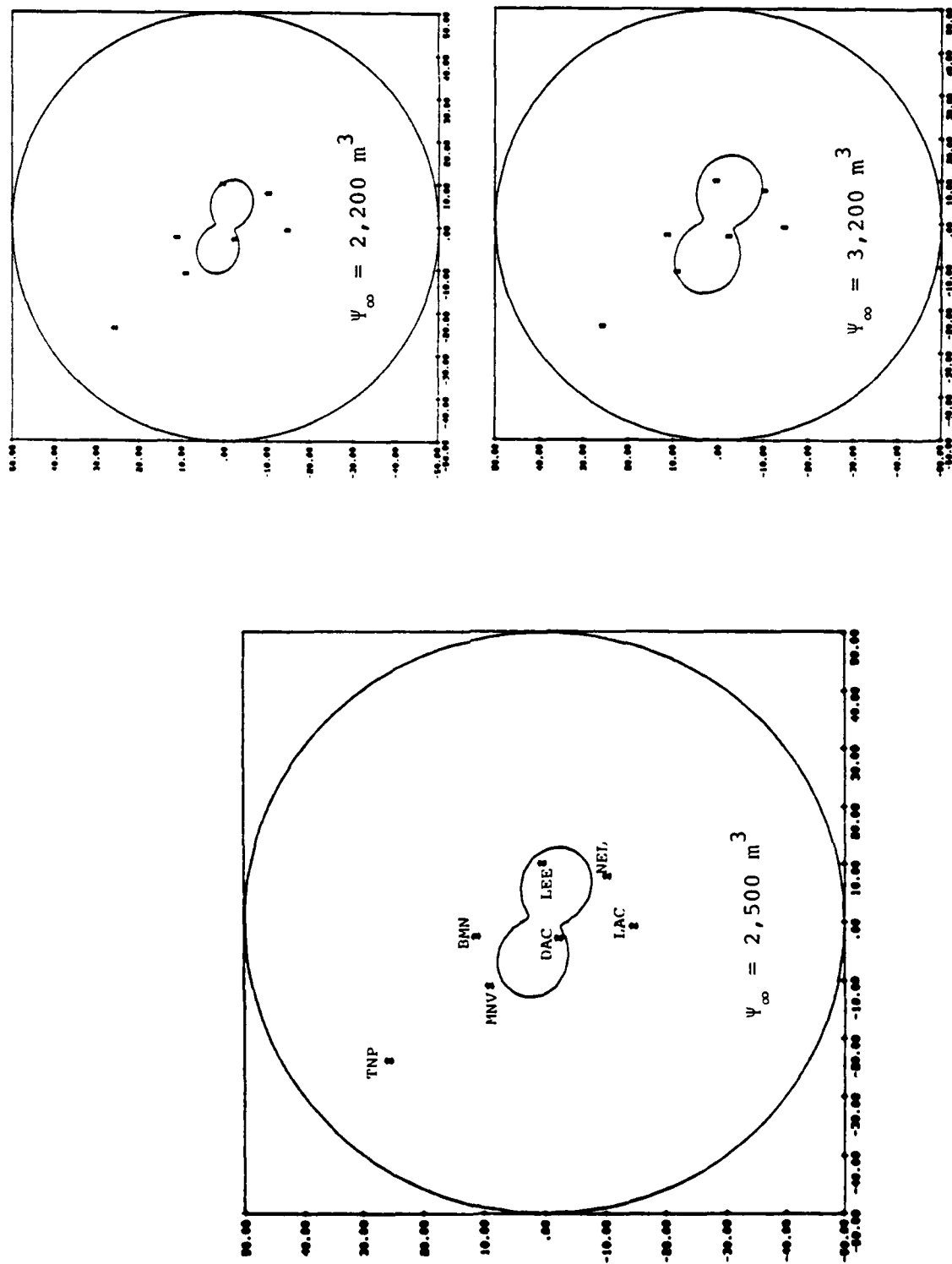


Figure 5.18. MIGHTY EPIC LR data compared to theoretical radiation patterns for $\theta_s = 152$, $\delta = 90$, $\lambda = 0$, $F = 0.65$ and three values of ψ_{∞} .

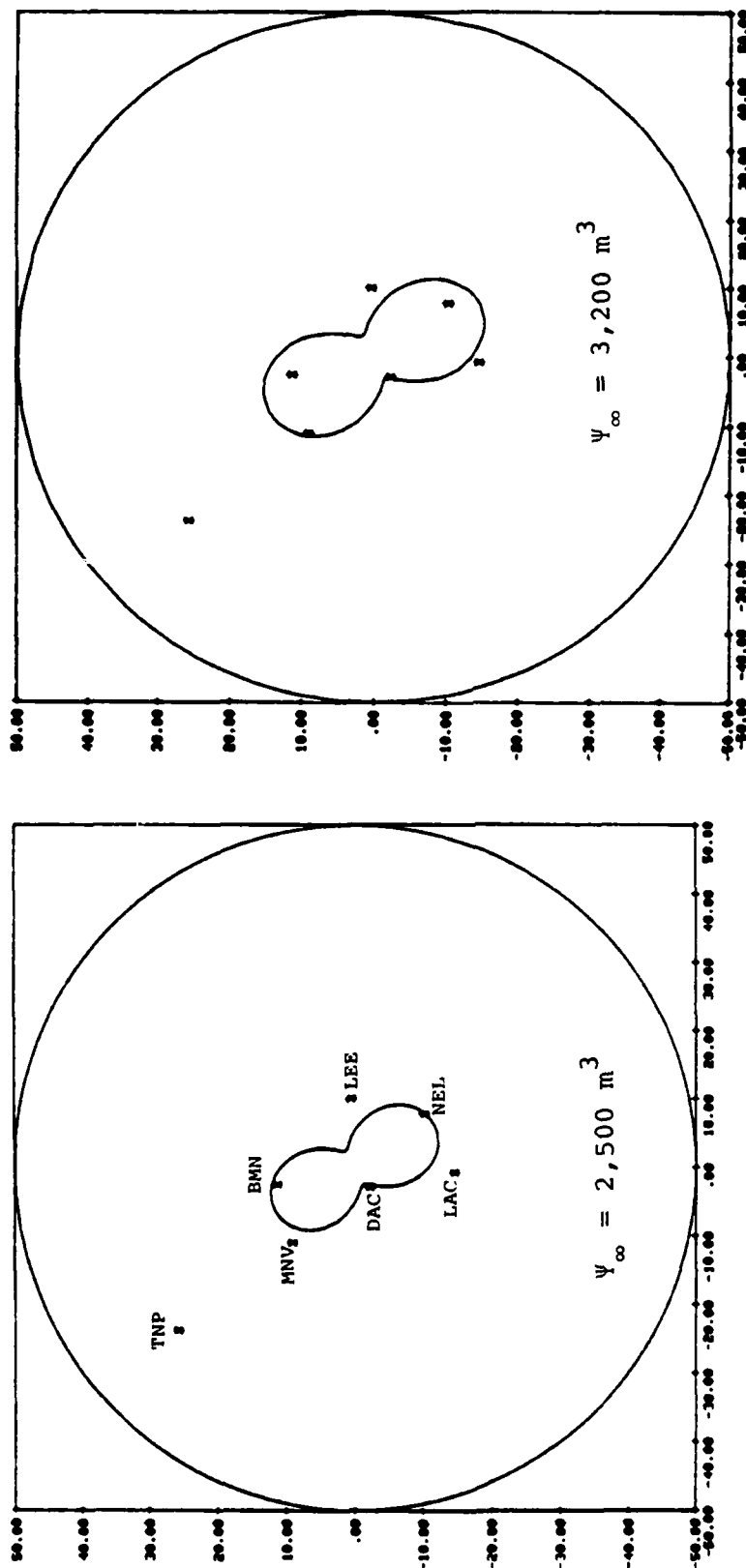


Figure 5.19. MIGHTY EPIC LR data compared to theoretical radiation patterns for the DIABLO HAWK double-couple orientation, $\theta_s = 16$, $\delta = 90$, $\lambda = 0$. The comparison is for $F = 0.65$ and two values of ψ_{∞} .

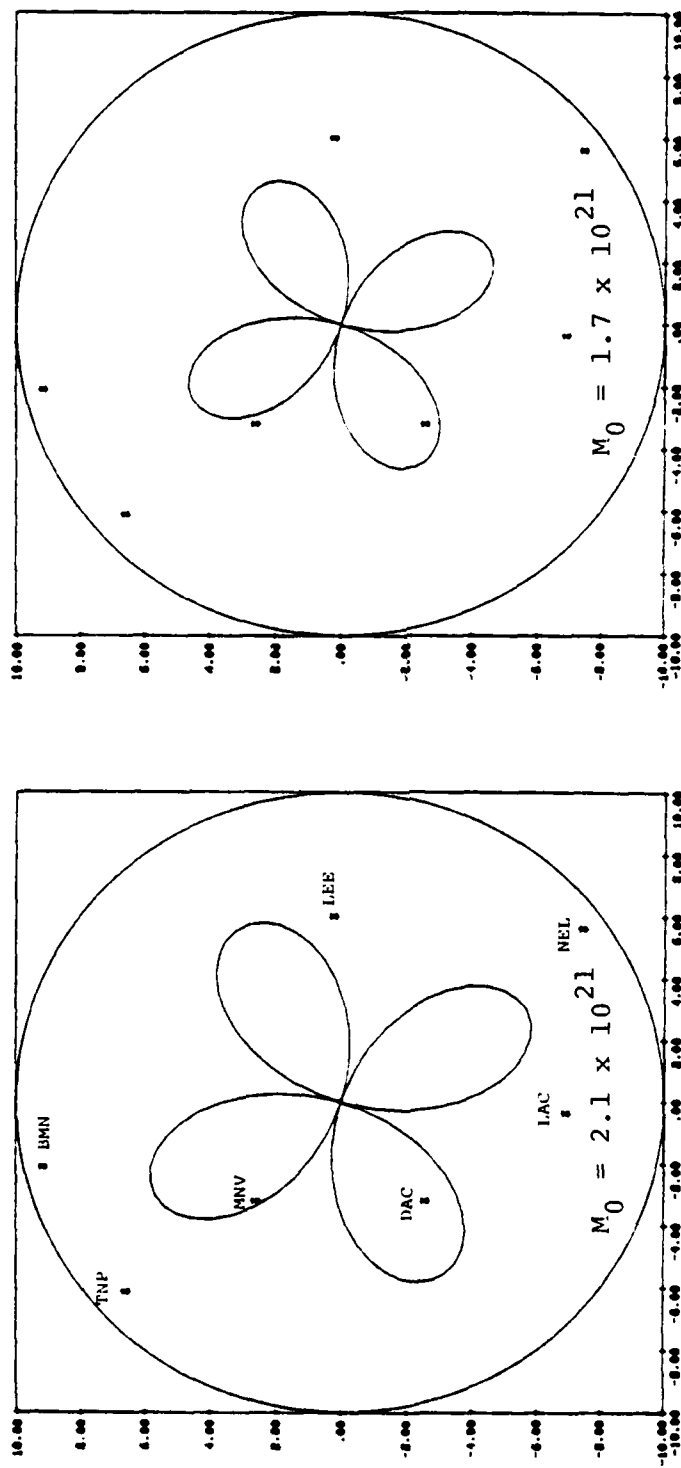


Figure 5.20. MIGHTY EPIC LQ data compared to theoretical radiation patterns for $\theta = 152$, $\delta = 90$, $\lambda = 0$, $F = 0.65$ and two values of the moment in dyne-cm.

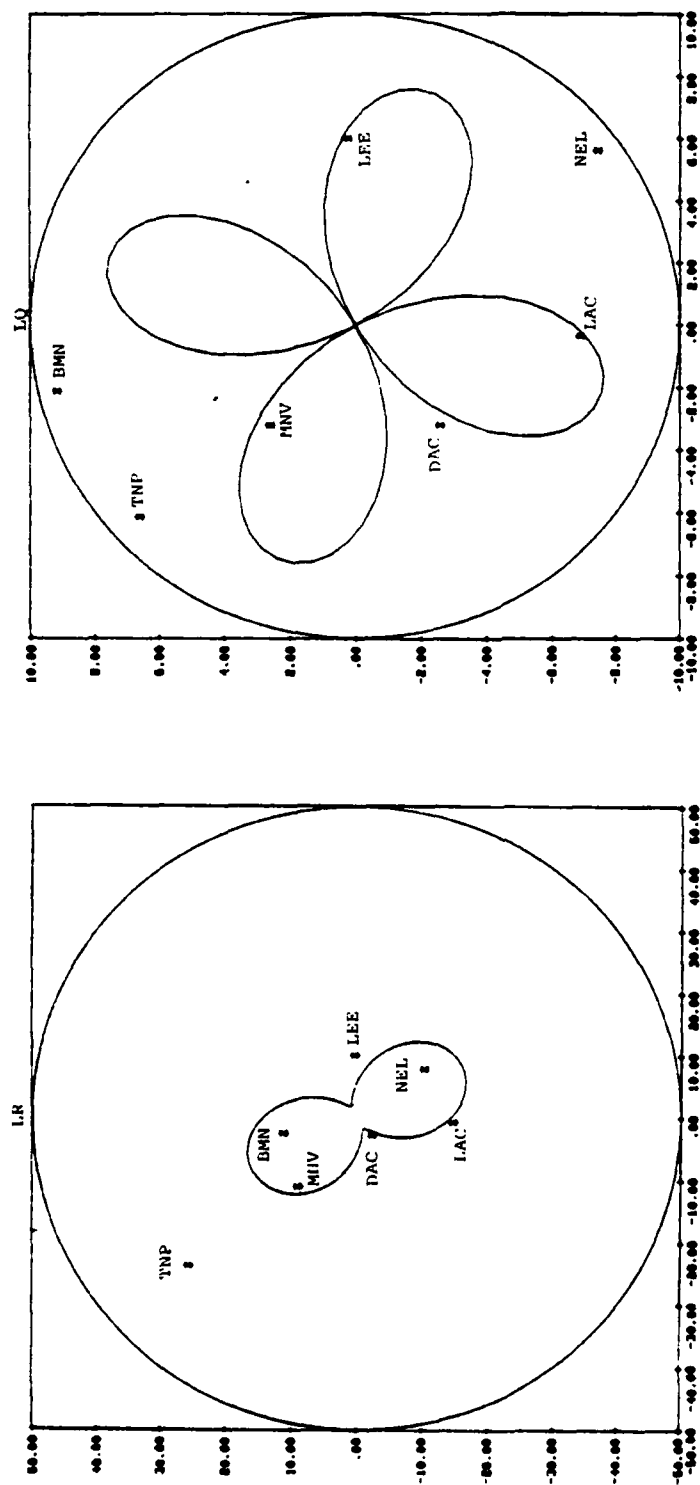


Figure 5.21. MIGHTY EPIC LR and LQ data compared to theoretical radiation patterns for $\theta_s = 16$, $\delta = 90$, $\lambda = 0$, $\psi_\infty = 3,200 \text{ m}^3$, $F = 0.8$, $M_0 = 2.6 \times 10^{21} \text{ dyne-cm}$.

However, since there are only seven points, the solution is not well constrained. Further, all seven points are not fit well by this solution, particularly DAC and LEE.

If we use this solution we find that the individual LR and LQ data are fit rather poorly. Our best solution seems to be the following:

Strike = N152°E or N28°W

F = 0.65

Ψ_{∞} = 3,200 m³

M_0 = 2.1×10^{21} dyne-cm

A solution for the explosion size (Ψ_{∞}) being nearly the same for both MIGHTY EPIC and DIABLO HAWK may be preferable. However, the smaller values of Ψ_{∞} (we show plots with Ψ_{∞} = 2,500) do not fit the LR and LQ data nearly as well.

If we assume the strike is N16°E, the same as for DIABLO HAWK, we actually get a better fit to the LR and LQ data. The LQ/LR data are fit as well except NEL and LAC. Our best fitting solution with this orientation is

Strike = N16°E

F = 0.8

Ψ_{∞} = 3,200 m³

M_0 = 2.6×10^{21} dyne-cm.

5.6 SUMMARY

We have assumed that the seismic source for DIABLO HAWK and MIGHTY EPIC is composed of a spherically symmetric explosion plus a double-couple. We then attempt to find the combination of these two source components that best fits the data.

The data we choose to fit are the fundamental mode Love and Rayleigh waves. Our most reliable estimate of the amplitude of these waves is at a period of six seconds. Using this long period, we ignore any source time difference between the explosion and double-couple components of the source.

The travel paths to the eleven seismic stations in our data base encounter different crustal structures. Different structures lead to different excitation of the fundamental mode Love and Rayleigh waves. Therefore, we classify the stations into broad groups and apply corrections computed with theoretical models. The station classification is based on the observed group velocity dispersion.

After classifying the stations, correcting for path differences and correcting all data to a common range, we obtain our final estimates for the Rayleigh (LR), Love (LQ) and LQ/LR amplitudes. These data are then fit with our explosion plus double-couple composite source. The most reliable data should be the LQ/LR because it is least sensitive to individual path characteristics.

The largest data set is for DIABLO HAWK and we examine the solution with some care for this case. If we assume that the double-couple source is vertical strike-slip, we find the best fitting solution to be

$$\begin{aligned} \text{Strike} &= \text{N}16^{\circ}\text{E} \\ \delta, \lambda &= 90, 0 \\ F &= 0.575 \\ \psi_{\infty} &= 2,200 \text{ m}^3 \\ M_0 &= 1.3 \times 10^{21} \text{ dyne-cm.} \end{aligned}$$

There is actually an entire family of solutions, depending on our assumptions about the dip (δ) and slip (λ) of the fault plane. For other than vertical strike slip ($\delta, \lambda \neq 90, 0$), the solutions have larger F and M_0 while the Ψ_∞ is unchanged.

There are, of course, other trade-offs in the solution. For a vertical strike-slip we could keep $F = 0.575$ and fit the LR and LQ data, perhaps as well, with larger values of Ψ_∞ and M_0 . We show the solution for $\Psi_\infty = 3,200 \text{ m}^3$ and $M_0 = 1.85 \times 10^{21} \text{ dyne-cm}$. The fit to LQ is better than with the smaller Ψ_∞ and M_0 , while the fit to LR is poorer.

Our solution for MIGHTY EPIC is not nearly as well constrained. A key aspect of the MIGHTY EPIC data is that the long period amplitudes are larger than those for DIABLO HAWK at nearly all common stations. We saw this in a spectral analysis in Section IV and we see it again here in our study of Rayleigh and Love wave amplitudes. There are in essence two ways to explain this amplitude difference. First, the MIGHTY EPIC double-couple orientation could coincidentally be oriented to enhance the radiation of both Rayleigh and Love waves at the sparse network of common stations. This seems unlikely. Second, the total long period source level, explosion and double-couple, could be larger for MIGHTY EPIC than for DIABLO HAWK. We consider this to be more likely.

The LQ/LR for MIGHTY EPIC suggest a double-couple fault orientation that is $N152^\circ E$ or rotated 44° with respect to that for DIABLO HAWK. We think this is poorly constrained and suggest that the evidence, on balance, indicates that the double-couple has nearly the same orientation for both events. With this orientation, our estimate for the best MIGHTY EPIC solution is

Strike = N16°E

δ, λ = 90, 0

F = 0.8

Ψ_{∞} = 3,200 m³

M_0 = 2.6×10^{21} dyne-cm.

VI. BOUNDS FOR THE BLOCK MOTIONS

We have estimated the moment of the double-couple associated with DIABLO HAWK and MIGHTY EPIC. From this moment estimate we can proceed to bound the size of the block motions that excited the observed waves. These may be block motions that are passive and not associated with the release of tectonic stress or they may be motions associated with a release of stored strain energy.

There are five basic mechanisms for exciting shear waves, and therefore Love and Rayleigh wave radiation patterns, by explosions. These are:

1. The outgoing P waves encounter boundaries that refract a portion of the energy as S waves.
2. The expansion of the explosion shock wave is not spherically symmetric, but is asymmetric due to anisotropic properties of the surrounding medium. For example, an explosion in a cylindrical cavity generates a source that includes a double-couple in addition to the spherically symmetric part.
3. The explosion shock waves cause differential movement along faults, joints and other planes of weakness. This "driven" block motion partitions the outgoing wave field into spherically symmetric and double-couple components.
4. The medium includes stored tectonic stresses. The explosion creates a zone of markedly reduced shear strength (the cavity and surrounding region of crushed and cracked material) which releases the local tectonic stresses, generating seismic waves with a double-couple radiation pattern. The volume of this cavity is a subject for speculation

and, therefore, debate. Some (e.g., R. Duff of S³) believe that the weakened zone must be quite small. Others (e.g., C. Archambeau, University of Colorado) would argue that the zone of reduced shear strength might be nearly as large as the elastic radius. We are unaware of experiments or calculations that conclusively resolve this issue.

5. The medium includes stored tectonic stresses. The explosion triggers earthquake-like motion along nearby fault planes, releasing some of the stress.

It is certain that each of these mechanisms occurs to some degree. It is generally believed that the first is relatively minor. The more convincing evidence for this conclusion results from comparative studies of the radiation from explosions and the associated cavity collapse events (e.g., Brune and Pomeroy, 1963). The Love/Rayleigh ratio for the collapse events is very much smaller than for the explosion.

The second two mechanisms involve "passive" block motions and no energy is added by the wave field partitioning associated with these mechanisms. On the other hand, the last two listed mechanisms are associated with the release of stored tectonic strains which is an independent source of seismic energy. Toksöz, et al. (1965) show that the ratio of the energy from the tectonic strain release double-couple to that from the explosion is approximately $4F^2/3$. The F factors for MIGHTY EPIC and DIABLO HAWK are pretty clearly between 0.5 and 0.8. A tectonic release source accounting for F values this high would have energy that is 0.33-0.85 times that from the explosion itself, at least at the period (6 seconds) for which our solution was deduced.

In summary, we believe the first mechanism is small and it will be ignored. The other four all probably contribute to the double-couple radiation pattern. The second two

mechanisms are for "passive" or non-energetic double-couple generation. The last two involve the release of tectonic strain energy. Note that to be a substantial source of horizontally polarized (SH) shear waves and Love waves, the asymmetries, planes of weakness or tectonic strains must be oriented so the induced differential motions are not too different from the vertical strike-slip orientation. Another way to look at this is to recall from Section 5.5 that our estimate for F , and therefore M_0 , is a lower bound estimate since we assumed a vertical strike-slip orientation.

For three of the last four possible mechanisms there is a theoretical framework within which we can estimate some bounds for the block motions consistent with our estimates for the double-couple moment. The exception is the second (source asymmetry) in the list. In the subsequent discussion, we will ignore it.

Archambeau (1972) has derived a model for the seismic waves due to the sudden introduction of a spherical volume of weakness in a shear prestress field. This is the fourth mechanism on the list. We will use the Archambeau theory to examine this mechanism more closely. We point out that this mechanism predicts no block motion. The "differential" motions are from one side of the spherical volume of weakness to the other.

The moment, M_0 , for the double-couple resulting from the spherical volume source is (Minster and Suteau, 1977)

$$M_0 = \frac{60}{23} \pi \Delta\sigma R_0^3, \quad (6.1)$$

where $\Delta\sigma$ is the stress drop and R_0 is the radius of the spherical volume within which the stress is released.

Our best estimates for the moment were $M_0 = 1.3 \times 10^{21}$ dyne-cm for DIABLO HAWK and $M_0 = 2.6 \times 10^{21}$ dyne-cm for MIGHTY EPIC. Values of parameters satisfying (6.1) for these moments are listed below.

M_0 (dyne - cm)	$\Delta\sigma$ (bars)	R_0 (m)
1.3×10^{21}	20	199
(DIABLO HAWK)	40	158
	80	126
2.6×10^{21}	40	199
(MIGHTY EPIC)	80	158

These values are not entirely unreasonable but the R_0 do seem rather large. The solution is very sensitive to R_0 , a parameter that is very difficult to estimate. A reasonable guess for R_0 might be about 50 meters. Then, if 40 bars of stress were released in a volume this size, we would get $M_0 = 4.1 \times 10^{19}$ dyne-cm, which is only 3 percent of the M_0 estimated for DIABLO HAWK. Our best guess is that release by this mechanism is too small to account for most of the observed seismic waves.

Now consider the motion on pre-existing faults or planes of weakness, the mechanisms 3 and 5 on the list. In either case, the equation for moment is

$$M_0 = \mu SD, \quad (6.2)$$

where μ is the shear modulus, S is the area of the fault plane and D is the average displacement on this plane. Let us assume $\mu = 40$ kbar, as we have throughout this analysis. Then, if we assume that D and S are entirely independent, values consistent with our moment estimates are listed below:

M_0 (dyne-cm)	S (km ²)	D (cm)
1.3×10^{21}	0.325	10
(DIABLO HAWK)	0.130	25
	0.065	50
	0.043	75
	0.033	100
2.6×10^{21}	0.650	10
(MIGHTY EPIC)	0.260	25
	0.130	50
	0.087	75
	0.065	100

This table shows that large average displacements (≥ 50 cm) are consistent with the inferred moment only if they occur on rather small fault areas. For example, for DIABLO HAWK $D = 75$ cm gives $S = 0.043 \text{ km}^2$, which could be a 100 m by 433 m rectangular fault plane.

A problem with this analysis is that D and S are assumed to be entirely decoupled when, of course, they really are not. If the mechanism is tectonic stress release, it takes large stress drops to get large differential displacements on a small fault plane. On the other hand, if the fault motion is driven, we would expect large stress concentrations if small fault areas were offset by large amounts. One way to couple D and S is to use a solution from crack theory. For circular faults an analytical solution relating stress drop, fault dimension and fault displacement was given by Eshelby (1957). This is

$$\Delta\sigma = \frac{7\pi}{16} \mu \frac{D}{a}, \quad (6.3)$$

where a is the radius of the circular fault plane. Of course, we have $S = \pi a^2$. Combining (6.2) and (6.3) we have

$$M_0 = \frac{16}{7} \Delta\sigma a^3. \quad (6.4)$$

Combinations of parameters satisfying this equation are given on the next page. Again, we assume $\mu = 40$ kbar. Then a strain drop of 10^{-3} corresponds to $\Delta\sigma = 40$ bars. We do not expect the strain drop to be too much larger than this.

M_0 (dyne-cm)	$\Delta\sigma$ (bars)	a (m)	S (km ²)	D (cm)
1.3×10^{21} (DIABLO HAWK)	20	305	0.29	11
	40	242	0.18	18
	80	192	0.12	28
	120	168	0.089	37
2.6×10^{21} (MIGHTY EPIC)	20	385	0.46	14
	40	305	0.29	22
	80	242	0.18	35
	120	212	0.14	46

From this table we see that large fault displacements imply large stress drops (or large residual stress concentrations). Rather small average dislocations (10-50 cm) on a total fault plane area of 0.1-0.5 km² can account for the observed double-couple.

The values in these tables can also be interpreted in terms of several smaller segments that sum to give the total moment. For example, assume the stress drop is the same on all segments, then it can easily be shown that the total fault area (πa^2) can include many segments of radius a_i with

$$a^3 = \sum_{i=1}^N a_i^3. \quad (6.5)$$

For each segment we have

$$D_i = \frac{16 a_i}{7\pi\mu} \Delta\sigma. \quad (6.6)$$

As an example, assume that the DIABLO HAWK total faulting includes five segments of equal size and with stress drop $\Delta\sigma = 40$ bars on each. Then each of the five segments has $a_i = 142$ m and $D_i = 10$ cm.

In summary then we conclude the following:

- Large average dislocations (> 50 cm) occur only if there are segments with quite large stress drop (> 120 bars). There can be regions where the dislocations are higher, but these must be rather small in extent.
- The inferred moment for MIGHTY EPIC is twice as large as that for DIABLO HAWK. This means that the product of fault area and dislocation differ by a factor of two. The inferred block motions are therefore not very different.
- The bounds for the fault area and displacement apply as well to driven fault motions and to those due to tectonic strain release. The actual source probably included some of each.
- These bounds are based on elastic theory. Fault motion that is decoupled from the elastic continuum representing the earth cannot be bounded with these methods.
- Fault motions that occur in the region of highly nonlinear material behavior cannot be bounded. For these two events the elastic radius is about 160 m (N. Rimer, private communication), though the material behavior is not too nonlinear over much of this radius.

REFERENCES

- Archambeau, C. B. (1972), "The Theory of Stress Radiation from Explosions in Prestressed Media," *Geophys. J. R. Astr. Soc.*, 29, pp. 329-366.
- Bache, T. C. and D. G. Lambert (1976), "The Seismological Evidence for the Triggering of Block Motion by Large Explosions," *Systems, Science and Software Report*, DNA 4323T.
- Bache, T. C. and D. G. Lambert (1978), "A Review of Regional Seismic Data and Its Utility for Estimating the Double-Couple Associated with Area 12 Explosions," *Systems, Science and Software Topical Report*, SSS-R-78-3598, April.
- Bache, T. C., W. L. Rodi and D. G. Harkrider (1978), "Crustal Structures Inferred from Rayleigh-Wave Signatures of NTS Explosions," *BSSA*, 68, pp. 1399-1413.
- Bendat, J. S. and A. G. Piersol (1971), *Random Data: Analysis and Measurement Procedures*, Wiley, New York.
- Brune, J. N. and P. W. Pomeroy (1963), "Surface Wave Radiation Patterns for Underground Nuclear Explosions and Small-Magnitude Earthquakes," *J. Geophys. Res.*, 68, pp. 5005-5028.
- Denny, M. D. and R. C. Y. Chin (1976), "Gaussian Filters for Determining Group Velocities," *Geophys. J. R. Astr. Soc.*, 45, pp. 495-525.
- Denny, M. D. (1977), "The Installation of Horizontal Seismometers in the LLL Seismic Net and their Calibration," Lawrence Livermore Laboratory, Report UCRL 52216.
- Dziewonski, A., S. Bloch and M. Landisman (1969), "A Technique for the Analysis of Transient Seismic Signals," *BSSA*, 59, pp. 427-444.
- Eshelby, J. D. (1957), "The Determination of the Elastic Field of an Ellipsoidal Inclusion and Related Problems," *Proc. of Roy. Soc. of London*, 241, pp. 376-396.
- Harkrider, D. G. (1964), "Surface Waves in Multilayered Elastic Media, 1. Rayleigh and Love Waves from Buried Sources in a Multilayered Elastic Half-Space," *BSSA*, 54, pp. 627-680.

- Kaiser, J. F. and W. A. Reed (1977), "Data Smoothing Using Low-Pass Digital Filters," Rev. Sci. Instrum., 49, pp. 1147-1157.
- Minster, J. B. and A. M. Suteau (1977), "Far Field Waveforms from an Arbitrarily Expanding Transparent Spherical Cavity in a Prestressed Mechanism," Geophys. J. R. Astr. Soc., 50, pp. 215-233.
- Priestley, K. and J. Brune (1978), "Surface Waves and the Structure of the Great Basin of Nevada and Western Utah," J. Geophys. Res., 83, pp. 2265-2272.
- Toksöz, M. N., D. G. Harkrider and A. Ben-Menahem (1965), "Determination of Source Parameters by Amplitude Equalization of Seismic Surface Waves, 2. Release of Tectonic Strain by Underground Nuclear Explosions and Mechanisms of Earthquakes, J. Geophys. Res., 70, pp. 907-922.
- Toksöz, M. N., K. C. Thomson and T. J. Ahrens (1971), "Generation of Seismic Waves by Explosions in Prestressed Media," BSSA, 61, pp. 1589-1623.
- Toksöz, M. N. and H. H. Kehrner (1972), "Tectonic Strain Release by Underground Nuclear Explosions and Its Effect on Seismic Discrimination," Geophys. J. R. Astr. Soc., 31, pp. 141-161.

APPENDIX A

This appendix contains seismograms from MIGHTY EPIC and DIABLO HAWK which have not been placed in the body of the report. We include them here so as to have as complete a record as possible of the Lawrence Livermore Laboratories, Sandia Laboratories and Systems, Science and Software (S³) data.

Figures A.1 through A.4 show the radial components of ground velocity (both broad band and bandpass filtered) for the six stations which recorded both events. These figures accompany the reduced travel time plots in the text, Figures 5.3a through 5.6b.

Figures A.5 through A.9 show single station seismograms at locations where only one of the two events was recorded. Each figure displays, for all three components of motion, both the broad band signal and the bandpass filtered signal.

Figures A.10 through A.18 display the initial onset (P_n or P_g) for several of the stations.

MIGHTY EPIC, R

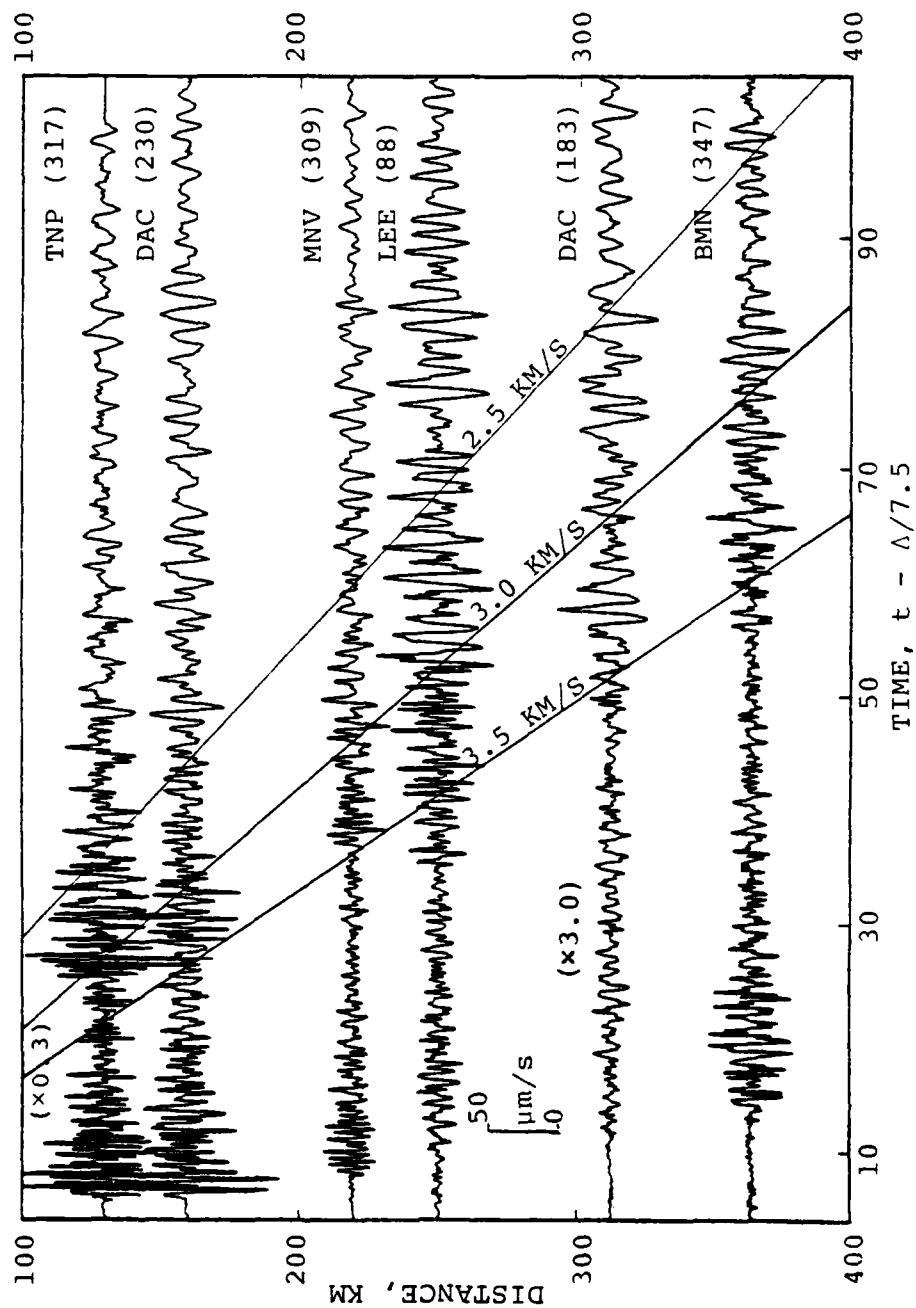


Figure A.1. Radial velocities for MIGHTY EPIC.

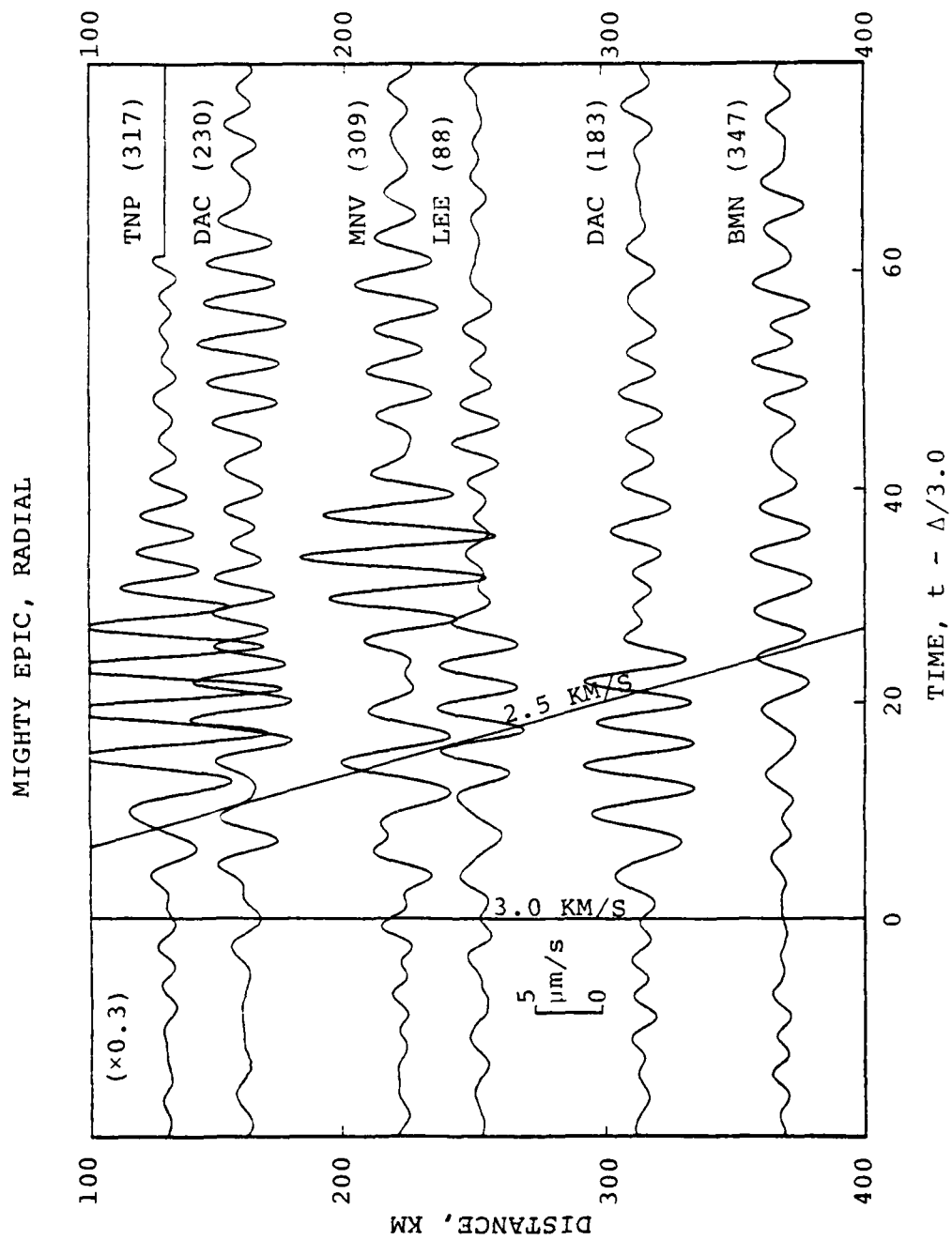


Figure A.2. Radial velocities for DIABLO HAWK.

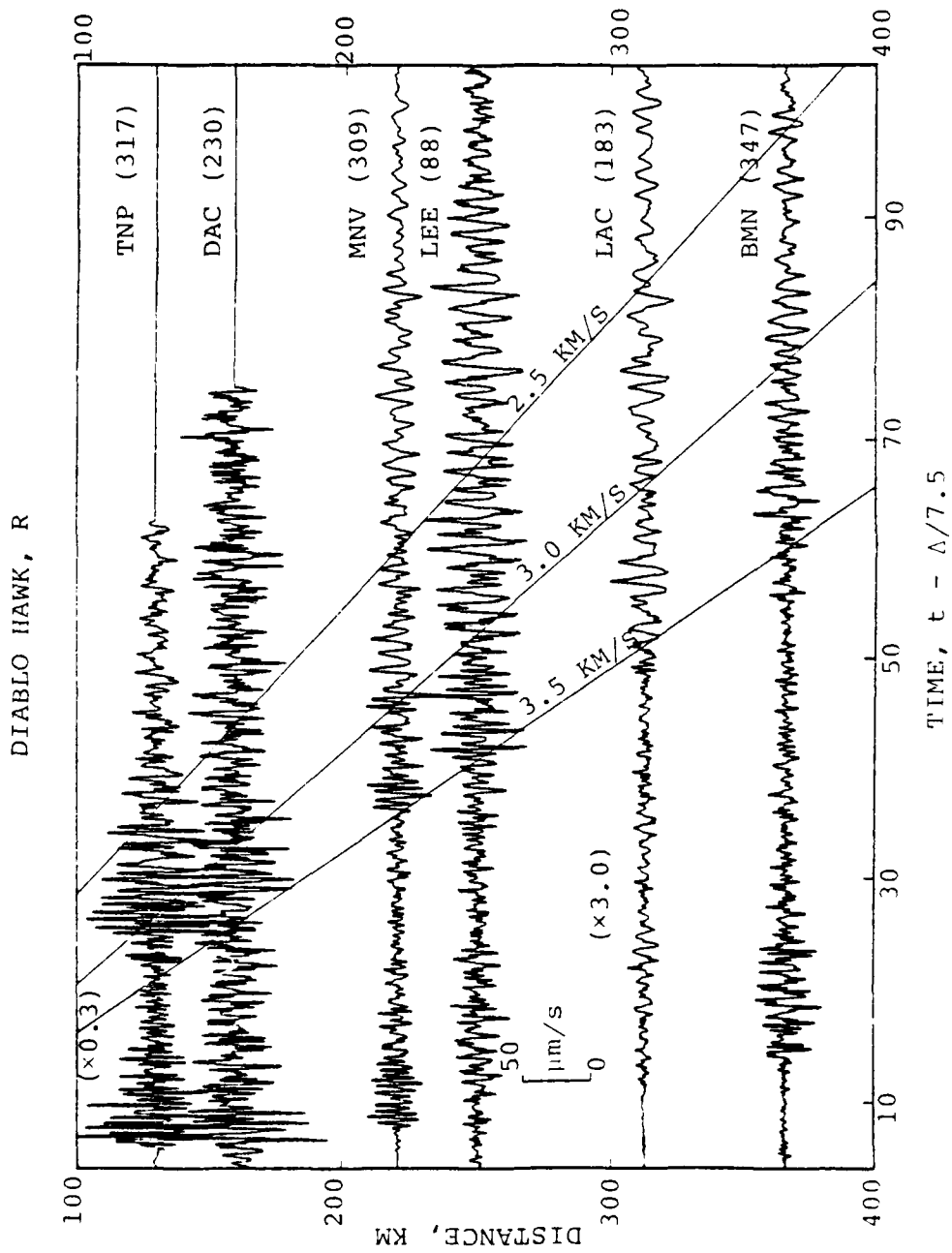


Figure A.3. Radial velocities for MIGHTY EPIC after filtering with a 4-8 second bandpass filter.

DIABLO HAWK, RADIAL

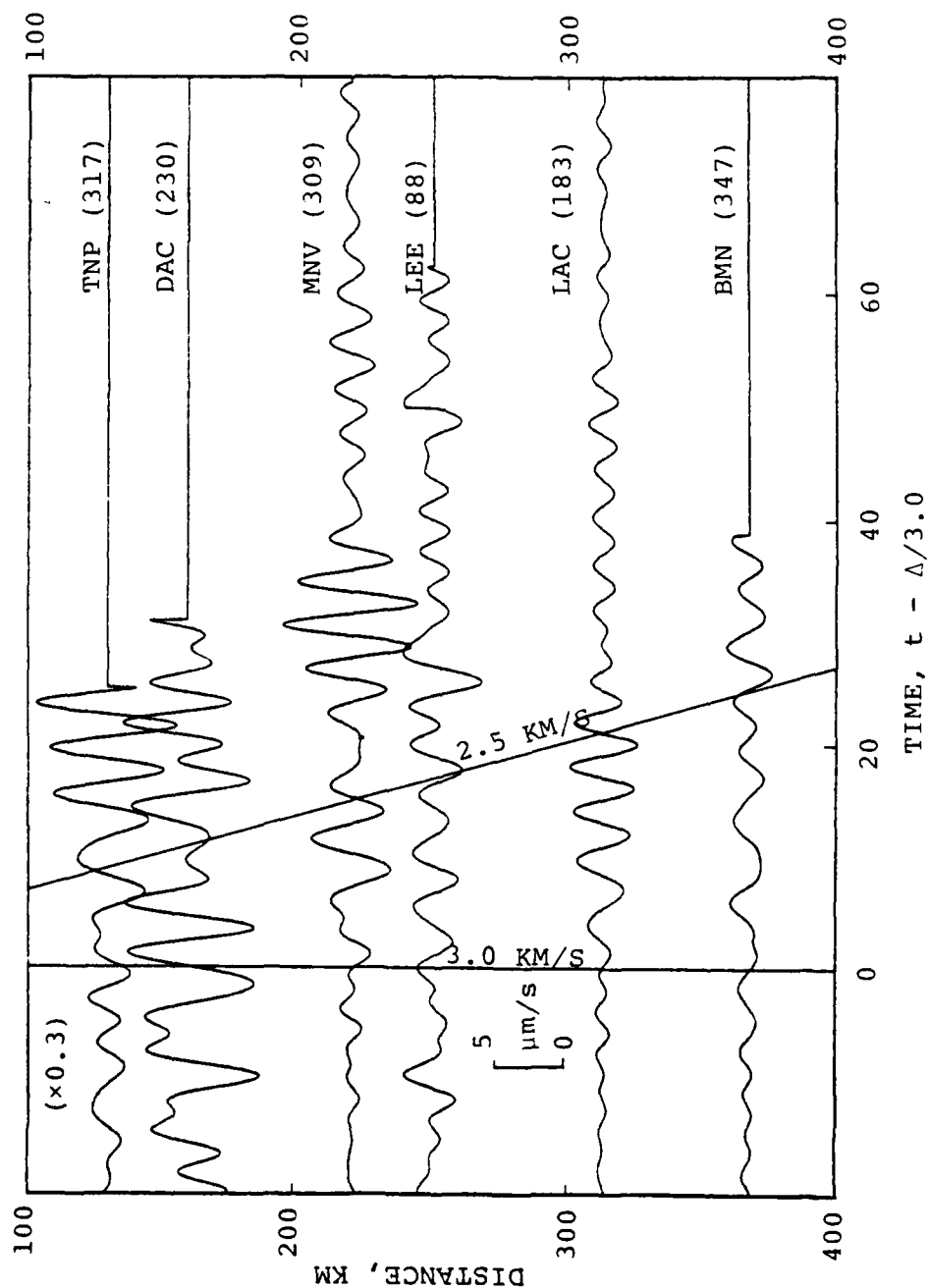


Figure A.4. Radial velocities for DIABLO HAWK after filtering with a 4-8 second bandpass filter.

DIABLO HAWK, BIG PINE

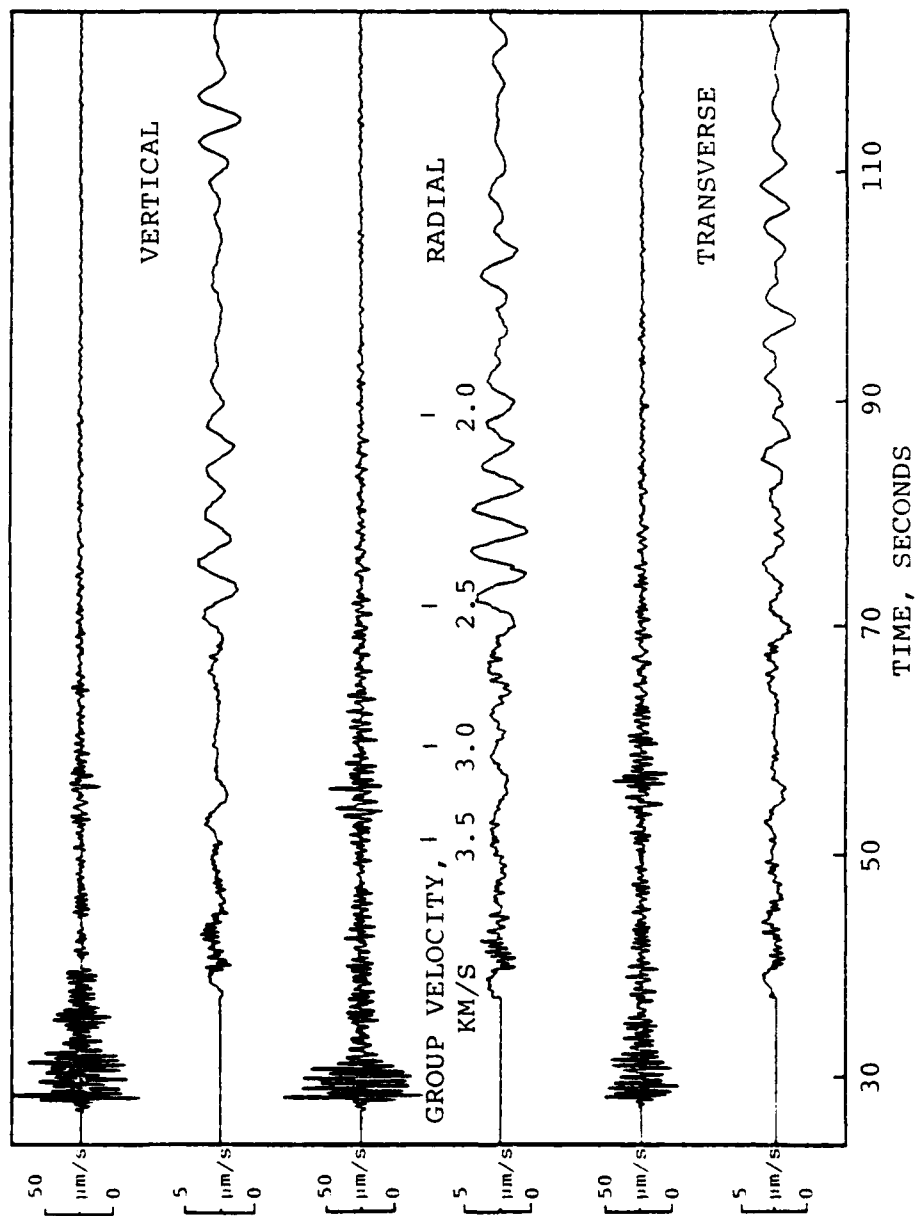


Figure A.5. Sprengnether seismograms for DIABLO HAWK recorded at Big Pine, California. In each pair of traces the upper curve shows the broad band signal and the lower curve shows the 4-8 second bandpass filtered signal.

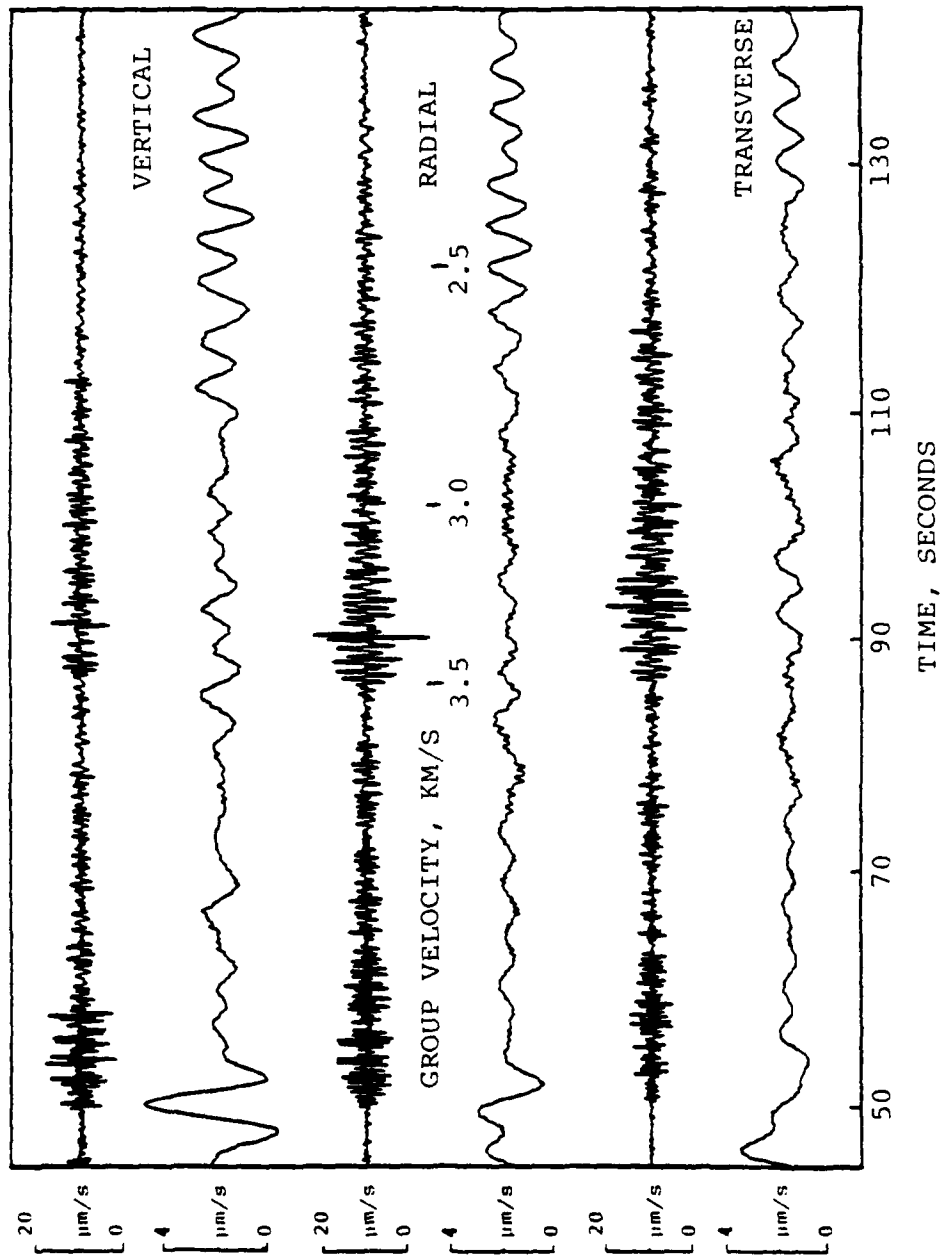


Figure A.6. Sprengnether seismograms for DIABLO HAWK recorded at Minersville, Utah. In each pair of traces the upper curve shows the broad band signal and the lower curve shows the 4-8 second bandpass filtered signal.

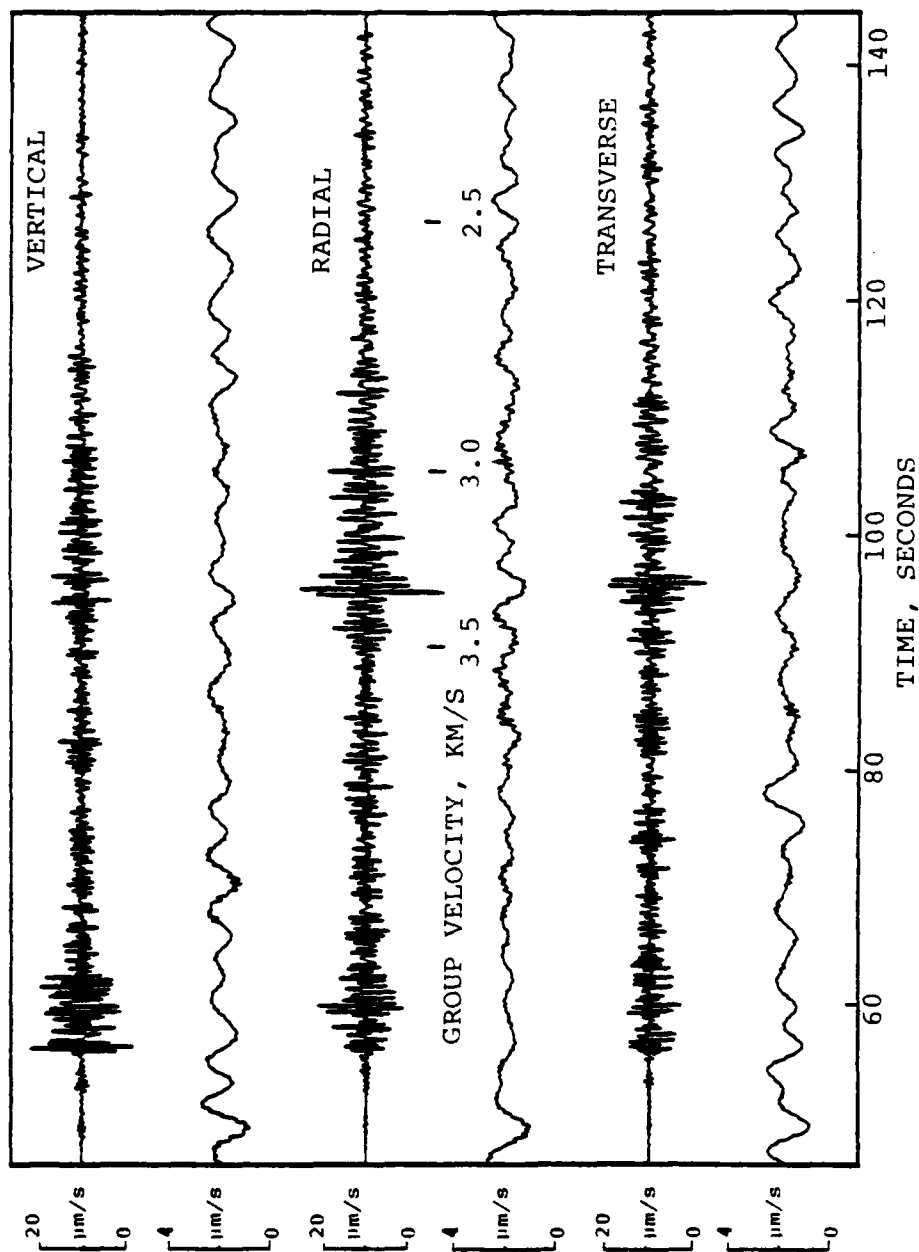


Figure A.7. Sprengnether seismograms for DIABLO HAWK recorded at Shellbourne, Nevada. In each pair of traces the upper curve shows the broad band signal and the lower curve shows the 4-8 second bandpass filtered signal.

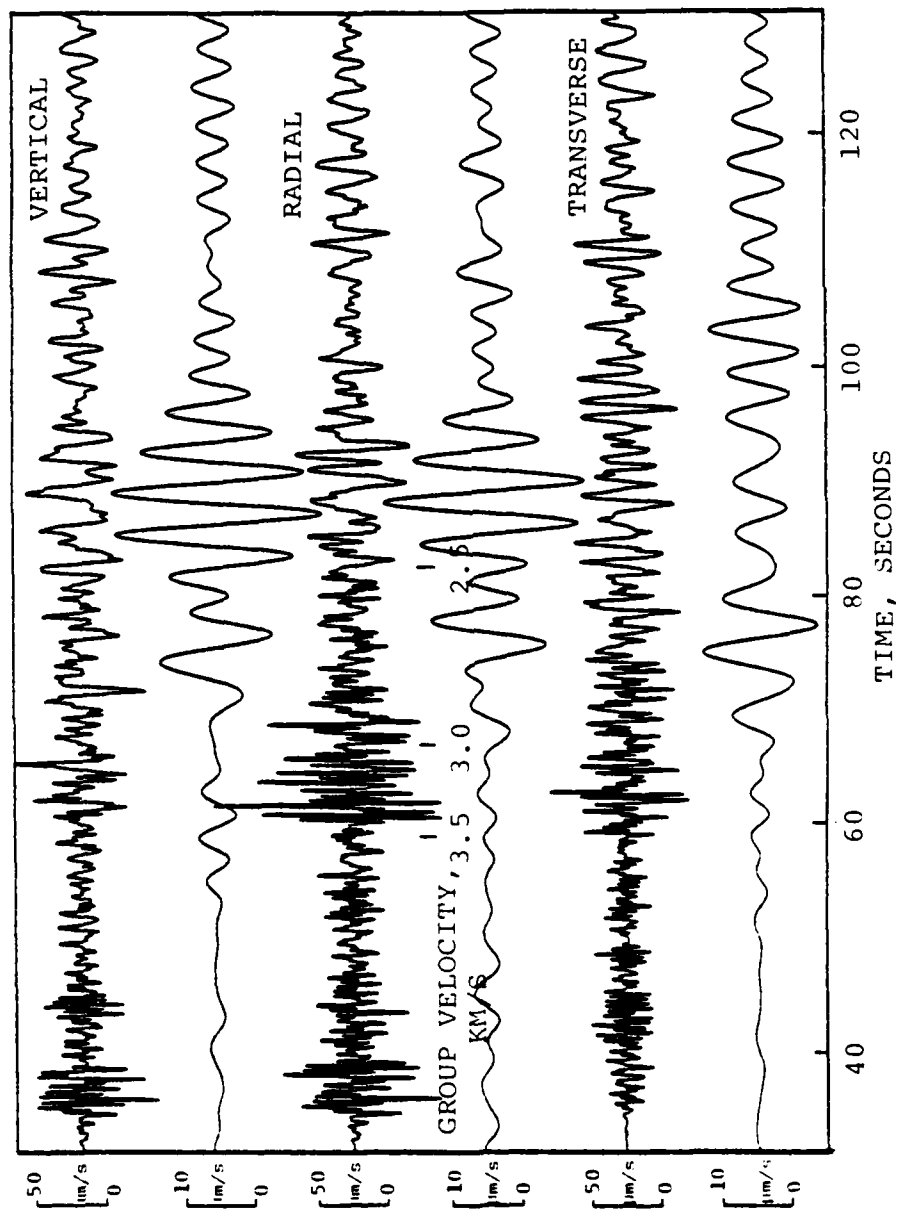


Figure A.8. Seismograms for MIGHTY EPIC recorded at Sandia station, Nelson, Nevada. In each pair of traces the upper curve shows the broad band signal and the lower curve shows the 4-8 second bandpass filtered signal.

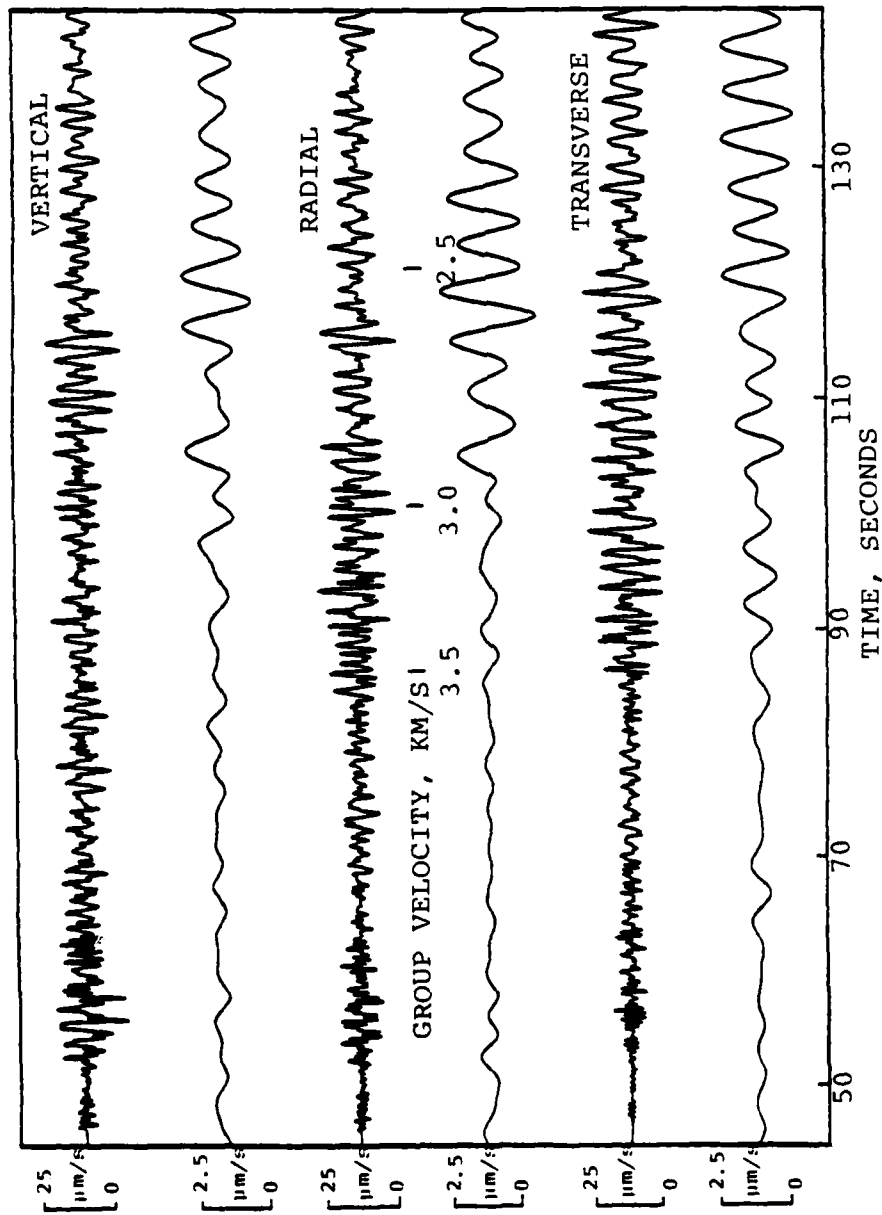


Figure A.9. Seismograms for DIABLO HAWK recorded at LLL station, Kanab, Utah. In each pair of traces the upper curve shows the broad band signal and the lower curve shows the 4-8 second bandpass filtered signal.

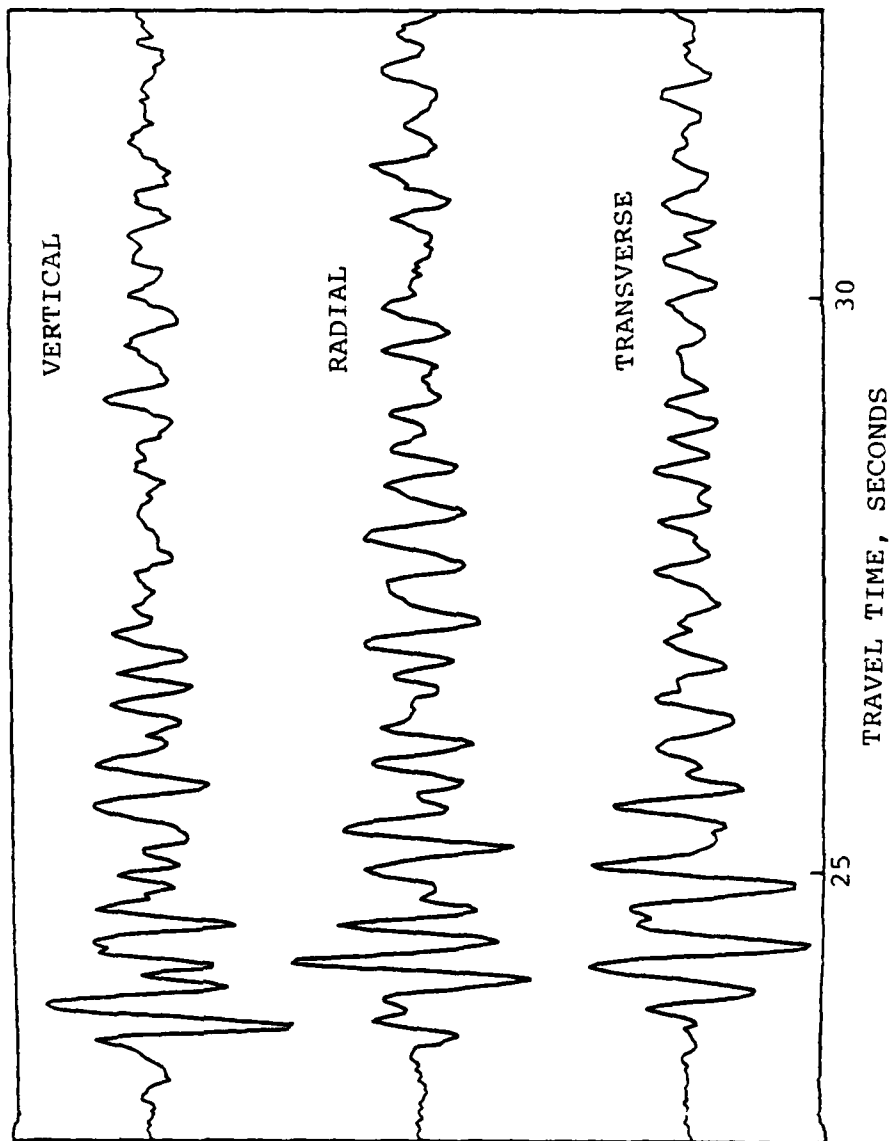


Figure A.10. The first ten seconds of the seismograms from MIGHTY EPIC recorded at Tonopah.

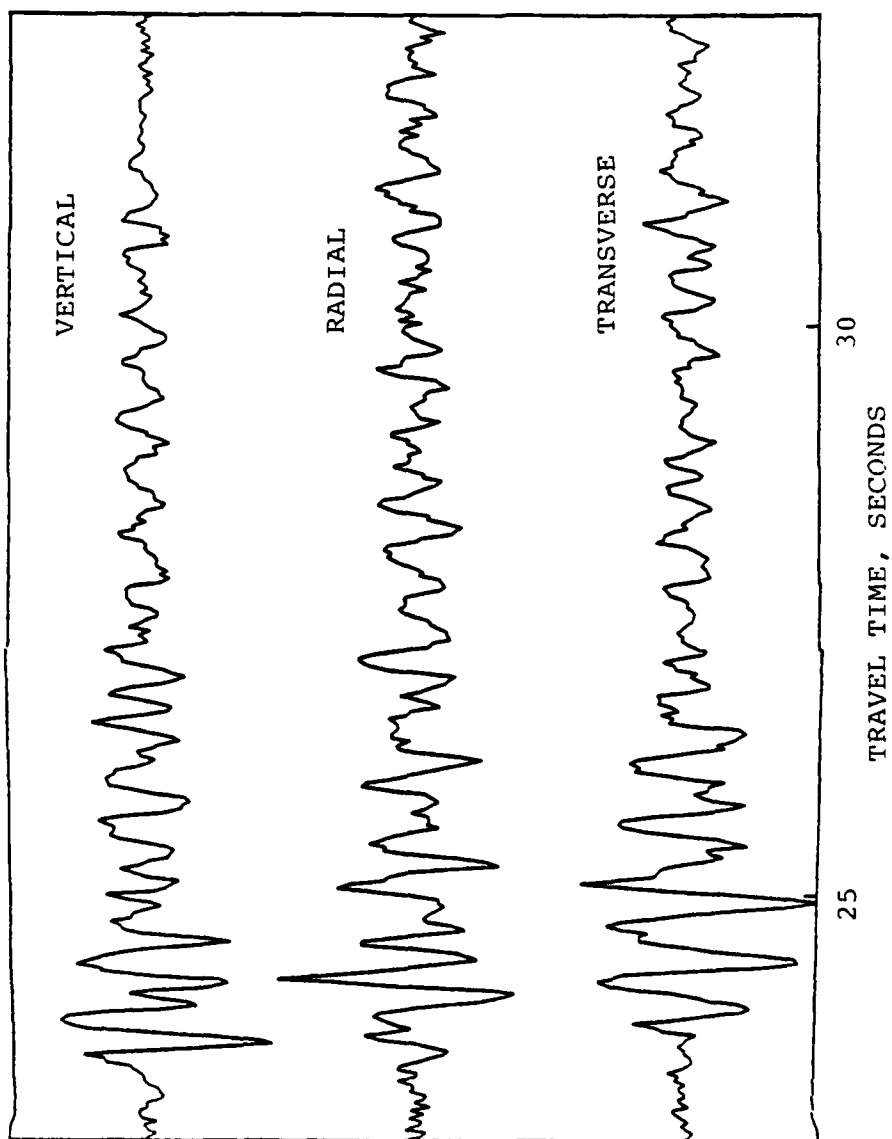


Figure A.11. The first ten seconds of the seismograms from DIABLO HAWK recorded at Tonopah.

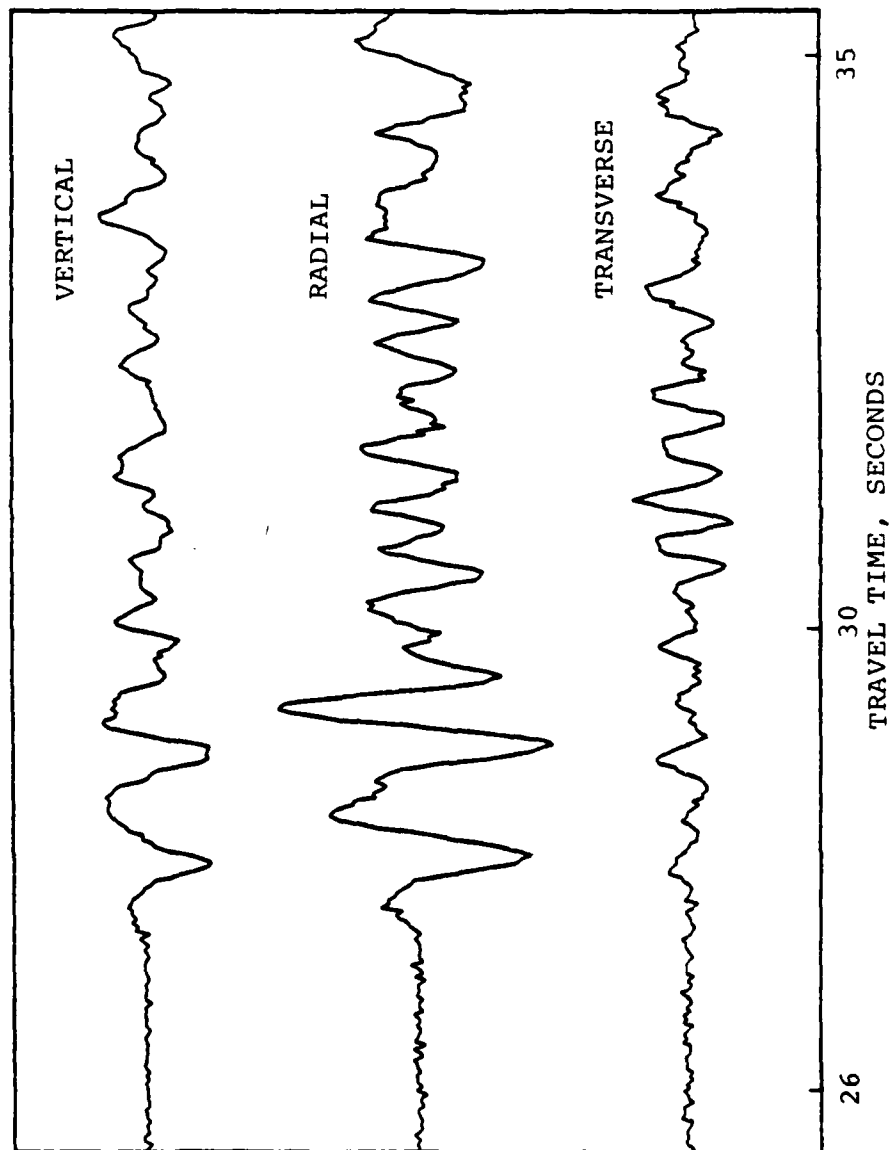


Figure A.12. The first ten seconds of the seismograms from MIGHTY EPIC recorded at Darwin.

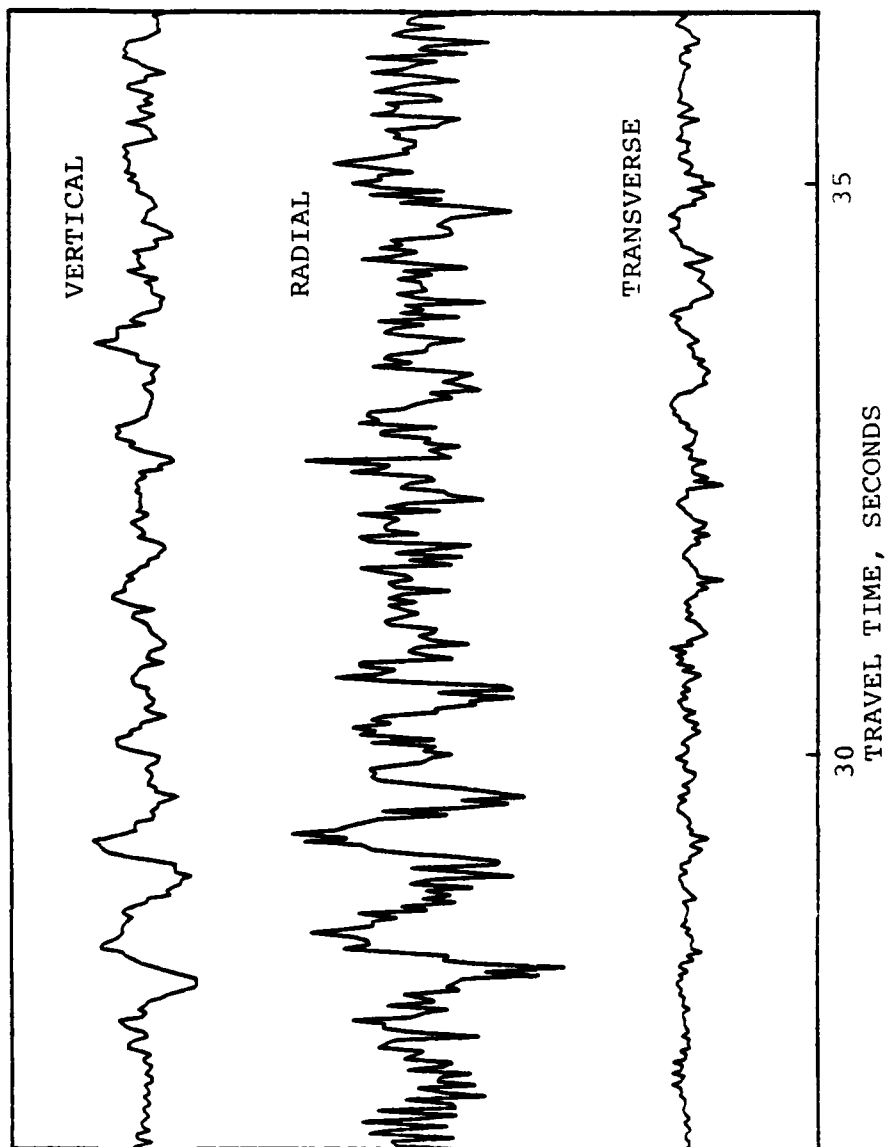


Figure A.13. The first ten seconds of the seismograms from DIABLO HAWK recorded at Darwin.

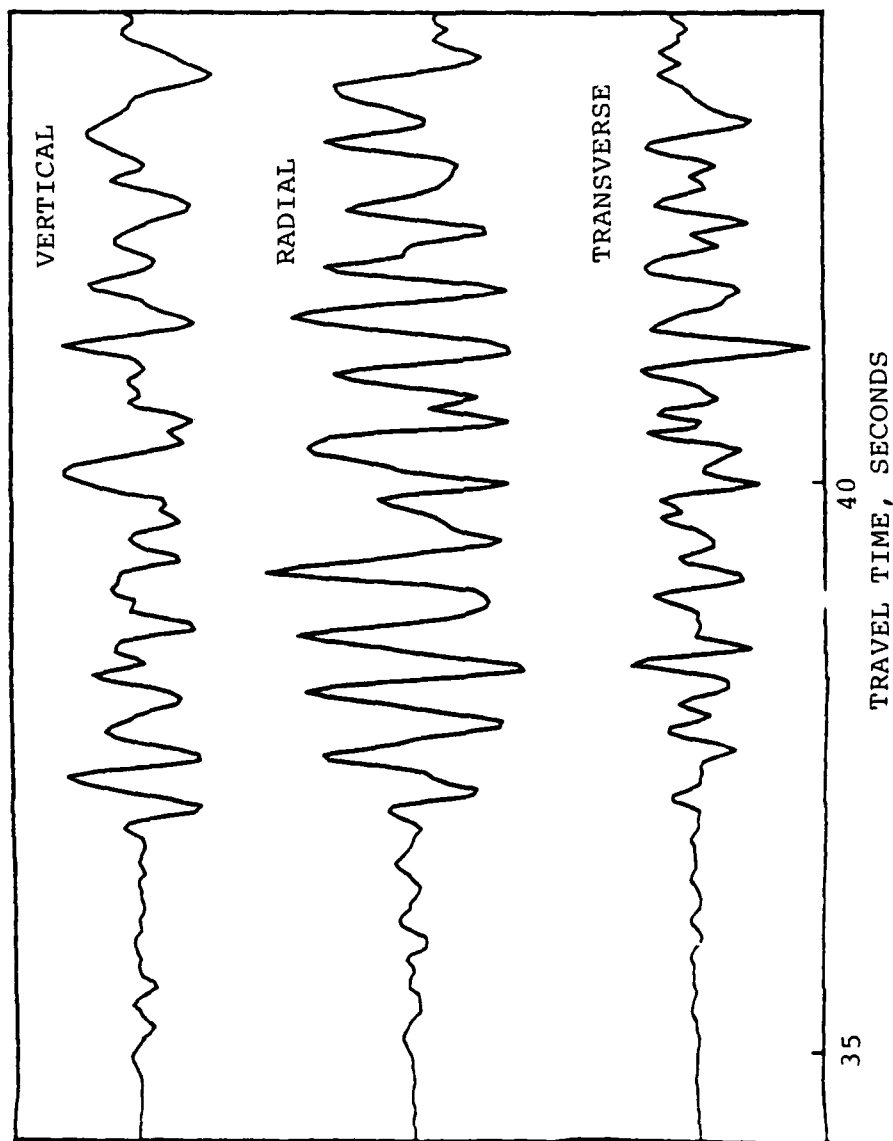


Figure A.14. The first ten seconds of the seismograms from MIGHTY EPIC recorded at Mina.

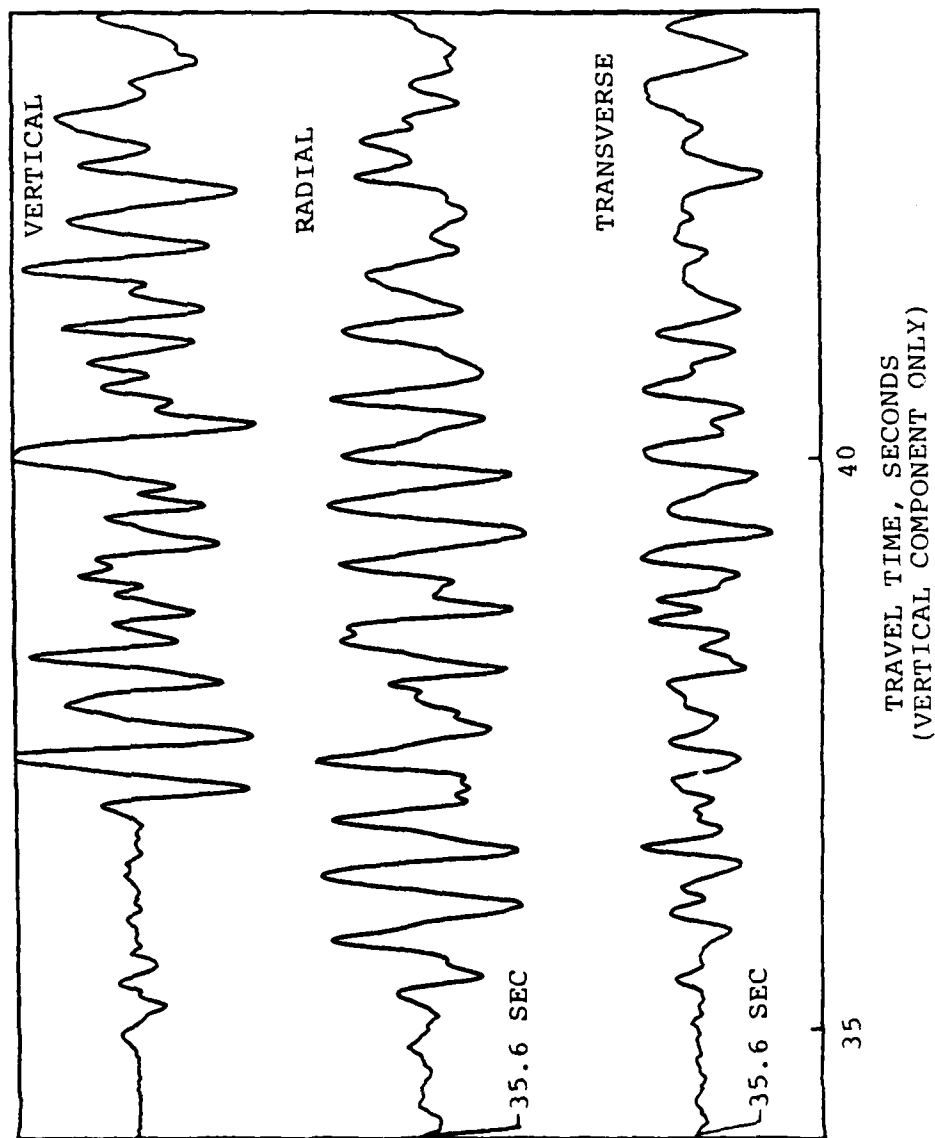


Figure A.15. The first ten seconds of the seismograms from DIABLO HAWK recorded at Mina.

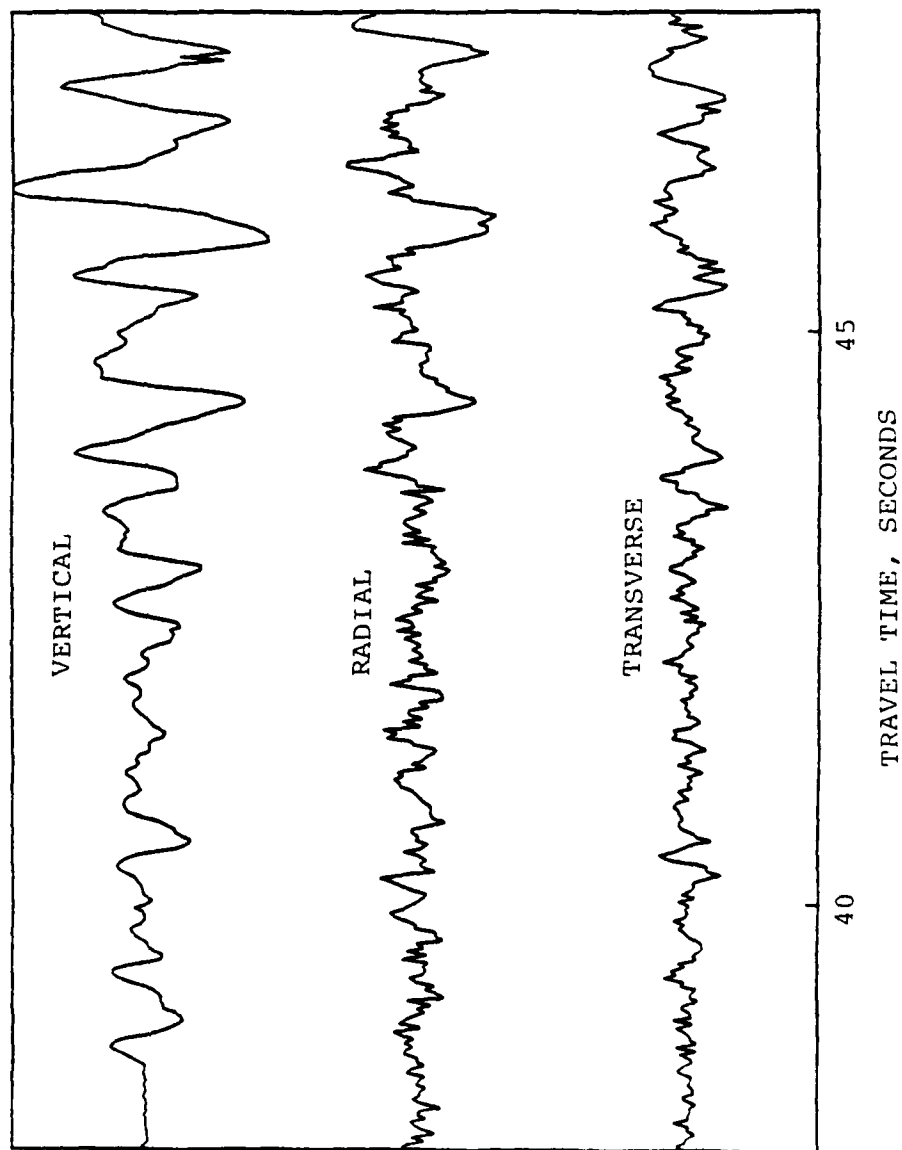


Figure A.16. The first ten seconds of the seismograms from MIGHTY EPIC recorded at Leeds.

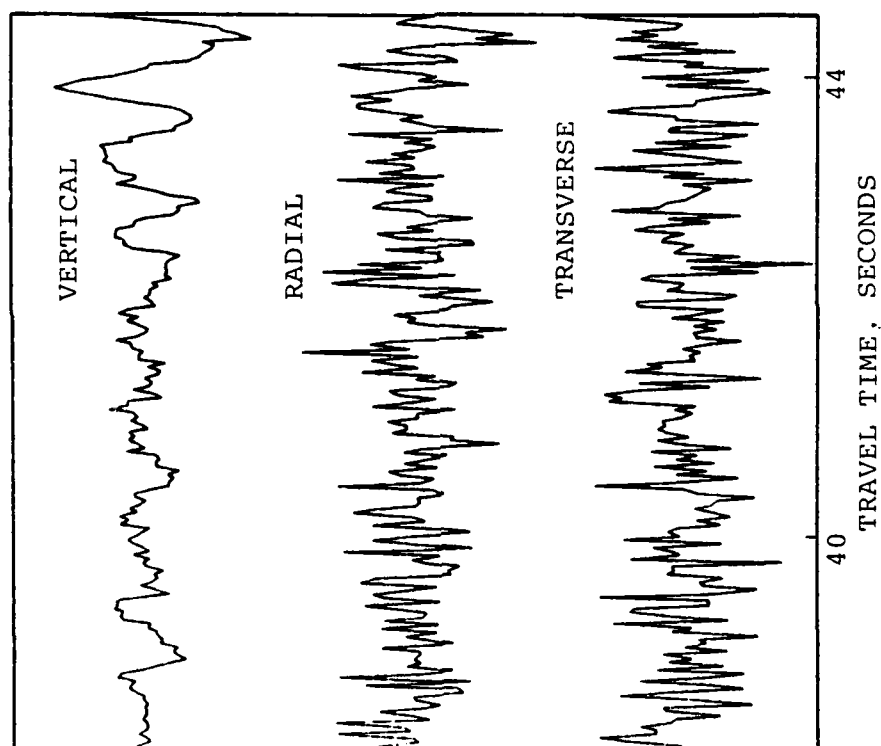


Figure A.17. The first six and one half seconds of the seismograms from DIABLO HAWK recorded at Leeds.

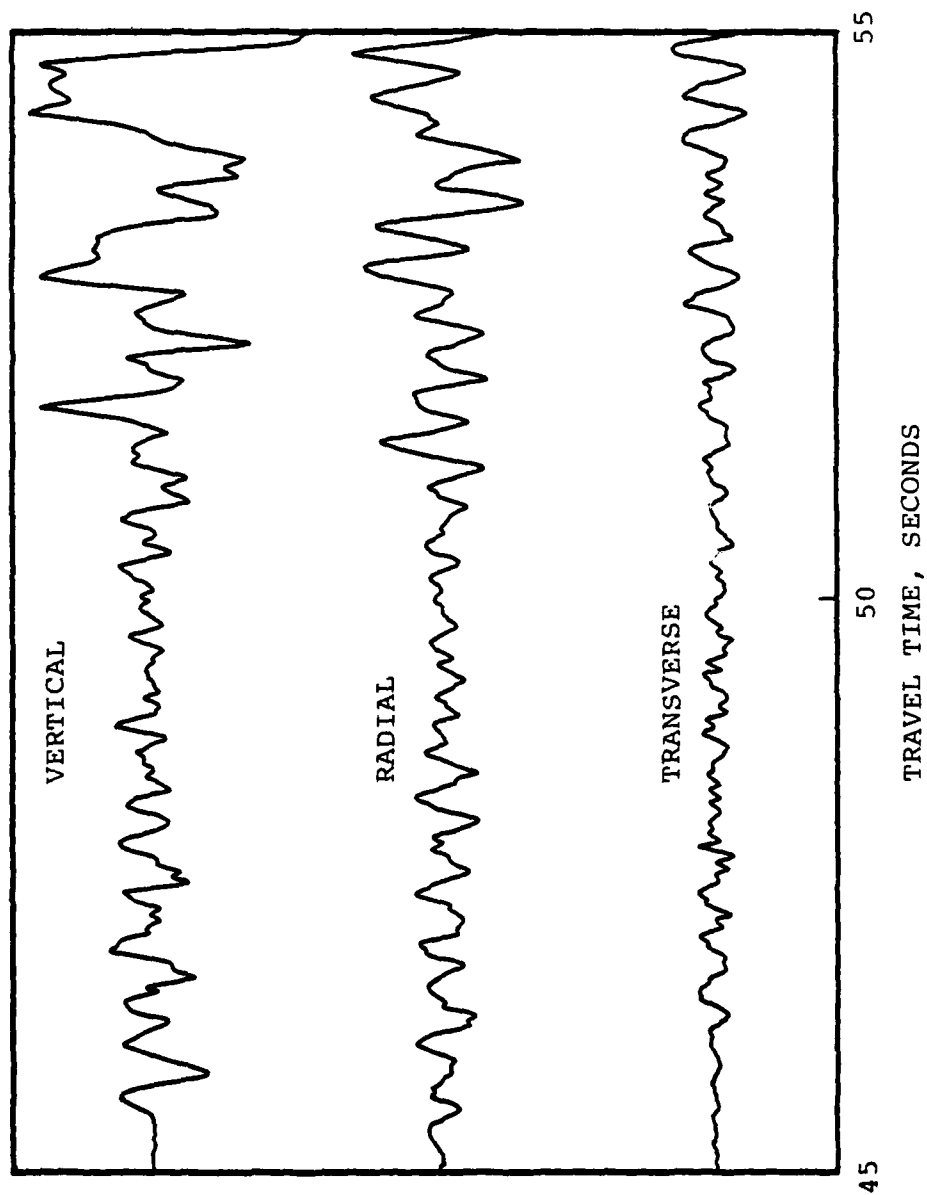


Figure A.18. The first ten seconds of the seismograms from DIABLO HAWK recorded at Kanab.

PRECEDING PAGE BLANK-NOT FILMED

DISTRIBUTION LIST

DEPARTMENT OF DEFENSE

Assistant to the Secretary of Defense
Atomic Energy
ATTN: Executive Assistant

Defense Advanced Rsch. Proj. Agency
ATTN: TIO

Defense Communications Agency
ATTN: Code 670, R. Lipp

Defense Intelligence Agency
ATTN: DB-4N
ATTN: DB-4C, E. O'Farrell
ATTN: DB-4C2, T. Ross

Defense Nuclear Agency
ATTN: DDST
ATTN: RAEV
ATTN: STRA
ATTN: STVL
2 cy ATTN: SPTD
2 cy ATTN: STSP
3 cy ATTN: SPSS
4 cy ATTN: TITL

Defense Technical Information Center
12 cy ATTN: DD

Federal Emergency Management Agency
ATTN: Hazard Eval. & Vul. Red. Div., G. Sisson

Field Command
Defense Nuclear Agency
ATTN: FCPR
ATTN: FCTMD
ATTN: FCTMOF
2 cy ATTN: FCTMO
4 cy ATTN: FCTMC

Field Command
Defense Nuclear Agency
Livermore Division
ATTN: FCPRL

Field Command
Defense Nuclear Agency
Los Alamos Branch
ATTN: FCPRA

Field Command, Test Directorate
2 cy ATTN: FCTC, J. LaComb

Interservice Nuclear Weapons School
ATTN: TTV

Joint Chiefs of Staff
2 cy ATTN: J-5

Joint Strat. Tgt. Planning Staff
ATTN: JLTW-2
ATTN: NRI-STINFO Library

DEPARTMENT OF DEFENSE (Continued)

NATO School (SHAPE)
ATTN: U.S. Documents Officer

Undersecretary of Def. for Rsch. & Engrg.
ATTN: Strategic & Space Systems (OS)

DEPARTMENT OF THE ARMY

BMD Advanced Technology Center
Department of the Army
ATTN: 1CRDABH-X
ATTN: ATC-T

BMD Program Office
Department of the Army
ATTN: DACS-BMT

BMD Systems Command
Department of the Army
ATTN: BMDSC-HW, R. DeKalb
ATTN: BMDSC-H, N. Hurst

Chief of Engineers
Department of the Army
ATTN: DAEN-RDM
ATTN: DAEN-MCE-D

Construction Engineering Rsch. Lab.
Department of the Army
ATTN: CERL-SOI-L

Deputy Chief of Staff for Ops. & Plans
Department of the Army
ATTN: MOCA-ADL

Deputy Chief of Staff for Rsch., Dev. and Acq.
Department of the Army
ATTN: DAMA-CSS-N
2 cy ATTN: DAMA-CSS

Harry Diamond Laboratories
Department of the Army
ATTN: DELHD-N-P
ATTN: DELHD-N-EM
ATTN: DELHD-I-TL
ATTN: DELHD-N-RBH, A. Baba
ATTN: DELHD-N-P, J. Gwaltney

U.S. Army Ballistic Research Labs.
ATTN: DRDAR-TSB-S
ATTN: DRDAR-BLV
ATTN: DRDAR-BLT, W. Taylor
ATTN: DRDAR-BLE, J. Keefer

U.S. Army Cold Region Res. Engr. Lab.
ATTN: Commander and Director

U.S. Army Communications Command
ATTN: Technical Reference Division

DEPARTMENT OF THE ARMY (Continued)

U.S. Army Engineer Center
ATTN: DT-LRC

U.S. Army Engineer, Dist. Omaha
ATTN: MROED-D, C. Distefano

U.S. Army Engineer Div., Huntsville
ATTN: C. Huang
ATTN: HNDSD-SR

U.S. Army Engineer Div., Ohio River
ATTN: ORDAS-L

U.S. Army Engr. Waterways Exper. Station
ATTN: WESSE, L. Ingram
ATTN: J. Strange
ATTN: WESSD, G. Jackson
ATTN: J. Ingram
ATTN: Library
ATTN: WESSA, W. Flathau
ATTN: WESSS, J. Ballard
ATTN: J. Day
ATTN: J. Drake
ATTN: P. Miakar

U.S. Army Materiel & Mechanics Rsch. Ctr.
ATTN: Technical Library

U.S. Army Materiel Dev. & Readiness Cmd.
ATTN: DRXAM-TL

U.S. Army Missile Command
ATTN: RSIC
ATTN: DRSMI-RKP, W. Thomas

U.S. Army Nuclear & Chemical Agency
ATTN: Library for ATCA-NAW
ATTN: Library

DEPARTMENT OF THE NAVY

Naval Construction Battalion Center
ATTN: Code L51, S. Takahashi
ATTN: Code L51, R. Odello
ATTN: Code L51, W. Shaw
ATTN: Code L08A
ATTN: Code L51, J. Crawford
ATTN: Code L44, H. Haynes

Naval Electronic Systems Command
ATTN: PME 117-21
ATTN: PME 117-211, B. Kruger

Naval Facilities Engineering Command
ATTN: Code 03T
ATTN: Code 04B
ATTN: Code 09M22C

Naval Materiel Command
ATTN: MAT 08T-22

Naval Plant Representative Office
Strategic Systems Project Office
Lockheed Missile and Space Company
2 cy ATTN: SPL 325

DEPARTMENT OF THE NAVY (Continued)

Naval Postgraduate School
ATTN: Code 0142

Naval Research Laboratory
ATTN: Code 2627

Naval Surface Weapons Center
ATTN: Code F30, K. Enkenhaus
ATTN: Code F30
ATTN: Code F31

Naval Surface Weapons Center
ATTN: Technical Library & Information
Service Branch

Naval War College
ATTN: Code E-11

Naval Weapons Evaluation Facility
ATTN: Code 10

Naval Underwater Systems Center
ATTN: Code EM, J. Kalinowski

Office of Naval Research
ATTN: Code 474, N. Perrone
ATTN: Code 715

Office of the Chief of Naval Operations
ATTN: OP 981
ATTN: OP 03EG

Strategic Systems Project Office
Department of the Navy
ATTN: NSP-27331
ATTN: Document Control Off. for SP272,
H. Nakayama
ATTN: NSP-27201
ATTN: NSP-43
ATTN: NSP-273
ATTN: NSP-272

DEPARTMENT OF THE AIR FORCE

Air Force Geophysics Laboratory
ATTN: LWL, K. Thompson

Air Force Institute of Technology
ATTN: Library

Air Force Systems Command
ATTN: DLW
ATTN: Technical Library
ATTN: R. Cross

Assistant Chief of Staff, Intelligence
Department of the Air Force
ATTN: INT

Ballistic Missile Office
Air Force Systems Command
ATTN: DEB

Operations, Plans and Readiness
Department of the Air Force
ATTN: AFXODC

DEPARTMENT OF THE AIR FORCE (Continued)

Air Force Weapons Laboratory
Air Force Systems Command

ATTN: DYC
ATTN: DES, J. Shinn
ATTN: DES, R. Jolley
ATTN: DYV
ATTN: DES, J. Thomas
ATTN: DE, M. Plamondon
ATTN: NT, D. Payton
ATTN: DES-C, R. Henny
ATTN: NT
ATTN: SUL
ATTN: DED
ATTN: NS
2 cy ATTN: DY

Ballistic Missile Office
Air Force Systems Command

ATTN: MNH
ATTN: MMH
ATTN: MNN
ATTN: MNNH

Research, Development, & Acq.
Department of the Air Force
ATTN: AFRDQSM, L. Montulli
ATTN: AFRDQSM

Logistics & Engineering
Department of the Air Force
ATTN: LEEF

Foreign Technology Division
Air Force Systems Command
ATTN: SDBF, S. Spring
ATTN: SDBG
ATTN: TQTD
ATTN: NIIS Library

Headquarters Space Division
Air Force Systems Command
ATTN: Director, ABRES

Headquarters Space Division
Air Force Systems Command
ATTN: RSSE
ATTN: RSS

Rome Air Development Center
Air Force Systems Command
ATTN: TSLD

Strategic Air Command
Department of the Air Force
ATTN: NRI-STINFO Library

Vela Seismological Center
ATTN: G. Ullrich

DEPARTMENT OF ENERGY

Department of Energy
Albuquerque Operations Office
ATTN: CTIU

Department of Energy
ATTN: Document Control for OMA

DEPARTMENT OF ENERGY (Continued)

Department of Energy
Nevada Operations Office
ATTN: Mail & Records for Tech. Library

DEPARTMENT OF ENERGY CONTRACTORS

Lawrence Livermore Laboratory
ATTN: Document Control for J. Shearer
ATTN: Document Control for J. Morton
ATTN: Document Control for L-125, J. Keller
ATTN: Document Control for L-38, H. Reynolds
ATTN: Document Control for L-45, T. Boster
ATTN: Document Control for L-34, R. Birkett
ATTN: Document Control for Technical
Information Department Library
ATTN: Document Control for H. Heard
ATTN: Document Control for L-113, V. Karpenko
ATTN: Document Control for L-24, O. Vik
ATTN: Document Control for L-21, D. Oakley
ATTN: Document Control for L-96, L. Woodruff
ATTN: Document Control for L-18, J. Carothers

Los Alamos Scientific Laboratory
ATTN: Document Control for B. Killian
ATTN: Document Control for J. Johnson
ATTN: Document Control for L. Germaine
ATTN: Document Control for R. Brownlee
ATTN: Document Control for F. App
ATTN: Document Control for P. Ginsberg
ATTN: Document Control for R. Skaggs
ATTN: Document Control for MS 364
ATTN: Document Control for R. Bridwell
ATTN: Document Control for R. Dingus
ATTN: Document Control for J. McQueen
ATTN: Document Control for P. Whalen
ATTN: Document Control for J. Fuller

Oak Ridge National Laboratory
ATTN: Civil Def. Res. Proj.
ATTN: Document Control for Central Research
Library

Sandia Laboratories
Livermore Laboratory
ATTN: Document Control for Library & Sec.
Class. Div.

Sandia Laboratories
ATTN: Document Control for L. Vortman
ATTN: Document Control for A. Chabai
ATTN: Document Control for B. Bader
ATTN: Document Control for L. Hill
ATTN: Document Control for C. Broyles
ATTN: Document Control for J. Plimpton
ATTN: Document Control for G. Kinoshita
ATTN: Document Control for W. Weart
ATTN: Document Control for 3141
ATTN: Document Control for L. Tyler
ATTN: Document Control for J. Kennedy

OTHER GOVERNMENT AGENCIES

Central Intelligence Agency
ATTN: OSI/NED, J. Ingley

Department of the Interior
Bureau of Mines
ATTN: Technical Library

OTHER GOVERNMENT AGENCIES (Continued)

Department of the Interior
U.S. Geological Survey
ATTN: R. Carroll
ATTN: W. Twenhofel

DEPARTMENT OF DEFENSE CONTRACTORS

Aerospace Corp.
ATTN: V. Stephenson
ATTN: J. McClelland
ATTN: Technical Information Services
ATTN: P. Mathur
ATTN: R. Crolius
ATTN: S. Bower
ATTN: F. Hai
ATTN: L. Selzer

Agbabian Associates
ATTN: M. Agbabian
ATTN: C. Bagge

Analytic Services, Inc.
ATTN: G. Hesselbacher

Applied Theory, Inc.
2 cy ATTN: J. Trulio

Artec Associates, Inc.
ATTN: S. Gill

AVCO Research & Systems Group
ATTN: Library A830

BDM Corp.
ATTN: T. Neighbors
ATTN: Corporate Library

BDM Corp.
ATTN: Library

Boeing Co.
ATTN: J. Wooster
ATTN: R. Dyrdaahl
ATTN: Aerospace Library
ATTN: M/S, 42/37, K. Friddell
ATTN: T. Berg
ATTN: H. Leistner

California Institute of Technology
ATTN: T. Ahrens

California Research & Technology, Inc.
ATTN: K. Kreyenhagen
ATTN: S. Shuster
ATTN: Library

California Research & Technology, Inc.
ATTN: D. Orphal

Calspan Corp.
ATTN: Library

Civil Systems Inc.
ATTN: J. Bratton
ATTN: C. Melzer

Civil Systems, Inc.
ATTN: S. Blouin

DEPARTMENT OF DEFENSE CONTRACTORS (Continued)

University of Denver
ATTN: Sec. Officer for J. Wisotski

EG&G Washington Analytical Services Center, Inc.
ATTN: Library

Electromechanical Sys. of New Mexico, Inc.
ATTN: R. Shunk

Eric H. Wang
Civil Engineering Rsch. Fac.
University of New Mexico
ATTN: N. Baum
ATTN: G. Leigh

Foster-Miller Associates, Inc.
ATTN: J. Hampson for E. Foster

Franklin Institute
ATTN: Z. Zudans

Gard, Inc.
ATTN: G. Neidhardt

General Electric Co.
ATTN: N. Dispenziere

General Electric Company-TEMPO
ATTN: DASIAC

H-Tech Labs, Inc.
ATTN: B. Hartenbaum

IIT Research Institute
ATTN: R. Welch
ATTN: M. Johnson
ATTN: Documents Library

University of Illinois, Consulting Services
ATTN: N. Newmark
ATTN: W. Hall
ATTN: A. Hendron

Institute for Defense Analyses
ATTN: Classified Library

IRT Corp.
ATTN: C. Pepper

J. H. Wiggins Co., Inc.
ATTN: J. Collins

Kaman Avidyne
ATTN: N. Hobbs
ATTN: E. Criscione
ATTN: Library

Kaman Sciences Corp.
ATTN: W. Ware
ATTN: W. Rich
ATTN: Library
ATTN: D. Foxwell
ATTN: H. Hollister
ATTN: F. Shelton

DEPARTMENT OF DEFENSE CONTRACTORS (Continued)

Lockheed Missiles & Space Co., Inc.

ATTN: L. Chase
ATTN: Technical Information Center
ATTN: S. Salisbury
ATTN: T. Geers

Lockheed Missiles & Space Co., Inc.

ATTN: J. Wilson
ATTN: A. Risso
ATTN: E. Smith

Lovelace Biomedical & Environmental Res. Inst., Inc.

ATTN: Technical Library
ATTN: R. Jones

Massachusetts Institute of Technology

ATTN: W. Brace

McDonnell Douglas Corp.

ATTN: H. Berkowitz
ATTN: R. Halprin
ATTN: J. Kirby

Merritt CASES, Inc.

ATTN: Library
ATTN: J. Merritt

Mission Research Corp.

ATTN: Sec. Ofc. for C. Longmire

Mission Research Corp.

ATTN: D. Merewether

Mission Research Corp.-San Diego

ATTN: V. Van Lint

Mitre Corp.

ATTN: Technical Report Center

University of New Mexico

ATTN: G. Triandafalidis

Northwestern University Technology Institute

ATTN: T. Belytschko

Pacific-Sierra Research Corp.

ATTN: H. Brode

Pacifica Technology

ATTN: G. Kent
ATTN: R. Bjork

Physics International Co.

ATTN: C. Vincent
ATTN: E. Moore
ATTN: L. Behrmann
ATTN: C. Godfrey
ATTN: F. Sauer
ATTN: J. Kochley
ATTN: J. Thomsen
ATTN: Technical Library

R & D Associates

ATTN: H. Cooper

Rand Corp.

ATTN: Library
ATTN: A. Laupa

DEPARTMENT OF DEFENSE CONTRACTORS (Continued)

R & D Associates

ATTN: W. Graham, Jr.
ATTN: J. Lewis
ATTN: Technical Information Center
ATTN: C. MacDonald
ATTN: R. Port
ATTN: D. Shrinivasa
ATTN: W. Wright, Jr.
ATTN: F. Field
ATTN: R. Schaefer
ATTN: J. Carpenter
ATTN: A. Latter

Science Applications, Inc.

ATTN: R. Parkinson
ATTN: O. Nance
ATTN: Technical Library

Science Applications, Inc.

ATTN: R. Miller

Science Applications, Inc.

ATTN: J. Hill

Science Applications, Inc.

ATTN: D. Bernstein
ATTN: Technical Library
ATTN: D. Maxwell

Science Applications, Inc.

ATTN: B. Chambers III

Southwest Research Institute

ATTN: W. Baker
ATTN: A. Wenzel

SRI International

ATTN: Y. Gupta
ATTN: B. Holmes
ATTN: T. Morita
ATTN: G. Carpenter
ATTN: D. Keough
ATTN: B. Gasten
ATTN: G. Abrahamson
ATTN: H. Lindberg

Systems, Science & Software, Inc.

ATTN: T. Riney
ATTN: T. Cherry
ATTN: W. Wray
ATTN: P. Coleman
ATTN: R. Duff
ATTN: T. Bache
ATTN: b. Pyatt
ATTN: D. Grine
ATTN: Library
ATTN: C. Dismukes
ATTN: W. Farrell
ATTN: D. Lambert

Systems, Science & Software, Inc.

ATTN: J. Murphy

Teledyne Brown Engineering

ATTN: M. Patel

Tetra Tech, Inc.

ATTN: T. Simpson

DEPARTMENT OF DEFENSE CONTRACTORS (Continued)

Terra Tek, Inc.
ATTN: H. Pratt
ATTN: A. Abou-Sayed
ATTN: Library
ATTN: S. Green

Tetra Tech, Inc.
ATTN: Library
ATTN: L. Hwang

Texas A & M University System
ATTN: J. Handin

Theodore B. Belytschko
ATTN: T. Belytschko

TRW Defense & Space Sys. Group
ATTN: G. Hulcher
ATTN: E. Wong

DEPARTMENT OF DEFENSE CONTRACTORS (Continued)

TRW Defense & Space Sys. Group
ATTN: Technical Information Center
ATTN: P. Bhutta
ATTN: D. Cramond
ATTN: P. Dai

Universal Analytics, Inc.
ATTN: E. Field

Weidlinger Assoc., Consulting Engineers
ATTN: I. Sandler
ATTN: M. Baron

Weidlinger Assoc., Consulting Engineers
ATTN: J. Isenberg

Westinghouse Electric Corp.
ATTN: W. Volz